TABLE OF CONTENTS

Preface . . . . iii 1/A8

CHAPTER I **Introductory Considerations** 1 1/A10

1. Description of the Hypothetical Helicopter Configuration 2 1/A11
1.1 Weights 3 1/A12
1.2 Main Rotor and Tail Rotor Geometry 4 1/A13
1.3 Transmission Limits 7 1/B2
1.4 Airframe Configuration 8 1/B3

2. Performance Summary 8 1/B3

3. Engine Performance 9 1/B4
3.1 General Characteristics of Shaft Turbines 9 1/B4
3.2 Power Ratings & Effects of Ambient Conditions on Engine Characteristics 10 1/B5
3.3 Powerplant for Hypothetical Helicopter 11 1/B6
3.4 Engine Power Constraints 13 1/B8
3.5 Engine Installation Losses 14 1/B9

4. Standard Day Atmosphere 15 1/B10

References for Chapter I 19 1/B14

CHAPTER II **Single-Rotor Helicopter & Vertical-Climb Performance** 20 1/C1

1. Hover Out-of-Ground-Effect Performance 22 1/C3
1.1 General Procedure 22 1/C3
1.2 Power vs Thrust Calculations 23 1/C4
1.3 Example of the Main Rotor Power Required 27 1/C8
1.4 Tail-Rotor Power Required 34 1/D1
1.5 Fuselage Download 37 1/D4
1.6 Transmission and Accessory Losses 43 1/D10

2. Hover In-Ground-Effect (IGE) Performance 44 1/D11
2.1 Rotor Thrust Variation, IGE 44 1/D11
2.2 IGE Download 44 1/D11

3. Hover Ceiling OGE and IGE 46 1/D13

4. Vertical-Climb Capability 48 1/E1
4.1 Detailed Analysis 48 1/E1
4.2 Simplified Vertical Climb Predictions 54 1/E8

References for Chapter II 56 1/E10

CHAPTER III **Forward-Flight Performance** 57 1/E11

1. Introductory Remarks 59 1/E13

2. Drag Estimates 60 1/E14
2.1 Drag of Streamlined Components 61 1/F1
2.2 Drag of Nonstreamlined Components 65 1/F5
2.3 Trim Drag 69 1/F9
2.4 Miscellaneous Items 72 1/F12
2.5 Net Engine Thrust 73 1/F13
2.6 Detailed Sample Drag Calculations for the Hypothetical Helicopter 74 1/F14

3. Methodology for Determining Level-Flight Power Required 78 1/G4
3.1 Trim Analysis Computer Program 79 1/G5
3.2 Nonuniform Downwash (NUD) Correction 82 1/G8
3.3 Parasite Power Correction 87 1/G13
3.4 Determination of Low-Speed Power Required 88 1/G14

4. Examples of Level-Flight Power Required Predictions for the Hypothetical Single-Rotor Aircraft 90 2/A6
4.1 Power Required Based on the Trim Analysis 90 2/A6
4.2 Simplified SHP_{req} Estimates vs Trim Analysis Program 94 2/A10

5. Power Required in Climb and Descent 98 2/A14
5.1 Climb Power Required 99 2/B1
5.2 Descent Power Required 100 2/B2

6. Level Flight and Maneuver Airspeed Envelope 101 2/B3
6.1 Rotor Stall Limits Methodology 103 2/B5
6.2 Level-Flight Airspeed/Altitude Structural Envelope 112 2/B14
6.3 Maneuver Capability 114 2/C2

7. Calculation of Forward-Flight Performance Capability 116 2/C4
7.1 Mission Performance 116 2/C4
7.2 Payload/Range Capability 118 2/C6
7.3 Payload/Endurance Capability 125 2/C13
7.4 Ferry-Range Capability 129 2/D3
7.5 Speed Capability 135 2/D9
7.6 Forward-Flight Climb Capability 135 2/D9
7.7 Service Ceiling 137 2/D11

References for Chapter III 140 2/D14

CHAPTER IV **Winged Helicopter Performance** 143 2/E3

1. Introductory Remarks 144 2/E4

2. Description of the Winged Helicopter 146 2/E6

2.1 Planform Area/Flap Geometry 146 2/E6
2.2 Wing Aspect Ratio 148 2/E8
2.3 Taper Ratio 149 2/E9
2.4 1/4-Chord Sweep 149 2/E9
2.5 Wing Location 150 2/E10
2.6 Airfoil Section 151 2/E11

3. Hover and Vertical-Climb Performance 151 2/E11

3.1 Wing Download OGE 151 2/E11
3.2 Wing Download IGE 155 2/F1
3.3 Hover Ceiling 155 2/F1
3.4 Vertical Climb Performance 156 2/F2

4. Forward-Flight Performance 156 2/F2

4.1 Effect of Wings on Parasite Drag/Power 157 2/F3
4.2 Effect of Wing Unloading on Induced and Profile Power of the Rotor 165 2/F11
4.3 Determination of Optimum Cruise Unloading 167 2/F13
4.4 Level Flight Performance 169 2/G1
4.5 Climb and Autorotation 174 2/G7
4.6 Maneuver Capability 179 2/G12

References for Chapter IV 181 2/G14

CHAPTER V **Tandem-Rotor Helicopter Performance** 182 3/A5

1. Introductory Remarks 183 3/A6

2. Description of the Tandem-Rotor Helicopter 184 3/A7

2.1 Overlap 184 3/A7
2.2 Gap/Stagger 185 3/A8
2.3 Weights 186 3/A9
2.4 Fuselage Configuration 186 3/A9
2.5 Rotor Hub 186 3/A9
2.6 Engines/Transmissions 187 3/A10

3. Hover Performance 187 3/A10

3.1 Isolated Rotor Power Required 187 3/A10
3.2 Induced Power Overlap Correction 187 3/A10
3.3 Fuselage Download, OGE 188 3/A11
3.4 Ground-Effect Correction 192 3/B3
3.5 Total Hover Power Required Sample Calculations 193 3/B4
3.6 Hover Ceiling Capability 185 3/A8

4. Forward-Flight Performance 195 3/B6

4.1 Level Flight Power Required 195 3/B6
4.2 Power Required in Climb and Descent 206 3/C5
4.3 Structural Envelope 207 3/C6
4.4 Performance Capability 210 3/C9

References for Chapter V 213 3/C12

Appendix A *Performance Guarantees* 214 3/C13
Appendix B *Aircraft Growth* 223 3/D9

Item 830-H-14
NAS1.26:3083

MAR 2 0 1979

NASA Contractor Report 3083

Rotary-Wing Aerodynamics

Volume II - Performance Prediction of Helicopters

COMPLETED
ORIGINAL

C. N. Keys

Microfilmed From
Best Available Copy

CONTRACT NAS2-7007
JANUARY 1979

NASA

243

NASA Contractor Report 3083

Rotary-Wing Aerodynamics

Volume II - Performance Prediction of Helicopters

C. N. Keys
Boeing Vertol Company
Philadelphia, Pennsylvania

Prepared for
Ames Research Center
under Contract NAS2-7007

National Aeronautics
and Space Administration

Scientific and Technical
Information Office

1979

Rotary-Wing Aerodynamics:
Volume I: Aerodynamic Theories
Volume II: Performance Prediction of Helicopters

Editor–In–Chief: W. Z. Stepniewski
Associate Editor: Wanda L. Metz

Abstract

Performance Prediction of Helicopters is the second volume of a two-volume series. This volume provides complete examples of performance predictions for (1) conventional single-rotor helicopter, (2) winged version of (1), and (3) tandem rotors to illustrate the application of the aerodynamic theories presented in Volume I. A direct comparison of performance capabilities of these three versions is obtained by assuming the same power installed and the same design gross weight for each. The appendices at the conclusion are devoted to (a) determination of guaranteed performance, and (b) techniques of "growing" a helicopter to compensate for unexpected increases in weight empty.

PREFACE

It is generally recognized that the educational value of a textbook is enhanced when numerical examples are included in the text. The readers and students not only become acquainted with computational procedures, but they also acquire an awareness regarding the magnitude of various values encountered in practice.

This need for illustrating theories by showing their practical application through numerical examples and special problems can be satisfied through two approaches.

(1) *The classroom approach*, used in many technical textbooks, is based on the incorporation of mutually unrelated, or only loosely related, short problems—quite often with answers—usually presented at the end of chapters or even shorter sections. This philosophy may be especially appealing to professors and instructors as being better suited for purely academic applications.

(2) *The total project approach* represents another way of providing the necessary illustrative material. Here, the submitted example is patterned on the actual industrial practice of dealing with a complete task which, in this case, is the prediction of helicopter performance. Various phases of performance calculations are related to suitable theoretical counterparts, thus providing examples for their reduction to practice. In addition to the purely illustrative aspect, a unified picture of the application of aerodynamic theory to performance predictions along with the computational methods used in industry can be presented.

Since the completed text is destined not only for classroom use, but also is intended to be of some help to the practicing engineer, the second approach was selected. Consequently, this volume was written to complement the rotary-wing aerodynamic theories discussed in Volume I, and contains complete and detailed performance calculations for conventional single-rotor, winged, and tandem-rotor helicopters.

Volume II is divided into five chapters and two appendices. Chapters I, II, and III describe detailed performance techniques for a single-rotor helicopter in hover, vertical ascent, and forward flight. Winged and tandem-rotor helicopter performance calculations are presented in Chapters IV and V as extensions and modifications of single-rotor methodology. The Appendices deal with the following special problems: (a) determination of guaranteed performance values based on both theory and test data , and (b) techniques of "growing" an aircraft to offset unprojected increases in weight empty.

Many of the sample calculations presented in Volume II employ computers to integrate the blade element expressions derived in Volume I. Computer data based on the vortex theory is compared with the approximate results obtained from the simplified momentum theory and blade element solution. In many cases correction factors or adjustments to the expressions are determined from these comparisons, and are often used to develop practical short-cut, but sufficiently accurate, prediction methods.

The calculations reflect up-to-date practices used in industry. Although the methods are chiefly based on those used by Boeing Vertol Company, they may be considered typical of the techniques used by a majority of helicopter manufacturers. This premise was borne out factually and enhanced through extensive reviews.

The presented text was first critically examined by Mr. A. Morse and Dr. F. H. Schmitz of Ames Directorate of AMRDL. Then, to further assure that the material was in compliance with generally accepted computational methods, the manuscript was submited to representatives of research institutions, industry, and universities as suggested by Dr. I. Statler of AMRDL. Many valuable technical and editorial inputs resulted from the reviews, and most or them were incorporated by the editors into a revised version.

The editors regret that manuscript deadlines prevented conversion of this volume to the SI (International Metric System) units; however, all formulae presented in Volume I are given in both SI and English units.

The author and editors wish to express their sincere appreciation to all those who devoted their time and effort in reviewing the text, and especially to Dr. I. Statler, Mr. A. Morse, and Dr. F. H. Schmitz of AMRDL; Dr. Andrew Z. Lemnios and staff of Kaman Aerospace Corporation; Professor Barnes W. McCormick, Dept. of Aerospace Engineering, The Pennsylvania State University; and personnel of Langley Directorate, AMRDL; Bell Helicopter Textron; Hughes Helicopters; and Sikorsky Aircraft.

W. Z. Stepniewski

CHAPTER 1

INTRODUCTORY CONSIDERATIONS

This chapter contains a description of the hypothetical single-rotor helicopter configuration, performance summary, engine performance characteristics, and the standard-day atmosphere relationships used to define ambient pressure, temperature, and density ratio.

Principal notation for Chapter I

c	chord	ft
c_d	airfoil section drag coefficient	
c_ℓ	airfoil section lift coefficient	
c_m	airfoil section moment coefficient	
DW	design gross weight	lb
h	altitude	ft
FUL	fixed useful load	lb
f_e	equivalent drag flate plate area	ft^2
INT	intermediate	
M	Mach number	
N	rotational speed	rpm, or rps
p	pressure	lb/ft^2, or in. of Hg
R	gas constant	ft/°C
R	rotor radius	ft
R_e	Reynolds number	
r	radial distance from rotor axis	ft
SL	sea level	
STD	standard	
sfc	specific fuel consumption	lb/hp;hr
V	velocity	fps or kn
W	weight, or gross weight	lb
WE	weight empty	lb
$T = 273.2 + t°C$	absolute temperature	K
t	temperature	°C, or °F
x	abscissa	in, or ft
y	ordinate	in, or ft
$\delta = p/p_o$	pressure ratio	
$\theta = T/288.2$	temperature ratio	
ρ	air density	slugs/ft^3
$\sigma_\rho = \rho/\rho_o$	density ratio	

Performance

Subscripts

F	fuel
o	initial, or SL/STD
p	pressure
t	tip
tr	tail rotor
ρ	density

Superscripts

	derivative with respect to time	per s, or hr

1. DESCRIPTION OF THE HYPOTHETICAL HELICOPTER CONFIGURATION

A typical 15,000-lb gross weight aircraft with a 50-ft diameter main rotor was chosen to illustrate the techniques used to predict single-rotor helicopter performance. To make the aircraft as realistic as possible, the configuration design is similar to one of the studies of the Utility Tactical Transport Aircraft System (UTTAS) helicopters. A detailed description of this configuration is given in Table I-1, and a 3-view drawing of the aircraft is shown in Fig 1.1. A brief discussion of the most important features of this design is presented below.

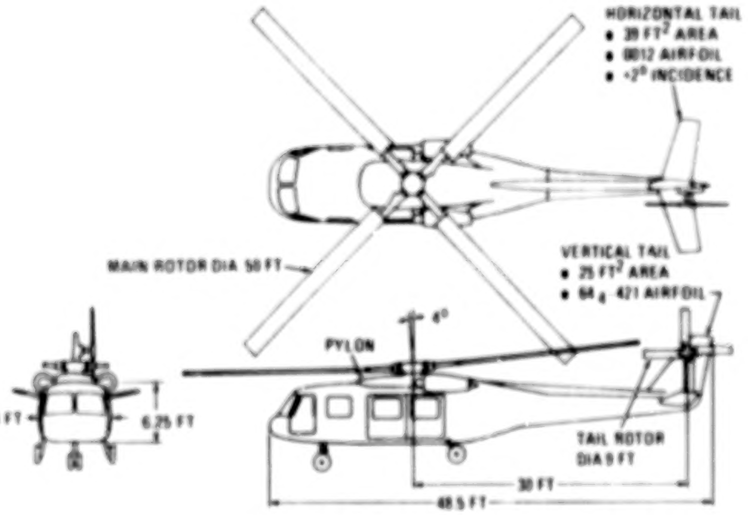

Figure 1.1 Three-view drawing of the hypothetical single-rotor helicopter

WEIGHTS	
Maximum Gross Weight	18,000 lb
Design Gross Weight	15,000 lb
Disc Loading @ Design Gross Weight	7.64 lb/ft^2
Weight Empty	9,450 lb
Weight Empty/Design Gross Weight	0.630
Fixed Useful Load (2 Crew @ 200 lb es, and 30 lb trapped liquid)	430 lb
Fuel Capacity (354 gal, JP-4)	2,300 lb
MAIN ROTOR	
Diameter	50 ft
Chord	24 in
Solidity	0.102
Tip Speed	700 fps
Number of Blades	4
Airfoil	V23010-1.58
Twist	-10°
Cutout (r/R)	20%
RPM	267.4
TAIL ROTOR	
Diameter	9 ft
Chord	9 in
Solidity	0.212
Tip Speed	700 fps
Number of Blades	4
Airfoil	V23010-1.58
Twist	-8°
Cutout r/R	20%
Type	Pusher
AIRFRAME	
Parasite Drag	19.0 ft^2
Landing Gear	fixed
ENGINES (HYPOTHETICAL)	
Number	2
Rating SL/STD (INT/Max Cont)	1600/1300
Lapse Rate	5.0 hp/°F
Installation Losses	1%
TRANSMISSION RATINGS	
Dual Engine (SL/82°F–INT Power)	2900 SHP
Single Engine (SL/STD - INT Power)	1600 SHP

TABLE I-1 CONFIGURATION DEFINITION

1.1 Weights

As shown in Table I-1, the helicopter has a design gross weight *(DW)* of 15,000 lb, and a maximum gross weight *(W_{max})* of 18,000 lb. The weight empty *(WE)* is 9,450 lb, or 63 percent of the *DW*. Subtracting the full fuel weight *(W_F = 2,300 lb)*, fixed useful load *(FUL = 430 lb)*, and weight empty from the design gross weight results in a payload capability of *PL = 2,820 lb.* This is equivalent to taking off with a full load of fuel and approximately 14 passengers.

1.2 Main Rotor and Tail Rotor Geometry

The main rotor is a four-bladed hingeless rotor design having a 50-ft diameter and 2-ft chord. The dimensions of the main rotor are close to figures obtained during an optimization process aimed at a minimization of weight and costs (see Ch X of Vol I) which was performed during preliminary design studies of an actual UTTAS-type helicopter. The selection of the hingeless configuration was also the result of comparative design studies of various rotor types–chiefly articulated and hingeless. In this process, advantages and disadvantages were weighed, and both concepts were evaluated taking into account such criteria as performance (parasite drag), controllability, permissible limits for c.g. travel, vibration, maintenance time, and dimensions affecting air transportability. However, in this text dealing with performance, the lower drag of the hingeless configuration, at least in principle, served as sufficient justification for preferring it over the completely articulated one.

The hingeless feature of this rotor means that there are no lead-lag or flapping hinges; however, flapping and lead-lag motions still occur through bending of the entire blade. The resulting blade motion is similar to the flapping characteristics of an articulated rotor with a relatively large hinge offset[1]. For this reason, rotor performance and stability evaluations are often conducted using an articulated rotor analysis while assuming a virtual or equivalent hinge offset as shown in Fig 1.2. A more detailed discussion is contained in Sect 4.3, Ch I, Vol I. This simulation gives the correct trim attitude for fuselage drag and download calculations.

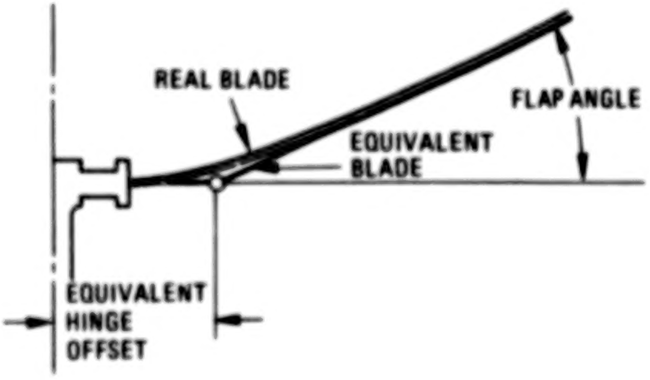

Figure 1.2 Equivalent hinge offset representation of a rigidly-attached blade

By analyzing the forces at the virtual flapping hinge, it can be shown that a hub moment is created when the tip-path plane deviates from the rotor-disc plane. This moment is one advantage of the hingeless rotor because it provides a more rapid response to control movements than fully-articulated rotors having a small (2 to 3 percent) or no flapping hinge offset which leads to improved maneuverability. In actual design practice, however, this and other previously mentioned advantages of the hingeless configuration must be weighed against dynamic couplings which are usually more complicated, resulting in vibratory problems more difficult to solve than those encountered in the low-offset, articulated rotors.

Other characteristics of the hypothetical helicopter main rotor given in Table I-1 show that the rotor operates at a tip speed of $V_t = 700$ *fps*, and has a cambered V23010-1.58 airfoil section similar to the NACA 23010 series except that the leading-edge radius is increased to 1.58 percent of the chord. The cambered airfoil was selected because of the following advantages over symmetrical sections: (1) higher $c_\ell^{3/2}/c_d$ values; resulting in an improved figure-of-merit in hover (Sect 9, Ch VI, Vol I); and (2) higher $c_{\ell_{max}}$ coefficients, leading to the retreating-blade-stall retardation in forward flight.

The coordinates of the V23010-1.58 airfoil are also presented in Table I-2. It should be noted that a trailing edge tab extends over 4 percent of the chord. In order to reduce the pitching moment coefficient resulting from the camber, the tab is deflected up 1.7° relative to the chordline. The basic characteristics of this airfoil as they appear in the Airfoil DATCOM[2] with tab deflected 3° up are shown in Fig 1.3. Further details of this family of airfoils and methods for interpolation of the data are included in this reference.

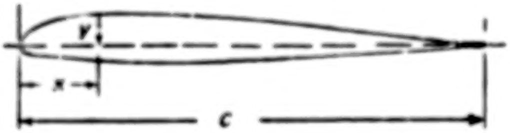

x/c	*y/c (upper)*	*y/c (lower)*	*x/c*	*y/c (upper)*	*y/c (lower)*
0.0	0.0006	-0.0006	0.40	0.0609	-0.0364
0.01	0.0198	-0.0145	0.45	0.0578	-0.0352
0.02	0.0276	-0.0170	0.50	0.0540	-0.0335
0.03	0.0337	-0.0184	0.55	0.0496	-0.0312
0.05	0.0434	-0.0200	0.60	0.0449	-0.0285
0.075	0.0520	-0.0221	0.65	0.0397	-0.0252
0.10	0.0576	-0.0242	0.70	0.0339	-0.0220
0.125	0.0618	-0.0263	0.75	0.0283	-0.0184
0.15	0.0647	-0.0286	0.80	0.0231	-0.0148
0.20	0.0667	-0.0322	0.85	0.0171	-0.0111
0.25	0.0664	-0.0349	0.90	0.0116	-0.0075
0.30	0.0654	-0.0364	0.95	0.0057	-0.0038
0.35	0.0634	-0.0367	1.00	0.00	0.00

Leading-edge circle radius = 0.0158c

Center at: x/c = 0.0158
y/c = 0.0004

Trailing-edge tab: from x/c = 0.96 to x/c = 1.00

TABLE I-2 COORDINATES OF THE V23010-1.58 AIRFOIL

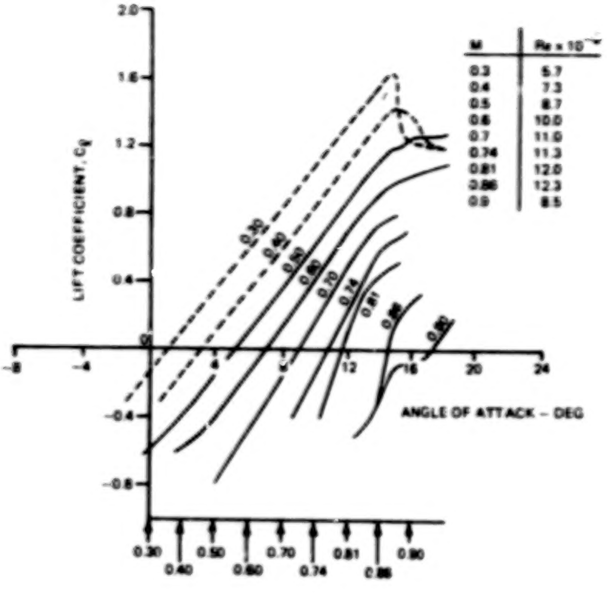

Figure 1.3a

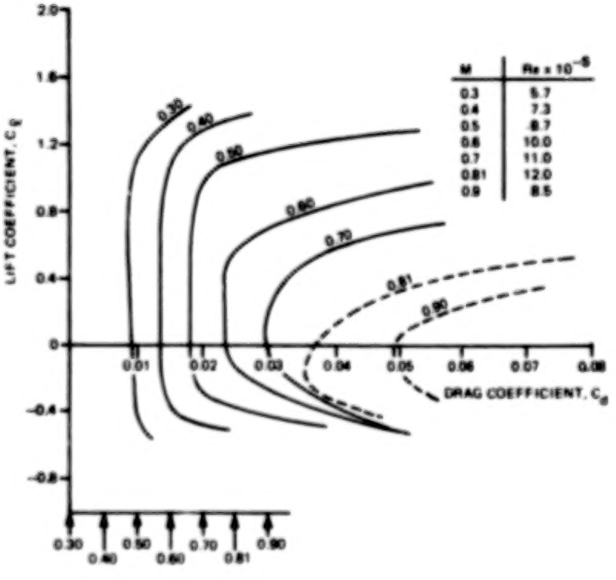

Figure 1.3b

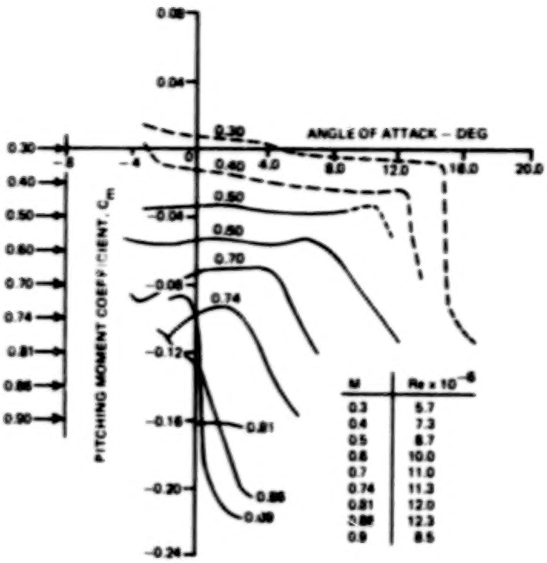

Figure 1.3c

Figure 1.3 Basic aerodynamic characteristics of V23010-1.58 airfoil with T.E. tab deflected 3° up

The tail rotor of the hypothetical aircraft is a 9-ft diameter, four-blade design having a 9-in chord and a V23010-1.58 airfoil section. The tail rotor is sized to provide adequate directional control in hover and forward flight and operates at a nominal tip speed of $V_{t_{tr}} = 700$ *fps.*

1.3 Transmission Limits

Helicopter transmissions are primarily limited by stress considerations corresponding to a given torque level. For an aircraft designed to operate at one rotor speed, as assumed for the hypothetical example, the torque limit becomes synonymous with a specific power-available limitation. As indicated in Table I-1, a dual engine transmission limit of 2900 hp was selected, which provides sufficient hover and vertical climb capability at low altitudes and high gross weights corresponding to INT power at SL/82°F. The selection of a single-engine gearbox rating corresponding to intermediate power at SL/STD atmosphere ($SHP_{int} = 1600$) was dictated by the consideration that with one engine out, the other can still be used to its maximum capability without exceeding the gearbox limits.

1.4 Airframe Configuration

The helicopter fuselage selected for the sample calculations is similar to a version of the UTTAS design which was tested in a wind tunnel. The availability of tunnel data is the primary reason for using this particular airframe configuration, since it affords an opportunity to verify the accuracy of drag prediction techniques and provides some insight into the order-of-magnitude of the drag of various components. Parasite drag estimates, which will be discussed in detail later in Sect 3.1, show that the airframe shape is aerodynamically clean, as expressed by the ratio of the gross weight *(W)* to the equivalent flat plate area (f_e), when compared with current production helicopters (Fig 1.4).

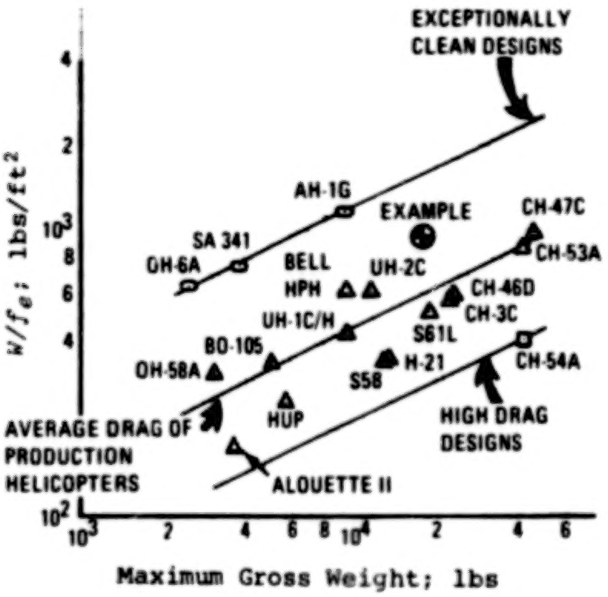

Figure 1.4 Helicopter drag trends

2. PERFORMANCE SUMMARY

An introductory discussion of a new helicopter design would not be complete without some reference to its performance capability. Therefore, a summary of the hypothetical helicopter performance is presented in Table I-3 for *DW = 15,000 lb.* The information shown in this table is typical of the type of performance calculations described in the text and includes hover, vertical climb and forward flight data at both standard day and 4000 ft/95°F conditions. The latter represents a primary design condition for new U.S. Army helicopters.

SPEED CAPABILITY Maximum continuous power, 4000 ft/95°F	161 kn
RANGE CAPABILITY Full fuel, 2-min. warmup, 10% fuel reserve, 4000 ft/95°F	330 n.mi.
ENDURANCE CAPABILITY Full fuel, 2-min. warmup, 10% fuel reserve, loiter at minimum power speed, 4000 ft/95°F	2.9 hr
HOVER CEILING Out-of-ground effect, 95°F, intermediate power	5700 ft
HOVER CEILING In-ground effect (5-ft wheel height), 95°F, intermediate power	9800 ft
VERTICAL CLIMB CAPABILITY 4000 ft/95°F, intermediate power	800 fpm
FORWARD FLIGHT CLIMB CAPABILITY Maximum continuous power, 4000 ft/95°F, dual engine	1900 fpm
SINGLE ENGINE SERVICE CEILING Standard day, intermediate power	13,700 ft

TABLE I-3 PERFORMANCE SUMMARY AT 15,000–LB DESIGN GROSS WEIGHT

3. ENGINE PERFORMANCE

3.1 General Characteristics of Shaft Turbines

Shaft turbines are continuous gas-flow engines (Fig 1.5). Consequently the power available at the shaft depends on (1) the amount of heat energy introduced in the form of fuel per pound of ambient air, and (2) rate of air flow ($\dot{W}_A$; lb/s) through the engine.

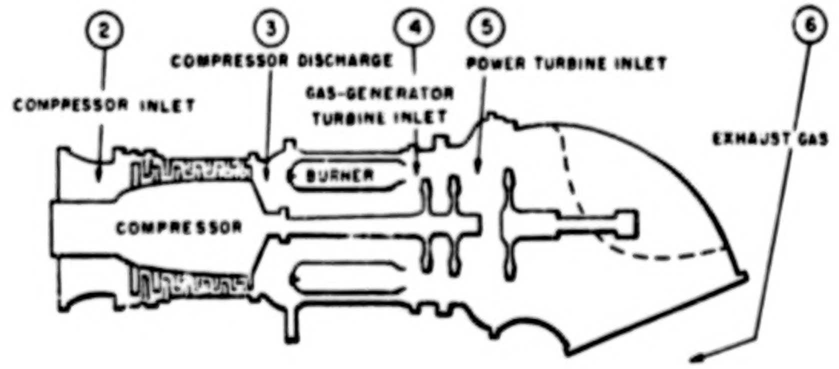

Figure 1.5 Typical gas flow diagram showing stations used in performance analysis

The amount of heat energy per pound of air (ΔE) will be

$$\Delta E = c_p(T_4 - T_3) \tag{1.1}$$

where T_3 and T_4 are absolute temperatures at the burner entrance and gas-generator inlet respectively, while c_p is the specific heat at constant pressure.

It becomes clear from Eq (1.1) that T_4 should be as high as possible in order to maximize the ΔE value. Understandably, however, the T_4 is limited by the state of technology as to the ability of turbine blades to withstand high operational temperatures. To assure that T_4 does not exceed values endangering the structural integrity of the turbine, the gas temperature must be monitored. Because of the ease of installing thermocouples, this temperature monitoring is usually done at the power turbine inlet, and the permissible T_5 values–instead of the T_4 which are obviously higher–are specified in operational manuals.

It should be realized from Eq (1.1) that since T_4 is limited, and also since T_3 increases with ambient temperature for a given compression ratio, an increase in the ambient temperature would reduce the amount of energy per pound of ingested air.

The rate of air flow ($\dot{W}_A$) is dependent on both ambient pressure and temperature. The effect of air pressure is straightforward. As the ambient pressure drops, the air density also drops. Consequently,

$$\dot{W}_A \sim p,$$

however, the influence of the ambient temperature is somewhat more complicated. Air density is inversely proportional to the absolute ambient temperature (T); but the speed of molecular motion is proportional to $\sqrt{T}$ (see Vol I, Ch VI). This effect contributes to the increase in the speed of flow through the duct represented by the powerplant as a whole. The combined effect of these two influences is such that the rate of air flow through the engine would vary inversely proportional to $\sqrt{T}$. Now the air flow under a given ambient T and p condition becomes:

$$\dot{W}_A \sim p/\sqrt{T}. \tag{1.2}$$

It can be seen from Eqs (1.1) and (1.2) that the amount of heat energy ($\Delta E\ \dot{W}_A$) introduced each second into the engine cycle is directly related to the ambient temperature and pressure. It may be expected hence, that the shaft power available, which is proportional to the $\Delta E\ W_A$ product, will also be influenced by the ambient condition.

3.2 Power Ratings and Effects of Ambient Conditions on Engine Characteristics

From the preceding discussion, it can be seen that power ratings of a turbine-type engine are related to the gas temperature level (as expressed by the T_5 values). For instance, $T_5 \approx 850^\circ C$ allows the engine to operate for a limited stretch of time of no more than 30 minutes. Consequently, the corresponding *intermediate* rating (SHP_{int}) is used for takeoff, or emergency situations. However, when the gas temperature is sufficiently lowered (say, $T_5 \approx 750°C$), the engine can be operated for an unlimited time, and the corresponding rating becomes *maximum continuous* ($SHP_{m.c.}$).

In Armed Forces Specifications, the two above-mentioned power settings are also often called *military* (SHP_{mil}) and *normal rated* ($SHP_{n.r.}$) ratings.

It is now clear that turbine engine characteristics are such that the relationship of $SHP/\delta\sqrt{\theta}$ vs T_5/θ essentially results in a single curve. Then, having this curve and T_5 for a given power rating, the available power for any ambient condition can be determined. In addition to power, other engine characteristics are also corrected in order to relate them to SL/STD conditions.:

Power: $SHP_o = SHP/\delta^*$ (a)
Fuel Flow: $\dot{W}_{F_o} = \dot{W}_F/\delta\sqrt{\theta}$ (b)
Air Flow: $\dot{W}_{A_o} = \dot{W}_A\sqrt{\theta}/\delta$ (c) (1.3)
Gas Generator, or Power Turbine Speed: $N_o = N/\sqrt{\theta}$ (d)

---

* For given rating and ambient temperature.

3.3 Powerplant for Hypothetical Helicopter

The powerplant used in the sample calculation consists of two hypothetical turbo-shaft engines with the following power ratings at SL/STD: intermediate, $SHP_{int} = 1600$ *hp*; and maximum continuous, $SHP_{m.c.} = 1300$ *hp*.

The variation of power available versus altitude for standard and 95°F conditions is shown in Fig 1.6. Performance was established using the generalized power available from the engine manufacturer's data shown in Fig 1.7. Altitude effects are taken into account according to Eq (1.3a).

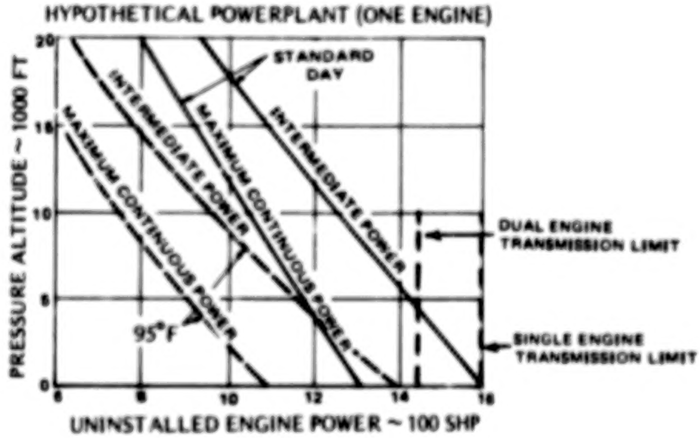

Figure 1.6 Uninstalled power available

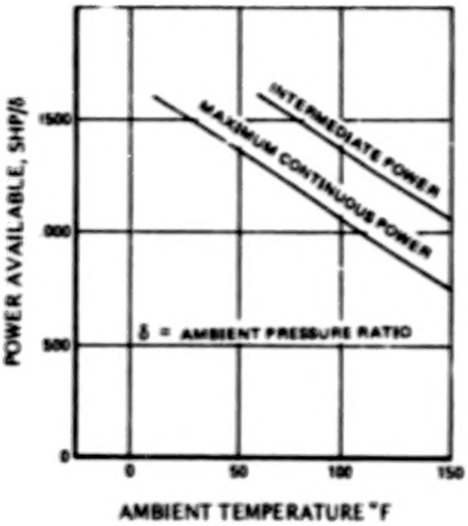

Figure 1.7 Generalized plot of power available

The slope of the intermediate and maximum continuous power lines at sea level ($\delta = 1.0$) is $-6\ hp/^{\circ}F$, which is typical of lapse rates for current engines of similar size.

The hypothetical engine fuel flow characteristics are shown in Fig 1 8 in terms of the parameters $\dot{W}_F/\delta\sqrt{\theta}$ (Eq (1.3b)) and $SHP/\delta\sqrt{\theta}$.

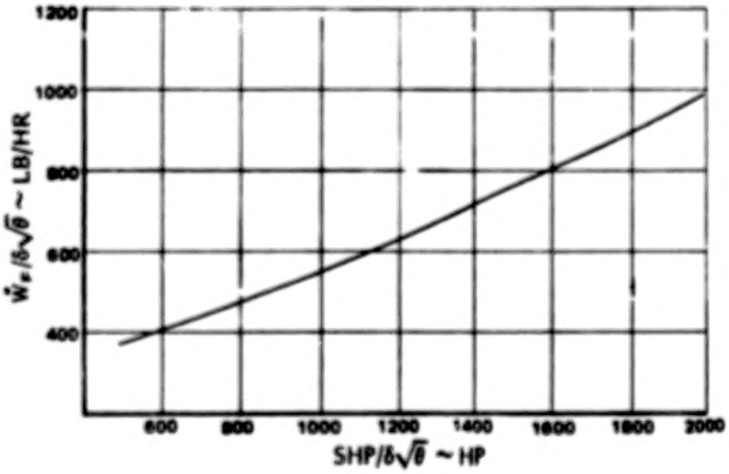

Figure 1.8 Fuel flow for hypothetical engine

This relationship was developed on the basis of trend curves for similar size engines, and results in $sfc = (\dot{W}_F/SHP)$ versus percent of military power as illustrated in Fig 1.9 As noted, at 60 percent of intermediate power, which corresponds to a cruise power setting, $sfc = 0.56$ *lb/hr SHP.*

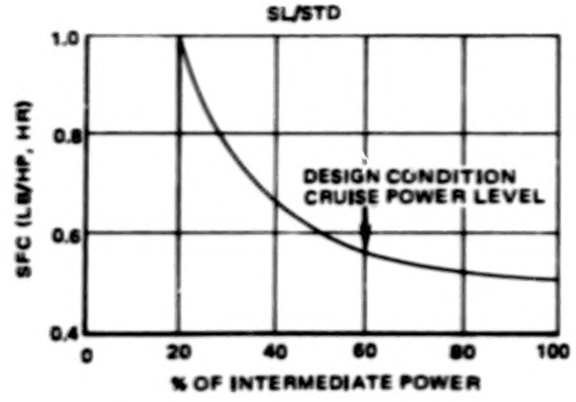

Figure 1.9 Hypothetical engine specific fuel consumption

3.4 Engine Power Constraints

Maximum power available is enclosed within an envelope formed by various constraints. For example, engine *SHP* vs ambient temperature ($p = p_0$) is shown in Fig 1.10. For $t > t_0$ and gas temperature (T_5) fixed, the power lapse rate with ambient temperature forms one of the constraining boundaries. As ambient temperature becomes lower than t_0, one might expect that engine power would increase, maintaining the same *SHP* vs t slope as for the $t > t_0$ region. However, the full benefit of this potential power increase usually cannot be realized because of the gas generator speed limit (N_1). At still lower ambient temperatures, a new stronger constraint in the form of the fuel-flow limit appears.

Finally, for an engine installed on a helicopter, two additional constraints associated with strength of the transmission for both dual and single-engine operations may appear.

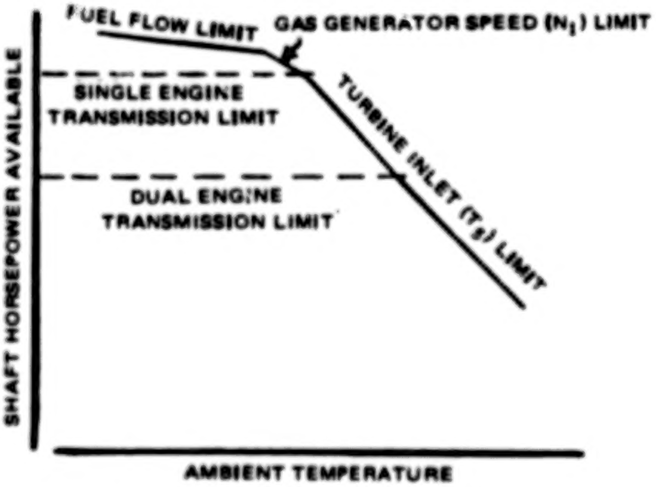

Figure 1.10 Typical constraints for engine power available

3.5 Engine Installation Losses

Installation of the engines on the airframe generally results in a decrease in performance when compared to the engine manufacturer's performance specifications. Losses associated with engine installation can be divided into (1) inlet losses, (2) exhaust losses, and (3) losses due to bleed air extraction. A brief discussion of each of these items is presented in the following paragraphs.

Inlet Losses. Inlet losses result from either a rise in temperature or a pressure drop at the inlet. In hover, the predominant effect is the temperature rise due to the recirculation of hot exhaust gases which occurs primarily in ground effect. A rise in inlet air temperature may also occur for installations with the gearbox located in front of the inlet. Pressure losses generally result from flow disturbances or separation at, or ahead of, the inlet. These effects are especially noticeable in forward flight, where flow separation may result in sizeable pressure losses; however, these losses are often offset by a decrease in flow velocity and and an increase in air pressure as it enters the inlet (ram recovery). When particle separators or screens are installed, additional sizeable losses may occur both in hover and forward flight.

Exhaust Losses. Exhaust losses are caused by backpressure normally resulting from a redirection or rerouting of the exhaust flow, from the installation of equipment such as an infrared suppressor, or from nozzeling to reduce parasite drag.

Extracting Bleed Air. Additional losses are incurred if bleed air is extracted from the compressor for anti-ice protection of the engine inlets when operating under cold ambient temperatures or for cabin or cockpit air-conditioning systems under hot ambient conditions.

For designs having podded engines, as assumed for the hypothetical aircraft, the engine installation losses are minimized because the engines are essentially detached from the airframe. Based on flight test experience, the power losses for this type of installation are generally less than one percent. Therefore, the one-percent loss assumed for all sample calculations is conservative. In addition, it is conservatively assumed that there is no increase in the power available due to ram recovery effects in forward flight.

Loss of power due to the inlet pressure drop (as a result of engine installation) also leads to a corresponding decrease in fuel flow (Eq (1.3b)). Typically, a loss in pressure will result in a reduction in fuel flow of 0.5 percent or less for each one-percent decrease in power available, thus resulting in a net increase in sfc. By contrast, a temperature rise will produce approximately equal power and fuel flow reductions with no net sfc change. Assuming, for the hypothetical helicopter, that a reduction in fuel flow amounts to 0.5 to 1 percent for 1 percent of power decrement, the installed fuel flow versus power relationship would remain within 0.5 percent of the uninstalled curve in Fig 1.8. Since these tolerances are small, this figure will be used as a basis for the installed fuel flow. However, in calculating performance, the sfc is increased 5 percent[3,4] over the values resulting from Fig 1.8. This increase, required by Military Specifications, accounts for (1) engine and airframe deterioration, and (2) nonoptimum piloting techniques.

4. STANDARD DAY ATMOSPHERE

The performance capability of an aircraft depends on the density of the surrounding air which, in turn, is a function of the local ambient conditions (temperature and pressure). This makes it difficult to compare the performance of various aircraft, or even the same aircraft from one day to another, unless the data is reduced to some standard conditions. An international standard atmosphere has been established for this purpose with air density varying with altitude as shown in Fig 1.11.

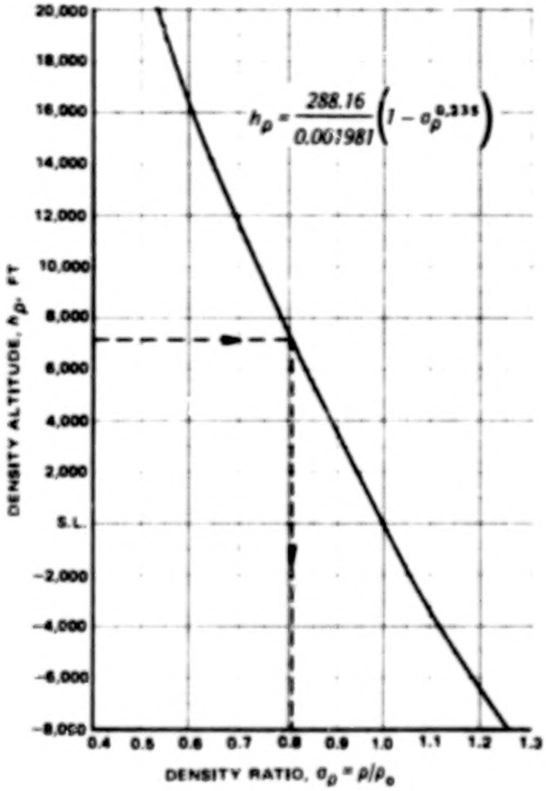

Figure 1.11 Density altitude vs density ratio (standard atmosphere)

In this case, altitude is not a "tape-measured" elevation over sea level, but is a hypothetical height referred to as *density altitude* based on the following criteria for standard atmosphere[5]:

(1) The air is assumed to be a perfect dry gas having a constant of $R = 96.04$ ft/°C.
(2) The pressure at sea level is $p_0 = 29.92$ *Hg*.
(3) The temperature at sea level is $t = 15°C$ (59°F).
(4) The temperature varies linearly with altitude according to the expression $t = 15° - 0.001981h$; where altitude h is expressed in feet, and temperature in °C.

The linear temperature gradient or lapse rate assumed for standard day conditions approximates the average actual year-round temperature variation with altitude which occurs in North America at about 40° latitude[6,7].

Pressure altitude, defined as "the altitude at which a given pressure p is found in the standard atmosphere"[8], is again a "non-tape-measured" hypothetical height more frequently used than density altitude in performance calculations.

Using the equation of state for an ideal gas, and accounting for gravitational effects, the following expression for pressure altitude (h_p) in feet can be developed[7].

$$h_p = (288.16/0.001981)[1 - (p/p_o)^{0.1903}]. \tag{1.4}$$

Pressure altitude, therefore, is solely a function of the ambient pressure ratio. The practical advantage of this concept lies in the fact that pressure altitude is directly measured by aircraft altimeters which are essentially barometers calibrated according to Eq (1.4). By contrast, density altitude must be computed from altimeter and temperature readings. Consequently, performance data is generally quoted for a given pressure altitude and ambient temperature rather than density altitude. If an altitude is not qualified, then it is generally assumed to be pressure altitude.

Knowing the pressure altitude in feet and temperature in °C, the density ratio $\sigma_\rho = \rho/\rho_o$; pressure ratio $\delta = p/p_o$, and temperature ratio $\theta = T/T_o$ can be computed using the following relationships:

$$\delta = [1 - (0.00198h_p/288.16)]^{5.256} \tag{1.5}$$

$$\theta = (t + 273.16)/288.16 \tag{1.6}$$

$$\sigma_\rho = \delta/\theta = 288.16/((t + 273.16)[1 - (0.00198h_p/288.16)]^{5.256} \tag{1.7}$$

where t is in °C.

The ratios defined by Eqs (1.5) through (1.7) are used throughout this textbook to reduce performance predictions to SL/STD atmosphere conditions. In actual calculations, however, it is generally more convenient to use tabulations of δ and σ_ρ values as defined in Refs 5 and 7, or to obtain these ratios from charts (Figs 1.11 through 1.13). For instance, values of the pressure ratio δ, which are often needed in engine performance, can be more easily obtained from a graph such as the one shown in Fig 1.12 rather than computing them from Eq (1.5).

Computations of the absolute temperature ratio (Eq (1.6)) are so simple that no graphical help is required.

Graphs are also quite useful in determining values of density ratios (σ_ρ) which are required in calculations of such aerodynamic quantities as lift, drag, and induced velocity. For example, to compute the density ratio at 4000-ft pressure altitude/95°F, a density altitude of 7100 feet is read from Fig 1.13. The density ratio is then found from Fig 1.11 ($\sigma_\rho = 0.81$). The exact value from Eq (1.7) is $\sigma_\rho = 0.8076$, where $h_\rho = 7123$ ft.

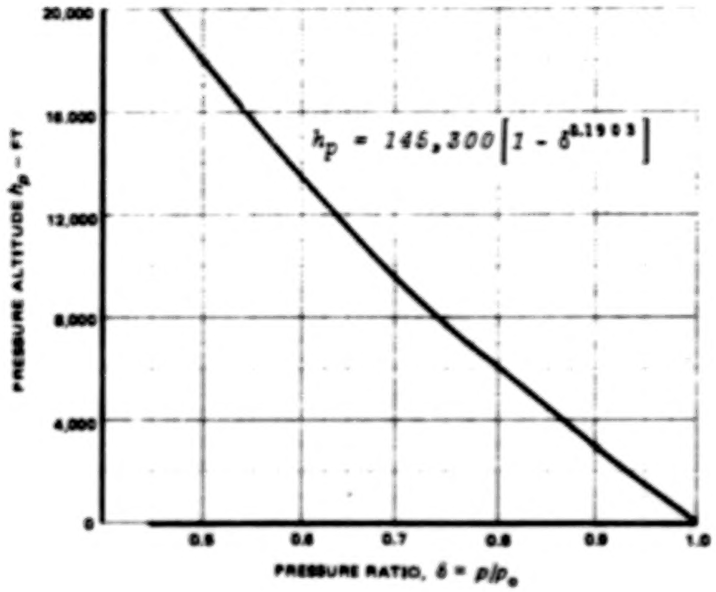

Figure 1.12 Ambient pressure ratio δ

The density ratio, σ_p, is also used in the preparation of flight manuals. Here, it is needed to convert true airspeed (ground speed in zero wind) to that indicated in the cockpit because airspeed measurement is, in practice, a measure of dynamic pressure ($\frac{1}{2}\rho V^2$). For more detail on this subject, see Appendix A, Supplement 3.

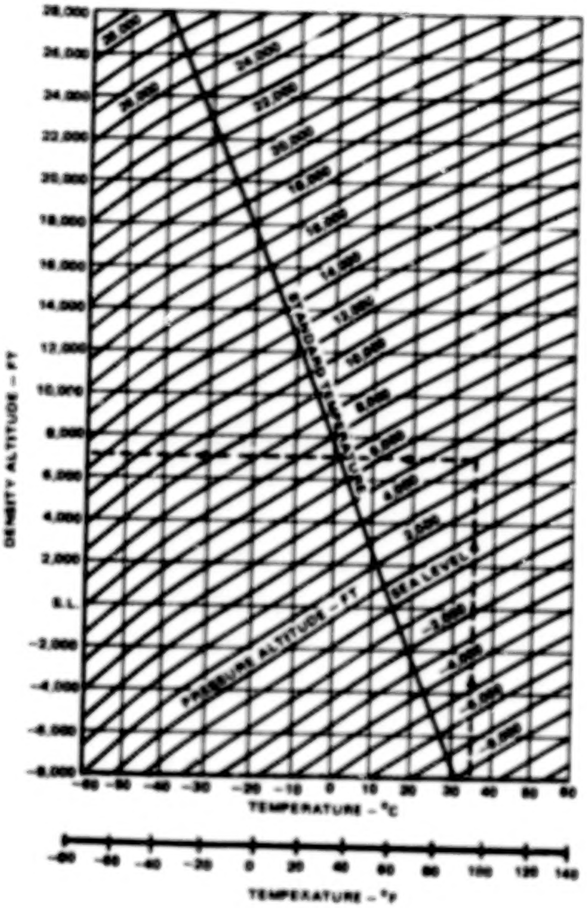

Figure 1.13 Density altitude chart

References for Chapter I

1. Reichert, G. *Basic Dynamics of Rotor Control and Stability of Rotary-Wing Aircraft Aerodynamics and Dynamics of Advanced Rotary-Wing Configurations.* AGARD Lecture Series No. 63, March 1973.

2. Dadone, L.U. *U.S. Army Helicopter Design DATCOM – Volume I, Airfoils.* Contract NAS2-8637, May 1976.

3. MIL-M-7700C (USAF). *Military Specification – Manuals, Flight.* 15 May 1977.

4. MIL-C-005011B (USAF). *Military Specification – Charts: Standard Aircraft Characteristics and Performance, Piloted Aircraft (Fixed-Wing).* 21 June 1977.

5. International Civil Aviation Organization. *Manual of the ICAO Standard Atmosphere Calculations by the NACA.* May 1954.

6. Gregg, Willis Ray. *Standard Atmosphere Supplements.* NACA Report 147, 1922.

7. *U.S. Standard Atmosphere Supplements.* NASA CR-88870, 1966.

8. von Mises, Richard. *Theory of Flight.* Published by Dover, 1959 Edition.

CHAPTER II

SINGLE ROTOR HELICOPTER HOVER AND VERTICAL CLIMB PERFORMANCE

Hover out-of ground effect (OGE) capability, in-ground effect (IGE), and vertical climb prediction techniques are discussed in this chapter. Detailed calculations for the single-rotor hypothetical helicopter are presented to illustrate these techniques.

Principal Notation for Chapter II

A	area	ft^2
a $(a_o = 1116.4\ fps)$	speed of sound	fps
b	number of blades	
C_D	body drag coefficient	
$C_P = P/\rho\pi R^2 V_t^3$	rotor power coefficient	
$C_Q = Q/\rho\pi R^3 V_t^2$	rotor torque coefficient	
$C_T = T/\rho\pi R^2 V_t^2$	rotor thrust coefficient	
c	chord	ft
c_d	profile drag coefficient	
c_ℓ	profile lift coefficient	
$c_{\ell\alpha}$	lift curve slope	rad^{-1} or deg^{-1}
D	drag	lb
d	rotor diameter	ft
H	height	ft
H_z	rotor height above fuselage	ft
IGE	in-ground effect	
INT	intermediate (power rating)	
k_d	downwash development factor	
k_g	download correction factor	
$k_{ind} = RP_{ind}/RP_{id}$	induced power correction factor	
k_p	climb efficiency factor	
k_v	vertical loading coefficient	
ℓ	length, or distance	ft
$M = V/a$	Mach number	
N	rotational speed	rpm
OGE	out-of-ground effect	
P	power	ft-lb/s, or hp
P_T	thrust power	ft-lb/s, or hp
Q	torque	ft-lb
R	rotor radius	ft
RHP	rotor horsepower	hp
RP	rotor power	ft-lb/s, or hp

R_e	Reynolds number	
r	radial distance	ft
S_v	vertical fin area	ft^2
SHP	engine shaft horsepower	hp
SL/STD	sea-level standard	
SP	engine shaft power	ft-lb/s, or hp
s	tail rotor fin separation	ft
T	rotor thrust	lb
$T = 273.2 + t\,°C$	absolute temperature	K
t	temperature	°C, or °F
V	velocity in general	fps
v	induced velocity	fps
W	weight	lb
w	width	ft
α	airfoil angle-of-attack (measured up from zero-lift chord)	rad, or deg
$\delta = p/p_o$	pressure ratio	
ζ	distance from rotor disc leading edge	ft
$\theta = T/T_o$	absolute temperature ratio	
η	efficiency	
$\sigma = bcR/\pi R^2$	rotor solidity	
$\sigma_\rho = \rho/\rho_o$	density ratio	

Subscripts

a	accessory
av	available
c	climb, or compressible
d	divergent, or downwash
e	equivalent
f	fuselage
h	hover
i	incompressible
id	ideal
ind	induced
mr	main rotor
n	indicator of numerical order
o	initial, or SL/STD
pr	profile
r	rotor
ref	referred
t	tip
tm	transmission
tr	tail rotor
v	vertical

Performance

Superscripts

– average

1. HOVER OUT-OF-GROUND EFFECT PERFORMANCE

1.1 General Procedure

The hover OGE performance calculation procedure, in principle, consists of comparing helicopter shaft power required for a given ambient condition with the engine installed power available.

As diagrammatically shown in Fig 2.1, several intermediate calculations must be performed in order to determine these two quantities.

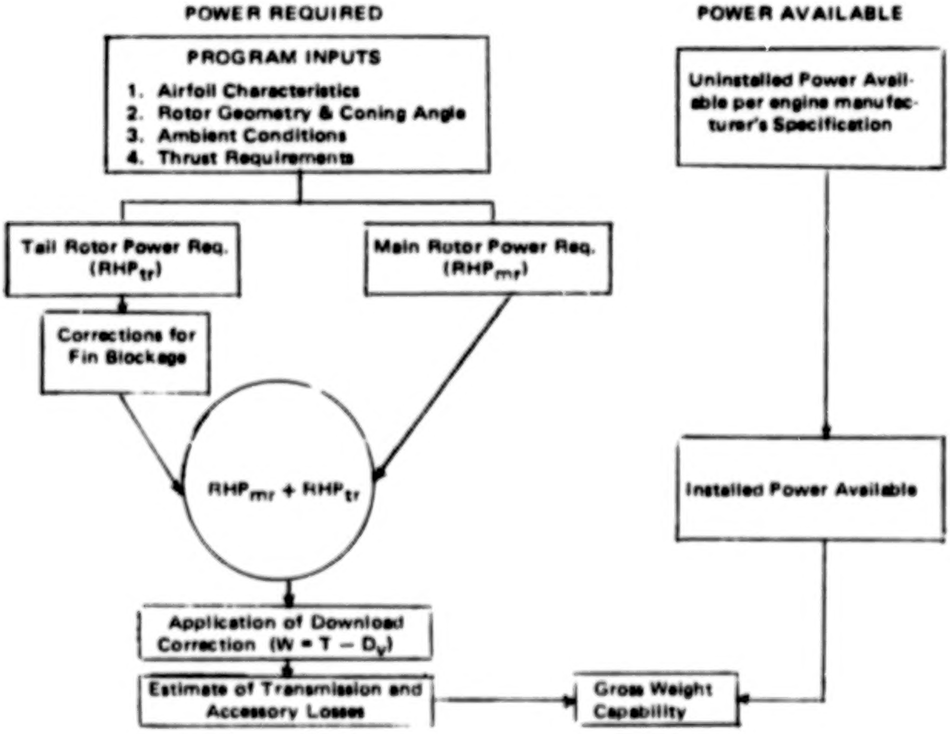
POWER REQUIRED
POWER AVAILABLE
PROGRAM INPUTS
1. Airfoil Characteristics
2. Rotor Geometry & Coning Angle
3. Ambient Conditions
4. Thrust Requirements
Uninstalled Power Available per engine manufacturer's Specification
Tail Rotor Power Req. (RHP_{tr})
Main Rotor Power Req. (RHP_{mr})
Corrections for Fin Blockage
$RHP_{mr} + RHP_{tr}$
Installed Power Available
Application of Download Correction ($W = T - D_v$)
Estimate of Transmission and Accessory Losses
Gross Weight Capability

Figure 2.1 Hover OGE performance calculation procedure

Power Required. Airfoil characteristics, rotor and blade geometry, ambient conditions, and assumed thrust of the main rotor (close to the anticipated gross weight) represent initial inputs. Next, both the main and tail rotor power required are computed either manually or through the use of computer programs. These calculations may be based on any acceptable theory relating rotor thrust to rotor power required (i.e., combined blade element and momentum theory, vortex, local momentum, or potential theories). However, the computer programs most frequently used in industrial practice are based on the vortex theory.

After corrections to power required by the tail rotor due to the aerodynamic interference of the vertical fin are made, the total power required by the main and tail rotors is determined.

The gross weight (W) corresponding to the originally assumed thrust (T) can be resolved through computation of the vertical drag (D_v). Application of transmission and accessory losses allows one to establish a relationship between gross weight and shaft power required: $SHP_{req}(W)$.

Power Available. Determination of the shaft power available begins with uninstalled SHP as set by the engine manufacturers for assumed ambient conditions. Accounting for installation losses leads to the establishment of the shaft horsepower actually available (SHP_{av}).

A comparison of $SHP_{req}(W)$ with SHP_{av} permits one to determine the gross weight of the aircraft in hover OGE under given ambient conditions.

1.2 Power vs Thrust Calculations

An actual computer program of one of the helicopter manufacturing companies was used in performance calculations of the hypothetical helicopter.

An isolated rotor nonuniform downwash analysis described as the *Explicit Vortex Influence Technique* was used to predict both the main and tail rotor power required. This represents the prescribed wake approach, which is discussed in more detail in Ch 4 of Vol I. Only the more salient features of this technique are recalled here. The technique is basically an extension of the fixed-wing, lifting-line theory where each blade is represented by a lifting line and trailing vortex wake. This wake is composed of an infinite number of weak vortex filaments which the theory mathematically approximates by a finite number of vortices streaming from various radial locations. The positioning of the vortices below the rotor is indicated by the semi-empirical prescribed rate of wake contraction since the vortex filaments must travel at the velocity of the surrounding fluid. The contraction rate, specified as a function of the thrust coefficient $C_T = T/\rho\pi R^2 V_t^2$, is determined by analytical studies of finite-core vortex ring flows and by correlation of calculated and measured propeller static performance. As the wake is defined empirically rather than allowing it to form freely, this type of model is defined as a prescribed wake. This method is generally preferred over the free-wake method throughout the industry in order to obtain reasonable computer run time (Vol I, Ch IV.6).

The strength of the vortices is determined by the section lift (c_ℓ) distribution using the Kutta-Joukowski theorem. The angle-of-attack and hence, the c_ℓ distribution is determined by the downwash velocity induced by the vortices defined by the Biot-Savart law. An iterative technique is used to obtain a mutually consistent c_ℓ and downwash distribution. Once an agreement is achieved, the c_ℓ and section drag (c_d) distributions are integrated taking into consideration the local downwash angle, thus thrust and power required are obtained. If the computed thrust and the desired thrust do not agree, the collective pitch angle setting is changed and the entire process is repeated.

The iterative calaculations described above require the use of a high-speed computer. A simplified block diagram of the computer program is presented in Fig 2.2. As shown in this figure, the inputs required are:

- airfoil section c_ℓ and c_d characteristics
- rotor geometry
- ambient condition
- required thrust.

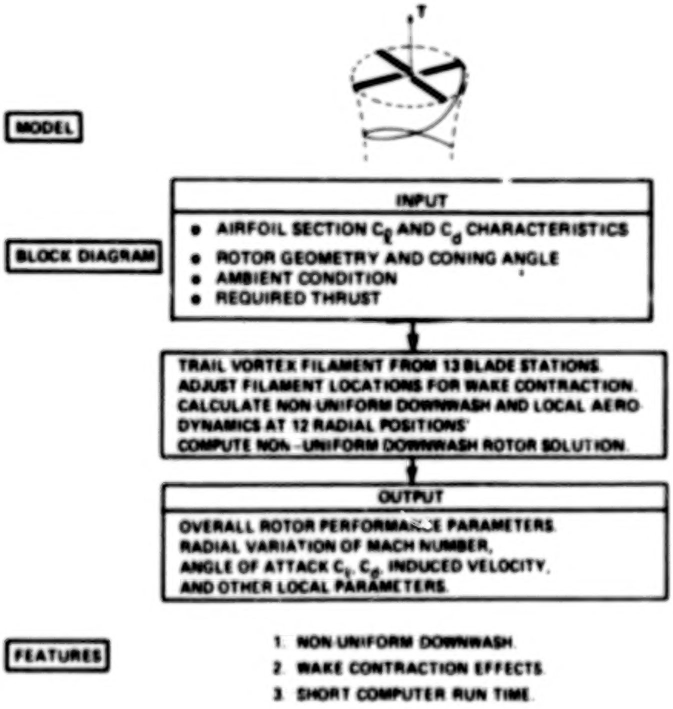
T
MODEL
INPUT
BLOCK DIAGRAM
• AIRFOIL SECTION C_ℓ AND C_d CHARACTERISTICS
• ROTOR GEOMETRY AND CONING ANGLE
• AMBIENT CONDITION
• REQUIRED THRUST
TRAIL VORTEX FILAMENT FROM 13 BLADE STATIONS.
ADJUST FILAMENT LOCATIONS FOR WAKE CONTRACTION.
CALCULATE NON-UNIFORM DOWNWASH AND LOCAL AERODYNAMICS AT 12 RADIAL POSITIONS
COMPUTE NON-UNIFORM DOWNWASH ROTOR SOLUTION.
OUTPUT
OVERALL ROTOR PERFORMANCE PARAMETERS.
RADIAL VARIATION OF MACH NUMBER,
ANGLE OF ATTACK C_ℓ, C_d, INDUCED VELOCITY,
AND OTHER LOCAL PARAMETERS.
FEATURES
1. NON-UNIFORM DOWNWASH.
2. WAKE CONTRACTION EFFECTS.
3. SHORT COMPUTER RUN TIME.

Figure 2.2 Hover performance analysis computer program (explicit vortex influence technique)

A brief description of the specific computer program input parameters for the hypothetical aircraft are presented below.

Airfoil Section Aerodynamic Characteristics. As noted in Ch I, the hypothetical aircraft design uses V23010-1.58 airfoil sections for both the main and tail rotors. The lift characteristics of this airfoil are illustrated in Fig 2.3, where lift coefficient versus angle-of-attack is shown at Mach numbers from 0.3 to 0.9. This data is based on wind-tunnel testing conducted in the Boeing two-dimensional wind tunnel. The high Mach number data has lower $c_{\ell_{max}}$ values and higher lift-curve slopes (c_{ℓ_α}). The actual variation of the lift-curve slope with Mach number (for the anticipated M-value range) agrees

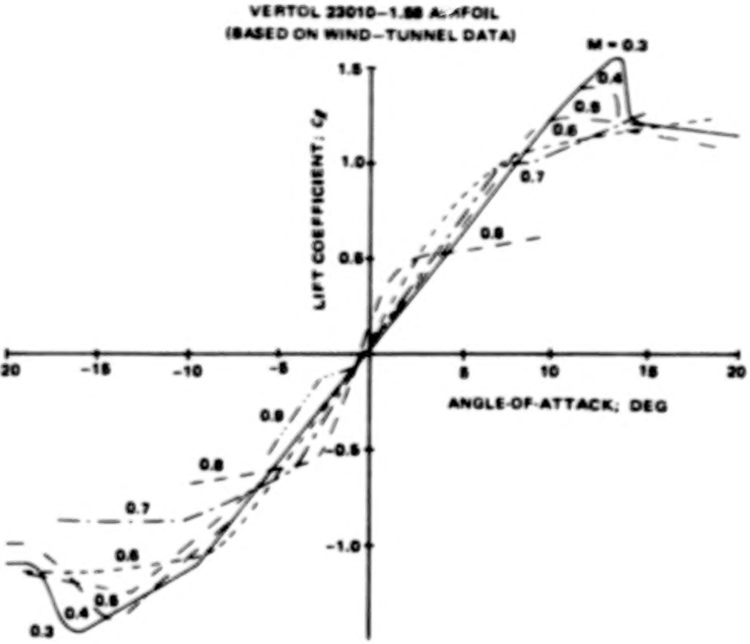

Figure 2.3 Variation of section-lift characteristics with Mach number

well with the Prandtl-Glauert expression (see Vol I, Ch VI)

$$c_{\ell a_c} = c_{\ell a_i}/\sqrt{1 - M^2}$$

where $c_{\ell a_c}$ is the slope corrected for compressibility effects ($M > 0$), and $c_{\ell a_i}$ corresponds to the incompressible case ($M = 0$).

The V23010-1.58 section drag characteristics are presented in Fig 2.4 as a function of Mach number for various angle-of-attack settings. The airfoil c_d varies from 0.008 to 0.018 at Mach numbers lower than the drag divergent Mach number (M_d). M_d is defined as the Mach number where the the slope $\Delta c_d/\Delta M = 0.1$. It represents the Mach number at which a weak oblique shock forms on the crestline (tangential point of freestream velocity with the upper surface of the airfoil) resulting in separation of the boundary layer. As noted in Fig 2.4, the drag divergence Mach number decreases with increasing angle-of-attack. This variation is due to an increase in local velocity on the upper surface, and movement of the crestline chordwise location forward into the high velocity region near the airfoil leading edge.

The data presented in Figs 2.3 and 2.4 was obtained at full-scale Reynolds number (R_e) corresponding to a CH-47C helicopter rotor blade, with a chord of 25.25 inches, operating at a tip speed of approximately 750 fps. A Reynolds number drag correction must be applied to use this data for the hypothetical aircraft. The variation in section c_d with Reynolds number is shown in Fig 2.5. This data is based on two-dimensional

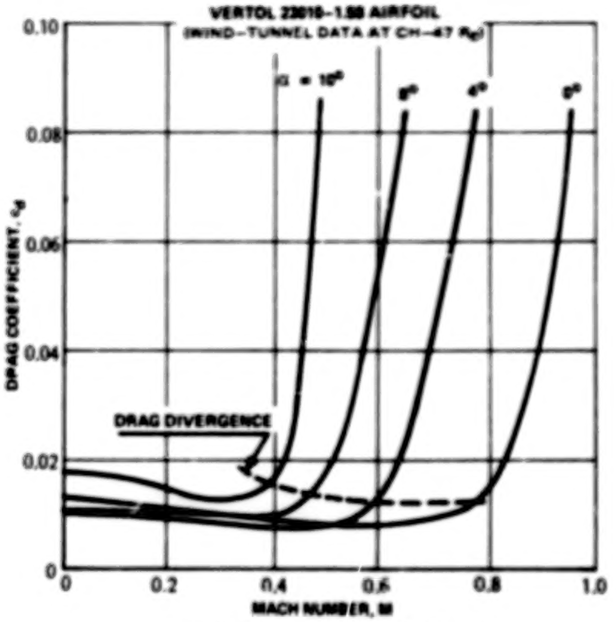

NOTE: ADD Δc_d = .0027 FOR TAIL ROTOR
(DUE TO R_e EFFECT)

Figure 2.4 Variation of section-drag characteristics with Mach number

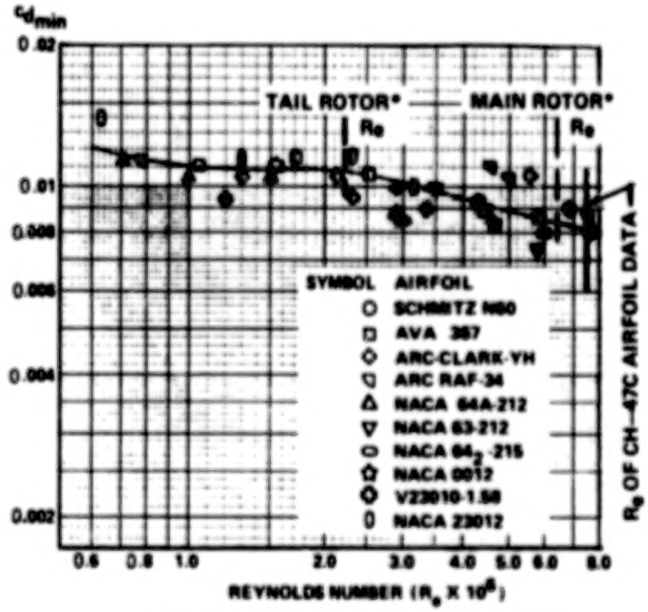

*R_e AT 3/4 RADIUS IN HOVER AT SL/STD

Figure 2.5 Reynolds number effect on airfoil section drag

testing and the trend was confirmed by model rotor data using the 3/4-radius location to define the average blade Reynolds number. Since the R_e values for the CH-47C rotor blades and those of the main rotor of the hypothetical helicopter are quite close, the CH-47C airfoil c_d data is sufficiently accurate for estimating the main rotor c_d values. It is not suitable, however, for use in defining tail rotor drag coefficients. The c_d increment due to the difference between the tail rotor Reynolds number and the airfoil data Reynolds number is $\Delta c_d = 0.0027$. Therefore, this Δc_d correction, representing a 34-percent increase in drag, is applied to all tail rotor performance predictions in this text.

Rotor Geometry and Coning Angle. The geometry of both the main and tail rotors is defined in Ch I. The elastic coning angles, which exclude any built-in coning, may be approximately computed from the relationships given in Vol I, Ch I, using the virtual flapping-hinge concept. This can also be done utilizing the simplified calculations discussed in Ref 2. Most industrial organizations have in-house trim analysis computer programs from which values of the coning angle can be found.

Ambient Conditions. Hover performance is a function of the air density and ambient temperature. The air density is either computed from inputs of pressure altitude and ambient temperature as defined by the equations found in Ch I, or determined from appropriate graphs. The number of computed conditions can be kept to a minimum by nondimensionalizing the power required and rotor thrust for air density as described later in this chapter. The only stipulation is that the blade tip Mach number must be correct. For an aircraft which is designed to operate at one rotor speed, such as the hypothetical helicopter, the tip Mach number variation can be satisfied by considering a range of ambient temperatures.

Rotor Thrust. Thrust values ranging from the minimum flying weight (weight empty, fixed useful load, and fuel reserve) to the maximum gross weight were inputted into the computerized program used in the case of the hypothetical helicopter. Additional calculations extending to zero thrust were also obtained to provide a comparison with the momentum theory predictions at low thrust levels.

1.3 Example of the Main Rotor Power Required

The hypothetical helicopter nondimensionalized main rotor power required is shown in Fig 2.6. Thrust coefficient $C_T = T/\rho\pi R^2 V_t^2$ is shown as a function of power coefficient $C_P = (RHP \times 550)/\rho\pi R^2 V_t^3$ for various tip Mach numbers, M_t. It should be noted that the fan shape formed by the C_P/C_T curves for various Mach number values is due to compressibility effects which become negligible at $M_t \leqslant 0.606$ and $C_T/\sigma < 0.1$. At 700 fps tip speed, $M_t < 0.606$ corresponds to ambient temperatures above 95°F.

Presenting the rotor performance in a nondimensional form is quite convenient during aircraft concept definition and preliminary design phases when a number of configurations must be evaluated and compared. However, the values of C_P and C_T are small; typically, $C_P = 0.0005$ and $C_T = 0.005$, which many find difficult to interpret and cumbersome to use when computing detailed performance for a given aircraft. For this reason, once a design is finalized, the nondimensional method of presenting power required is often replaced by a dimensional method known as the *referred power/referred thrust* (weight) *method.* Referred is based on the fact that at a given set of C_P

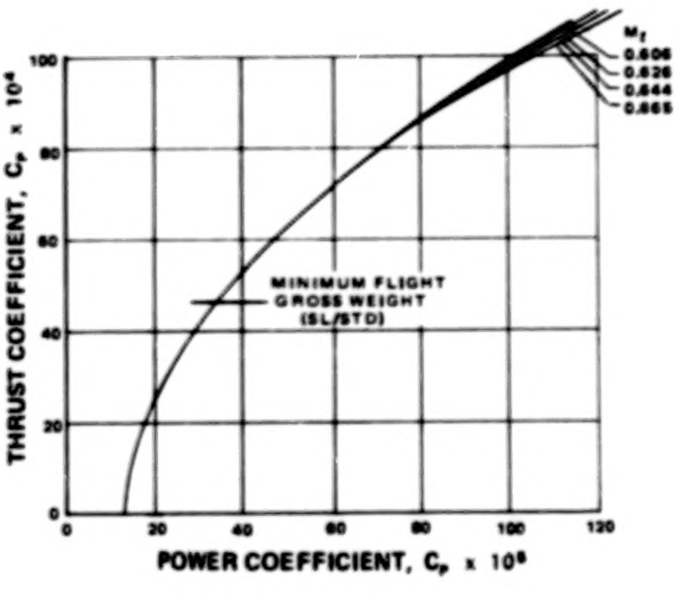

Figure 2.6 Main rotor hover out-of-ground effect power required

and C_T values, power is proportional to $\rho\pi R^2 V_t^3$ and thrust is proportional to $\rho\pi R^2 V_t^2$; therefore, the rotor horsepower (*RHP*) and thrust (*T*) at any altitude and tip speed can be referred to the equivalent SL/STD density altitude conditions shown below:

$$\begin{aligned} RHP_{ref} &= (RHP/\sigma_\rho)(V_{t_{ref}}/V_t)^3 = C_P \rho_0 \pi R^2 V_{t_{ref}}{}^3/550 \\ T_{ref} &= (T/\sigma_\rho)(V_{t_{ref}}/V_t)^2 = C_T \rho_0 \pi R^2 V_{t_{ref}}{}^2 \end{aligned} \qquad (2.1)$$

where $\sigma_\rho = \rho/\rho_0$
RHP_{ref} = power required at SL/STD
T_{ref} = thrust at SL/STD
$V_{t_{ref}}$ = reference operating tip speed.

Referred thrust for the sample problem aircraft is plotted as a function of referred power in Fig 2.7, assuming a reference tip speed of $V_{t_{ref}} = 700$ *fps*. Compressibility effects must be accounted for by referring along lines of constant Mach number. Tip Mach number can be related to tip speed in a more convenient way by noting that

$$M_t = V_t/a_0\sqrt{\theta}$$

where

a_0 = speed of sound at 59°F (15°C); fps.

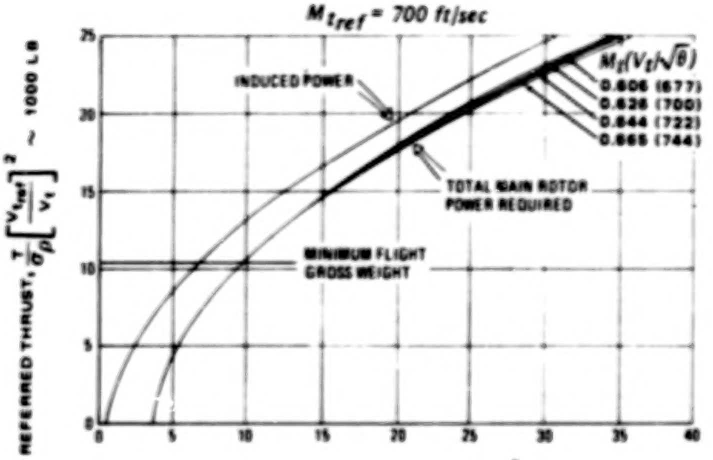

Figure 2.7 Main rotor power required (hover OGE)

The lines of constant Mach number in Fig 2.7, therefore, are also lines of constant $V_t/\sqrt{\theta}$. It should be noted that for a known rotor radius (in this case, $R = 25\ ft$), V_t can be replaced by an equivalent expression containing rpm, since $V_t = \Omega R = \pi\, rpm\, R/30 = 26.2\, rpm$.

The induced power component of the main rotor power required is also shown in this figure. In the case of a complete computer program based on the vortex theory, the induced power can be computed by making an input of the section $c_d = 0$. It can be seen that under SL/STD atmosphere conditions, the induced power amounts to approximately 80 percent of the total RHP at $T = 15{,}000\ lb$. The power difference between induced and total power represents the profile power, including the compressibility penalty.

A detailed breakdown of the profile power and induced power under SL/STD atmosphere is presented in Fig 2.8. The ideal induced power and simplified blade element theory profile power required (assuming $\bar{c}_d = 0.008$) are also shown for comparison with vortex theory results. The vortex theory induced power is considerably higher than the ideal power given by the momentum theory. At $T = 15{,}000\ lb$, for example, the vortex theory induced power is 15 percent greater than its ideal value. This difference is primarily due to the fact that nonuniform downwash effects and tip losses are not taken into account when determining ideal power. The induced power correction factor k_{ind_h}, defined as the ratio of the actual induced power to the ideal induced power (Vol I, Ch II) is also shown in Fig 2.8. It can be seen that k_{ind_h} increases from $k_{ind_h} = 1.08$ at $T = 10{,}000\ lb$, to $k_{ind_h} = 1.22$ at $T = 20{,}000\ lb$.

The general trend of k_{ind_h} increasing with T or, more strictly speaking, with C_T, is probably correct. However, it should be emphasized that the trend shown in Fig 2.8 is the result of a program based on the prescribed wake approach where wake contraction

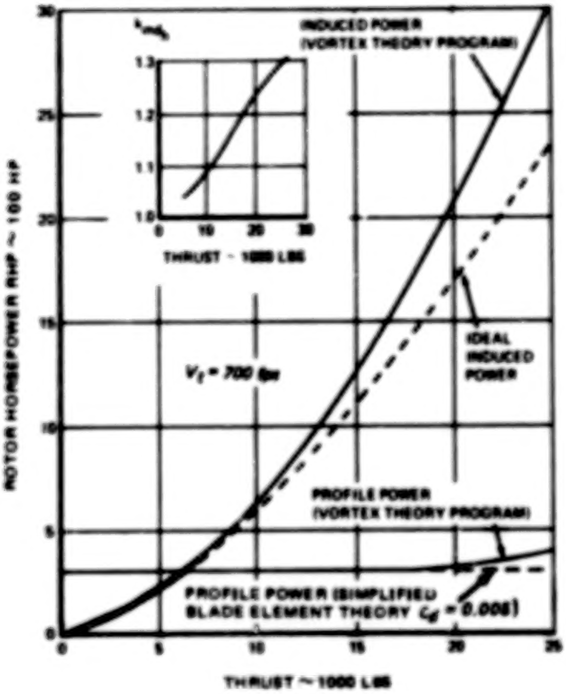

Figure 2.8 Main rotor induced and profile power

was empirically determined as a function of C_T. Consequently, an extrapolation to C_T values higher than actually tested may lead to error. Furthermore, it should also be remembered that blade section lift coefficients also become higher with increasing C_T and thus, c_d values also increase–sometimes quite rapidly, due to adverse $c_\ell - M$ combinations. Hence, caution must be exercised in the "bookkeeping" so that the induced and profile power effects are properly registered.

With these words of warning, let it be assumed that the relationship shown in Fig 2.8 is correct. Therefore, the thrust scale of the k_{ind_h} chart can be nondimensionalized in terms of C_T to predict the performance of other rotor configurations. The only stipulations are that the designs have four blades and −10° linear twist. Due to such airfoil characteristics as camber, lift-curve slope, and trailing-edge tab setting, some variation in k_{ind_h} may occur when changes are made in the airfoil section.

The variation of the induced power factor versus C_T, linear twist, and number of blades is illustrated in Figs 2.9 and 2.10[3]. In Fig 2.9, it can be seen that the benefits of twist begin to decrease at twist values $>|-10°|$. For typical rotor designs having C_T/σ levels (*0.06* to *0.08*) and twist values between *−5* and *−15°*, the induced power varies approximately 1 percent per degree of twist.

As shown in Fig 2.10, the induced power correction factor decreases with increasing number of blades. This trend may be expected because as the number of blades increase, the rotor approaches an actuator disc consisting of an infinite number of blades

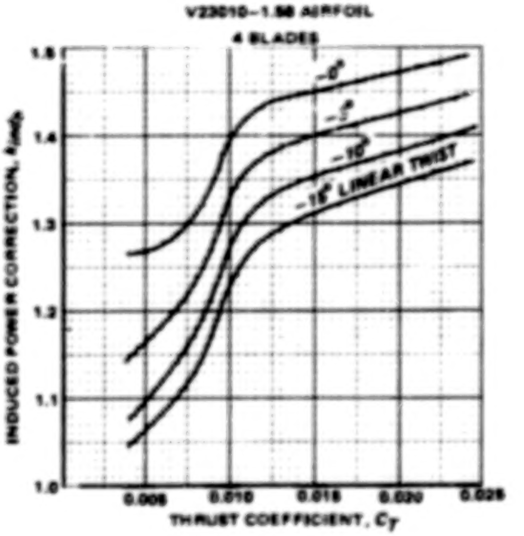

Figure 2.9 Variation of induced power factor with thrust coefficient and blade twist

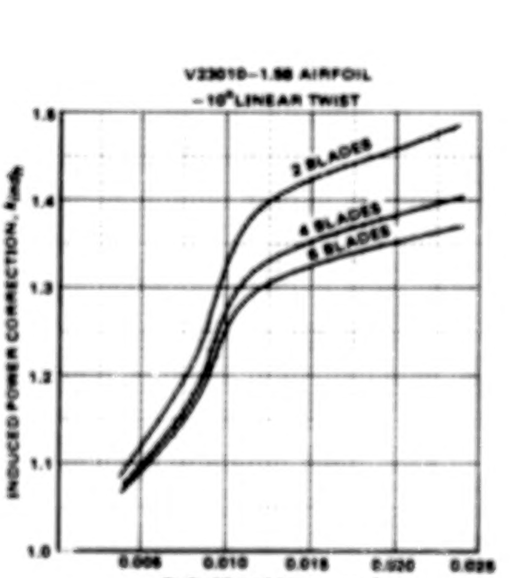

Figure 2.10 Variation of induced power factor with thrust coefficient and blade number

of infinite aspect ratio. However, the actual rate of improvement becomes lower as the number of blades increases. This is due to the fact that as the distance between the blades decreases, the trailing vortices from the preceding blade move closer to the following blade; causing adverse changes in its lift distribution.

In contrast to the above-discussed comparison of induced power predicted by the simple momentum versus vortex theories, predictions of profile power based on the simple element theory using a constant $\bar{c}_d$ value show good correlation with those obtained from the vortex theory (Fig 2.8). Both methods agree for thrust levels up to $T \leq 15{,}000$ *lb*. For $T > 15{,}000$ *lb*, the vortex theory predictions of profile power show gradually increasing values caused by compressibility effects, as well as an increase in c_d values due to the increasing level of local blade lift coefficient (c_ℓ).

The profile power (RHP_{pr}) shown by the dashed line in Fig 2.8 was determined using the following expression derived in Vol I, Ch III.1.3.

$$RHP_{pr} = (1/4400)\sigma\pi R^2 \rho \bar{c}_d V_t^3. \qquad (2.2)$$

The term $\bar{c}_d$ in this equation is the average blade airfoil section drag coefficient. It is determined using airfoil section data at the average section lift coefficient $\bar{c}_\ell$ and representative Mach number $\bar{M}$ of the rotor where $\bar{c}_\ell$ is defined from such blade element considerations as: $\bar{c}_\ell = 6C_T/\sigma$, and $\bar{M} = 0.75V_t/a$.

For the hypothetical helicopter, the airfoil section data given in Figs 2.3 and 2.4 was used. For profile power predictions based on blade element theory, it is generally more convenient to present this data in drag polar form as shown in Fig 2.11. As noted in this figure, $\bar{c}_\ell$ goes up to *0.64* for a thrust level of 25,000 lb at SL/STD atmosphere conditions and the corresponding Mach number (at 75-percent radius) is $M = 0.47$. At this Mach number, the average drag coefficient would be *0.008*, and would not vary significantly with lift coefficient for c_ℓ values up to *0.7*.

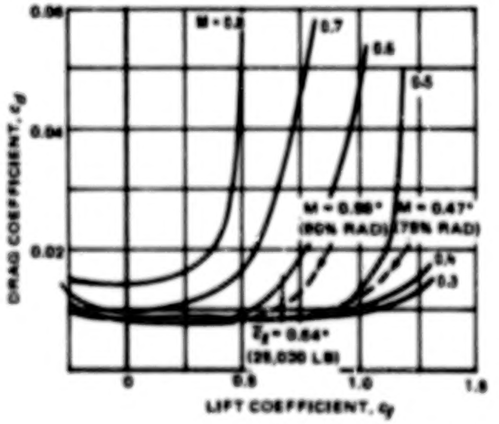

*SL/STD, V_t = 700 FT/SEC

Figure 2.11 Vertol 23010-1.58 airfoil section drag polars

However, due to compressibility effects which cause a rise in drag at the blade tip at high thrust levels, the assumption that the representative Mach number occurs at the 3/4-blade radius location becomes invalid. The two profile power predictions shown in Fig 2.8 can be made to agree reasonably well if the average drag coefficient and associated Mach number are assumed to occur at 90 percent instead of 75 percent of the blade radius. As shown in Fig 2.11, at $T = 25{,}000\ lb$ and SL/STD conditions, c_d increases from $c_d = 0.008$ to $c_d = 0.0102$ as the representative Mach number increases from $M = 0.47$ at the 75-percent radius to $M = 0.56$ at the 90-percent radius.

A more rigorous method of accounting for compressibility is to apply profile power corrections obtained from the computer program based on the vortex theory. An example of this correction for the hypothetical helicopter is shown in Fig 2.12 as $\Delta C_P/\sigma$ versus tip Mach number for various C_T/σ values. The same correction can be used as an approximation for other airfoil sections provided they have a thickness ratio of from 10 to 12 percent.

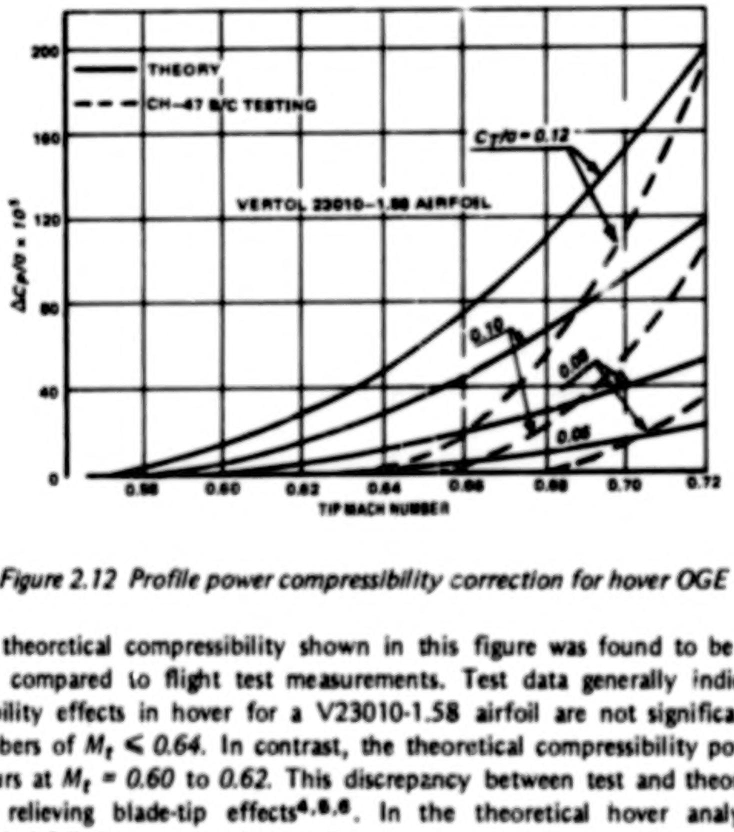

Figure 2.12 Profile power compressibility correction for hover OGE

The theoretical compressibility shown in this figure was found to be conservative when compared to flight test measurements. Test data generally indicates that compressibility effects in hover for a V23010-1.58 airfoil are not significant for tip Mach numbers of $M_t < 0.64$. In contrast, the theoretical compressibility power divergence occurs at $M_t = 0.60$ to 0.62. This discrepancy between test and theory is attributed to relieving blade-tip effects[4,5,6]. In the theoretical hover analysis, two-dimensional airfoil data were used to predict power required; however, it did not account for the reduced local velocities that occur at the blade tip due to three-dimensional flow effects.

The induced and profile power discussion presented above indicates that calculations based on simple momentum and blade element theories can be modified to account for nonuniform downwash and compressibility effects so that reliance on large and expensive high-speed computers is not necessary. These shortcut techniques are particularly valuable for preliminary design studies where many different configurations must be evaluated within a limited budget. Additional information on shortcut methods can be found in the HESCOMP User's Manual (Helicopter Sizing and Performance Computer Program)[3].

1.4 Tail Rotor Power Required

The solidity of tail rotors is generally larger than that of the main rotors in order to obtain acceptable average lift coefficients or C_T/σ values both in equilibrium and in maneuvers.

The tail rotor must produce sufficient thrust in equilibrium to compensate the main rotor torque in hover. This trim condition requirement can be expressed as

$$T_{tr_{net}} \ell_{tr} = Q \tag{2.3}$$

and

$$Q = 5252\,RHP_{mr}/N \tag{2.4}$$

where

Q = main rotor torque; ft-lb
$T_{tr_{net}}$ = net tail rotor thrust
ℓ_{tr} = moment arm (line from tail rotor shaft perpendicular to main rotor shaft); ft
N = main rotor rpm.

Substituting Eq (2.4) into Eq (2.3) gives

$$T_{tr_{net}} = 5252\,RHP_{mr}/N\ell_{tr}. \tag{2.5}$$

For the hypothetical helicopter,

$$T_{tr_{net}} = 5252\,RHP_{mr}/(267.4 \times 30) = 0.655\,RHP_{mr}.$$

The tail rotor power required corresponding to this net tail rotor thrust level was determined for the hypothetical helicopter by applying the same vortex theory analysis technique used to predict main rotor hover performance. However, in order to determine the net tail rotor thrust, an additional correction must be applied to account for fin blockage effects which, due the vertical fin side force, decreases the thrust of the isolated rotor. A discussion of isolated tail rotor power required calculations and fin blockage effects is presented below.

Isolated Tail Rotor Power Required. The isolated tail rotor performance, as in the case of the main rotor, can be determined using any appropriate theory. In this particular case, the existing hover analysis computer program based on the explicit vortex influence technique was used. The computer input requirements are similar to those defined for the main rotor (Fig 2.1). It should be emphasized at this point that airfoil drag characteristics were significantly different from those of the main rotor; therefore an increment of

$\Delta c_d = 0.0027$ was added to the main rotor section drag data to account for R_e effects (Fig 2.5).

The power required for the hypothetical aircraft tail rotor for SL/STD atmosphere is presented in Fig 2.13. Total power, induced power, and profile power obtained from the vortex theory program are compared to the ideal induced power and simplified blade element theory profile power predictions. As shown, the total rotor thrust required to hover at $W = 15{,}000$ *lb* is $T_{tr} = 1{,}170$ *lb*. The corresponding power predicted by the vortex theory is $RHP_{tr} = 210$ *hp*, consisting of 87 percent induced and 13 percent profile power. The vortex theory induced power is 30 to 50 percent higher than that predicted by the simple momentum theory. This percentage difference is almost twice as large as the values noted in the main rotor discussion because the tail rotor operates at much higher disc loadings or thrust coefficients where nonuniform downwash effects become more significant. Unfortunately, there is no full-scale test data to verify or deny the unusually high differences between the vortex-theory-predicted and the ideal-induced powers. Assuming that the computer program results are correct, the tail rotor induced power factor k_{ind_h} varies from 1.3 to 1.5; depending on the value of C_T. For tail rotor applications where $C_T > 0.01$, a mean value of $k_{ind_h} = 1.4$ can be used to estimate the tail rotor performance as shown in Figs 2.9 and 2.10.

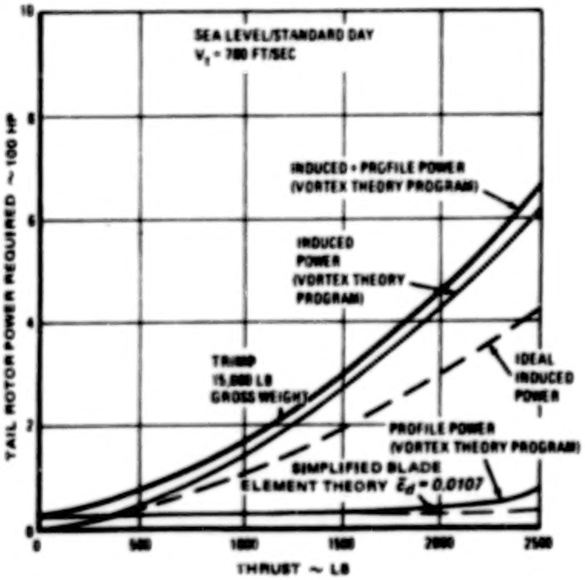

Figure 2.13 Tail rotor induced and profile power

Comparisons of profile power required are also shown in Fig 2.13. The tail rotor power required, as predicted by the blade element theory, agrees with the vortex theory computer program estimates at thrust levels up to approximately $T_{tr} = 1200$ *lb*. Above this value, the vortex theory shows higher power required due to compressibility effects. As described in the main rotor analysis, better agreement can be achieved at higher thrust levels if a 90-percent radius representative section Mach number instead of the 3/4-radius value is utilized or, if the correction shown in Fig 2.12 is applied. In general, however, the tail rotor operates in trimmed hover conditions at C_T/σ values sufficiently low that the compressibility power increment represents a relatively small percentage of the total power required and therefore, can be neglected for most preliminary design studies.

Vertical Fin Blockage Effects. Since this is assumed to be a pusher-type tail rotor, the inflow, in hover, is blocked by the vertical tail and a fin force is generated which acts to reduce the net thrust available for antitorque purposes. The tractor-type tail rotor downwash impinges on the vertical tail; again, creating a fin force reducing the net rotor thrust. In either case, isolated tail-rotor performance must be adjusted for the blockage effect by increasing the thrust required as shown in Fig 2.14. This data was obtained by measuring the fin force and thrust of various model fin and tail rotor configurations[7]. The configurations tested included both pusher and tractor-type tail rotors located at varying distances from the vertical fin (s). The ratio of the tail rotor thrust to net thrust is a function of the fin/rotor separation (s/R_{tr}) and the fin area to rotor-disc area ratio ($S_v/\pi R_{tr}^2$). Utilizing the thrust ratio from Fig 2.14 and Eq (2.5), it can be shown that the isolated rotor thrust required to trim the aircraft is as follows:

$$T_{tr} = \left(\frac{T_{tr}}{T_{tr_{net}}}\right)\left(\frac{5252\,RHP_{mr}}{N\ell_{tr}}\right). \tag{2.6}$$

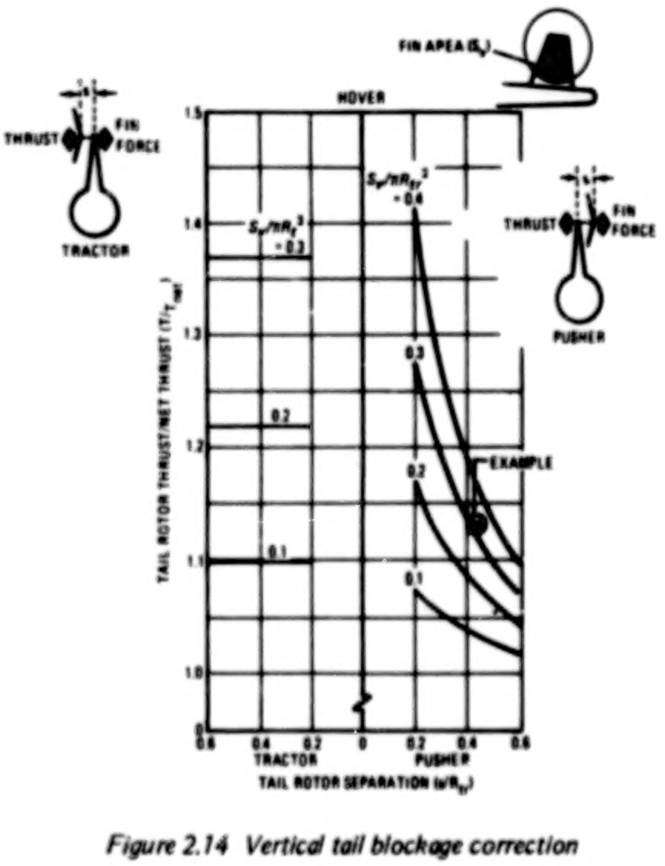

Figure 2.14 Vertical tail blockage correction

The hypothetical aircraft has a pusher-type tail rotor with a fin separation ratio $s/R_{tr} = 0.426$ and a fin area to rotor-disc area ratio $S_v/\pi R_{tr}^2 = 0.32$. As noted in Fig 2.14, the thrust ratio for this configuration is $T/T_{net} = 1.13$. The effect of vertical tail blockage on tail rotor power required is shown in Fig 2.15, where net thrust is presented as a function of power required with and without the vertical tail installed. It can be seen that the blockage correction increases the tail rotor power required at the $T = 15{,}000$-lb trim point by 18 percent, which is equivalent to approximately a 2-percent increase in total aircraft power required. For preliminary design studies, this penalty may be neglected since it is relatively small; however, for detailed performance predictions, it should be included in the calculations.

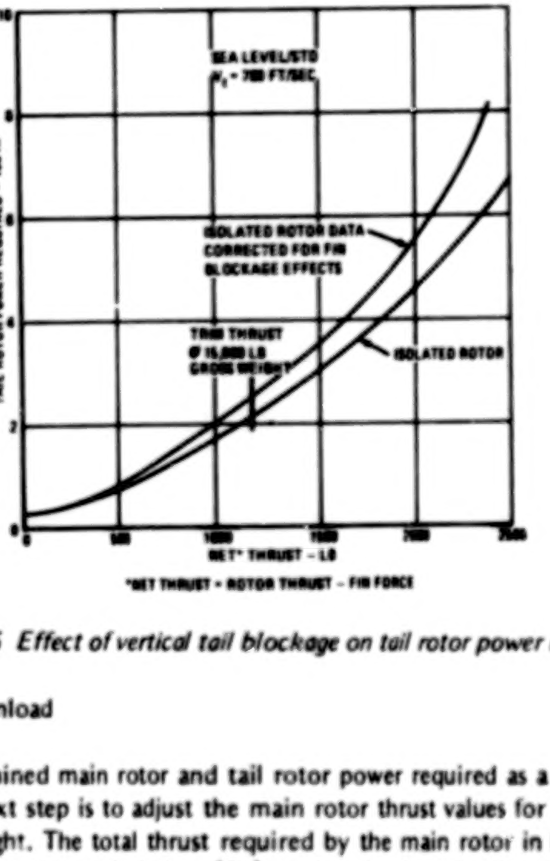

Figure 2.15 Effect of vertical tail blockage on tail rotor power required

1.5 Fuselage Download

Having determined main rotor and tail rotor power required as a function of main rotor thrust, the next step is to adjust the main rotor thrust values for download effects to obtain gross weight. The total thrust required by the main rotor in hover is equal to the gross weight plus the vertical drag (D_v) or download on the fuselage caused by the rotor downwash velocity ($T = W + D_v$). Vertical drag is calculated by combining the estimated fuselage vertical drag coefficients with downwash velocity distributions based, preferably, on wind-tunnel testing; or analytical predictions, if test results are lacking. The calculation procedure involves dividing the fuselage into segments and computing the drag increments of each segment. For example, the incremental download ΔD_v of segment n to $n+1$ is

$$\Delta D_{v_n} = \int_{\zeta_n}^{\zeta_{(n+1)}} C_{D_v} \tfrac{1}{2}\rho v^2 \, w_n \, d\zeta \tag{2.7}$$

where w_n is the average segment width, C_{D_v} is the local drag coefficient, and v is the downwash velocity acting on the area $w_n d\zeta$. The parameter ζ is the distance from the forward edge of ther rotor disc to segment n, and is measured along the fuselage centerline shown in Fig 2.16.

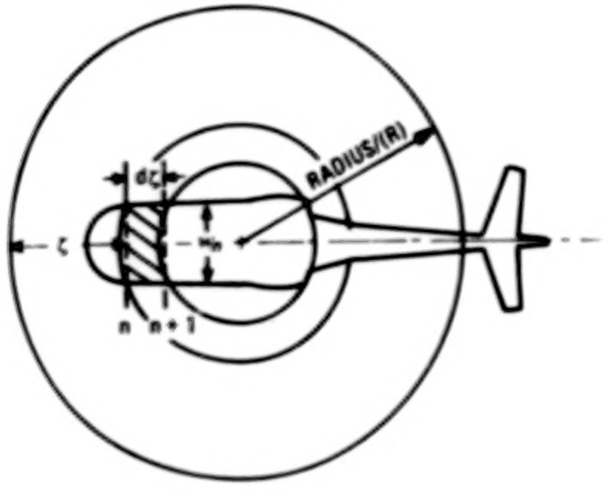

Figure 2.16 Incremental fuselage area

Assuming that w_n and $C_{D_{v_n}}$ are constants for a given segment, Eq (2.7) can be rewritten as

$$\Delta D_{v_n} = C_{D_{v_n}} \tfrac{1}{2}\rho w_n \int_{\zeta_n}^{\zeta_{n+1}} v^2 \, d\zeta. \tag{2.8}$$

From momentum theory,

$$T = 2\rho\pi R^2 v_{id}^2. \tag{2.9}$$

Dividing Eq (2.8) by (2.9) results in the nondimensional download expression

$$\Delta D_{v_n}/T = C_{D_{v_n}} W_n/4\pi R \int_{(\zeta/R)_n}^{(\zeta/R)_{n+1}} (v/v_{id})^2 \, d(\zeta/R) \tag{2.10}$$

where $\Delta D_v/T$ and ζ/R are defined as percentages.

The term $\int(v/v_{id})^2 \, d(\zeta/R)$ in Eq (2.10) is equal to the area under a plot of $(v/v_{id})^2$ versus (ζ/R) between stations n and $n+1$. To simplify the integration procedure, a variable

$$k_{v_n} = \int_{0}^{(\zeta/R)_n} (v/v_{id})^2 d(\zeta/R)$$

is introduced. Substituting this expression in Eq (2.10) gives:

$$\Delta D_{v_n}/T = (C_{D_{v_n}} w_n/4\pi R^2)(k_{v_{n+1}} - k_{v_n}). \tag{2.11}$$

To illustrate the download prediction technique outlined above, detailed sample calculations for the hypothetical helicopter are presented in Table II-1. The fuselage is divided into five segments. The cross-section shape of each segment and the corresponding C_{D_v} are defined in Fig 2.17. The drag coefficients are based on wind-tunnel pressure and force measurements obtained on numerous fuselage shapes.

STEP	①	②	③	④	⑤	⑥	⑦	⑧	⑨
ITEM	ζ (ft)	ζ/R (%)	$k_{v_{n+1}}$	k_{v_n}	Δk_v	C_{D_v}	w (ft)	$C_{D_v}w/4\pi R$	$\Delta D_v/T$ (%)
CALCULATION PROCEDURE		① /25	See Fig 2.19		③ − ④	Fig 2.17	Segment Width	⑥ × ⑦ /4π × 25	⑧ × ⑤
SEGMENT (n)									
1-2 COCKPIT	09.3	037	138	087	51	0.5	6.00	0.00955	0.49
2-3 CABIN	12.7	051	205	1.38	67	0.4	8.00	0.01020	0.68
3-4 NACELLE	25.9	104	210	205	05	1.2	8.65	0.03300	0.17
4-5 AFTERBODY									
	31.1	124	225	210	15	0.5	6.50	0.01035	0.16
	33.6	134	252	225	27	0.5	5.34	0.00850	0.23
	36.1	144	298	252	46	0.5	4.18	0.00665	0.31
5-6 TAILBOOM									
	39.5	158	385	298	87	0.5	2.66	0.00423	0.37
	44.6	178	410	385	25	0.5	2.00	0.00318	0.08
	50.0	200		410					

D_v/T = 2.49%
D_v/W = 2.55%

TABLE II-1 DOWNLOAD CALCULATIONS

Download drag coefficients for typical fuselage section shapes based on wind-tunnel tests are illustrated in Fig 2.18. Additional drag data applicable to download predictions can be found in Ref 8; however, this data applies to two-dimensional shapes and must be adjusted for three-dimensional effects if it is to be used for fuselage sections near the cockpit. An estimate of three-dimensional effects can be obtained from Ref 9.

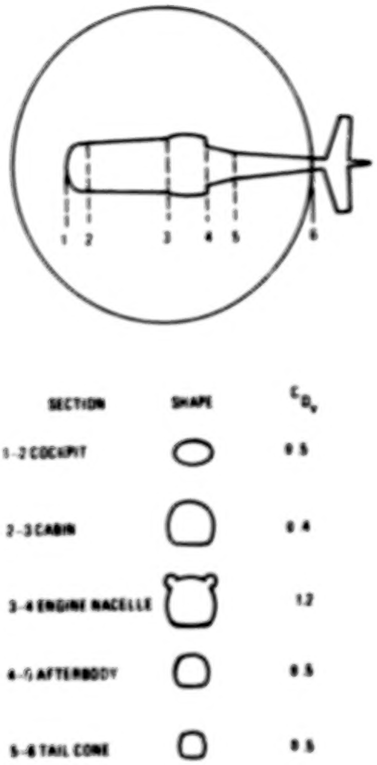

Figure 2.17 Hypothetical helicopter vertical drag coefficients

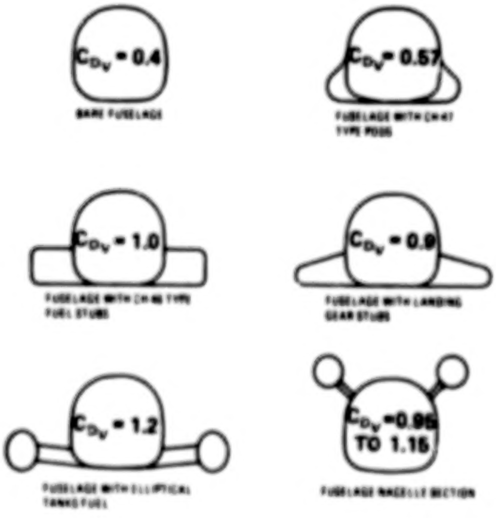

Figure 2.18 Typical helicopter fuselage section vertical drag coefficients

The download increment for each of the five fuselage segments is then calculated by combining the drag coefficientd with the downwash velocity. The downwash profile applicable to single-rotor helicopters is illustrated in Fig 2.19. The nondimensional velocity ratios, v/v_{id}, $(v/v_{id})^2$ and k_v values in this figure are plotted as a function of distance from the forward tip of the rotor in percent radius ζ/R. This data is based on Universal Helicopter Model (UHM)* measurements, with the front rotor removed.

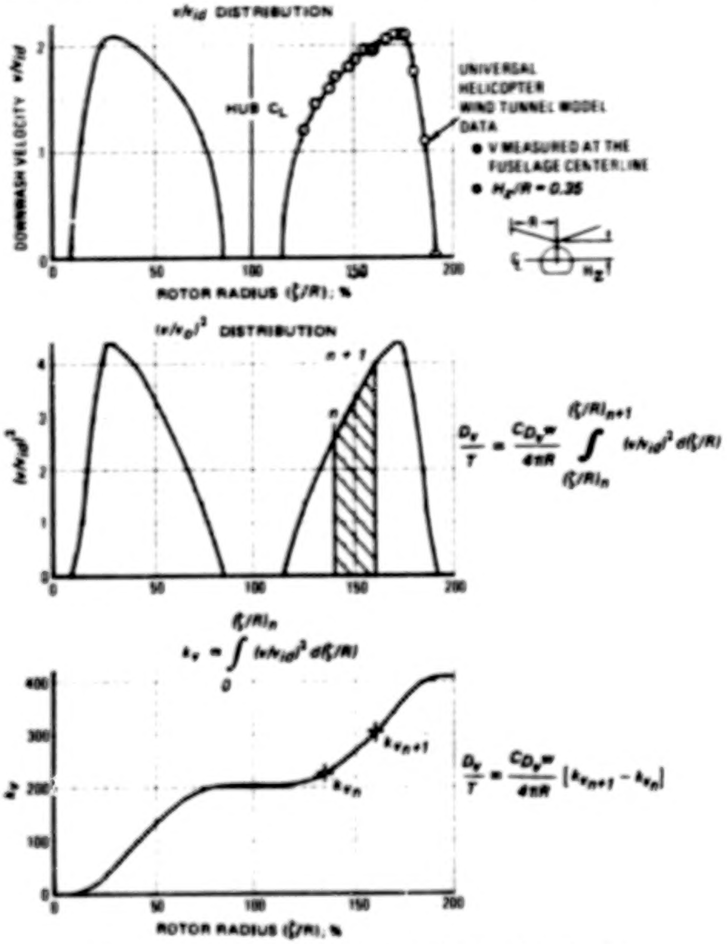

Figure 2.19 Hover downwash velocity distribution

A photograph of the UHM tandem configuration installed in the tunnel is shown in Fig 2.20. The model tested was a 5.35-ft diameter rotor having -9° linear twist, a solidity of 0.0619 and a rotor height above the fuselage of $H_z/R = 0.3$. Of these parameters, the rotor height has the most significant effect on download. For rotor configurations with H_z/R values lower than that of the model—such as the hypothetical helicopter which has a $H_z/R = 0.2$—the model data represents a conservative estimate of downwash velocity since the downwash velocity decreases with decreasing rotor-to-fuselage clearance.

---

*The name of this model reflects its versatility, permitting one to test tandem rotors in various geometric configurations, or to obtain measurements on one rotor only.

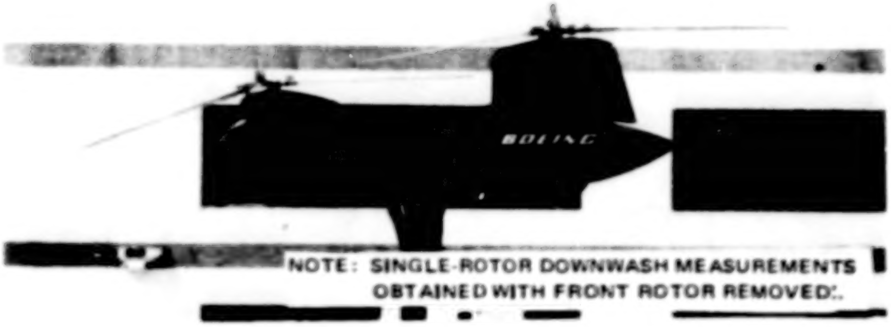

NOTE: SINGLE-ROTOR DOWNWASH MEASUREMENTS OBTAINED WITH FRONT ROTOR REMOVED.

Figure 2.20 Universal Helicopter wind-tunnel model

The last step in the calculations is the summation of the $\Delta D_v/T$ increments. As noted at the bottom of Table II-1, the download (D_v) of the hypothetical helicopter is 2.49 percent of thrust—or 2.55 percent of gross weight. The relationship between D_v/T and D_v/W is

$$D_v/W = (D_v/T)/(1 - D_v/T).$$

The sample problem main rotor thrust versus rotor power required data presented in previous sections can now be converted to gross weight versus power required, using the D_v/W value derived above:

$$W = T/(1 + D_v/W). \tag{2.12}$$

The hypothetical helicopter combined main and tail rotor power required as a function of gross weight is shown in Fig 2.21. The tail rotor power required—including compressibility effects—is also shown in this figure. As noted, at 15,000 lb gross weight

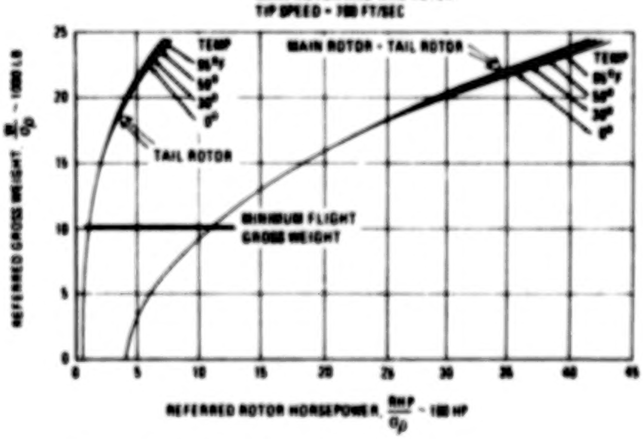

Figure 2.21 Total hover (OGE) power required

under SL/STD conditions, the tail rotor power required amounts to 12 percent of the total required RHP. The percentage varies from 10 percent at $W = 10{,}000\ lb$ to 14 percent at $W = 18{,}000\ lb$. Compressibility effects do not significantly influence these percentages for referred weights below 17,000 lb.

The download prediction methodology described above will give slightly conservative answers because of thrust recovery effects. The main rotor operates in partial ground effect, provided by the upper surface of the airframe. This results in an increased thrust capability at a fixed power available level. The amount of gain is a function of blade twist, blade cutout, and rotor/fuselage clearance[10]. It should be noted that a similar phenomenon is also encountered in the tail operation; hence, the predicted vertical fin blockage corrections for tractor rotors may be conservative.

1.6 Transmission and Accessory Losses

The rotor horsepower required (*RHP*) shown in Fig 2.21 was computed at the rotor shaft, and does not take into account losses which occur in the transmission of power from the engine shafts, nor the additional power required to operate accessories. The total shaft horsepower (*SHP*) required of the engines is

$$SHP = RHP/\eta_t + P_a \tag{2.13}$$

where

η_t = transmission efficiency,
P_a = accessory power.

A detailed discussion of transmission and accessory losses is presented below.

Transmission Losses. Gearbox losses are generally considered as a fixed percentage of the input SHP, and are usually determined by totaling the estimated losses for each gear mesh in the drive system. The following loss-per-mesh values were used for the sample calculations:

(1) 0.5 percent for low and intermediate-speed bevel and planetary gears;
(2) 1.0 percent for high-speed bevel gears.

Estimated losses for the hypothetical helicopter at the 2900 SHP transmission limit power setting are presented in Table II-2. Transmission losses amount to two percent of the power available. Tail rotor transmission losses are so small that they are not considered in these calculations.

Accessory Losses. Accessory losses include power extraction for items such as engine and transmission cooling blowers, electrical power generation, and hydraulic power supplies. For the hypothetical helicopter, accessory losses are assumed to be 30 hp, or approximately one percent of the transmission limit. Therefore, the total transmission plus accessory losses incurred at the transmission limit is about three percent. This value is typical of losses measured during flight test evaluations of current production aircraft. The final expression for converting RHP to SHP for the hypothetical aircraft is

$$SHP = (RHP/0.98) + 30.$$

ASSUMED NUMBER AND TYPE OF TRANSMISSION	POWER AT GEAR MESH	% POWER LOSS/MESH	POWER LOSS (ΔSHP)
ENGINE GEARBOXES:			
2 High-Speed Bevels	1450	1.0	29.0
MAIN ROTOR:			
2 Intermediate Speed Bevels	1450	0.5	14.5
1 Planetary	2900	0.5	14.5
		TOTAL	58.0
		PERCENTAGE OF 2900 SHP	2.0

TABLE II-2 TRANSMISSION LOSS AT THE TRANSMISSION LIMIT POWER SETTING

2. HOVER IN-GROUND-EFFECT (IGE) PERFORMANCE

When helicopters hover close to the ground, the power/thrust relationships undergo changes, depending on the relative height (H_r/d) of the rotor disc above the ground. This is due to the fact that induced velocity decreases close to the ground, causing a drop in induced power. By the same token, at a fixed power setting, the main rotor thrust increases, and the fuselage download decreases. Because of the mathematical complexity of the problem, semi-empirical methods are usually used to evaluate the ground effect. This approach is also applied to the prediction of IGE performance capability of the hypothetical helicopter.

2.1 Rotor Thrust Variation, IGE

Correction factors to out-of-ground effect values were developed from flight test and model rotor data. The ratio of thrust IGE at constant power settings for various single-rotor aircraft (based on flight-test measurements[11]) as a function of H_r/d is presented in Fig 2.22. It can be seen that the inception of ground effect occurs at $H_r/d < 1.3$. For the hypothetical helicopter, the thrust ratio at a wheel height of 5 feet from the ground–corresponding to $H_r/d = 0.3$–is $T_{IGE}/T_{OGE} = 1.14$ (Fig 2.23).

Other possible methods of correcting OGE performance for IGE effects can be based on the SHP_{IGE}/SHP_{OGE} at a fixed thrust level. However, the approach based on thrust-ratio data at constant SHP provides more useful generalized trends because it eliminates the influence of variation in profile power, tail rotor power, and transmission accessory power which, at constant SHP, remain the same regardless of the thrust value. To separate induced power from other power components, generalized power required data must be analyzed by comparing $C_P^{2/3}$ versus C_T.

2.2 IGE Download

When using the thrust ratio in determining in-ground-effect hover capability, it is necessary to apply another empirical correction to account for the reduction in vertical

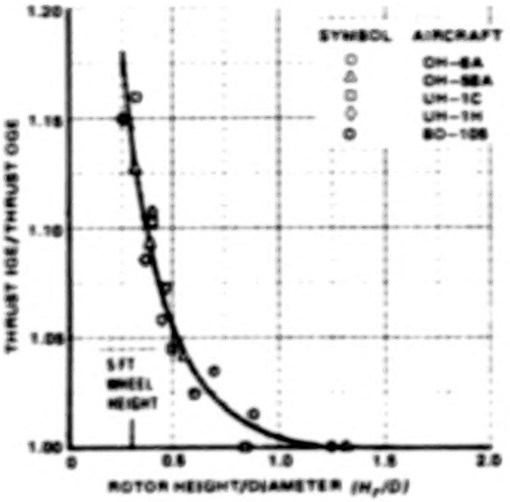

Figure 2.22 Thrust variation in-ground-effect at constant power

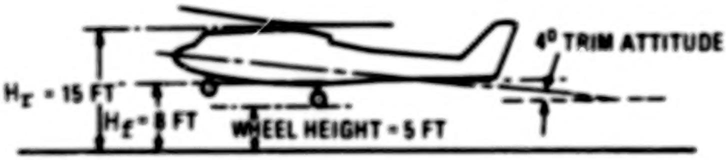

Figure 2.23 Hypothetical helicopter geometric parameters (IGE)

drag (D_v) which occurs in this regime of flight. This decrease in IGE download results from favorable interference effects between the lower surface of the airframe and the ground, as the pressure on the lower half of the fuselage increases due to higher static pressure in the surrounding downwash field.

The download correction factor (k_g), derived from the model rotor test data shown in Fig 2.24, is defined as

$$k_g = D_{v_{IGE}}/D_{v_{OGE}}.$$

In this figure, k_g is presented as a function of the ratio of average distance between the fuselage lower surface and the ground (H_f), and rotor diameter (d). For the hypothetical helicopter having a 5-ft wheel height, $k_g = 0.09$, and the download becomes zero at a wheel height of 3.4 ft, or $H_f/d = 0.13$.

Since k_g is used to compute the gross weight ratio W_{IGE}/W_{OGE} from the thrust ratio data presented in Fig 2.22 by noting that $T = W + D_v$; and since $D_{v_{IGE}} = k_g D_{v_{OGE}}$, then

$$\frac{T_{IGE}}{T_{OGE}} = \frac{W_{IGE}\ 1 + k_g(D_v/W)_{OGE}}{W_{OGE} + (D_v/W)_{OGE}}. \tag{2.14}$$

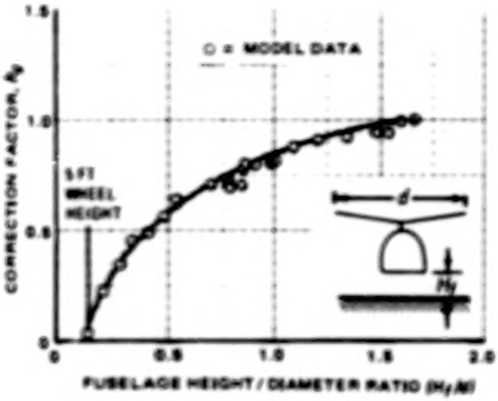

Figure 2.24 Effect of ground proximity on hover download

It should be noted that although the thrust curve shown in Fig 2.22 is based on the gross weight data presented in Ref 8, corrections for download effects (utilizing Eq (2.14)) were applied, thus obtaining a relationship between the IGE and OGE rotor thrust values.

As shown in Fig 2.23, the hypothetical helicopter rotor and fuselage height parameters at a typical ground-effect wheel height of 5 ft are $H_r/d = 0.3$ and $H_f/d = 0.16$. The average height of the cabin and tail boom above the ground at the nominal hover attitude of 4° (nose up) was used to define H_f; however, the distance between the bottom of the cabin and the ground at 0° pitch attitude can also be used with no significant reduction in accuracy. The thrust augmentation in-ground-effect and the download correction factors obtained from Figs 2.22 and 2.24 are $T_{IGE}/T_{OGE} = 1.14$ and $k_g = 0.09$. Substituting these values in Eq (2.14) and noting that $(D_v/W)_{OGE} = 0.0255$ for the hypothetical helicopter, we obtain $W_{IGE}/W_{OGE} = 1.17$. Therefore, the IGE gross weight capability of the hypothetical helicopter at a 5-ft wheel height is 17 percent higher than when out-of-ground effect, assuming constant power available. This analysis also assumes zero wind. In general, wind tends to reduce IGE thrust augmentation by deflecting the rotor downwash.

3. HOVER CEILING OGE AND IGE

Hover ceiling capability is calculated by matching the power available (see Ch I) with the power required for a range of operational altitudes. OGE and IGE hover ceilings for the hypothetical aircraft are presented in Fig 2.25 under standard atmosphere and 95° F ambient conditions. As shown, the helicopter has a 16,000-lb OGE gross weight capability at 4000 ft/95°F. The IGE capability is restricted–due to the maximum weight limit of the aircraft–to $W = 18{,}000$ *lb*. Detailed sample calculations for these two points are presented below to illustrate the calculation procedure. The main rotor tip speed is $V_t = 700$ *fps*, and the ambient constants at 4000 ft/95°F are $\sigma_p = 0.8076$ and $\sqrt{\theta} = 1.034$ (as defined in Ch I).

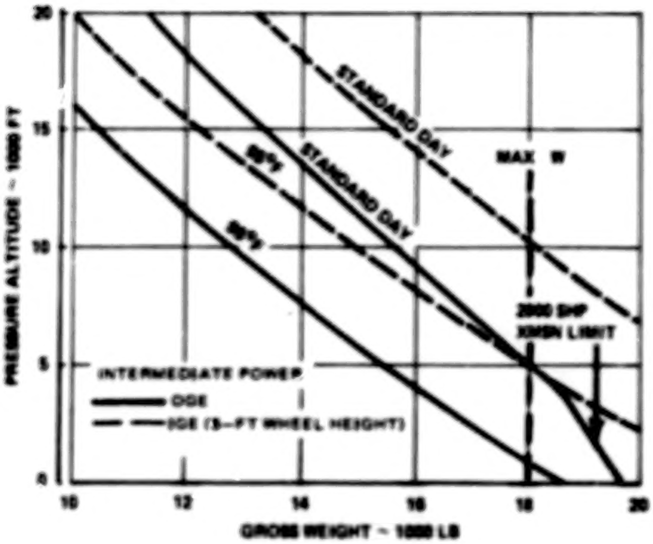

Figure 2.25 Hover ceiling in-and-out-of-ground effect

Starting with the above inputs, further calculations are performed using the following steps:

(1) Determine engine power available from Fig 1.7:

$SHP = 1196\ hp$ (one engine, intermediate (INT) power).

(2) Correct for installation losses (-1 percent):

$SHP = 0.99(1196 \times 2) = 2368\ hp$ (two engines).

(3) Convert SHP to RHP:

$RHP = 0.98(SHP - 30)$

$RHP = 0.98(2368 - 30) = 2291\ hp.$

(4) Calculate referred power at $V_t = 700\ fps$:

$RHP_{ref} = (RHP/\sigma_p)(700/Vt)^3$

$RHP_{ref} = (2291/0.8076) = 2835\ hp.$

(5) Compute $V_t/\sqrt{\theta}$:

$V_t/\sqrt{\theta} = 700/1.034 = 677\ fps.$

(6) From Fig 2.21, at $V_t/\sqrt{\theta} = 677\ fps$; the referred gross weight,

$W_{ref} = 19{,}820\ lb.$

(7) Calculate HOGE gross weight:

$W_{OGE} = W_{ref} \times \sigma_p(V_t/700)^3$

$W_{OGE} = 19820 \times 0.8076 = 16{,}010\ lb.$

(8) Calculate IGE weight from the OGE weight:

$W_{IGE} = 1.17\ W_{OGE}$

$W_{IGE} = 18{,}730\ lb.$

Since this weight exceeds the maximum operational weight limitation, the HIGE capability is restricted to a gross weight of 18,000 lb.

4. VERTICAL CLIMB CAPABILITY

The hypothetical helicopter vertical climb capability as a function of gross weight for maximum continuous and intermediate power settings is presented in Fig 2.26 at SL/STD and 4000 ft/95°F ambient conditions. For a design gross weight of 15,000 lb, V_c = *900 fpm* at intermediate power and 4000 ft/95°F conditions. A description of the method used to compute this performance data, including detailed basic sample calculations, is presented in the following paragraphs. In addition, a simplified method of computing vertical climb performance using potential energy considerations is provided.

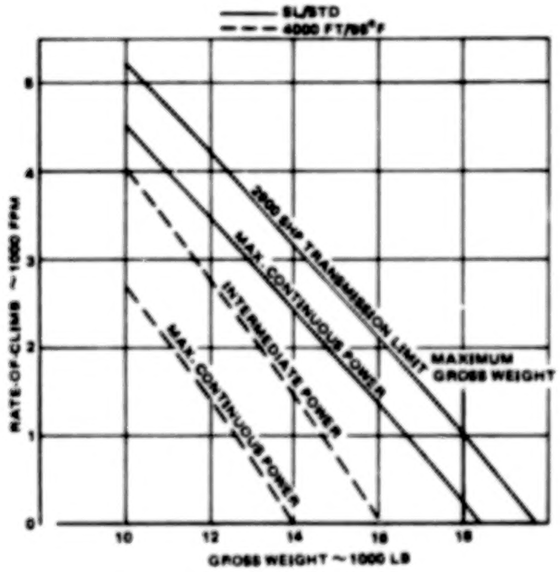

Figure 2.26 Vertical climb capability

4.1 Detailed Analysis

The relationships used to calculate vertical climb performance are based on the momentum theory expressions developed in Vol I, Ch II.4. To account for nonuniform downwash effects, the ideal induced velocity (v_{id}) and ideal thrust horsepower $[P_{T_{id}} = T(V_c + v_{id})/550]$ defined by the momentum theory can be replaced by an equivalent induced velocity $v_e = k_{ind}\, v_{id}$ and the *actual* thrust horsepower (P_T) determined from the vortex theory. This procedure is shown below:

$$T = \rho \pi R^2 (V_c + v_e) 2 v_e \tag{2.15}$$

and

$$P_T = T(V_c + v_e)/550 \tag{2.16}$$

where

V_c = climb velocity; fps

T = main rotor thrust; lbs.

Rearranging Eq (2.16) gives:

$$V_c = (550P_T/T) - v_e. \tag{2.17}$$

Vertical rate of climb, therefore, is a function of (1) main rotor thrust power, (2) thrust, and (3) equivalent induced velocity. Knowing the main rotor power available ($RHP_{av_{mr}}$), the corresponding available rotor thrust power ($P_{T_{av}}$) can be determined as shown below:

$$P_{T_{AV}} = RHP_{av_{mr}} - P_{pr} \tag{2.18}$$

where P_{pr} is the main rotor profile power, and

$$RHP_{av_{mr}} = (SHP_{av} - P_a)\eta_t - P_{tr};$$

SHP_{av} being engine shaft power available; P_{tr}, the tail rotor power required; and P_a is the accessory power.

In this relationship, the tail rotor power requirements in climb are assumed to be equal to the value needed to trim the aircraft in hover at $RHP_{av_{mr}}$, and the main rotor profile power in climb is assumed to be equal to the hover profile power for the same thrust level ($P_{pr_c} = P_{pr_h}$ if $T_h = T_c$). The tail rotor power and main rotor profile power variation between hover and climb conditions is usually small enough at low-to-moderate climb rates to justify these assumptions.

The remaining unknown parameter in Eq (2.17) is the equivalent induced velocity. This term is determined by noting that if the thrust in hover is equal to the thrust in climb, $T_h = T_c$; and that $V_c = 0$ for hover, then from Eq (2.15),

$$\rho\pi R^2 v_{e_h} 2v_{e_h} = \rho\pi R^2 (V_c + v_{e_c}) 2v_{e_c}. \tag{2.19}$$

Defining $(V_c + v_e c)$ as U, Eq (2.19) becomes

$$v_{e_c} = v_{e_h}^2/U. \tag{2.20}$$

Knowing the actual induced main rotor hp in hovering (P_{ind_h}), and having thrust power available in climb (Eq (2.17)), it can be seen from Eq (2.16) that v_{e_h} and U in Eq (2.20) are

$$v_{e_h} = 550P_{ind_h}/T \tag{2.21}$$

and

$$U = 550P_{T_{av}}/T. \tag{2.22}$$

Substituting Eqs (2.21) and (2.22) in Eq (2.20) and then substituting the resulting equation in Eq (2.17) gives the vertical rate of climb in fps:

$$V_c = (550/T)[P_{T_{av}} - (P_{ind_h}^2/P_{T_{av}})]. \tag{2.23}$$

The method described above is based on rotor thrust which should be corrected for download effects. Download or vertical drag in climb is estimated by adjusting the hover download for the inflow velocity variations that occur in axial translation because of the change in induced velocity and the vertical climb velocity component.

The download adjustment procedure consists of first dividing the airframe into segments as described in the hover download discussion in Ch II.1.4. The download of each segment is

$$D_v = \tfrac{1}{2}\rho V'^2 A C_{D_v} \tag{2.24}$$

where

V' = total vertical velocity at the fuselage; fps
A = planform area of the segment; ft^2.

The velocity V' can be expressed as a function of vertical climb velocity, and the equivalent induced velocity at the rotor as follows:

$$V' = V_c + k_d v_e. \tag{2.25}$$

The parameter k_d in this equation is the downwash development factor defined as the ratio of the induced velocity at the fuselage to the induced velocity at the rotor disc. For fully-developed flow, $k_d = 2.0$ as defined by the momentum theory. However, most airframes are located sufficiently close to the rotor so that the downwash is less than its fully-developed value.

To determine the degree of downwash development at the fuselage, model rotor measurements (Fig 2.19) were compared with theoretical induced velocity predictions at the rotor disc. The latter was based on the vortex theory. These comparisons indicate that for fuselages located within a distance of $H_z \approx 0.3$, the average $k_d \approx 1.6$. For configurations with $H_z/R > 0.3$, the $k_d = 1.6$ value will result in optimistic download estimates, and for aircraft, such as the hypothetical helicopter and most of today's aircraft having $H_z < 0.3$, the 1.6 value will give a conservative estimate of download.

Knowing k_d, C_{D_v}, and the area A of each segment, the vertical climb download (D_{v_c}) can be expressed as a function of the hover download (D_{v_h}):

$$D_{v_c} = \left[\frac{\Sigma C_{D_v} A (V_c')^2}{\Sigma C_{D_v} A (V_h')^2}\right] D_{v_h}. \tag{2.26}$$

Substituting Eq (2.25) in Eq (2.26), D_{v_c} becomes

$$D_{v_c} = k_1 \left[\frac{k_2 U^2 + v_h^2 + k_3 v_e^2}{V_h^2}\right] D_{v_h}. \tag{2.27}$$

The terms k_1, k_2, and k_3 in this expression are constants.

In order to simplify the above described calculation procedure, a first approximation to download in climb can be obtained by assuming an average fuselage vertical drag coefficient ($\overline{C}_{D_v}$), and neglecting contraction effects. Then,

$$D_{v_c} = \tfrac{1}{2}\rho A_f U^2 \bar{C}_{D_v} \qquad (2.28)$$

where A_f is the total fuselage planform area. Substituting Eq (2.22) in Eq (2.28) gives

$$D_{v_c} = \tfrac{1}{2}\rho A_f (550 P_{T_{av}}/T)^2 \bar{C}_{D_v}. \qquad (2.29)$$

The corresponding hover equation is

$$D_{v_c} = \tfrac{1}{2} A_f (550 P_{ind_h}/T)^2 \bar{C}_{D_v}. \qquad (2.30)$$

Dividing Eq (2.30) by (2.29) gives

$$D_{v_c}/D_{v_h} = (P_{T_{av}}/P_{ind_h})^2. \qquad (2.31)$$

Step-by-step sample calculations are presented in Tables II-3 and II-4 for the hypothetical single-rotor helicopter operating at $SHP = 2900$ *hp* (transmission limit) and SL/STD atmosphere ambient conditions. Although, in principle, intermediate power rating could have been used for climb, this cannot be done since the aircraft is transmission limited at this ambient condition.

The initial calculations are shown in Table II-3 where the rate-of-climb is computed for five thrust levels. Eqs (2.15) through (2.23) serve as the basis for steps (1) through (11) in this table. The thrust values were then corrected for climb download effects. These computations are based on Eqs (2.24) through (2.27). The constants k_1, k_2, and k_3 used in the calculations were obtained from Table II-4. As shown in this table, the fuselage is divided into eight segments. The downwash development factor for airframe segments in the rotor downwash is $k_d = 1.6$, and a value of $k_d = 0$ is used for areas not located in the rotor wake, such as the fuselage sections under the cutout region of the rotor disc and the horizontal tail.

A first approximation to the download in climb can be determined by substituting the tabulated values of induced power shown in steps (4) and (6) into Eq (2.31). This procedure replaces the lengthy calculations in Tables II-3 and II-4. The results of the so-abbreviated calculations, together with the more detailed method, are shown in Fig 2.27, where performance is shown for two cases: (1) where download is constant as in the case of hover ($D_{v_h} = 0.025W$), and (2) where D_v varies with the rate of climb: $D_v = f(V_c)$. In the latter case, download estimates based on both the detailed calculation method and the first approximations are shown. It can be seen that the climb download correction is negligible at rates of climb less than approximately 1000 fpm. At higher climb rates, either the detailed calculation method or the first approximation of climb effects should be used. This figure indicates that the first approximation method will give a slightly conservative estimate of climb capability when compared with the detailed technique; primarily due to neglecting wake contraction effects. Wake contraction, being more pronounced in hover, contributes more to the increase of download in hover than in vertical climb.

FUSELAGE SEGMENT	A (FT^2)	C_{D_v}	$C_{D_v}A$	k_d	V' $U + (k_d - 1)v_e$	$(V')^2$	$C_{D_v}A(V')^2$
1. NOSE	20.4	0.5	10.2	1.6	$U + 0.6 v_e$	$U^2 + 1.2 U v_e + 0.36 v_e^2$	$10.2 U^2 + 12.24 U v_e + 3.67 v_e^2$
2. CABIN	61.1	0.4	24.4	1.6	$U + 0.6 v_e$	$U^2 + 1.2 U v_e + 0.36 v_e^2$	$24.4 U^2 + 29.28 U v_e + 8.78 v_e^2$
3. CUTOUT	71.1	0.8	56.8	0	$U - v_e$	$U^2 - 2 U v_e + v_e^2$	$56.8 U^2 - 113.6 U v_e + 56.8 v_e^2$
4. NACELLE	18.0	1.2	21.6	1.6	$U + 0.6 v_e$	$U^2 - 1.2 U v_e + 0.36 v_e^2$	$21.6 U^2 + 25.92 U v_e + 7.78 v_e^2$
5. AFTERBODY	43.8	0.5	21.9	1.6	$U + 0.6 v_e$	$U^2 - 1.2 U v_e + 0.36 v_e^2$	$21.9 U^2 + 26.28 U v_e + 7.88 v_e^2$
TAILBOOM:							
6. UNDER ROTOR	24.4	0.5	12.2	1.6	$U + 0.6 v_e$	$U^2 + 1.2 U v_e + 0.36 v_e^2$	$12.2 U^2 + 14.64 U v_e + 4.39 v_e^2$
7. AFT OF ROTOR	3.3	0.5	1.7	0	$U - v_e$	$U^2 - 2 U v_e + v_e^2$	$1.7 U^2 - 3.4 v_e + 1.7 v_e^2$
8. HORIZONTAL TAIL	39.0	1.2	46.8	0	$U - v_e$	$U^2 - 2 U v_e + v_e^2$	$46.8 U^2 - 93.6 U v_e + 46.8 v_e^2$

$$\left[\Sigma C_{D_v} A (V')^2\right]_c = 196.6 U^2 - 102.24 U v_e + 137.81 v_e^2$$

$$\left[\Sigma C_{D_v} A (V')^2\right]_h = 231.17 v_h^2$$

DERIVATION OF CONSTANTS:

$$D_{v_c} = \left[\frac{\left[\Sigma C_{D_v} A (V')^2\right]_c}{\left[\Sigma C_{D_v} A (V')^2\right]_h}\right] D_{v_h}$$

$$= \left[\frac{0.846 U^2 - 0.442 v_h^2 + 0.596 v_e^2}{v_h^2}\right] D_{v_h} \quad \text{where } v_h^2 = U v_e$$

$$D_{v_c} = 0.0442 \left[\frac{-1.91 U^2 + v_h^2 - 1.35 v_e^2}{v_h^2}\right] D_{v_h} \quad \text{where } k_1 = -0.0442;\ k_2 = -1.91;\ k_3 = -1.35$$

TABLE II-4 DETERMINATION OF VERTICAL CLIMB DOWNLOAD CONSTANTS

STEP NO.	PROCEDURE	THRUST (T): LBS				
		10260	13330	16410	19490	20200
①	W_h (lb): $T/[1+(D_v/W)]$	10000	13000	16000	19000	19700
②	RHP_{mr}: Required in Hover	968	1318	1750	2275	2420
③	$RHP_{av_{mr}}$	2420	2420	2420	2420	2420
④	P_{ind_h} (RHP)	670	1020	1460	1960	2090
⑤	P_{pr} (RHP): ② – ④	298	298	290	315	330
⑥	$P_{T_{av}}$ (RHP: ③ – ⑤	2122	2122	2130	2105	2090
⑦	v_h (fps): (④ × 550)/T	35.92	42.09	48.93	55.31	56.90
⑧	v_h^2 (fps^2)	1290	1770	2394	3059	3238
⑨	U (fps): (⑥ × 550)/T	113.75	87.55	71.39	59.40	56.90
⑩	v_e (fps): ⑧ / ⑨	11.34	20.22	33.53	51.50	56.90
⑪	V_c (fpm): 60[⑨ – ⑩]	6144	4038	2272	747	0
⑫	D_{v_h} (lb): T – ①	260	330	410	490	500
⑬	U^2 (fps^2): ⑨^2	12940	7665	5097	3528	3238
⑭	v_e^2 (fpm^2): ⑩^2	128.6	408.9	1124	2652	3238
⑮	$k_2U^2 = -1.91$ ⑬ (fps^2)	–24715	–14640	–9735	–6738	–6185
⑯	$k_3v_e^2 = -1.35$ ⑭ (fps^2)	–173.6	–551.9	–1518	–3580	–4371
⑰	⑮ + ⑯ + ⑧ (fps^2)	–23599	–13422	–8859	–7259	–7318
⑱	⑰ / ⑧ (fps^2)	–18.29	–7.58	–3.70	–2.37	–2.26
⑲	k_1 ⑱ = –0.442 ⑱	8.08	3.35	1.64	1.04	1.00
⑳	D_{v_c} = ⑲ × ⑫ (lv)	2101	1106	672	510	500
(21)	Climb Gross Weight (lb): T – ⑳	8159	12224	15738	18980	19700

TABLE II-3 DETAILED VERTICAL CLIMB SAMPLE CALCULATION

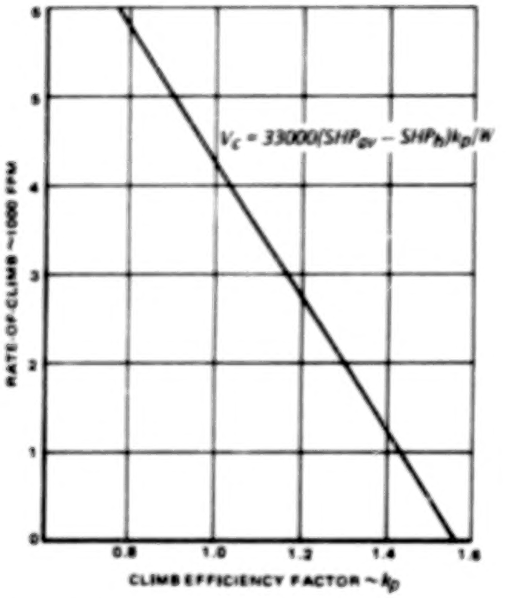

Figure 2.27 Effect of download on vertical climb performance

4.2 Simplified Vertical Climb Predictions

The calculation procedure described above is generally too detailed and time-consuming to be used for preliminary design performance estimates. A simplified method of estimating vertical climb performance can be developed by assuming that the excess shaft horsepower over that required in hover ($\Delta SHP = SHP_{av} - SHP_h$) times a correction factor is used entirely for moving the gross weight (W) against the pull of gravity:

$$550\,\Delta SHP\,k_p = V_c W \tag{2.32}$$

where

V_c = rate of climb; fps
k_p = climb efficiency factor
$\Delta SHP = SHP_{av} - SHP_h$
SHP_h = hover OGE shaft horsepower required.

The rate-of-climb in fpm can now be obtained from Eq (2.32):

$$V_c = \frac{33000\,\Delta SHP\,k_p}{W}. \tag{2.33}$$

For a given gross weight and available engine power, climb capability can be estimated if the climb efficiency factor, k_p, is known. On one hand, this factor should reflect the power losses–transmission efficiency, nonuniform downwash, tip losses, and tail and accessory power requirements–contributing to the difference between the ideal power available at the rotor and SHP. On the other hand, one should take into account the gains resulting from a reduction in induced power due to the increase in inflow velocity resulting from the rate of climb. It should be remembered, however, that an increase in the rate of climb usually leads to higher download values.

The k_p factor for the hypothetical hleicopter shown in Fig 2.28 was computed on the basis of the detailed calculations discussed in the previous section. From this figure, it can be noted that kp varies from 1.5 at a 500 fpm rate of climb, to 1.0 at 4170 fpm.

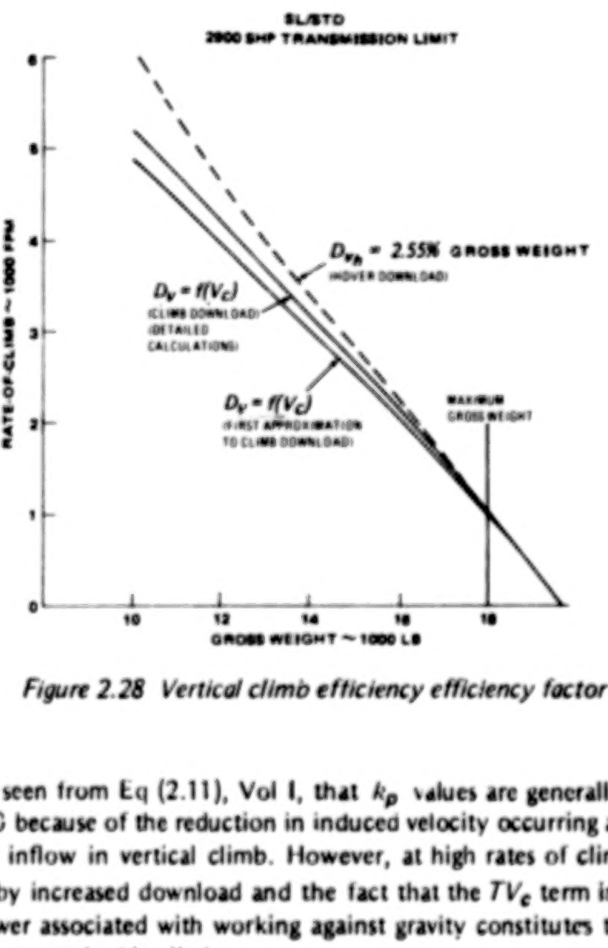

Figure 2.28 Vertical climb efficiency efficiency factor

It can be seen from Eq (2.11), Vol I, that k_p values are generally expected to be greater than 1.0 because of the reduction in induced velocity occurring as the result of an increased rotor inflow in vertical climb. However, at high rates of climb, this improvement is offset by increased download and the fact that the TV_c term in Eq (2.17) representing the power associated with working against gravity constitutes the major portion of the total power required in climb.

For preliminary design purposes, the k_p vs V_c relationship shown in Fig 2.28 can be used to predict the vertical climb capability of other helicopters similar to the hypothetical aircraft. However, for more rigorous evaluations, the procedure described in Sect 4.1 should be followed.

References for Ch II

1. Magee, J. P.; Maisel, M. D.; and Davenport, F. J. *The Design and Performance Prediction of a Propeller/Rotor for VTOL Applications.* Proceedings of the 25th Annual AHS Forum, No. 325. May 1969.

2. Gessow, Alfred; and Myers, Garry C. Jr. *Aerodynamics of the Helicopter.* Frederick Ungar Publishing Co., New York. Originally published in 1951 and republished in 1967.

3. Davis, S. Jon; and Wisniewski, J. S. *User's Manual for HESCOMP, the Helicopter Sizing and Performance Computer Program.* Report D210-10699-2 (Contract NAS2-6107) by Boeing Vertol Co. for NASA-Ames Research Center, Moffett Field, Ca. Nov. 1974.

4. Prouty, R. *Tip Relief for Drag Divergence.* Journal of the American Helicopter Society, Vol. 16, No. 4.

5. LeNard, John M.; and Boehler, Gabriel. *Inclusion of Tip Relief in the Prediction of Compressibility Effects on Helicopter Rotor Performance.* USAAMRDL Tech. Report 73-7, Dec. 1973.

6. LeNard, John M. *A Theoretical Analysis of the Tip Relief Effect on Helicopter Rotor Performance.* USAAMRDL Tech. Report 72-7, Aug. 1972.

7. Wiesner, Wayne; and Kohler, Gary. *Design Guidelines for Tail Rotors.* USAAMRDL Tech. Report D210-10687-1, Sept. 1973.

8. Delany, N. K.; and Sorensen, N. E. *Low-Speed Drag of Cylinder of Various Shapes.* NACA TN-3038, Nov. 1953.

9. Hoerner, S. F. *Fluid-Dynamic Drag.* Published by the author, 1965.

10. Fradenburgh, E.A. *Aerodynamic Factors Influencing Overall Hover Performance.* Paper No. 7 presented at AGARD Specialists Meeting on Aerodynamics of Rotary Wings, Marseille, France. Sept. 1972.

11. Lewis, Richard B., II. *Army Helicopter Performance Trends.* Journal of the American Helicopter Society, Vol 17, No. 2. April 1972.

CHAPTER III

FORWARD FLIGHT PERFORMANCE

The procedures for estimating airframe drag in forward flight are presented first. This is followed by an explanation of the method of determining power required in horizontal flight; illustrated by examples based on the hypothetical helicopter. Predictions of forward flight climb and descent, as well as the level-flight maneuver envelope, is also discussed. A complete presentation of forward-flight performance capabilities of the hypothetical helicopter concludes this chapter.

Principal notation for Chapter III

A	area	ft^2
AR	aspect ratio	
b	number of blades	
C	correction term	
C_D	body drag coefficient	
$C_P = 550\,HP/\pi R^2 \rho V_t^3$	rotor power coefficient	
$C_T = T/\pi R^2 \rho V_t^2$	rotor thrust coefficient	
$C'_T = L/\pi R^2 \rho V_t^2$	rotor lift coefficient	
$C_Q = Q/\pi R^3 \rho V_t^2$	rotor torque coefficient	
C_f	skin friction drag coefficient	
c	blade chord	ft
c_d	section drag coefficient	
$c_{l\alpha}$	lift-curve slope	per radian
D	drag	lb
D_n	nacelle diameter	ft
f_e	equivalent flat-plate area	ft^2
g	acceleration of gravity	32.2 fps^2
h	altitude	ft
I	interference factor	
I	moment of inertia	slugs ft^2
IGE	in-ground-effect	
k	grain size	in, or ft
k_c	cooling system design factor	
k_p	vertical flight correction factor	
k_{pt}	pressure drag factor	
k_s	supervelocity correction factor	
$k_{3\text{-}D}$	three-dimensional correction factor	
k_v	download factor	
L	rotor lift (rotor thrust component ⊥ to distant flow)	ft
l	length	ft
$M = V/a$	Mach number	
M	moment	ft.lb

Performance

m	mass	slugs
N	rotationsl speed	rpm
NUD	nonuniform downwash	
OEI	one-engine-inoperative	
P	power	ft.lb/s
PL	payload	lb
Q	torque	ft.lb
QSP	empirical stall parameter	
q	dynamic pressure	lb/ft^2
R	rotor radius	ft
$R_e = V\ell/\nu$	Reynolds number	
r	radial distance	ft
SR	specific range	n.mi/lb
T	rotor thrust	lb
T	absolute temperature	K
TOGW	takeoff gross weight	lb
t	time	s, or hr
U	velocity	fps
V	velocity of distant flow, or speed of flight	fps, or kn
W	weight (gross weight in particular)	lb
w	width	ft
X	rotor propulsive force	lb
$x = r/R$	nondimensional radial distance	
y	lateral distance	ft
z	hub elevation over pylon	ft
α	angle-of-attack	deg, or rad
β	sideslip angle	deg, or rad
$\gamma = \rho c_{\ell\alpha} c R^4 / I_b$	blade Lock number	
Δ	increment	
$\delta = p/p_o$	ambient pressure ratio	
η	efficiency	
η_t	transmission efficiency	
$\theta = T/T_o$	ambient temperature ratio	
ϑ	angle	
$\mu = V_{\parallel}/V_t$	rotor advance ratio	
ν	kinematic coefficient of viscosity ($\nu_o = 1/6380$)	ft^2/s
ρ	air density	$slugs/ft^3$
$\sigma = bcR/\pi R^2$	rotor solidity ratio	
$\sigma_\rho = \rho/\rho_o$	ambient density ratio	
ψ	azimuth angle ($\psi = 0$ for downwind position)	deg, or rad

Subscripts

a	air
b	blade
c	contraction

c	compressible
c	climb
d	divergent
d	descent
E	empty
e	equivalent
ex	exit, or exhaust
F	fuel
f	fuselage
f	forward
h	hover
i	initial
id	ideal
ind	induced
$inst$	installed
mr	main rotor
nu	nonuniform
o	initial
o	SL/STD
p	pylon
p	propulsive
s	stall
t	tail (horizontal)
tr	tail rotor
u	uniform
w	wetted
●	cross-section
$\parallel$	parallel
$\perp$	perpendicular

Superscripts

$-$	average
$-$	nondimensional
$\cdot$	derivative with respect to time

I. INTRODUCTORY REMARKS

The forward flight performance of a helicopter is primarily composed of (1) speed capability, (2) range and endurance levels, (3) rate of climb, (4) service ceiling, and (5) autorotational characteristics. To compute these items, power required as a function of airspeed, weight, and altitude must be determined. The following step-by-step procedures should be executed when estimating power required or when computing the forward flight performance of new helicopter designs:

1. Estimate the airframe drag, lift, side-force, and pitching and rolling moments.

2. Determine the complete level-flight power-required curve through the following intermediate steps:

   a. Calculate power required for aircraft trimmed conditions using a uniform downwash approach. (Note: An existing trim analysis computer program was used for the hypothetical helicopter.)
   b. Correct power required for nonuniform downwash effects.
   c. Apply parasite power correction.
   d. Define low-speed power required.

3. Determine climb and descent power required through the use of climb efficiency and descent calculation factors.

4. Apply the structural airspeed limitations associated with rotor stall.

5. Calculate performance capability by matching engine performance with speed.

Each step of the techniques used for performance predictions is explained in this chapter with detailed sample calculations for the hypothetical single-rotor aircraft. It should be noted that all airspeeds are considered as true airspeed which, under no-wing conditions, is equal to the ground speed.

2. DRAG ESTIMATES

The total parasite drag of the hypothetical helicopter can be determined by adding the incremental equivalent flat-plate area (Δf_e) of each of the components given in Table III-1.

	ESTIMATE		WIND TUNNEL TEST RESULTS	
ITEM	Δf_e; ft^2		Δf_e; ft^2	
BASIC FUSELAGE & PYLON		2.35		2.5
LANDING GEAR		4.56		4.9
MAIN	*(2.82)*		*(2.9)*	
NOSE	*(1.74)*		*(2.0)*	
MAIN ROTOR HUB		5.22		4.3
ENGINE NACELLES		1.09		1.7
VERTICAL & HORIZONTAL TAIL		0.83		0.7
TAIL ROTOR HUB ASSEMBLY		1.19		1.4
TRIM DRAG		0.80		0.7
SUBTOTAL		16.04		16.2
ESTIMATED ITEMS:				
ROUGHNESS & LEAKAGE	*(1.0)*		*(1.0)*	
PROTUBERANCES	*(1.6)*		*(1.6)*	
COOLING LOSSES	*(0.3)*	2.90	*(0.3)*	2.90
GRAND TOTAL		18.94		19.1

TABLE III-1 HYPOTHETICAL HELICOPTER PARASITE DRAG ESTIMATES

Both wind-tunnel test results and predicted drag values are shown in this table. Test data is available because the hypothetical helicopter fuselage is similar to an early version of a UTTAS prototype aircraft evaluated in the tunnel. The similarity of the two airframes is evident in the drawings and photograph presented in Fig 3.1.

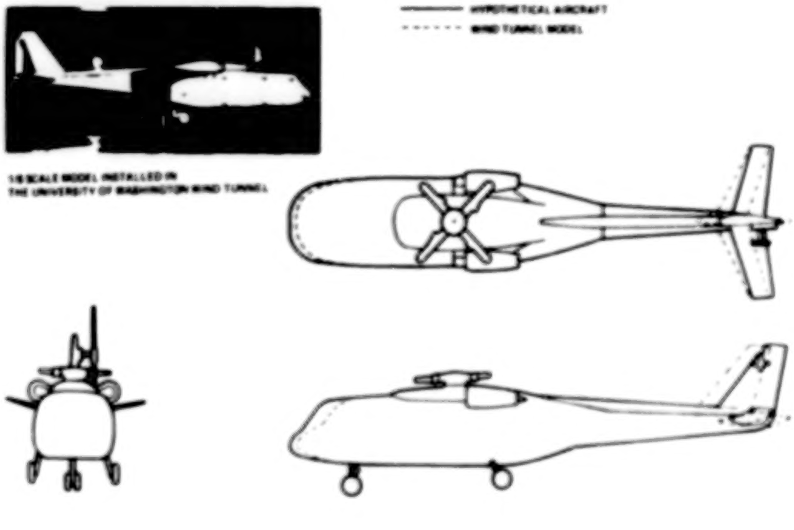

Figure 3.1 Fuselage configuration comparison

One may notice that the estimated and wind-tunnel measured subtotal drag values shown in Table III-1 are very close. A further examination of the table indicates that this is partially due to a random averaging of differences existing in predicted and measured drag values of individual items. However, even these individual differences are not too high, which may be due to the availability of wide wind-tunnel based general information on drag of various components. Without this background material, much larger discrepancies between predicted and measured drag levels of components and the total airframe may be expected.

The drag of the components shown in Table III-1 reflects values representative of streamlined items and nonstreamlined bodies. It also includes trim drag due to fuselage angle-of-attack effects and miscellaneous items resulting from roughness due to rivets, skin waviness, protuberances (antennas, lights, etc.), leakage, and cooling air momentum losses.

The total wind-tunnel value, $f_e = 19.1\ ft^2$, will be used for all forward flight performance of the hypothetical helicopter in this volume. A discussion of the differences in the accuracy of drag predictions for individual items such as the hub and engine nacelles, including prediction techniques, scale model effects, and an evaluation of the differences is presented below.

2.1 Drag of Streamlined Components

Although the streamlined components which include the basic fuselage (nose, cabin, and tail boom), pylon or crown area, tails, engine nacelles, and stub wings are larger in size, they account for only 16 percent of the total drag of the hypothetical helicopter (Table III-1). This is due to the fact that the drag of these items consists primarily of skin friction resulting from shearing stresses developed in the boundary layer of the fluid.

The method of predicting the drag of the streamlined components consists of estimating the skin friction drag coefficient C_f, corresponding to the fully turbulent flow over the flat plate area at the same Reynolds number as that of the part itself, and then applying correction factors to account for three-dimensional and mutual interference effects between the components[1,2]. A fuselage angle-of-attack of zero degrees is assumed for these calculations. The Δf_e is then computed using the wetted, or exposed, surface area A_w as a reference.

$$\Delta f_e = C_f A_w (1 + k_{3\text{-}D}) I \tag{3.1}$$

where

$k_{3\text{-}D}$ = three-dimensional correction
I = interference factor.

The skin friction coefficient in Eq (3.1) is based on the assumption of a fully turbulent boundary layer and thus, varies with Reynolds number and surface roughness[1] as shown in Fig 3.2. The use of C_f values based on this state of flow is valid because the surface is generally sufficiently rough due to rivets, seams, skin waves, etc., to cause the boundary layer to transition near the component leading edge. The data shown in this figure can also be used to correct wind-tunnel results for Reynolds number effects, provided transition strips were used to fix the model boundary layer transition near the leading edge.

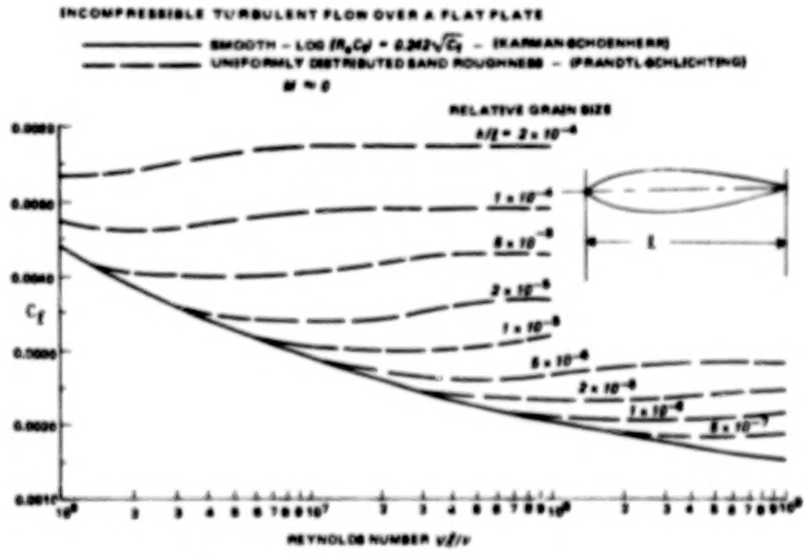

Figure 3.2 Average skin friction coefficient

There are two categories of roughness in the drag accounting system; either surface or discrete, depending on size. Surface roughness refers to the grain size of the paint or surface finish. As noted in Fig 3.2, grain size is specified in terms of the equivalent average grain size (k) to body length (ℓ) ratio. An equivalent value is required to utilize the experimental data. A typical value of k for mass production spray-painted finishes is 1.2×10^{-3} (Ref 2). Surface roughness does not include larger surface discontinuities such as rivet seams, or waviness, which is defined as discrete roughness.

Three-Dimensional Effects. For three-dimensional bodies, additional corrections ($k_{3\text{-}D}$) must be applied to the flat-plate skin-friction drag estimates to account for the following:

Supervelocity effect – due to local speed of flow exceeding the freestream value.

Pressure drag – resulting from the loss of momentum in the boundary layer.

Additional drag increase – resulting from the fact that the body surface is not a flat plate, but usually resembles a cylinder. The three-dimensional boundary layer of a cylinder is thinner than that of the flat-plate at the same R_e values.

The parameter $k_{3\text{-}D}$ can be determined from Ref 2 for optimum streamlined bodies of revolution and for wing and tail surfaces. Minor adjustments to these expressions are required to predict the drag of helicopter fuselage shapes because they are generally not bodies of revolution. The equation for $k_{3\text{-}D}$, including these adjustments, is presented below.

$$k_{3\text{-}D} = \underbrace{0.001(\ell/d)}_{\substack{\text{skin friction}\\ \text{drag due to}\\ \text{warping effect}}} + \underbrace{1.5(d/\ell)^{3/2}}_{\substack{\text{supervelocity}\\ \text{effect}}} + \underbrace{8.4(d/\ell)^{3}}_{\substack{\text{pressure}\\ \text{drag}}} + C \tag{3.2}$$

where

ℓ/d = effective length-to-diameter ratio (with d/ℓ as its reciprocal).

C = correction factor for noncircular cross-section shapes ($C = 0.05$ is a typical value for helicopters).

Eq (3.2) applies to the basic fuselage and engine nacelles. For tail surfaces, the expression for $k_{3\text{-}D}$ is

$$k_{3\text{-}D_{(tails)}} = k_s(t/c) + k_{p_t}(t/c)^4 \tag{3.3}$$

where

t/c = average thickness in percent of chord

k_s = supervelocity factor

k_{p_t} = pressure drag factor.

Additional details concerning $k_{3\text{-}D_{(tails)}}$ can be found in Ch IV, Sect 4.1 (Fig 4.14).

The last term in Eq (3.1) is the interference factor I. This factor accounts for the mutual interference drag which occurs when one body is placed in the vicinity of, or attached to, another. The increase in velocity and/or separation at the juncture point causes the combined drag of the two or more bodies to be greater than the sum of their individual values. The magnitude of interference effects are difficult to assess because they vary greatly with the basic shape of the two bodies and location of one relative to the other. The 0.6 ft^2 difference between the engine nacelle predictions and test results shown in Table III-1 illustrates this point.

The hypothetical helicopter nacelle interference drag may be reduced by locating the nacelles further outboard of the airframe. As shown by the CH-47 data in Fig 3.3, interference drag is minimized when the nacelles are located at least one diameter away from the basic fuselage[3]. The effect of different fillets on such an installation are almost impossible to evaluate accurately without wind-tunnel test data.

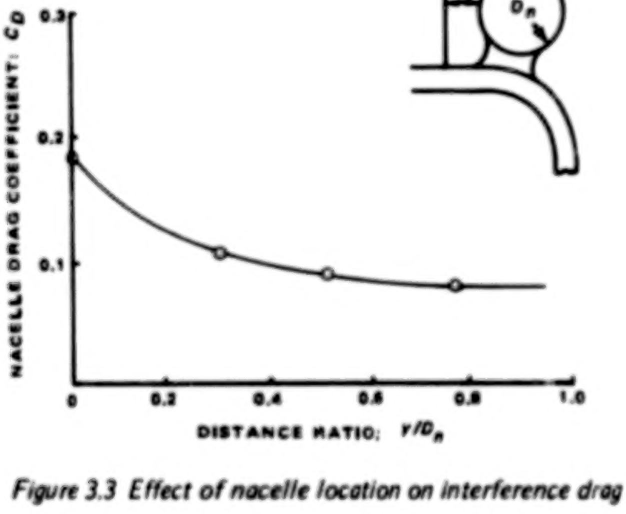

Figure 3.3 Effect of nacelle location on interference drag

The interference factor is usually determined from wind-tunnel tests or from information presented in Refs 1 and 2. In the absence of more reliable experimental data, a minimum value of 1.2 times the isolated component drag can be used to account for a typical level of interference between helicopter components and the basic fuselage. To facilitate "bookkeeping", interference drag should be included in the component drag values rather than charged to the fuselage.

The discussion presented above applies to streamlined fuselage shapes having no significant afterbody or aft section separation. For fuselage configurations employing the abrupt afterbody contraction required for rear-loading designs, additional drag terms must be added to Eq (3.1). In this case, based on Boeing Vertol test data[2,3], drag increments resulting from separation due to the adverse pressure gradient must be accounted for by such corrections as those shown in Fig 3.4. For afterbodies with symmetrical shapes in the side-view, and little or no lateral contraction, the correction expressed in terms of equivalent flatplate area is as follows:

$$\Delta f_{e_{cont}} = 0.008[6(d_e/\ell_c)^{5/2} - 1]A_e. \tag{3.4}$$

However, for afterbodies having their side-view mean-line turned up (cambered) as shown in Fig 3.5 (but still having little, or no lateral contraction), another pressure drag correction must be applied because of still stronger three-dimensional flow effects.

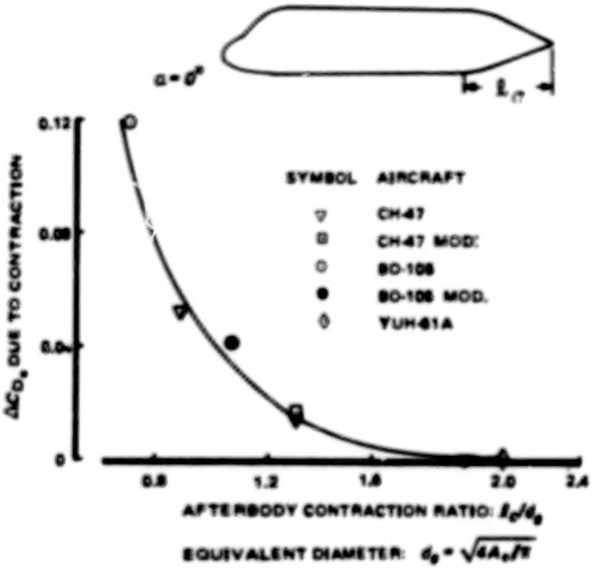

Figure 3.4 Effect of afterbody contraction ratio on drag

This drag increment ($\Delta f_{e_{camb}}$) can be approximated for afterbody shapes such as the CH-47 aircraft as follows:

$$\Delta f_{e_{camb}} = 0.0959(x/d_e)A_e \tag{3.5}$$

where

x/d_e = afterbody camber ratio.

A less abrupt contraction (high ℓ_c/d_e values) will, to some extent, counterbalance the effects of camber. However, more data is required to totally define this interaction. For example, the graph shown in Fig 3.5 indicates that a lateral contraction ratio of 1.3 or higher is required for the CH-47-type afterbody to minimize the drag due to negative camber.

2.2 Drag of Nonstreamlined Components

The major nonstreamlined components are the main rotor hub, tail rotor hub, and landing gear. As illustrated in Table III-1, the hubs and landing gear account for over 50 percent of the total aircraft drag; 30 percent of the total drag is due to the hubs. The drag of these components consists primarily of pressure drag resulting from large separated areas at the base of the component. The technique for estimating this drag

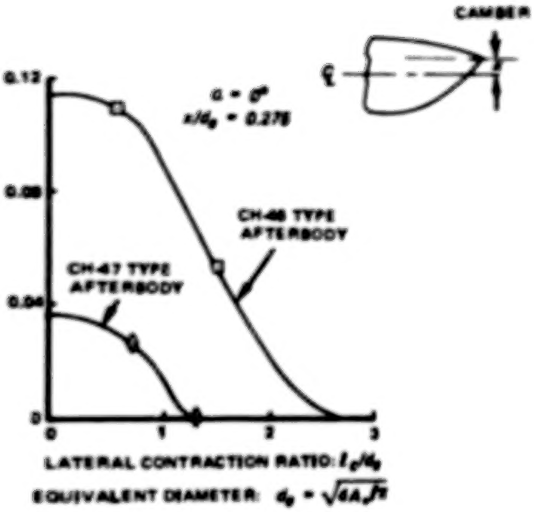

Figure 3.5 Effect of camber on drag

consists of obtaining representative drag coefficients and interference factors from Hoerner[1] or from past wind-tunnel test results and computing the equivalent flat plate area $\Delta f_e = C_{D_e} A_e I$ where C_{D_e} is based on frontal area A_e and I is the interference factor.

Landing Gear Drag. If wind-tunnel results are not available, the drag coefficient of the landing gear can usually be computed using the data from Ref 1. If test results are available, care should be taken to account for Reynolds number effects when applying the model results to the full-scale aircraft. Wind-tunnel model landing gear struts are usually tested at subcritical Reynolds numbers, while those of the full-scale aircraft operate in cruise at supercritical Reynolds number. Due to this correction, the drag of the full-scale landing gear would be about 10 to 15 percent lower than that indicated by wind-tunnel results for typical models (scale about 1:8).

Skid gears, rather than wheeled ones, are often utilized on single-rotor aircraft. A comparison of skid and wheeled gear drag trends is presented in Fig 3.6. For a helicopter of 20,000-lb gross weight, the skid drag is approximately 40 percent lower than that of the wheeled gear. Also, even lower values of drag can be achieved by streamlining the skids and support structure[3].

The wind-tunnel-determined landing gear drag for the hypothetical helicopter (4.9 ft^2) appears slightly lower than indicated by the wheeled-gear trend curve. This is due to such design aspects as location of the front-wheel torque scissors behind the main strut, and other similar design details.

Hub Drag. A slightly different approach must be taken to predict hub drag because of rotational and interference effects due to the proximity of the hub to the airframe. A summary of the calculation procedure described in detail in Ref 4 is presented below.

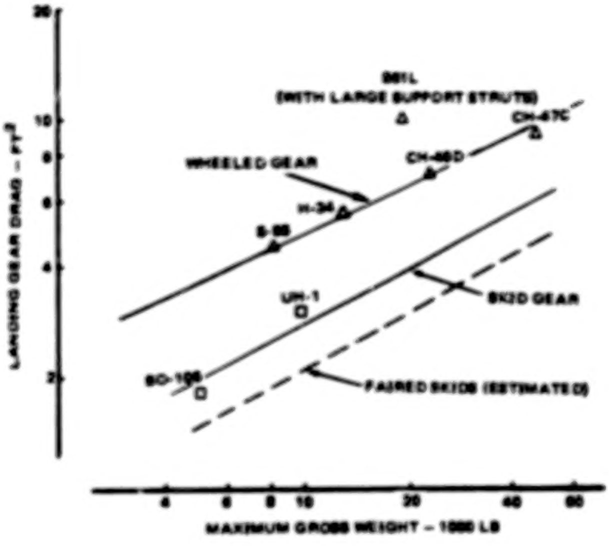

Figure 3.6 Landing gear drag trends

The initial step for predicting hub drag is to divide the hub into basic components consisting of shanks, blade attachment fittings, pitch housing and center-section as shown in Fig 3.7. The drag of the blade shank, attachment fittings, and pitch housing can be computed using the two-dimensional data published in Refs 1 and 5, and making

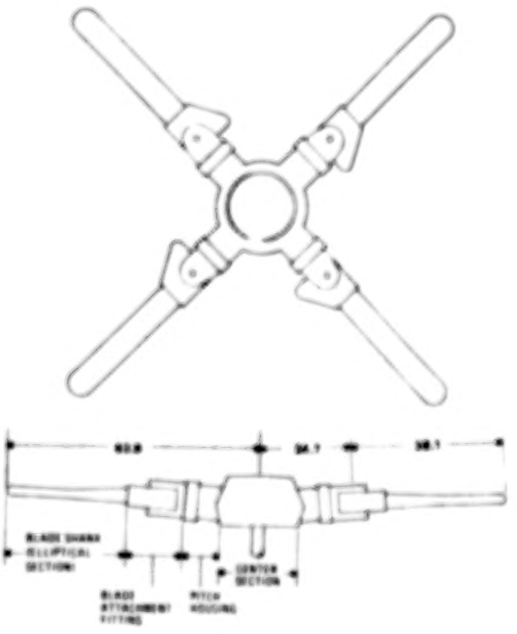

Figure 3.7 Hypothetical helicopter hub and blade shank

corrections for rotational effects. These corrections can be developed by noting that as each blade shank moves around the rotor azimuth, it encounters variations in dynamic pressure and projected frontal area. In the fore and aft position, this area may be assumed to be zero. At the advancing ($\psi = 90°$) and retreating ($\psi = 270°$) azimuthal positions, the frontal area is maximum, and the average dynamic pressure $\bar{q} = (q_{90°} + q_{270°})/2$. The Δf_e of the shank averaged over one revolution, is

$$\Delta f_e = \Delta D/q_o = c_{d_s} A_s(\bar{q}/q_s)/2 \tag{3.6}$$

where

c_{d_s} = shank section drag coefficient
A_s = frontal area of section at $\psi = 90°$ and $270°$
q_o = freestream dynamic pressure.

$\bar{q}$ is obtained by integrating the local velocities along the shank extending from radial station m to station n, selected in such a way that c_{d_s} may be considered constant within their limits.

$$\bar{q} = q_o\left\{1 + \left[\frac{(1/\mu_n)^3 - (1/\mu_m)^3}{3(1/\mu_n - 1/\mu_m)}\right]\right\} \tag{3.7}$$

Here, μ_m and μ_n are the advance ratios at radial stations m and n, respectively. Therefore, the total equivalent flat-plate area of the shanks for a hub with b blades is

$$\Delta f_e = D/q_o = (b/2)c_{d_s} A_s l(\bar{q}/q_o). \tag{3.8}$$

Using this approach, the drag of the shanks was charged to the airframe parasite drag thus leading to a clearer understanding of the influence of blade airfoil section characteristics and blade geometry on rotor performance. There are, however, aerodynamicists who prefer a different "bookkeeping" method where both drag and torque of blade shanks are accounted for in the rotor performance calculations.

The hub center-section drag contribution can be computed using drag coefficients based on wind-tunnel test results[4]. As shown in this report, the hub center-section drag coefficients based on the rotating projected frontal area at $0°$ angle-of-attack vary from $C_{D_s} = 0.55$ to 0.65. The tested configurations included two-bladed teetering rotors and three-bladed articulated hubs.

The C_{D_s} values noted above are for isolated hubs and do not include interference effects on the fuselage. However, for practical designs, interference drag can be significant, as shown in Fig 3.8. Here, interference factors based on wind-tunnel tests are presented as a function of the hub-gap to pylon-width ratio for various angles-of-attack. This data can be used to predict the interference effect of the outboard and center sections of the hub. For components located outboard of a circle defined by the width of the pylon, interference drag may be neglected. For example, for the hub center-section of the hypothetical helicopter, the gap is zero and the interference factor at zero degrees fuselage angle-of-attack is 1.97.

The technique outlined above was used to define the hypothetical helicopter hub drag shown in Table III-1. As noted in this table, the predicted hub-drag values are

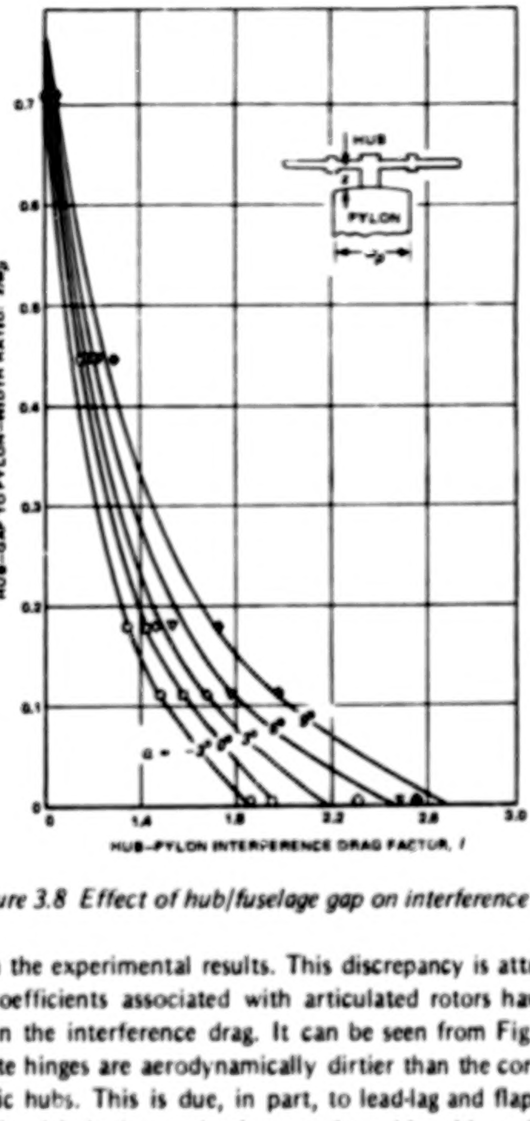

Figure 3.8 Effect of hub/fuselage gap on interference drag

0.9 ft^2 higher than the experimental results. This discrepancy is attributed to the use of component drag coefficients associated with articulated rotors having discrete hinges, and to variations in the interference drag. It can be seen from Fig 3.9 that articulated designs with discrete hinges are aerodynamically dirtier than the corresponding hingeless rotor or elastomeric hubs. This is due, in part, to lead-lag and flapping hinges, and lag dampers. An additional hub drag reduction can be achieved by utilizing flex-strap and elastomeric designs which eliminate the need for large pitch-bearing housings.

For preliminary estimates of hub drag when details of the hub components have not been defined, the trends shown in Fig 3.9 can be used. This data is based primarily on scale model tests, with no Reynolds number corrections. Comparisons of model and full-scale results show no significant effect of R_e on unfaired hub drag, although the local model shank and pitch-arm operate at Reynolds numbers below critical values. Additional testing is required to fully understand the effect of R_e on both faired and unfaired hub configurations.

2.3 Trim Drag

The component drag estimates discussed above are generally calculated at zero angles of attack unless information for other angles is available. A correction must be

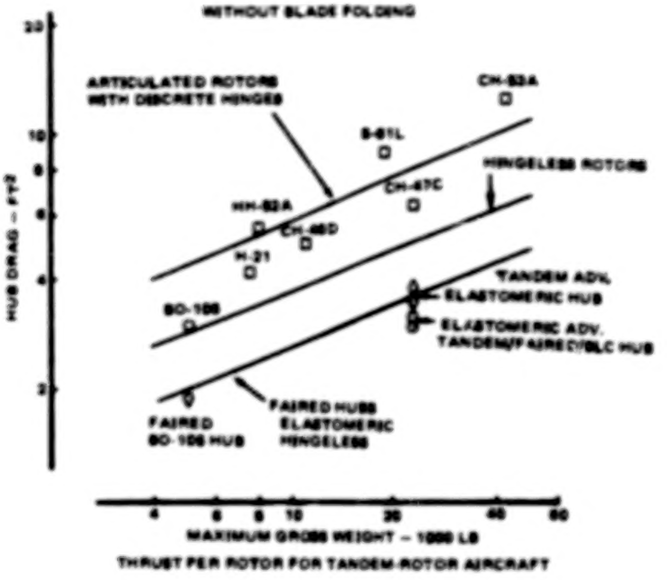

Figure 3.9 Hub drag trends

applied to the aircraft as a whole for the variation of data between zero degrees and cruise angle-of-attack which, for helicopter fuselages, is typically $\alpha_f = -4°$ to $-6°$ (nose down). For example, for the hypothetical helicopter, $\alpha_f = -5.2°$, which consists of a pitch or trim attitude of $-3.2°$ and $-2°$ of downwash angle at the following level flight trim conditions: *V = 140 kn; W = 15,000 lb; SL/STD day; 8-inch fwd c.g. position;* and *sideslip angle*, $\beta = 0°$.

The variation of fuselage drag with angle-of-attack is due primarily to the induced drag of the basic fuselage and stabilizer. There is no systematic data for determining the effect of trim attitude on drag for helicopter fuselage shapes. The only recourse is to rely on previous wind-tunnel tests for somewhat similar configurations. The trim drag of tail surfaces can be evaluated by the same method as was used for fixed wings[8,9]. The variation of drag with angle-of-attack of other components such as the hub, gear, etc., is generally negligible. The contribution of fuselage download—as is usually the case; or lift, which is seldom in horizontal flight—should also be taken into account when determining the forward-flight download factor (k_{v_f}).

The data presented in Ref 7 was used to determine the predicted hypothetical helicopter trim drag increment of 0.8 ft² between $\alpha_f = 0°$ and $-5°$. This drag value does not include any horizontal tail trim drag because the horizontal stabilizer angle-of-attack in cruise is $\alpha_t = -3°$; and at $\alpha_f = 0°$, $\alpha_t = 2°$. The difference in induced drag between these angles for the horizontal empennage is negligible.

To obtain the aircraft pitch attitude, the level flight fuselage angle-of-attack used in trim calculations is determined by solving the equations of motion for a force and moment balance about the c.g., and then adding the rotor downwash effects. The solutions to the complete set of trim equations, including a detailed analysis of rotor forces, was obtained for the hypothetical helicopter through the use of a computer as described later in this chapter. However, this can also be done through hand calculations by selecting a fixed speed in horizontal flight, and then writing an equilibrium equation for moments about the pitching axis; and another set of equilibrium equations for forces acting along the horizontal and vertical axes. Next, assuming a few (at least three) values of the fuselage angle-of-attack find, by interpolation, a α_f value for which moment and force equilibrium is reached.

When computing α_f, the effect of c.g., gross weight, and airspeed should be taken into account (Fig 3.10). The effect of c.g. on the hypothetical helicopter angle-of-attack is presented in the upper half of this figure. The most forward c.g. (8 inches forward) results in the largest negative angle-of-attack. At these c.g. positions, the aircraft must be trimmed more nose-down in order to achieve moment equilibrium.

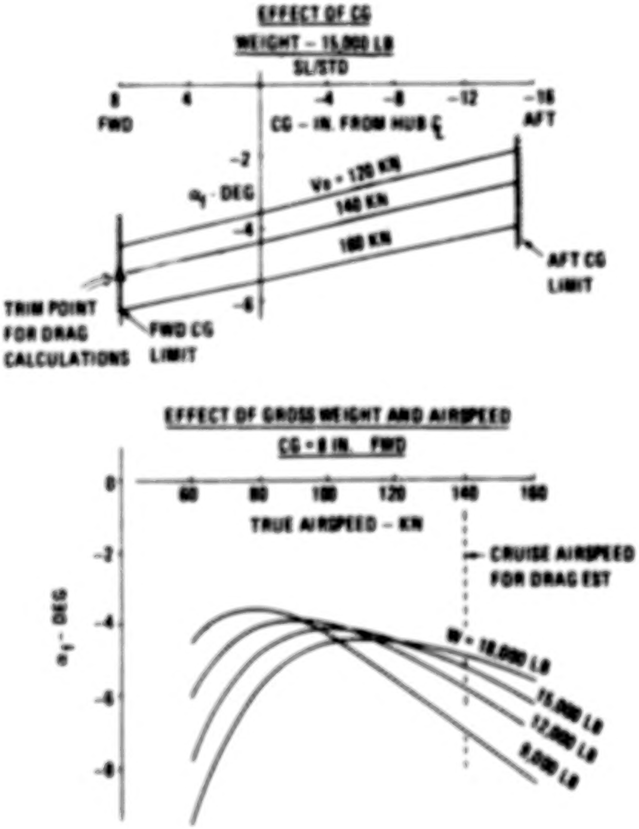

Figure 3.10 Effect of c.g., gross weight, and airspeed on fuselage angle-of-attack

Between the 15-inch aft and the 8-inch forward c.g. positions, there is a 2.5° difference in angle-of-attack. Performance data is typically presented at the most forward c.g. because this is the most adverse condition for single-rotor helicopters. All hypothetical helicopter performance presented in this text is based on the 8-inch forward c.g. position.

The effect of airspeed and gross weight on α_f is illustrated in the lower half of Fig 3.10. It can be seen that the airframe nose-down angle-of-attack increases with airspeed, due to the higher propulsive force requirements resulting from increased fuselage drag. This variation of cruise angle with airspeed is most prominant at the lower gross weights, since the thrust vector tilt required to achieve a given propulsive force is larger at these conditions. At speeds below approximately 80 kn, it should be noted that α_f becomes more negative as the speed decreases. This trend is due to higher rotor downwash and occurs regardless of the gross weight of the aircraft.

Trim analysis computations for the hypothetical helicopter at 140 kn indicate that approximately 4° of sideslip is required to trim at 0° roll attitude. Higher angles are required at lower airspeeds. The drag penalty associated with the $\beta = 4°$ trim change attitude is 0.6 ft^2 based on wind-tunnel test results. However, to simplify the sample calculations, this penalty is not included in the performance predictions.

2.4 Miscellaneous Items

Items included in the following discussion refer to the discrete roughness and leakage, protuberances, and cooling air momentum indicated at the bottom of Table III-1.

Discrete Roughness and Leakage. As noted previously, discrete roughness drag includes surface irregularities such as rivet heads, seams, waviness in the skin, etc. Leakage drag results from air that enters or exits the fuselage around cowlings, access doors, windows, etc. Data compiled in Ref 2 indicates that roughness and leakage effects increase the basic skin friction drag of current aircraft by 20 percent; 10 percent of which is due to roughness and 10 percent to leakage. A 20-percent increase in skin friction drag for the hypothetical helicopter is equivalent to a 5-percent increment of the total drag value.

Protuberances. Protuberances are represented by larger external items such as antennas, vents, drains, and anticollision lights. If detailed drawings are available to locate and define all of the protuberances, drag estimates can be obtained using data presented in Ref 1; however, for preliminary design work where such details are not available, the protuberances are generally accounted for by increasing the aircraft drag by 5 to 10 percent as suggested in Refs 2 and 5. A fixed amount of protuberances installed on a relatively clean fuselage such as that of the hypothetical design would lead to a larger relative drag increase than in the case of a "dirty" design. Therefore, a value of a 10-percent increment of the total aircraft drag (excluding the miscellaneous items) was assumed.

Cooling Momentum Drag. This drag results from the loss of air momentum as it enters and exits the cooling system of the hydraulic power supply, engines, and transmissions. Losses also occur due to air entering the heating and ventilation systems.

If details of the aircraft cooling system are available so that the mass flow through the system and the area of the inlet and exit ducts are defined, the cooling drag can be computed using the simple momentum relationship.

$$D = \dot{m}_a(V_o - V_{ex}\cos\theta_{ex}) \tag{3.9}$$

where

$\dot{m}_a$ = $\dot{W}_a/g$; mass flow ($\dot{W}_a \equiv$ weight of air-flow in lb/s, and $g \equiv$ acceleration of gravity)
V_0 = forward speed; fps
V_{ex} = exit velocity
θ_{ex} = exit angle relative to the freestream velocity.

With properly designed inlets and exits, much of the momentum loss that occurs at the inlet could be recovered at the exit. The only problem is that helicopter cooling systems have to be designed for hover, where the highest power and resulting operating temperatures occur. To satisfy these requirements, inlets and exits are usually designed as large openings located on top of the fuselage where the exit airflow cannot be readily directed aft. Cooling systems depend on the total pressure in the downwash, or freestream air flow, combined with pressure differential generated by blowers to move the air through the system. Typical exhaust velocities for blower installations are on the order of 60 to 80 fps to provide adequate cooling and to minimize power loss.

The procedure for estimating momentum drag may be simplified by taking the approach suggested in Ref 2, which indicates that the cooling momentum drag is proportional to the installed power available as shown below:

$$\Delta f_e = 2.5 \times 10^{-5}(SHP_{inst})k_c \tag{3.10}$$

where

k_c = cooling system design factor
SHP_{inst} = installed shaft horsepower available.

Depending on the design of their cooling systems, typical production helicopters have k_c values ranging from 4 to 6. A value of 4 is used for the hypothetical helicopter design. Therefore, the cooling air momentum losses at the 2900 SHP transmission limit results in a $\Delta f_e = 0.3\ ft^2$ drag penalty.

2.5 Net Engine Thrust

Turboshaft engines produce a net thrust, or drag, depending on the engine mass flow, exhaust direction and velocity, and flight speed. For typical installations, the airflow velocity originally decreases at the inlet; but is increased at the exhaust to provide thrust. The net resultant thrust, T_{net} is

$$T_{net} = \dot{m}(V_{ex} \cos \theta_{ex} - V_0) \tag{3.11}$$

where

$\dot{m}$ = engine mass flow; slug/s
V_{ex} = exhaust velocity; fps
θ_{ex} = exhaust velocity cant angle; deg.

For typical turboshaft installations, the engines provide a net thrust at speeds up to 140 to 150 kn; however, a momentum drag appears at higher speeds (Fig 3.11) The magnitude of this thrust or drag in cruise is normally small enough to be omitted from most performance calculations, but care must be taken when making exhaust modifications—

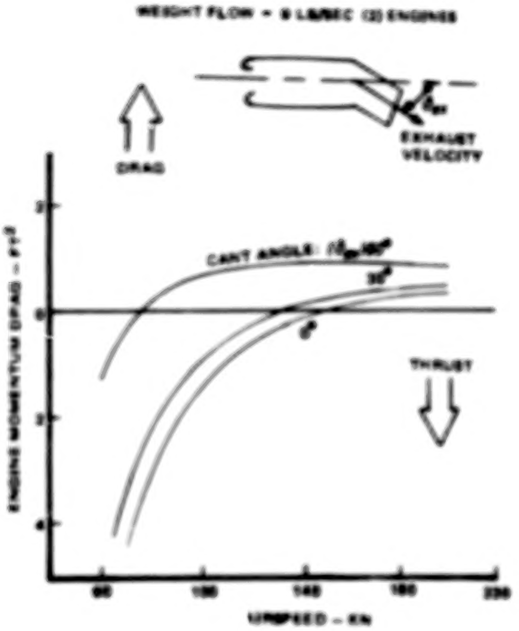

Figure 3.11 Example of engine momentum drag/thrust

for instance, installations of ejector shrouds and IRS suppressors, as they tend to reduce the exit velocity.

2.6 Detailed Sample Drag Calculations for the Hypothetical Helicopter

Details of the hypothetical helicopter drag calculations, including reference areas, drag coefficients, and interference factors are shown in Table III-2. The results were summarized and compared with wind-tunnel measurements in Table III-1. To further illustrate the procedure for estimating the drag of various components, the following step-by-step calculations are shown for streamlined (basic fuselage) and nonstreamlined (nose gear) items.

Streamlined Component – Calculation of the hypothetical helicopter basic fuselage drag (nose, cabin, and tail boom drag).

1. Determine skin friction drag coefficient, C_f, from Fig 3.2, where C_f is defined as a function of Reynolds number R_e, ($R_e = V\ell/\nu$), and equivalent roughness k/ℓ, where k is the grain size, ℓ is the characteristic body length, and ν is the kinematic coefficient of viscosity.

At 150 kn, SL/STD,

$$R_e = \frac{140 \times 1.682 \times 47}{1.564 \times 10^{-4}} = 7.1 \times 10^{7}$$

Assume an equivalent grain size, $k = 1.2 \times 10^{-3}$, for mass production spray-painted surfaces[3]:

ITEM	WETTED AREA (ft²)	FRONT AREA (ft²)	C_D; C_f	INTERFERENCE FACTOR (I)	Δf_e (ft²)	COMMENTS
BASIC FUSELAGE					1.92	*See Note 3*
Skin Friction (Flat Plate)	685		0.00235		1.61	
3-Dimensional Effects					0.31	
PYLON					0.43	*See Note 3*
Skin Friction (Flat Plate)	63		0.0027	1.40	0.40	
3-Dimensional Effects					0.03	
NOSE GEAR					1.36	*Strut airflow is supercritical*
Oleo Strut		0.3	0.5	1.25	0.18	
Scissors		0.65	0.6		0.39	
Wheels (2)		1.75	0.3	1.50	0.79	
MAIN GEAR					2.82	*Trailing arm airflow is supercritical*
Trailing Arm Strut (2)		1.48	0.5	1.25	0.92	
Wheels (2)		2.54	0.5	1.50	1.90	
MAIN ROTOR HUB					5.22	*C_D values and frontal areas defined at 0° shaft angle. Blade shanks have elliptical cross-section*
Center Section		1.55	0.55	1.97	1.74	
Pitch Housing		0.52(1)	0.4	1.70/1.02*	0.72	
Blade Attachment Fittings		0.78(1)	1.0	1.57/1.06*	2.50	
Blade Shanks		0.88(1)	0.15	1.00/1.20*	0.21	
ENGINE NACELLES (2)					1.09	*See Note 3*
Skin Friction (Flat Plate)	84		0.0034	2.0	0.37	
3-Dimensional Effects					0.40	
Base Drag (Fairing)					0.32	
VERTICAL TAIL					0.39	*See Note 3*
Skin Friction (Flat Plate)	53		0.0035	1.05	0.19	
3-Dimensional Effects					0.10	
Induced					0.10	
HORIZONTAL TAIL					0.44	*See Note 3*
Skin Friction (Flat Plate)	72		0.00385	1.05	0.29	
3-Dimensional Effects					0.08	
Induced					0.07	
TAIL ROTOR HUB ASSEMBLY					1.19	*Interference includes mutual interference between parts and effect on vertical tail*
Shaft		0.28	0.5	1.50	0.21	
Hub and Slider		0.61	1.0	1.50	0.92	
Base Fairing		0.21	0.2	1.50	0.06	
TRIM DRAG (Δ Drag between 0° and -5° α_f)					0.80	*Function of planform area and pressure drag*
				SUBTOTAL	(16.04)	

ROUGHNESS AND LEAKAGE	1.0	*Calculated as 20% of skin friction drag (10% roughness and 10% leakage; or 6% of subtotal)*
PROTUBERANCES	1.6	*Estimated to be 10% of subtotal*
COOLING LOSSES (Transmission and Engine)	0.3	*Proportional to installed power available*
SUBTOTAL	(2.90)	
GRAND TOTAL	18.94	

NOTES:
1. $R_e/ft = 1.51 \times 10^6$ *(140 kn, SL/STD)*
2. All items evaluated at $\alpha_f = 0°$
3. Surface roughness equivalent grain size $k = 1.2 \times 10^{-3}$ inches

* Rotational Effects $\bar{q}/q_0$; where $\Delta D/q = (b/2)C_d \cdot A_s](\bar{q}/q_0)$

TABLE III-2 PARASITE DRAG ESTIMATE

$$k/\ell = \frac{1.2 \times 10^{-3}}{47 \times 12} = 2.13 \times 10^{-6}$$

Hence, $C_f = 0.00235$ (Fig 3.2).

2. Calculate fuselage wetted area (A_w):

A quick method of estimating A_w based on a three-view drawing is presented below. This method assumes that the cross-section shape does not vary along the body length.

$$A_w = 2 \times \kappa(A_{top} + A_{side}) - A_{wp} \tag{3.12}$$

where

κ = circumference/2 (height + width) of cross-section
A_{top} = planform view area
A_{side} = side-view area
A_{wp} = pylon juncture wetted area.

Assuming the cross-section shown in Fig 3.1 is representative of the entire fuselage,

$$\kappa = 24/2(8 + 6.3) = 0.84,$$

and

$A_{top} = 230\ ft^2$
$A_{side} = 214\ ft^2$
$A_{wp} = 61\ ft^2$.

Now

$$A_w = 2 \times 0.84(230 + 214) - 61 = 685\ ft^2.$$

The fuselage should be divided into smaller segments if the shape of the cross-section varies considerably along the length.

3. Determine $k_{3\text{-}D}$ from Eq (3.2) as a function of ℓ/d and C, where

$\ell = 47\ ft$
$d_e = \sqrt{A_c 4/\pi} = \sqrt{(46 \times 4)/\pi} = 7.64\ ft,$
$\ell/d_e = 47/6.64 = 6.15$
$C = 0.05.$

Substituting these values in Eq (3.2) gives:

$$k_{3\text{-}D} = 0.142 + 0.05 = 0.192.$$

4. Compute basic fuselage Δf_e per Eq (3.1), assuming no significant afterbody separation:

$$\Delta f_e = C_f A_w (1 + k_{3\text{-}D})$$

$$\Delta f_e = 0.00235 \times 685(1 + 0.192) = 1.92\ ft^2.$$

Nonstreamlined Component – **Calculation of the hypothetical helicopter nose-gear drag.**

1. Using Fig 3.12, compute oleo strut and axle drag:

At 140 kn, SL/STD,

$$R_e = (140 \times 1.689 \times 3)/(12 \times 1.564 \times 10^{-4}) = 3.78 \times 10^5.$$

Depending on the relative roughness, $C_{D_e} = 0.3$ to 0.5 (Hoerner[1], pg 3-10). The higher value of 0.5 is used to provide a degree of conservatism and to account for discontinuities along the length of the strut. Assuming an interference factor of 25 percent (Ref 1, pp 8-9 and 8-19),

$$\Delta f_e = C_{D_e} A_e \times 1.25$$

$$\Delta f_e = 0.5 \times 0.9 \times 1.25 = 0.56\ ft^2$$

where

$$A_e = [(16)(1) + (4.5)(7.5) + (20)(3) + (4)(5)]/144 = 0.9\ ft^2.$$

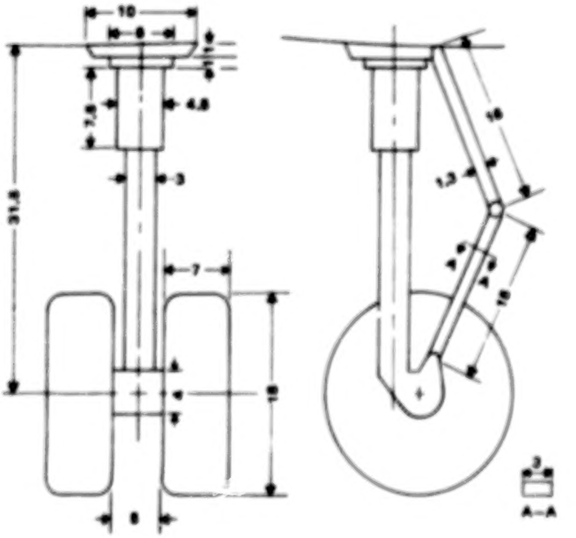

Figure 3.12 Nose-gear configuration (extended on flight position)

2. Calculate torque scissors drag:

Assuming $C_{D_e} = 1.2$ (flat plate), and local $q = 0.5q_o$ (freestream) due to strut wake,

$$\Delta f_e = 1.2 \times 0.65 \times 0.5 = 0.39\ ft^2$$

where

$$A_e = (3)(31)/144 = 0.65\ ft^2.$$

3. Estimate wheel drag:

According to Ref 1 (pg 13-24), $C_D = 0.3$, when based on an area (A) defined by tire width x maximum diameter:

$A = (18 \times 7)/(144 = 0.8$[illegible] ft^2.

Interference between the wheels and the struts is assumed to be 50 percent of wheel drag. This is based on previous test-versus-theory comparisons conducted on the CH-46 aircraft which has a similar nose-gear arrangement. Therefore, the drag of the two wheels is:

$$\Delta f_e = 2(0.3 \times 0.874 \times 1.5) = 0.79\ ft^2.$$

The total estimated gear drag is:

Oleo Strut	$\Delta f_e = 0.56$
Torque Scissors	$\Delta f_e = 0.39$
(2) Wheels	$\Delta f_e = 0.79$
TOTAL	$\Delta f_e = 1.74\ ft^2$.

3. METHODOLOGY FOR DETERMINING LEVEL FLIGHT POWER REQUIRED

The most widely used practical means of determining power required in horizontal flight consist of performing detailed computations for (1) flying speeds higher than about 60 kn, and (2) hovering. The $SHP = f(V_o)$ relationship for the $0 < V_o < 60$ interval is usually established by "guided" interpolation. Such a guide (determining the basic shape of the power-required curve within the low-speed region) can be provided by the simple momentum theory, taking into account the complete flow velocity through the disc ($\vec{V}' = \vec{V}_o + \vec{v}$) as indicated in Ch II of Vol I. It can also be obtained from vortex theory methods adapted to the low-speed region (Ch IV of Vol I).

With respect to flying speeds higher than ≈ 60 kn, the combined momentum and blade element theory (Ch III of Vol I) should provide a sufficiently accurate basis for routine engineering practice. This is especially true if performance predictions obtained in this manner are checked against flight test results, or more accurate (at least in principle) theoretical methods such as those based on vortex theories (Ch IV of Vol I). Should discrepancies—between either flight tests, or more sophisticated analytical procedures—be pinpointed with respect to the area of their occurrence (say, induced or profile power predictions), then appropriate correction factors could be established and applied.

In the particular case of the hypothetical helicopter, the level flight power required for speeds above ≈60 kn was determined using an available trim analysis computer program. The program employs a combination of blade element and momentum theory to compute the rotor and fuselage trim forces. The accuracy of the induced power prediction is improved by applying a nonuniform downwash correction to values obtained on the basis of uniform downwash. This correction is derived from comparisons of power levels theoretically predicted for forward flight; using uniform and nonuniform downwash analyses. In addition, an empirical correction based on wind-tunnel test results is applied to account for discrepancies between theoretical predictions and wind-tunnel measurements of parasite power.

Low-speed power required below 60 kn is determined by utilizing either the trim analysis program, or the basic momentum theory induced power relationships to define the shape of the low-speed power-required curve. When the uniform downwash theory is used, adjustments are required to have the hover point agree with the values given by the vortex theory, and the 60-kn point with nonuniform downwash predictions.

Details of the trim program and low-speed power required prediction techniques are presented on the following pages. Power required data and calculations for the hypothetical helicopter are provided to illustrate the methodology. At the end of this section, the trim program predictions are compared with the simplified power required expressions derived in Vol I.

3.1 Trim Analysis Computer Program

Aircraft trim for forward-flight conditions is determined by solving the six steady-state equations of motion developed from a force and moment balance about the center-of-gravity. The computer program for the hypothetical helicopter calculations was formulated in such a way that the flight conditions indicated in the input box in Fig 3.13 contained the following items: gross weight, speed of flight (horizontal), and sideslip angle. The results consisted of: fuselage pitch attitude (in this program, symbolized by θ), fuselage roll angle (ϕ), and longitudinal cyclic pitch angle.

In Sect 2.3 of this chapter, it was indicated that it is desirable to have the ϕ angle close to zero. This means that should the trim analysis indicate that ϕ does not equal zero (say $\phi > |0.1^\circ|$), new sideslip angles must be assumed; until the desired $\phi \approx 0$ is obtained. In this respect, it would be more desirable to develop a computer trim analysis program where $\phi = 0$ would be input as one of the flight conditions, and the output would be the fuselage yaw angle required to achieve $\phi = 0$.

As to the actual process of solving equations of equilibrium, iterative techniques are required because of the complexity of the rotor analysis needed to compute the rotor forces and moments. The rotor analysis is a subroutine in itself and uses a numerical approach for solving the rotor flapping and force equations. Blade stall, reverse flow, and compressibility effects are taken into account by the use of two-dimensional airfoil section data (see Ch II). However, in order to simplify this analysis, the following assumptions were made.

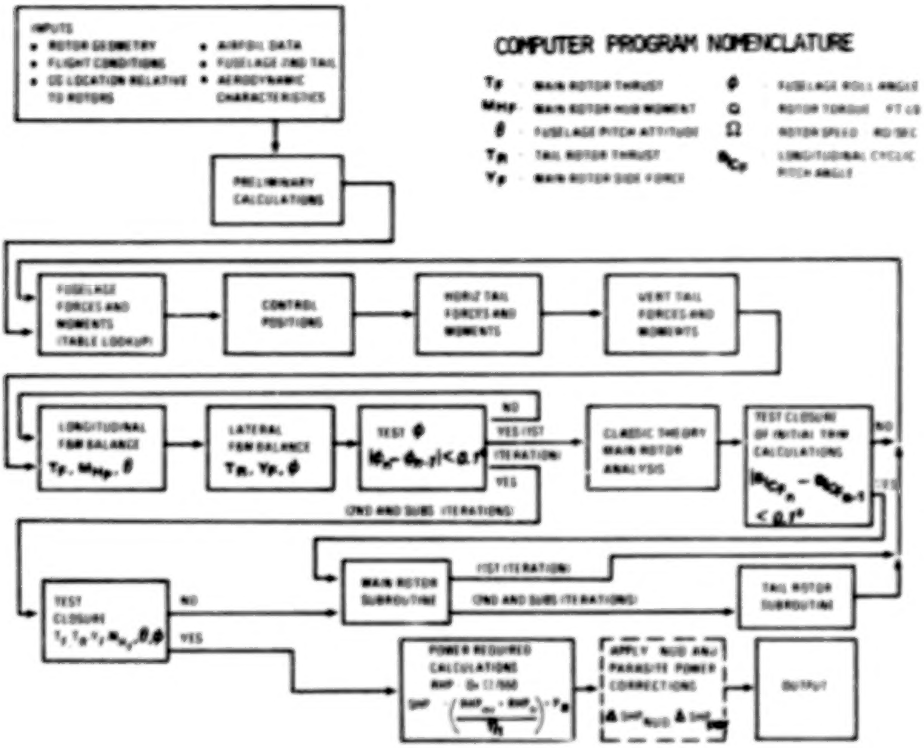
INPUTS
• ROTOR GEOMETRY
• FLIGHT CONDITIONS
• CG LOCATION RELATIVE TO ROTORS
• AIRFOIL DATA
• FUSELAGE AND TAIL
• AERODYNAMIC CHARACTERISTICS
PRELIMINARY CALCULATIONS
COMPUTER PROGRAM NOMENCLATURE
T_F - MAIN ROTOR THRUST
M_{HP} - MAIN ROTOR HUB MOMENT
θ - FUSELAGE PITCH ATTITUDE
T_R - TAIL ROTOR THRUST
Y_F - MAIN ROTOR SIDE FORCE
ϕ - FUSELAGE ROLL ANGLE
Q - ROTOR TORQUE FT LB
Ω - ROTOR SPEED RD/SEC
θ_{C_F} - LONGITUDINAL CYCLIC PITCH ANGLE
FUSELAGE FORCES AND MOMENTS (TABLE LOOKUP)
CONTROL POSITIONS
HORIZ TAIL FORCES AND MOMENTS
VERT TAIL FORCES AND MOMENTS
LONGITUDINAL F&M BALANCE T_F, M_{HP}, θ
LATERAL F&M BALANCE T_R, Y_F, ϕ
TEST ϕ $|\phi_n - \phi_{n-1}| < 0.1°$
NO
YES (1ST ITERATION)
YES
(2ND AND SUBS ITERATIONS)
CLASSIC THEORY MAIN ROTOR ANALYSIS
TEST CLOSURE OF INITIAL TRIM CALCULATIONS $|\theta_{C_{F_n}} - \theta_{C_{F_{n-1}}}| < 0.1°$
NO
YES
MAIN ROTOR SUBROUTINE
(1ST ITERATION)
(2ND AND SUBS ITERATIONS)
TAIL ROTOR SUBROUTINE
TEST CLOSURE $T_F, T_R, Y_F, M_{HP}, \theta, \phi$
NO
YES
POWER REQUIRED CALCULATIONS
RHP = QΩ/550
SHP = $\left(\frac{RHP_{MR} + RHP_{TR}}{\eta_T}\right) + P_A$
APPLY NUD AND PARASITE POWER CORRECTIONS
ΔSHP_{NUD} ΔSHP_{PAR}
OUTPUT

Figure 3.13 Block diagram for single-rotor trim analysis

1. Induced velocity distribution is assumed to be uniform.
2. Blade lag and all elastic degrees of freedom are neglected.
3. Unsteady aerodynamic and spanwise flow effects are ignored.
4. Three-dimensional compressibility effects at the blade tip are not considered.

Once the trim has been established, corrections to the power required for non-uniform downwash (NUD) and parasite power are added to the basic trim power required predictions. A discussion of these corrections is presented later in this chapter.

A complete block diagram of the single-rotor helicopter trim analysis is presented in Fig 3.13. The initial step in the iterative procedure is to compute the fuselage and tail forces and moments. A matrix of fuselage forces and moments is input into the program as a function of angle-of-attack ($\alpha_f = \pm 90°$), and sideslip angle ($\beta_f = \pm 90°$) based on wind-tunnel testing. An example of longitudinal fuselage and horizontal tail forces and moments used for the hypothetical helicopter is presented in Fig 3.14.

If wind-tunnel data is not available, the fuselage characteristics must be estimated. This involves predicting basic tail-off airframe characteristics plus the aerodynamic contriubtions of the tail surfaces. It can be seen from Fig 3.14 that the tails have a significant effect on the fuselage moments and forces. Their effects can be estimated from basic wing theory as, for instance, that presented in Ref 6. However, precise methods of estimating tail-off fuselage characteristics for helicopter-type shapes are not available. Consequently, previous wind-tunnel test results for similar configurations must be used as described in the discussion of trim drag (Sect 2.3).

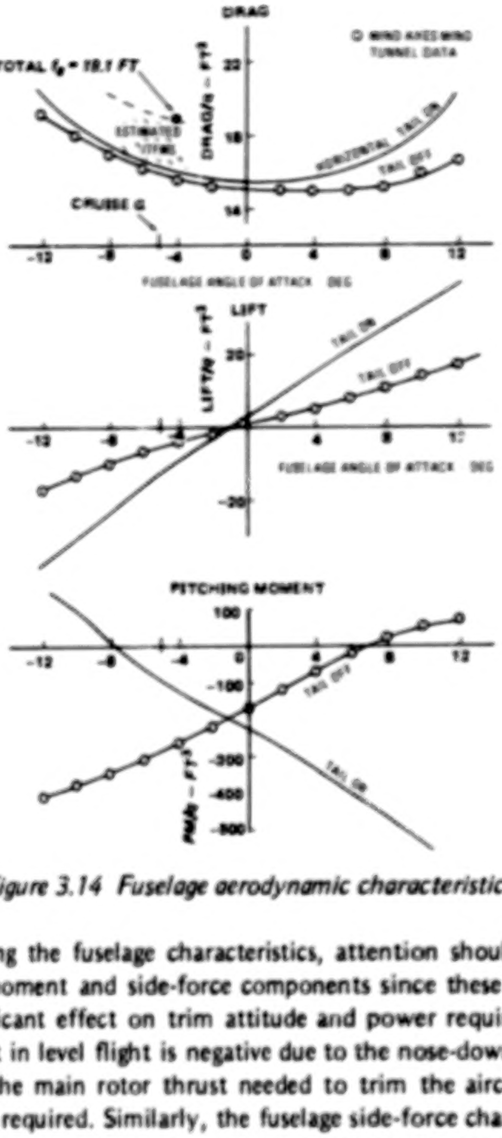

Figure 3.14 Fuselage aerodynamic characteristics

When computing the fuselage characteristics, attention should be focused on the drag, lift, pitching moment and side-force components since these forces and moments have the most significant effect on trim attitude and power required. As shown in Fig 3.14, the fusealge lift in level flight is negative due to the nose-down cruise attitude. The download increases the main rotor thrust needed to trim the aircraft, which results in an increase in power required. Similarly, the fuselage side-force characteristics determine the trim sideslip angle, which also contributes to an increase in parasite drag.

The main rotor forces and moments used in the trim iteration procedure outlined in Fig 3.13 are based on the classical blade element and momentum theory relationships for the first iteration (see Chs II and III of Vol I). For the second or subsequent iterations, a main and tail rotor subroutine is used to compute both the main and tail rotor trim forces (Fig 3.15). The subroutine uses collective pitch angle from the previous iteration to begin the computations. The next step is to define the blade flapping motion by summing the blade moments about the real or virtual flapping hinge. This involves solving a differential equation by numerical methods and incorporation of two-dimensional airfoil data, including blade stall and compressibility effects.

Having defined the blade motion, the next step in the rotor subroutine is to compute the rotor forces and moments by summing the elemental forces and moments of a

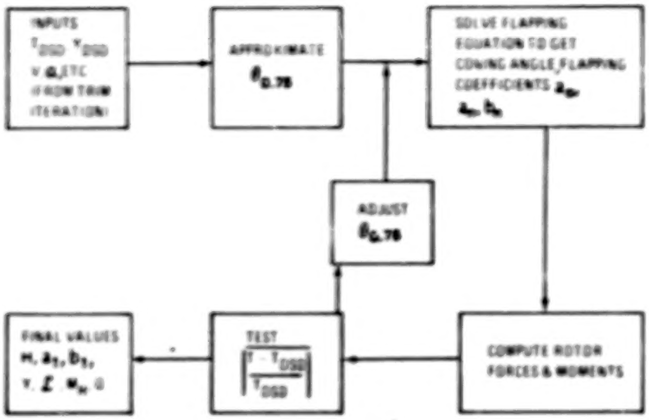

COMPUTER PROGRAM NOMENCLATURE

$\theta_{0.75}$ - COLLECTIVE PITCH ANGLE MEASURED AT 3/4 RADIUS
H - ROTOR H FORCE
a_n - nth HARMONIC OF LONGITUDINAL FLAPPING
a_0 - CONING ANGLE
b_n - nth HARMONIC OF LATERAL FLAPPING
£ - ROTOR ROLLING MOMENT
Q - ROTOR TORQUE
T_{DSD} - THRUST DESIRED
Y_{DSD} - SIDEFORCE DESIRED
V - AIRSPEED
α - ROTOR DISC ANGLE OF ATTACK

Figure 3.15 Rotor subroutine flow chart

specific number of discrete blade elements located at various radial positions, and then averaging these values at equally-spaced azimuthal locations around the disc. The thrust resulting from analysis is then compared with the desired value in a test for closure. If they don't agree, the collective pitch angle is adjusted accordingly and the rotor subroutine procedure is repeated until the thrust values are within 1 percent of the desired value. The remaining rotor forces and moments are then fed back into the main trim iteration routine shown in Fig 3.13 and the iteration is repeated until the six control variables defined in this figure (T_F, T_R, Y_F, M_{H_F}, θ, ϕ) converge within the prescribed tolerances.

The last step in the trim analysis computations shown in Fig 3.13 is to compute the shaft horsepower required, including transmission and accessory losses. The nonuniform downwash and parasite power corrections are also applied at this stage of the analysis. A detailed discussion of each of these corrections is presented in the following sections.

3.2 Nonuniform Downwash (NUD) Correction

A nonuniform downwash correction was developed by comparing power predictions for an isolated rotor obtained by a computer program based on the application of the vortex theory with another, based on the simple momentum theory.

In the vortex theory approach, it is assumed that the wake is rigid (Ch IV, Vol I); that is, there is no allowance for the wake contraction which occurs relatively far downstream of the rotor and thus, has little effect on performance. The rapid movement of the wake away from the rotor in forward flight also permits the use of other simplifying calculation techniques, such as assuming that the trailing vortices roll up into a concentrated tip vortex system after 45° of blade rotation. These assumptions reduce the computer run time substantially with no significant reduction in the accuracy of performance predictions.

Within this general approach, local induced velocities are determined from a trailed vortex system. Values of velocities induced by the vortex filaments are used to compute the blade loads which, in turn, serve as an input in recalculating the corresponding induced velocities. The iteration is continued until the airloads and induced velocities are mutually consistent.

A summary block diagram and list of features of the nonuniform downwash analysis used in the hypothetical helicopter calculations is presented in Fig 3.16. As noted, the program includes optional yawed flow, elasticity, and unsteady aerodynamic features.

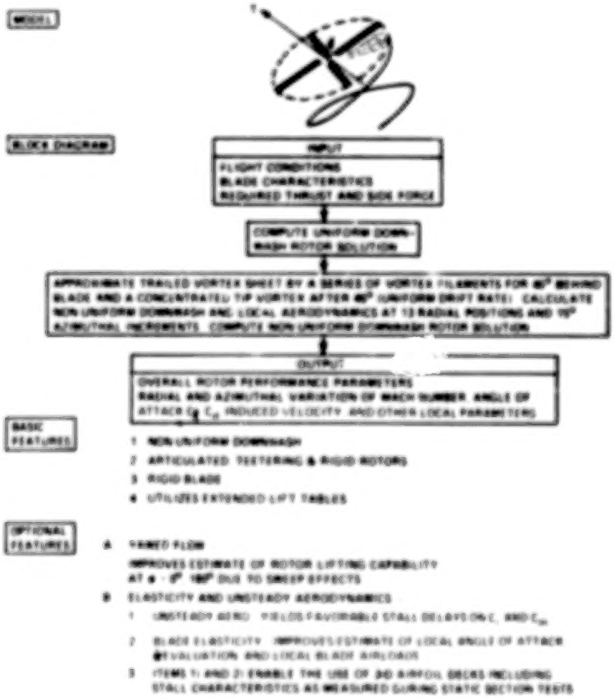
MODEL
V
BLOCK DIAGRAM
INPUT
FLIGHT CONDITIONS
BLADE CHARACTERISTICS
REQUIRED THRUST AND SIDE FORCE
COMPUTE UNIFORM DOWNWASH ROTOR SOLUTION
APPROXIMATE TRAILED VORTEX SHEET BY A SERIES OF VORTEX FILAMENTS FOR 45° BEHIND BLADE AND A CONCENTRATED TIP VORTEX AFTER 45° (UNIFORM DRIFT RATE). CALCULATE NON-UNIFORM DOWNWASH AND LOCAL AERODYNAMICS AT 13 RADIAL POSITIONS AND 15° AZIMUTHAL INCREMENTS. COMPUTE NON-UNIFORM DOWNWASH ROTOR SOLUTION
OUTPUT
OVERALL ROTOR PERFORMANCE PARAMETERS
RADIAL AND AZIMUTHAL VARIATION OF MACH NUMBER, ANGLE OF ATTACK, C_ℓ, C_d, INDUCED VELOCITY AND OTHER LOCAL PARAMETERS
BASIC FEATURES
1 NON-UNIFORM DOWNWASH
2 ARTICULATED, TEETERING & RIGID ROTORS
3 RIGID BLADE
4 UTILIZES EXTENDED LIFT TABLES
OPTIONAL FEATURES
A YAWED FLOW
IMPROVES ESTIMATE OF ROTOR LIFTING CAPABILITY AT $\psi = 0°, 180°$ DUE TO SWEEP EFFECTS
B ELASTICITY AND UNSTEADY AERODYNAMICS
1 UNSTEADY AERO: YIELDS FAVORABLE STALL DELAYS ON C_ℓ AND C_m
2 BLADE ELASTICITY: IMPROVES ESTIMATE OF LOCAL ANGLE OF ATTACK EVALUATION AND LOCAL BLADE AIRLOADS
3 ITEMS 1) AND 2) ENABLE THE USE OF 2D AIRFOIL DECKS INCLUDING STALL CHARACTERISTICS AS MEASURED DURING STATIC SECTION TESTS

Figure 3.16 Rotor airloads and performance analysis with nonuniform induced inflow

Regardless of the use of a considerable number of simplifying assumptions, the nonuniform downwash computer run time is still considerably higher and costlier than the uniform downwash program. For this reason, a simplified nonuniform downwash (NUD) correction was developed:

A flight velocity coordinate system was used to define rotor lift (L) and rotor equivalent drag (D_{e_r}) forces. The rotor lift is represented by the rotor-thrust component perpendicular to the flight velocity factor. This is presented nondimensionally under the form of the following coefficient:

$$C'_T = L/\rho A V_t^2, \text{ or } C'_T/\sigma = L/\rho A V_t^2 \sigma$$

The equivalent drag is interpreted as

$$D_{e_r} = 550\, RHP/V_o - X$$

where $550\ RHP/V_o$ represents the equivalent drag of the entire helicopter (based on RHP and not on SHP), and X is the rotor propulsive force.

In trimmed flight, X is equal to the fuselage drag, hence

$$D_{e_r} = (P_{ind} + P_{pr})/V_o.$$

Here, D_{e_r} combines the induced and profile power (P_{ind} and P_{pr}) into a synthetic drag and thus, converts rotor power required into a fundamental fixed-wing type of parameter. D_{e_r} can also be nondimensionalized by dividing it by $q_o d^2 \sigma$, where q_o is the velocity of flight dynamic pressure, and d is the rotor diameter.

At this point, it should be emphasized that although the D_{e_r} value actually depends on both P_{ind} and P_{pr}, it is assumed that differences between D_{e_r} values obtained by the uniform downwash approach and those obtained either through tests or more refined (nonuniform downwash) calculations are chiefly due to the induced power discrepancies. Consequently, all of the corrective action for D_{e_r} values is contained under the common name of NUD corrections.

These so-defined NUD corrections can be obtained as follows: (1) plot the isolated rotor performance, incorporating nonuniform downwash effects, in terms of C'_T/σ vs $D_{e_r}/q_o d^2 \sigma$ for selected values of μ and given rotor geometry (Fig 3.17), and (2) compare the so-obtained graphs with $C'_T/\sigma = f(D_{e_r}/q_o d^2 \sigma)$ derived under the uniform downwash assumption.

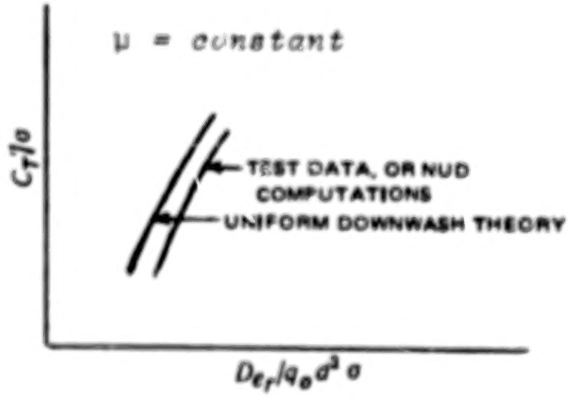

Figure 3.17 Effect of NUD on power required

It should also be pointed out that the D_{e_r} concept is also useful for evaluating rotor efficiency in terms of lift-to-drag ratio, L/D_{e_r}; while here in the NUD calculations, it is used as a means of isolating the induced and profile power from parasite components.

On the basis of a graph such as the one depicted in Fig 3.17, nondimensional equivalent rotor drag increments due to NUD effects ($\Delta D_e/q_0 d^2\sigma$) can be plotted as a function of rotor-lift coefficient C'_T/σ (Fig 3.18). The incremental data appeared to be reasonably linear for $C'_T/\sigma \leq 0.08$; thus a linear fairing passing through the origin was established for each value of μ.

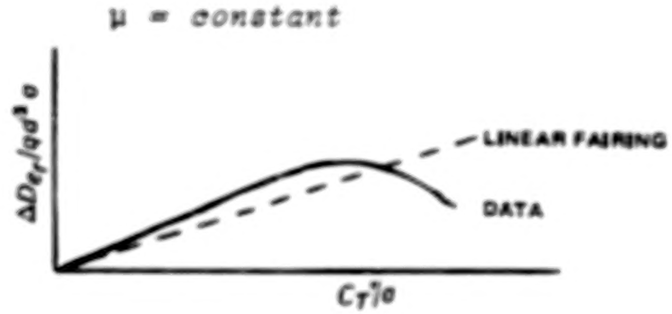

Figure 3.18 Incremental NUD power required

The slopes, $\partial(\Delta D_e/q_0 d^2\sigma)/(\partial(C'_T/\sigma)$, of these linear fairings were then plotted as a function of the variable $1/bAR_b$, where b = number of blades, and AR_b = blade aspect ratio, $(R/\bar{c})$. This relationship was again found to be linear, and the lines pass through the origin as shown in Fig 3.19.

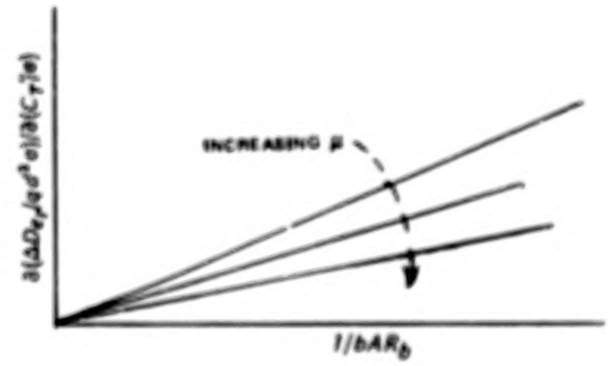

Figure 3.19 Effect of blade aspect ratio and number on NUD power increment

Based on the nondimensional data shown in Fig 3.19, an NUD incremental power penalty (ΔRHP_{nu}) can be estimated for any rotor geometry:

$$\Delta RHP_{nu} = k_n L \bar{c} V_t/432\, bd \tag{3.13}$$

where

$\bar{c}$ = average blade chord; ft
d = rotor diameter; ft
b = number of blades
L = rotor lift,

and

$$k_n = [\partial(\Delta D_e/qd^2\sigma)/\partial(C_T/\sigma)bAR]\mu^3.$$

The variable k_n represents the slope of the lines in Fig 3.19 times μ^3. The variation of k_n with advance ratio is illustrated in Fig 3.20, and is considered valid for computing performance at $0.15 \leq \mu \leq 0.4$. At μ values outside of the above boundaries, this method gives optimistic results. The k_n factor can be used to compute both main rotor and tail rotor NUD effects; however, the tail rotor correction is generally small enough to be neglected.

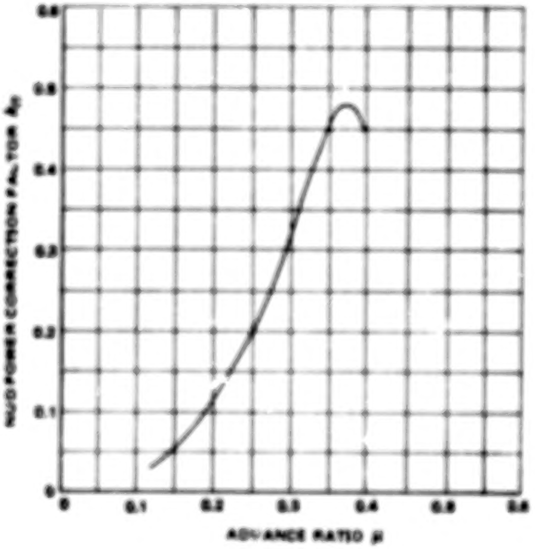

Figure 3.20 Nonuniform downwash incremental power correlation factor

It is interesting to note that k_n and the corresponding ΔRHP correction increases rapidly with advance ratio up to $\mu = 0.37$. This large variation in induced power is attributed to the fact that in forward flight, the rotor downwash varies with both the blade azimuth and radius. However, with increasing advance ratios, the azimuthal variation becomes more significant.

At this point, it should be emphasized that the above-described procedure for NUD corrections represents a method used by one company, and is not necessarily used throughout the industry. It is obviously possible to devise other approaches to this problem, but the experience of the company seems to support the practical validity of this approach.

To illustrate the NUD procedure, sample calculations for the hypothetical helicopter at $W = 15{,}000\ lb$ and $V = 150\ kn$ are presented below:

1. The required rotor geometry parameters are:
   $\ell = 2\ ft;\ d = 50\ ft;\ b = 4;\ V_t = 700\ fps;$
   $\mu = V_o/V_t = 0.36$; and $L \approx 15{,}000\ lb$.
2. From Fig 3.20, $k_n = 0.475$ at $\mu = 0.36$,
3. Substituting these values in Eq (3.13 gives:

$$\Delta RHP_{nu} = \frac{k_n L \ell V_t}{432 bd} = \frac{0.475 \times 15{,}000 \times 2 \times 700}{432 \times 4 \times 50}$$

$$\Delta RHP_{nu} = 115.5\ hp.$$

3.3 Parasite Power Correction

A comparison of model rotor parasite power measurements with theoretical uniform downwash performance predictions indicates that the theory underpredicts the power required to generate a given propulsive force. The ratio of theoretically predicted parasite power ($XV_o/550$) to that actually measured—called *propulsive efficiency* (η_p) is a function of advanced ratio (Fig 3.21). It should be noted that at advance ratios of

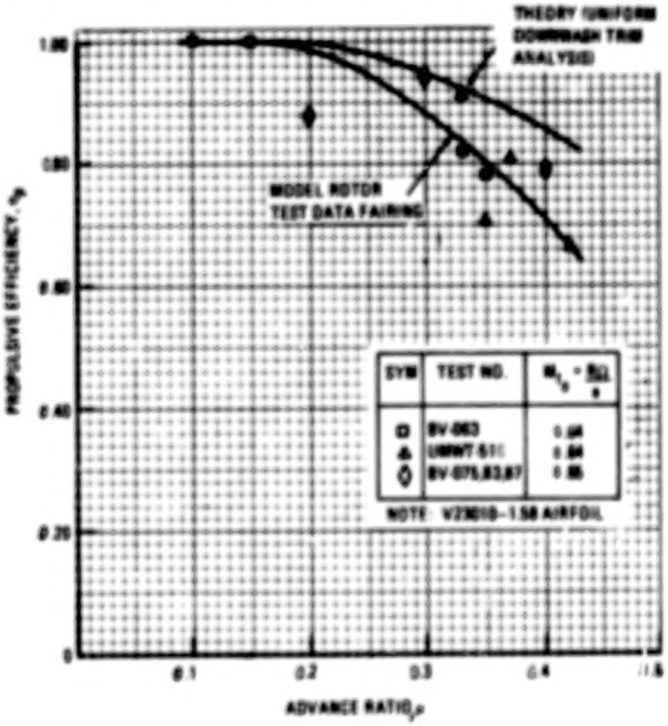

Figure 3.21 Parasite power correction

$\mu > 0.15$, the actual parasite power from model tests is higher than its theoretical value ($\eta_{p_{test}} < \eta_{p_{theory}}$). This disagreement in parasite power levels is not completely understood; however, it could be due to blade contributions to the total helicopter parasite drag (see Ch III, Vol I) resulting from local separation on the retreating blade tip, as well as in the reverse flow region. It can also mask nonuniform downwash or aeroelastic effects. If it is stall related, then differences between the Reynolds numbers used in theoretical predictions and those corresponding to the actual model test data shown in Fig 3.21 may be a factor. More experimental and theoretical investigations of this phenomena are required. Nevertheless, even without a complete understanding of the phenomena, a practical way of dealing with it must be developed. One approach in that respect is outlined below. However, no special claims are made as to its universal merits.

Using the data presented in Fig 3.21, the trim analysis parasite power is corrected to the test level by adding the following increment to the total power required:

$$\Delta RHP_{par} = \frac{XV_o}{550}\left(\frac{1}{\eta_{p_{test}}} - \frac{1}{\eta_{p_{theory}}}\right). \tag{3.14}$$

For example, neglecting the rotor profile drag component, the hypothetical helicopter propulsive force required to balance the airframe drag at 150 kn under SL/STD conditions is

$$X = drag = f_e \times q = 19.1\ ft^2 \times 76.4;$$

$X = 1460\ lb$

$\mu = V_o/V_t = 0.362.$

From Fig 3.21, $\eta_{p_{test}} = 0.78$ and $\eta_{p_{theory}} = 0.89$. The ΔRHP_{par} correction, therefore, is

$$\Delta RHP_{par} = \frac{1460 \times 253.5}{550}\left(\frac{1}{0.78} - \frac{1}{0.89}\right),$$

$\Delta RHP_{par} = 106\ hp.$

3.4 Determination of Low-Speed Power Required

Determination of the power required in the 0 to 60-kn speed range is necessary primarily to analyze takeoff and landing capability, and to determine the effect of wind on hover performance. Furthermore, this regime of flight is important, due to the increasing interest of the military in low-speed nap-of-the-earth (NOE) operations. In this speed range (approaching hover), wake contractions become significant. This may require development of a technique permitting a transition from the hover analysis employing an empirical wake contraction technique, to a forward-flight nonuniform downwash analysis based on a rigid wake. In addition, flow visualization studies[3.7] have shown that two concentrated wing-tip vortices form at the edge of the wake, resulting in an extremely complex wake structure.

TABLE OF CONTENTS

Preface . . . . iii 1/A8

CHAPTER I **Introductory Considerations** 1 1/A10

1. Description of the Hypothetical Helicopter Configuration 2 1/A11

1.1 Weights 3 1/A12
1.2 Main Rotor and Tail Rotor Geometry 4 1/A13
1.3 Transmission Limits 7 1/B2
1.4 Airframe Configuration 8 1/B3

2. Performance Summary 8 1/B3

3. Engine Performance 9 1/B4

3.1 General Characteristics of Shaft Turbines 9 1/B4
3.2 Power Ratings & Effects of Ambient Conditions on Engine Characteristics 10 1/B5
3.3 Powerplant for Hypothetical Helicopter 11 1/B6
3.4 Engine Power Constraints 13 1/B8
3.5 Engine Installation Losses 14 1/B9

4. Standard Day Atmosphere 15 1/B10

References for Chapter I 19 1/B14

CHAPTER II **Single-Rotor Helicopter & Vertical-Climb Performance** 20 1/C1

1. Hover Out-of-Ground-Effect Performance 22 1/C3

1.1 General Procedure 22 1/C3
1.2 Power vs Thrust Calculations 23 1/C4
1.3 Example of the Main Rotor Power Required 27 1/C8
1.4 Tail-Rotor Power Required 34 1/D1
1.5 Fuselage Download 37 1/D4
1.6 Transmission and Accessory Losses 43 1/D10

2. Hover In-Ground-Effect (IGE) Performance 44 1/D11

2.1 Rotor Thrust Variation, IGE 44 1/D11
2.2 IGE Download 44 1/D11

3. Hover Ceiling OGE and IGE 46 1/D13

4. Vertical-Climb Capability 48 1/E1

4.1 Detailed Analysis 48 1/E1
4.2 Simplified Vertical Climb Predictions 54 1/E8

References for Chapter II 56 1/E10

CHAPTER III **Forward-Flight Performance** 57 1/E11

1. **Introductory Remarks** 59 1/E13

2. **Drag Estimates** 60 1/E14

2.1 Drag of Streamlined Components 61 1/F1
2.2 Drag of Nonstreamlined Components 65 1/F5
2.3 Trim Drag 69 1/F9
2.4 Miscellaneous Items 72 1/F12
2.5 Net Engine Thrust 73 1/F13
2.6 Detailed Sample Drag Calculations for the Hypothetical Helicopter 74 1/F14

3. **Methodology for Determining Level-Flight Power Required** 78 1/G4

3.1 Trim Analysis Computer Program 79 1/G5
3.2 Nonuniform Downwash (NUD) Correction 82 1/G8
3.3 Parasite Power Correction 87 1/G13
3.4 Determination of Low-Speed Power Required 88 1/G14

4. **Examples of Level-Flight Power Required Predictions for the Hypothetical Single-Rotor Aircraft** 90 2/A6

4.1 Power Required Based on the Trim Analysis 90 2/A6
4.2 Simplified SHP_{req} Estimates vs Trim Analysis Program 94 2/A10

5. **Power Required in Climb and Descent** 98 2/A14

5.1 Climb Power Required 99 2/B1
5.2 Descent Power Required 100 2/B2

6. **Level Flight and Maneuver Airspeed Envelope** 101 2/B3

6.1 Rotor Stall Limits Methodology 103 2/B5
6.2 Level-Flight Airspeed/Altitude Structural Envelope 112 2/B14
6.3 Maneuver Capability 114 2/C2

7. **Calculation of Forward-Flight Performance Capability** 116 2/C4

7.1 Mission Performance 116 2/C4
7.2 Payload/Range Capability 118 2/C6
7.3 Payload/Endurance Capability 125 2/C13
7.4 Ferry-Range Capability 129 2/D3
7.5 Speed Capability 135 2/D9
7.6 Forward-Flight Climb Capability 135 2/D9
7.7 Service Ceiling 137 2/D11

References for Chapter III 140 2/D14

CHAPTER IV **Winged Helicopter Performance** 143 2/E3

1. **Introductory Remarks** 144 2/E4

2. **Description of the Winged Helicopter** 146 2/E6

2.1 Planform Area/Flap Geometry 146 2/E6
2.2 Wing Aspect Ratio 148 2/E8
2.3 Taper Ratio 149 2/E9
2.4 1/4-Chord Sweep 149 2/E9
2.5 Wing Location 150 2/E10
2.6 Airfoil Section 151 2/E11

3. Hover and Vertical-Climb Performance 151 2/E11

3.1 Wing Download OGE 151 2/E11
3.2 Wing Download IGE 155 2/F1
3.3 Hover Ceiling 155 2/F1
3.4 Vertical Climb Performance 156 2/F2

4. Forward-Flight Performance 156 2/F2

4.1 Effect of Wings on Parasite Drag/Power 157 2/F3
4.2 Effect of Wing Unloading on Induced and Profile Power of the Rotor 165 2/F11
4.3 Determination of Optimum Cruise Unloading 167 2/F13
4.4 Level Flight Performance 169 2/G1
4.5 Climb and Autorotation 174 2/G7
4.6 Maneuver Capability 179 2/G12

References for Chapter IV 181 2/G14

CHAPTER V **Tandem-Rotor Helicopter Performance** 182 3/A5

1. Introductory Remarks 183 3/A6

2. Description of the Tandem-Rotor Helicopter 184 3/A7

2.1 Overlap 184 3/A7
2.2 Gap/Stagger 185 3/A8
2.3 Weights 186 3/A9
2.4 Fuselage Configuration 186 3/A9
2.5 Rotor Hub 186 3/A9
2.6 Engines/Transmissions 187 3/A10

3. Hover Performance 187 3/A10

3.1 Isolated Rotor Power Required 187 3/A10
3.2 Induced Power Overlap Correction 187 3/A10
3.3 Fuselage Download, OGE 188 3/A11
3.4 Ground-Effect Correction 192 3/B3
3.5 Total Hover Power Required Sample Calculations 193 3/B4
3.6 Hover Ceiling Capability 185 3/A8

4. Forward-Flight Performance 195 3/B6

4.1 Level Flight Power Required 195 3/B6
4.2 Power Required in Climb and Descent 206 3/C5
4.3 Structural Envelope 207 3/C6
4.4 Performance Capability 210 3/C9

References for Chapter V 213 3/C12

Appendix A *Performance Guarantees* 214 3/013
Appendix B *Aircraft Growth*. 223 3/D9

Until practical vortex theory analyses applicable to predictions of low-speed performance are developed, the power required in this speed regime will continue to be defined by the shape of the *RHP = f(V)* curve based on simple momentum theory (uniform downwash). It was shown that power required trends in this speed range, predicted by momentum theory, usually agree with wind-tunnel measurements. However, incremental power corrections are needed in order to match the hover and 60-kn power required points determined by the nonuniform downwash approach. This correction is based on the assumption that the power adjustment at low speeds is proportional to that in hover, and follows the trend given by the momentum theory. The procedure for this calculation can be explained with the aid of the hypothetical helicopter power required shown in Fig 3.22. In this figure, uniform downwash and nonuniform downwash power required are shown at SL/STD conditions for a gross weight of 15,000 lb. Designating the values of the hover and 60-kn power required by a, b, c, and d as noted in this figure, the nonuniform downwash correction (ΔRHP_{nu}) for airspeeds of 0 to 60 kn is:

$$\Delta RHP_{nu} = \left(\frac{(a-b)-(c-d)}{(b-d)}\right)\left(RHP_u - d\right) + \left(c - d\right). \tag{3.15}$$

In this equation, RHP_u is the uniform downwash power required at the airspeed at which ΔRHP is being computed. The total power required, therefore, is

$$RHP = RHP_u + \Delta RHP_{nu}. \tag{3.16}$$

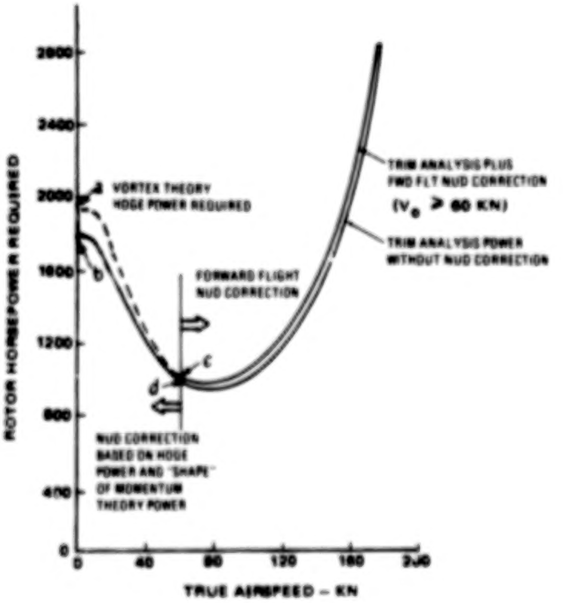

Figure 3.22 Determination of low-speed power required

To illustrate the above procedure, detailed calculations for the 25-kn point in Fig 3.22 are presented below.

1. From this figure:

$$\left.\begin{aligned} a &= 1813 \text{ hp} \\ b &= 1661 \\ c &= 896 \\ d &= 884 \\ RHP_u &= 1362 \end{aligned}\right\downarrow .$$

2. Substituting these values in Eqs (3.15) and (3.16),

$$\begin{aligned} RHP &= 1362 + 98 \\ RHP &= 1460. \end{aligned}$$

4. EXAMPLES OF LEVEL FLIGHT POWER REQUIRED PREDICTIONS FOR THE HYPOTHETICAL SINGLE–ROTOR AIRCRAFT

A discussion of the hypothetical helicopter forward flight power required based on the calculation procedure described above is presented in this section of the text. The discussion includes an evaluation of the referred and generalized data presentation techniques used to account for the effect of air density and compressibility at various ambient conditions. In addition, a comparison of trim analysis computer program predictions versus simplified calculations is provided.

4.1 Power Required Based on the Trim Analysis

Level flight power required is presented in Figs 3.23 and 3.24 for SL/STD and 4000 ft, 95°F ambient conditions. Speed power polars based on the trim analysis and correction factors discussed in the previous section are presented for gross weights from 9,000 to 18,000 lb. Increasing gross weights result in increased power and higher minimum-power airspeed. Due to the fact that the induced power changes become more rapid at low speeds, significant power required increments are most apparent in the speed range from $V = 0$ to that corresponding to minimum power. In contrast, at higher speeds, the induced power continues to decrease, resulting in a convergence of the speed power polars.

Engine power available and transmission power limits are also shown in Figs 3.23 and 3.24. For SL/STD conditions, it should be noted that the speed capability at 15,000 lb gross weight is 172 kn at max. cont. power and 178 kn at the transmission limit. A complete discussion of performance capabilities is presented in Sect 7 of this chapter.

The difference between the SL/STD and 4000 ft/95°F power required are due to effects of air density and compressibility.

Air Density. At 4000 ft/95°F, the air density is 0.808 of the SL/STD value. This tends to increase the hover and low-speed power required because of increased induced

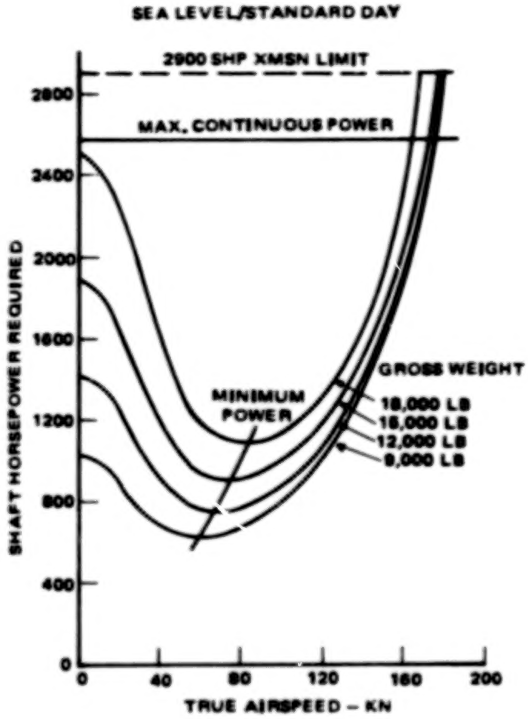

Figure 3.23 Level flight power required at SL/STD

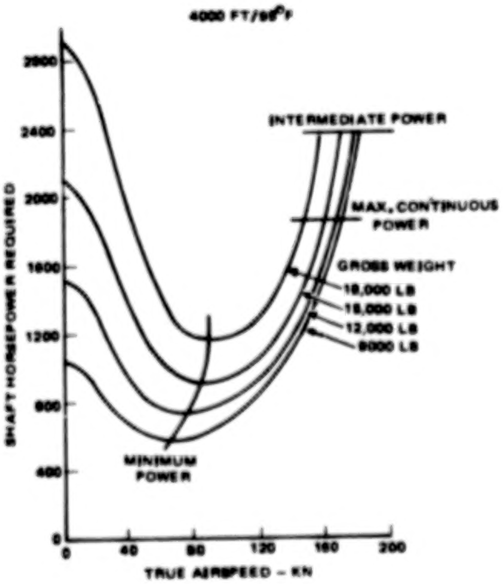

Figure 3.24 Level flight power required at 4000 ft/95° F

power. At high speeds, the lower air density reduces the total power required by decreasing the parasite drag, unless the rotor lift coefficient becomes sufficiently high to cause a divergence in power required due to rotor stall. The effect of density variations can be accounted for by dividing the rotor horsepower required (*RHP*) and weight (*W*) by the density ratio (σ_ρ), as illustrated in Fig 3.25. The parameters RHP/σ_ρ and W/σ_ρ are called referred power and referred weight, and they are developed from the basic C_p, C_T nondimensional relationships.

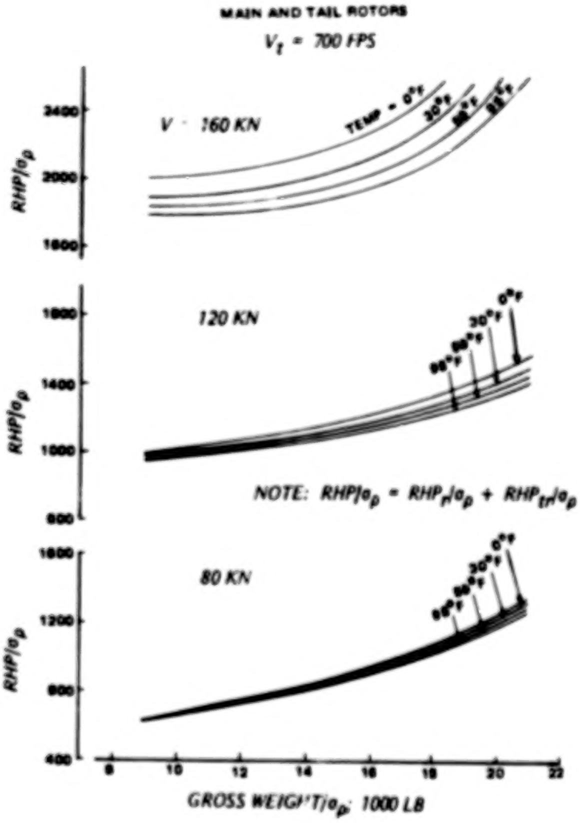

NOTE: $RHP/\sigma_\rho = RHP_r/\sigma_\rho + RHP_{tr}/\sigma_\rho$

Figure 3.25 Forward-flight compressibility power

Compressibility Effects. The graphs shown in Fig 3.25 also incorporate compressibility effects based on the two-dimensional airfoil characteristics shown in Figs 2.3 and 2.4. The variation in referred power with temperature is due primarily to the effect of compressibility on the main rotor. This effect on the tail rotor can be neglected since, at the speeds indicated in Fig 3.25, the tail rotor contributes only 3 to 5 percent of the total power required. Compressibility effects vary with increasing airspeed, gross weight, and temperature, since these parameters are a function of average rotor c_ℓ and advancing blade tip Mach number $M_{(t)90}$. The variation of $M_{(t)90}$ with forward speed and ambient temperature is apparent in the following chart:

TEMPERATURE	$M_{(t)90}$ @ 80 Kn	$M_{(t)90}$ @ 160 Kn
0°F	0.795	0.923
95°F	0.723	0.841

The effect of varying rotor rpm can be accounted for by taking advantage of the referred data in Fig 3.25. This is accomplished by using $(V_{t_o}/V_t)^2$ and $(V_{t_o}/V_t)^3$ values in addition to the W/σ_ρ and RHP/σ_ρ parameters as discussed in Ch II. Knowing the advance ratio μ, the flight speed should then be converted to referred airspeed $V_{rfd} = V(V_{t_o}/V_t)$ where V_{t_o} is the design tip speed. Compressibility effects due to RPM variations can be accounted for by changing the constant temperature lines in Fig 3.25 to lines of constant average Mach number $\bar{M}_t = \bar{U}_t/a$, where a is the speed of sound, and $\bar{M}_t$ is a function of $M_{(t)90}$:

$$\bar{M}_t = M_{(t)90}/(1 + \mu). \tag{3.17}$$

The referred weight and power parameters are more convenient to work with than the nondimensional coefficients C_T and C_P which have low values on the order of 0.005 and 0.0005, respectively.

A third method of determining power required, called the *generalized method*, is often used to present flight test data. This method converts C_P, C_T, μ, and M to the dimensional form of W/δ, $V/\sqrt{\theta}$, $N/\sqrt{\theta}$, and $SHP/\delta\sqrt{\theta}$ as shown below:

$$C_T = \left(\frac{30^2}{\rho_o A \pi^2 R^2}\right)\left(\frac{W/\delta}{(N/\sqrt{\theta})^2}\right)$$

$$C_P = \left(\frac{550(30)^3}{\rho_o A \pi^3 R^3}\right)\left(\frac{SHP/\delta\sqrt{\theta}}{(N/\sqrt{\theta})^3}\right)$$

$$\mu = \left(\frac{30}{\pi R}\right)\left(\frac{V/\sqrt{\theta}}{N/\sqrt{\theta}}\right)$$

$$M_{(t)90} = \left(\frac{R}{30a_o}\right)\left(\frac{N}{\sqrt{\theta}}\right)\left[1 + \left(\frac{30}{\pi R}\right)\left(\frac{V/\sqrt{\theta}}{N/\sqrt{\theta}}\right)\right]$$

where

a_o = speed of sound at SL/STD conditions
ρ_o = air density at SL/STD conditions
δ = ambient pressure ratio
θ = ambient temperature ratio
A = rotor area

N = rotor rpm
R = rotor radius.

Maintaining a constant W/δ and $N/\sqrt{\theta}$ is equivalent to a constant C_T; and a constant $V/\sqrt{\theta}$ and $N/\sqrt{\theta}$ is equivalent to a constant $M_{(t)90}$.

Even though the three methods are interchangeable, the generalized method is becoming increasingly popular, particularly for presenting flight test data where compressibility effects are significant. During performance test programs, it is easier to fly constant W/δ and $N/\sqrt{\theta}$ than it is to maintain a constant C_T and average Mach number, because the generalized parameters are readily determined from cockpit measurements of pressure altitude, rotor speed, and ambient temperature. Intermediate density altitude calculations are not necessary. When presenting generalized data, speed power polars for various W/δ levels are required for a range of $N/\sqrt{\theta}$ values.

The results of the trim analysis program (Fig 3.25) were based on two-dimensional airfoil characteristics. However, studies using the potential flow theory[9,10,11] indicate that drag divergence occurs at higher Mach numbers than given by the two-dimensional data. This three-dimensional *tip relief effect* is due to the spanwise movement of streamlines located within approximately one chord-length of the tip. Consequently, the flow encounters an apparent decrease in airfoil thickness, and local velocity at the thickest portion of the airfoil is reduced. This effect is similar to that encountered in swept fixed-wings.

4.2 Simplified SHP_{req} Estimates vs Trim Analysis Program

The theoretical relationships developed in Vol I, Chs II and III, and the trim analysis computer program used for the sample problem calculations employ the same fundamental momentum theory and blade element concepts for computing power required. The primary differences between the two techniques are: (1) the procedure used to integrate the blade element forces over the rotor disc, and (2) the trim analysis which inherently accounts for the effects of helicopter attitude on performance. In the classical method (without the use of computers), the rotor torque is determined with the help of an average rotor drag coefficient $\bar{c}_d$. The trim analysis uses numerical techniques programmed on the computer to average the force contributions of discrete blade sections located at various radial and azimuthal positions. Local effects such as compressibility and stall are accounted for in this manner.

In Fig 3.26, the power required computed by a simplified method is compared with the results obtained from trim analysis. Here, SHP_{req} at SL/STD was computed for 15,000-lb gross weight. To simplify this comparison, the NUD and parasite power corrections were not applied. The following equations from Vol I were reproduced for application to the hypothetical aircraft (all velocities are in fps):

$$SHP = (RHP_{mr} + RHP_{tr})/\eta_t + \Delta SHP$$

where

ΔSHP = accessory losses, and η_t = transmission efficiency.

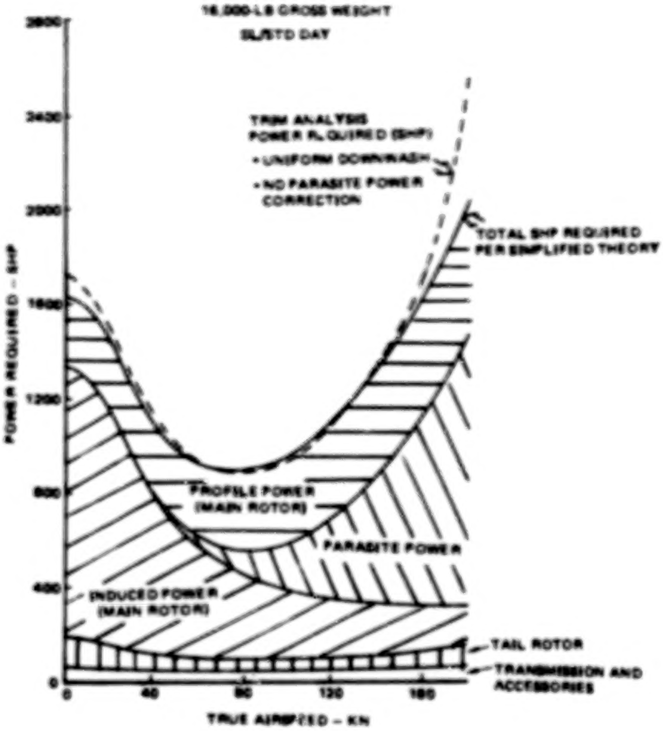

Figure 3.26 Simplified approach to power required

$$RHP_{mr} = \underbrace{\frac{T v_{i_f}}{550}}_{\text{Induced Power}} + \underbrace{\frac{\sigma \bar{c}_d (1 + 4.7\mu^2)\rho \pi R^2 V_t^3}{4400}}_{\text{Profile Power}} + \underbrace{\frac{f_e \rho V^3}{1100}}_{\text{Parasite Power}}$$

and

$$RHP_{tr} = \frac{T_{tr} v_{i_{f_{tr}}}}{550} + \frac{\sigma \bar{c}_d (1 + 4.7\mu^2)\rho \pi R_{tr}^2 V_{tr}^3}{4400}$$

The above induced velocities (v_{i_f} and $v_{i_{f_{tr}}}$, respectively) are computed as follows:

$$v_{i_f} = v_o \left[\sqrt{-(V/v_o)^2/2 + \sqrt{(V/v_o)^4/4 + 1}} \right]$$

where

$$v_o = \sqrt{T/2\rho \pi R^2 \bar{r}_e^2}$$

and

v_o = hover induced velocity per momentum theory

$\bar{r}_e$ = r_e/R, effective nondimensional rotor radius which extends from blade root cutout to $0.97R$, where tip losses become significant (see Vol I, Ch III for tip loss discussion).

These relationships can be further simplified by neglecting the fuselage download effects and tail rotor unloading due to the cambered vertical tail assumed in the sample problem. Therefore,

$$T_{mr} \approx W$$

and

$$T_{tr} \approx 5260\ RHP_{mr}/\ell_{tr}$$

where

ℓ_{tr} ≈ tail rotor moment arm.

In addition, it is assumed that

$\eta_t = 0.98$

$\bar{r}_e = 0.95 = \sqrt{(0.97)^2 - (0.2)^2}$, where cutout = $0.2R$ and effective rotor radius = $0.97R$

$\ell_{tr} = 30\ ft$

main rotor $\bar{c}_d = 0.008$, tail rotor $\bar{c}_d = 0.0107$ — For derivation, see Hover Section (Ch II, Sect 1.2 and 1.3)

$f_e = 19.1\ ft^2$ (fuselage cruise angle-of-attack = $-5°$)

$\Delta SHP = 30\ hp$ (accessory drive power)

σ, R, V_t, etc., see Table I-1.

Based on the above assumptions, the total power required calculated by the simplified method agrees well with the trim analysis results up to 140 kn–the only exception being small differences in the low-speed range (Fig 3.26). These differences are primarily due to the omission of the effect of the fuselage download on the main rotor induced power. The two approaches would result in an agreement if the 2.55 percent of gross weight hover download is included in the induced power required estimates for airspeeds up to approximately 60 kn. At speeds above 60 kn, cruise download can be approximately estimated from the fuselage aerodynamic characteristics presented previously in Fig 3.14, assuming a constant cruise angle-of-attack of $\alpha_f = -5°$; thus neglecting variations of the actual α_f values due to changing main rotor downwash.

As shown in Fig 3.10, the angle-of-attack at 15,000 lb is within ≈$1°$ of this angle for airspeeds between 60 and 140 kn.

Because of compressibility and stall effects above 140 kn, the simplified calculations under-predict the power required. However, theoretical stall and compressibility corrections can be added to the basic profile power expressions based on the equations developed by McCormick[13] and modified to agree with the vortex theory analysis[12]. For example, for the V23010-1.58 airfoil, an increment in the average rotor section drag coefficient due to compressibility ($\Delta\bar{c}_{d_c}$) is

$$\Delta\bar{c}_{d_c} = 0.2(M_{(t)90} - M_d)^3 + 0.0085(M_{(t)90} - M_d) \tag{3.18}$$

where M_d is the drag divergence Mach number defined empirically as

$$M_d = 0.82 - 2.4(C_T/\sigma). \tag{3.19}$$

In Eq (3.18), $M_{(t)90}$ is the advancing blade tip Mach number; therefore, the total profile power (RHP_{pr}) becomes

$$RHP_{pr} = \frac{\sigma(\bar{c}_d + \Delta\bar{c}_{d_c})(1 + 4.7\mu^2)}{4400}\rho\pi R^2 V_t^3 \tag{3.20}$$

For a rotor with the V23010-1.58 airfoil section, a similar average rotor blade section drag increment can be developed for predicting the increase in power due to stall, ($\Delta\bar{c}_{d_s}$).

$$\Delta\bar{c}_{d_s} = 18.3(1 - \mu)^2 F^3 \tag{3.21}$$

where

$$F = \left[\frac{C_T/\sigma}{(1 - \mu)^2}\right]\left[1 + \frac{f_e q}{W} - 0.1375\right]. \tag{3.22}$$

Equations for the NACA 0012, as well as advanced, airfoils can be found in Ref 12.

The agreement between calculations based on the simplified approach and the more sophisticated computerized procedure indicates that the first method can be used to reduce computer costs and increase turnaround time if compressibility, stall, nonuniform downwash and propulsive efficience effects are accounted for. For preliminary design work, the simplified relationships are particularly useful because they provide a cost-effective means of conducting parametric studies on many different helicopter configurations.

The simplified calculation techniques also give details concerning the power-required breakdown which provides some insight into means of optimizing a design for a specific mission. This breakdown was obtained for the hypothetical helicopter by applying the download, compressibility, NUD and parasite power corrections to the appropriate values of the power-required components predicted by the simplified approach and shown in Fig 3.26. Data for hover and airspeeds of 80 and 150 kn are presented in Table III-3.

TRUE AIRSPEED	HOVER	80 KN	150 KN
	% SHP		
Induced Power (Main Rotor)	72	40	19
Profile Power (Main Rotor)	16	38	30
Parasite Power	0	12	43
Tail Rotor Power	8	5	4
Transmission & Accessories	4	5	4

TABLE III-3 POWER REQUIRED BREAKDOWN (PERCENT)

It can be seen that in hover, the induced power accounts for 72 percent, and profile power for 16 percent, of the total SHP required. Therefore, to design a helicopter having a low energy consumption in hover and/or maximum vertical takeoff performance capability, the induced power should be kept to a minimum. Selection of a low disc loading and minimization of induced power losses through optimization of the blade twist and planform represent some of the design approaches which may be applied in this case.

At 80 kn, which is about the minimum power condition, the induced and profile powers are each approximately equal to 40 percent of the total. One-engine-inoperative (OEI) speed at which SHP_{req} is minimum, and that corresponding to maximum endurance usually coincide*. Therefore, to provide maximum OEI performance capability and maximum loiter time for endurance missions, more attention should be given to profile power: thus, tip speed and blade area should be optimized to minimize this quantity. However, since the induced power is also sizeable–decreasing the disc loading and reducing the nonuniformity of the rotor downwash (see Ch III, Vol I) will also significantly contribute to an improvement in performance.

At $V_o = 80$ *kn*, parasite power accounts for only 12 percent of the total SHP. Thus, even a sizeable drag reduction would provide only a limited benefit in this regime of flight. By contrast, at a cruise speed of 150 kn, the parasite drag is responsible for 43 percent of the total SHP required, while the profile and induced power represent 30 and 19 percent of the total, respectively. Therefore, means of reducing parasite drag should be explored in order to provide maximum speed and range capability.

5. POWER REQUIRED IN CLIMB AND DESCENT

Power required in climb or descent at airspeeds equal to, or exceeding, the minimum power speed can be computed using the trim analysis program; however, this can result in considerable run time. It is generally less costly and easier to take advantage of the approximate climb prediction method based on the excess of shaft horsepower available over that required for forward flight at a particular flight speed. In analogy to Eq (2.32) derived in the preceding chapter, the following expression can be written.

---

*Small deviations may occur due to the variation of specific fuel consumption with SHP, with the result that SHP_{min} does not coincide with minimum fuel flow in forward flight.

$$\Delta SHP = W(V_c)/33{,}000k_{p_c} \tag{3.23}$$

where

$\Delta SHP = SHP_{climb} - SHP_{level\ flight}$ = incremental climb power

V_c = rate of climb in fpm

k_{p_c} = climb efficiency factor.

The climb efficiency factor, which can be derived from flight test data, wind-tunnel tests, or more precise analytical calculations (e.g., trim analysis program), accounts for such factors as fuselage lift and drag, induced power, and tail rotor power being different in climb than in horizontal flight. It also covers transmission efficiency–reducing the excess power actually available for climb.

5.1 Climb Power Required

Assuming that profile power in climb remains the same as in horizontal flight, the most important influence of the variables that affect the additional power required to climb can be discussed in light of the momentum theory considerations presented in Ch II of Vol I. Using this approach, and assuming that the rotor plane is positioned almost horizontally,

$$\Delta SHP = \frac{W(V_c)}{33000}\left[\frac{k_{vf}}{\eta_t}\left(1 + \frac{v_c - v}{V_c}\right)\right] \tag{3.24}$$

where

k_{vf} = forward flight download factor

η_t = transmission efficiency

v_c = induced velocity in climb

v = induced velocity in forward flight.

Comparing Eqs (3.23) and (3.24), it can be seen that the variables in the brackets of Eq (3.24) are equal to the reciprocal of the climb efficiency factor k_{p_c}. It should also be noted that the efficiency factor is made up of the download factor k_{vf} which accounts for the increase in negative lift and rise in trim drag of the fuselage in climb and η_t. In addition, the term, $1 + (v_c - v)/V_c$, accounts for the variation in downwash velocity in climb. This is less than 1.0 for positive rates of climb, since $v_c < v$ in this flight regime. Therefore, it is apparent that the climb efficiency factor would be greater than 1.0 if there were no increase in download or transmission power losses.

In contrast to paired main rotor systems, the increase in tail rotor power required in climb for single-rotor configurations causes an additional reduction in the climb efficiency factor. Typically, $0.85 \leqslant k_{p_c} \leqslant 0.95$ for tandems; while for single-rotor aircraft, $0.80 \leqslant k_{p_c} \leqslant 0.90$.

Average k_{p_c} values for a specific range of weights, airspeed, and rates of climb are often used to reduce computer and calculation time. For example, computed values of k_{p_c} are presented in Fig 3.27 as a function of gross weight for airspeeds of 80 to 120 kn. Here, it is shown that k_{p_c} increases with decreasing speed. As discussed in Ch II, values on the order of 1.5 are achieved in hover. At 80 kn, $0.8 < k_{p_c} \leqslant 0.9$, depending on the rate of climb. Since most forward flight climb performance is calculated at the minimum power speed of $V \approx 80$ *kn* (where rate of climb is highest), an average value of $k_{p_c} = 0.85$ was selected for subsequent climb performance calculations.

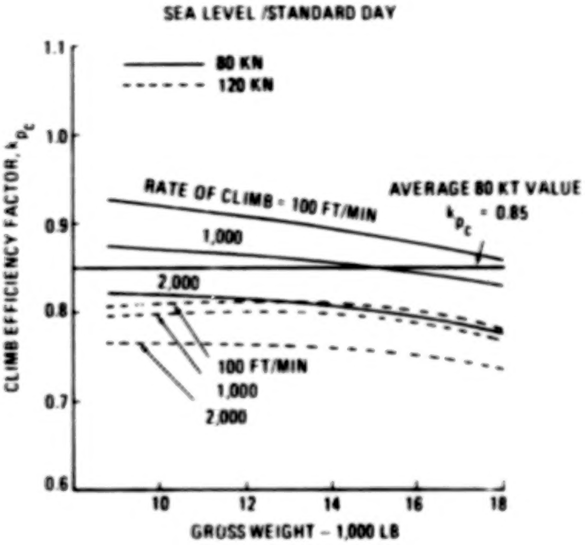

Figure 3.27 Climb efficiency factor

Power required at 100 fpm rate of climb is presented as a function of gross weight in Fig 3.28 to illustrate the application of the climb efficiency factor for minimum power speed (60 to 80 kn) in level flight. Here, it is shown that the incremental climb power at 15,000 lb is approximately 50 hp. The data is presented in the referred system for various ambient temperatures in order to illustrate compressibility effects at minimum power airspeeds, which can have an effect on service-ceiling calculations. For example, dual-engine operations at altitudes close to the service ceiling are often performed at low air densities and temperatures. This results in high rotor coefficients (C_T/σ) combined with increased advancing-blade Mach numbers.

5.2 Descent Power Required

Descent performance is treated as a negative rate-of-climb calculation. In descent, the induced velocity term in Eq (3.24) is less than 1.0, and the download and tail rotor power required are lower than in level flight. The result is that at autorotational rates of descent, $k_p \approx 1.0$ or even higher. For this reason, instead of being called an *efficiency* factor, it will be referred to as a descent *correction* factor (k_{p_d}) when applied to the potential energy expression in subsequent discussions.

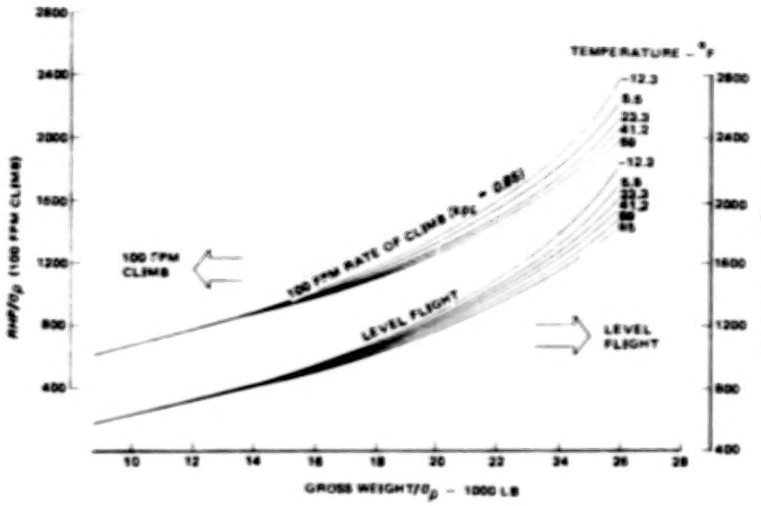

Figure 3.28 Hypothetical helicopter minimum power required

Based on the trim analysis program, sample calculations of the descent factor as a function of gross weight for the hypothetical helicopter at airspeeds of 80 to 120 kn are presented in Fig 3.29. Here, $k_{pd} = f(W)$ is shown for partial-power descent at rates of 500 and 2000 fpm. Boundaries defining autorotational rates of descent are also indicated. The autorotational rate of descent used to compute k_{pd} values varies with weight, and is determined for a given weight by plotting power required as a function of the descent rate and noting its value at zero power required. At 15,000 lb gross weight, the factor varies from $k_{pd} = 0.9$ at 500 fpm, to $k_{pd} = 1.0$ at 2000 fpm. Below a descent rate of 500 fpm, the same values as those for the average climb efficiency factor; i.e., $k_{pc} = 0.85$, can be used with reasonable accuracy to compute descent performance. At autorotational rates of descent, $0.9 \leqslant k_{pd} \leqslant 1.0$, and does not change significantly with airspeed. It appears that $k_{pd} = 1.0$ represents a good autorotational value and has been used successfully to predict the autorotational performance of tandems as well as single-rotor aircraft, as verified by flight-test measurements.

Empirical data indicates that k_{pd} increases rapidly as forward speed approaches zero. Values of well over 2.0 were recorded in vertical descent for isolated rotors. These high values are primarily due to the adverse effects of operating in the vortex ring state[14].

6. LEVEL FLIGHT AND MANEUVER AIRSPEED ENVELOPE

The level flight speed and maneuver capability of a helicopter is usually limited by one or more of the following items:

(1) power available
(2) transmission (torque) limits
(3) excess vibration/structural limits not related to stall
(4) compressibility effects on advancing blade
(5) stall inception.

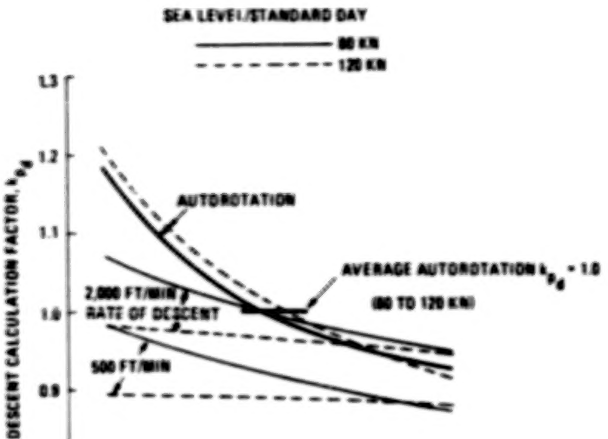

Figure 3.29 Descent calculation procedure

The power available and transmission limits were discussed briefly in Ch I, and further details will be provided in Sect 7 (Performance Capability). The third item, excess vibration/structural limits, is not a consideration for new designs because the dynamic system and airframe are (theoretically) designed to avoid this type of restriction.

Compressibility effects on the advancing blade pitching moment is another potential structural limitation. As pointed out by Dadone[15]

> *Only relatively recently the growth of pitching moments with Mach number has become a significant parameter. This has occurred with the introduction of cambered airfoils and structurally softer blades. The phenomenon has been referred to as "pitching moment break" or, borrowing the term from fixed-wing terminology, "Mach tuck." Essentially, this growth in pitching moment coincides with the onset of transonic flow conditions and it is associated with both a rearward shift in the aerodynamic center and an increase in pitching moments about the aerodynamic center.*

The development of pitching moment break along with other compressibility effects can be delayed by reducing the relative thickness and camber of the tip airfoil section, while deflecting the trailing edge tab upward would cause a general reduction of the negative pitching moment (see Ch VI, Vol I).

The remaining airspeed limitation criterion (rotor limits due to stall inception) is the primary constraint of the airspeed-altitude envelope for new helicopters. It is associated with the high alternating control system loads, and deterioration in stability and control resulting from retreating blade stall. For single-rotor helicopters such as the hypothetical aircraft, the effect of stall on component stress levels, rather than flying quality deterioration which may appear at the occurrance of stall, is generally the limiting criterion. Tandems are more prone to flying quality stall limitations since they chiefly depend on differential thrust between the forward and aft rotors for longitudinal control.

The methodology used to estimate rotor flying speed limitations resulting from control loads is discussed in the following sections. Included are sample calculations of the level-flight envelope and maneuver capability of the hypothetical helicopter based on model rotor test data.

6.1 Rotor Stall Limits Methodology

Level-flight rotor limits are encountered because of the development of stall on the retreating blade ($240 < \psi < 300°$). As the blade enters and leaves this region, the section pitching moment decreases abruptly due to moment stall of the airfoil section, and thus induces the aeroelastic phenomena known as stall flutter. Moment stall causes spikes in the blade torsional waveform as illustrated in Fig 3.30. The rate of growth of the peak alternating control loads is also shown in this figure. Therefore, operating the rotor at thrust or airspeeds beyond stall inception results in loads which build up quickly to the fatigue or endurance limit of the rotor control system because of the high alternating torsional laods feed directly into the system. This limitation has been the primary factor in defining helicopter structural envelopes. The rapid growth of the control loads after stall inception also restricts the amount by which the original envelope can be enlarged by strengthening the control system. For this reason, the structural flight envelopes of growth aircraft are often inside their power limits[16].

The endurance limit is defined as the maximum alternating load that can be sustained by a component for an indefinite number of cycles without fatigue failure. For instance, the CH-47C limit corresponds to approximately three times the unstalled alternating control load (Fig 3.30). However, with the increased requirements for highly maneuverable aircraft, a finite component life (typically, 4000 to 5000 hours) is accepted, thus allowing operation for a given percentage of time beyond the endurance limit.

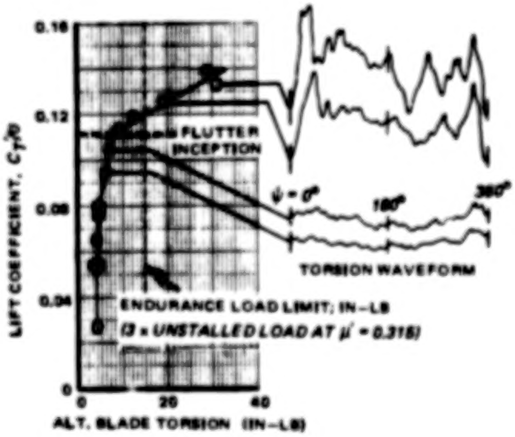

Figure 3.30 Stall flutter boundary determination

Various methods are used throughout the industry to define the rotor stall limits. These techniques include (1) nondimensionalizing flight test or wind-tunnel test data, and (2) pure theoretical rotor system loads and performance prediction programs. Currently, most companies rely on flight-test or wind-tunnel empirical techniques, since purely analytical stall load predictions have not been sufficiently developed to warrant their use as the primary means of determining rotor limits.

Use of Flight Test Data to Define Rotor Limits. Flight-test measurements of control system loads are used to detect stall inception and to define the rate of load growth in stall. The thrust and airspeed envelope determined by either the stall inception or endurance limit criteria can be nondimensionalized in terms of rotor-lift coefficient C_T/σ and μ where $C_T/\sigma = W/\rho\pi R^2\ V_t^2\sigma$. These two parameters can be used to predict the stall limits of other aircraft, provided the new helicopter design has a similar airfoil section, nondimensional propulsive force $\overline{X} = f_e/d^2\sigma$, and tip speed. An example of the nondimensional flight envelopes of some current production aircraft based on test data is presented in Fig 3.31. The data is based on level-flight airspeed limits published in military flight manuals for SL/STD ambient conditions.

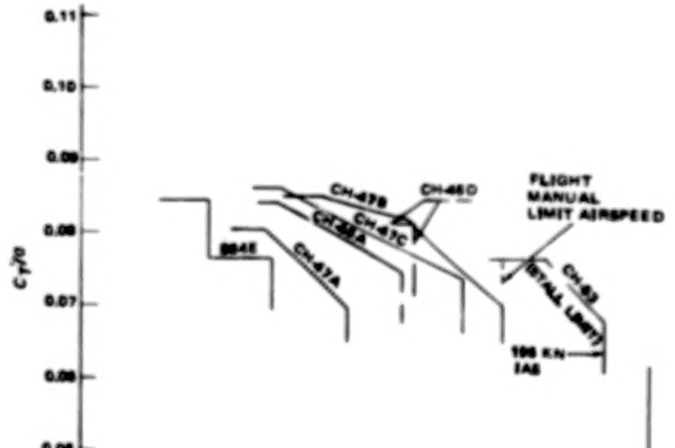

Figure 3.31 Nondimensional flight envelope limitations

The C_T/σ versus μ method of nondimensionalizing test data does not account for differences in blade torsional characteristics. To account for these effects, a second technique generalizing test-measured stall inception boundaries[17] was developed. Basically, this method establishes the stall limits in terms of a stall flutter parameter (SFP) and the retreating blade angle-of-attack, $\alpha_{(t)270}$. The SFP is an empirical quantity relating blade torsional properties to $\alpha_{(t)270}$ at given μ and V_t as well as air density corresponding to stall inception of the test aircraft. Here, $\alpha_{(t)270}$ is determined from the trim analysis computer program. SFP is also used to relate the stall limits of one aircraft to the rotor systems of other aircraft having the same airfoil. The advantage of this approach is that it automatically accounts for variations in $\bar{\lambda}$, however, based on recent studies, the validity of the torsional parameter is questionable as this approach is very sensitive to the aerodynamic model used to represent the blade.

A third method of generalizing test data is to correlate the inception of stall observed in flight test with predicted increases in inplane torque levels which occur at particular azimuthal positions[18]. The inplane torque per blade rises abruptly as the blade enters the stall region, due to increased drag on the outboard section of the blade. By comparing test and theoretical torque predictions, a nondimensional empirical stall parameter (*QSP*) can be defined as shown below:

$$QSP = bC_{Q_d}/\sigma \tag{3.25}$$

where

b = number of blades

σ = rotor solidity

$C_{Q_d} = (\sigma/2b)\int_0^{1.0} c_d \bar{U}_\perp^2\, \bar{r}\, d\bar{r}$ = profile drag torque coefficient per blade

$\bar{U}_\perp = U_\perp/R\Omega$ = component, perpendicular to the blade span, of the resultant inplane velocity at station $\bar{r}$, where $\bar{r} = r/R$.

This parameter can then be combined with theoretical rotor analyses to predict the stall boundaries of other rotor designs. A value of $0.0035 \leq QSP \leq 0.004$ has been shown to agree with test measurements of stall inception. One advantage of this technique is that it accounts for the stall and compressibility effects that occur in the third quadrant ($180° < \psi < 270°$) and is not limited to one azimuth angle ($\psi = 270°$) as in the SFP approach.

Development of Rotor Limits from Wind-Tunnel Test Data. Model data is often used to evaluate incremental variations in rotor limits due to blade geometry changes, airfoil section modifications, etc. In this respect, trends in performance improvements detected in the wind tunnel will also probably be found in full-scale aircraft in spite of the difference in Reynolds number values. However, a more careful interpretation of the influence of the Reynolds number levels should be applied when model tests are used to define the absolute stall flutter limits of new rotor designs.

The primary advantage of model testing is that the model can be "flown" well into stall under controlled conditions to provide sufficient data to accurately define both stall inception and endurance limits. The amount of full-scale flight-test data obtained beyond stall is generally limited by safety, vibration, weight, and power available restrictions.

The methods of nondimensionalizing wind-tunnel test data are identical to the flight-test techniques outlined in the previous section. Blade torsional loads or pitch-link loads are recorded until stall is observed. The inception points are then nondimensionalized; i.e., generalized, in terms of (1) C_T/σ and μ, (2) stall flutter parameter, or (3) the inplane torque parameter. It should be noted that when using wind-tunnel data to define absolute stall boundaries, no corrections to the model data for Reynolds number effects are currently applied; thus providing a degree of conservatism. As shown in Fig 3.32, comparisons of stall flutter boundaries based on full-scale flight tests of the 60-ft diameter CH-47C and 44-ft diameter H-21 rotor with those obtained from a 6-ft diameter model tested at the same tip speed show no significant Reynolds number effect for advance ratios of 0.2 to 0.4[16]. These results are attributed to the unsteady turbulent aerodynamic environment in forward flight which increases the effective Reynolds number of the model rotor. However, additional analyses and testing are required to fully understand Reynolds number effects.

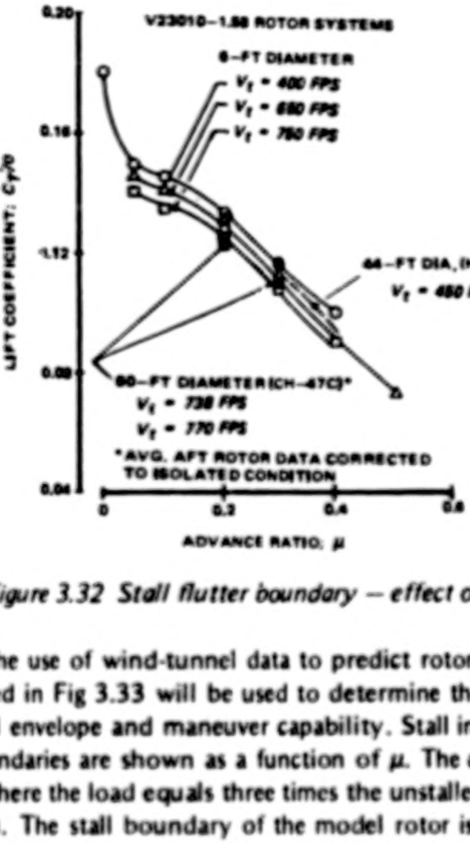

Figure 3.32 Stall flutter boundary – effect of scale

To illustrate the use of wind-tunnel data to predict rotor limits, the 6-ft diameter model data presented in Fig 3.33 will be used to determine the hypothetical helicopter level-flight structural envelope and maneuver capability. Stall inception and hypothetical endurance limit boundaries are shown as a function of μ. The endurance limit is defined as the C_T/σ value where the load equals three times the unstalled alternating loads (based on CH-47 test data). The stall boundary of the model rotor is corrected for propulsive force and tip speed differences between the model and full-scale rotor configurations. The level-flight structural envelopes developed in Sect 6.2 are based on the endurance limit boundary reduced 10 percent (thrust decrease at constant μ) in order to provide some margin for turbulence encountered in normal operation.

An additional boundary defined for a 2-g banked turn maneuver is also shown in Fig 3.33. The difference between the 1-g and 2-g boundary is the effect of pitch rate alleviation. The pitch rate generated in a banked turn permits a small amount of lift offset to occur, thus unloading the retreating blades slightly and extending the boundary. More details concerning the calculation of pitch rate effects will be presented later in Sect 6.3.

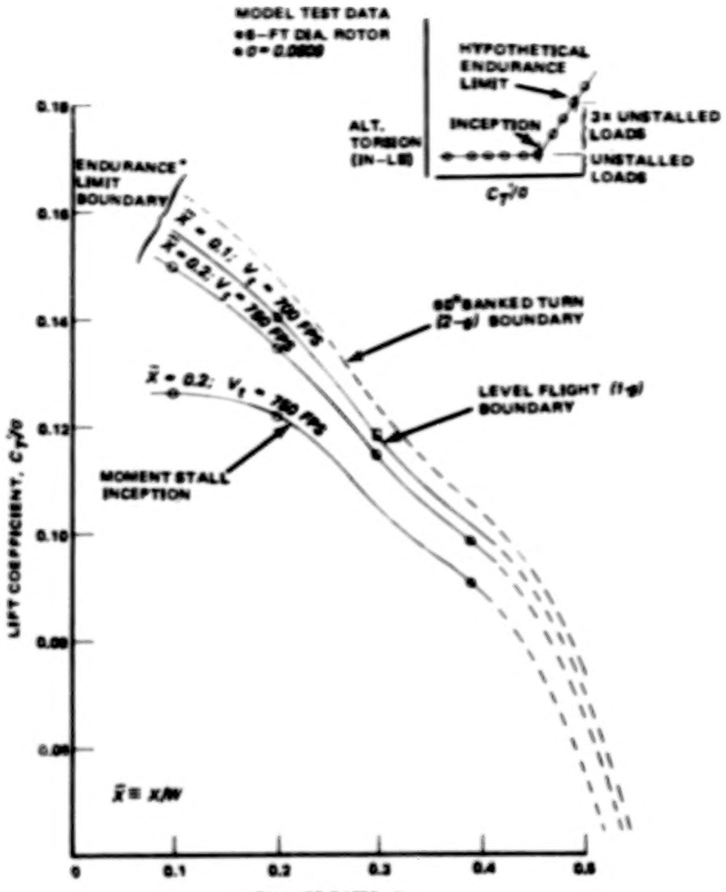

*HYPOTHETICAL ENDURANCE LIMIT - 3 TIMES UNSTALLED ALTERNATING TORSIONAL LOAD

Figure 3.33 Hypothetical helicopter moment stall limits

Theoretical Loads Prediction Computer Programs. It should be emphasized that theoretical methods of determining rotor stall boundaries from blade-load analysis have not, as yet, reached the state-of-the-art where they can be utilized as the sole means of defining structural flight-envelope limits. Consequently, the empirical methods described above are the primary means used to establish these boundaries for new aircraft. The difficulty in developing theoretical loads analysis lies in the establishment of a truly representative mathematical model, reflecting the complex unsteady aerodynamic environment and its interaction with blade elastic properties[19]. Although much work remains to be done, some progress has been made[20,21].

The latest loads prediction computer programs include shed and trailing vortex wake representations as well as elastic blade effects. Typically, a skewed helical trailing vortex system is used to account for the spanwise variation in lift. Shed vorticity (Fig 3.34) due to the azimuthal variation of lift is defined mathematically by applying Theodorsen's relationships of unsteady aerodynamics[22] to the helicopter rotor.

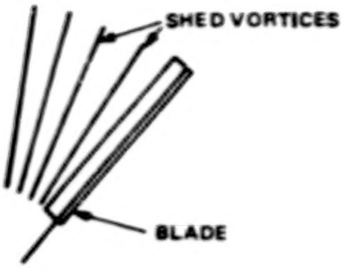

Two additional factors having a significant effect on stall inception and the resulting unsteady aerodynamic load growth are dynamic stall and spanwise flow. Consequently, they have been incorporated in the loads prediction programs.

Figure 3.34 Shed wake pattern

Dynamic effects alter the static airfoil-section stall characteristics. Due to blade flapping or pitching motion, the local blade section angle-of-attack and pitch rate vary periodically with the azimuth angle (Fig 3.35).

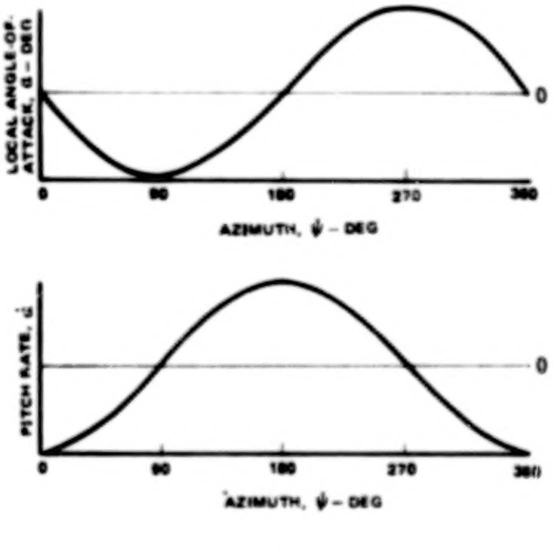

Figure 3.35 Variation of local angle-of-attack and pitch rate with the azimuth

Positive pitch rates are developed over the aft section of the rotor disc, and negative pitch rates over the forward section. Two-dimensional oscillating airfoil wind-tunnel tests[22] have shown that as the blade section angle-of-attack approaches stall, a hysteresis effect occurs which delays the stall at positive pitch rates ($\dot{\alpha}$) and promotes stall at negative values as shown in Fig 3.36.

The increase in two-dimensional airfoil stall angle-of-attack for both moment stall and lift stall for the V23010-1.58 airfoil section at $M = 0.4$ is shown in Fig 3.37 as a function of the nondimensional pitch rate factor $\sqrt{c\dot{\alpha}/2V}$. A physical interpretation of $\sqrt{c\dot{\alpha}/2V}$ can be obtained by noting that c/V is approximately the time it takes for a particle of

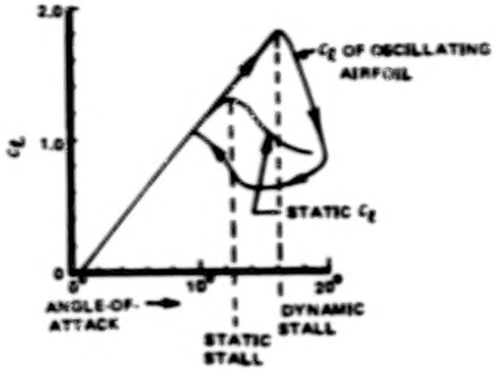

Figure 3.36 Effect of pitch oscillation on stall

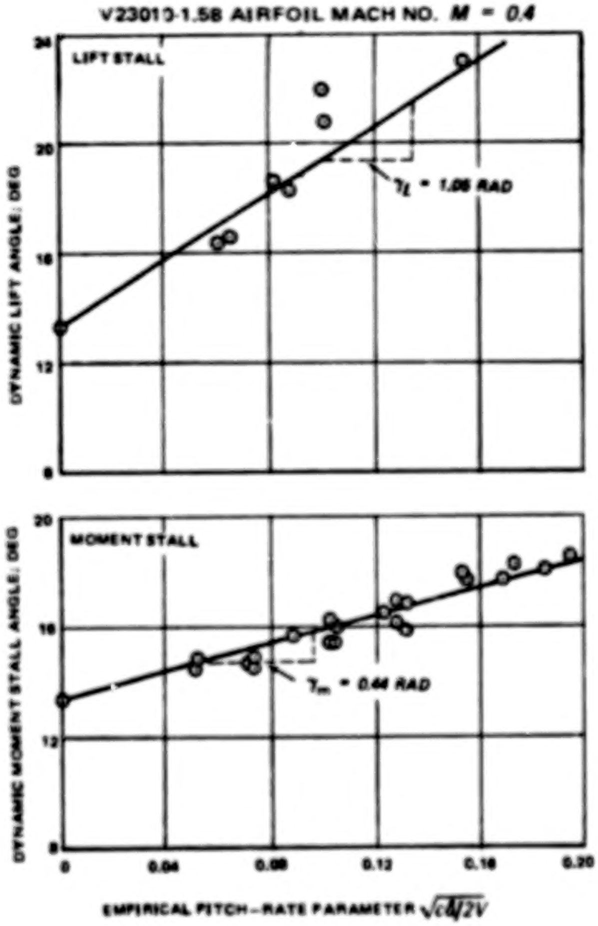

Figure 3.37 Dynamic stall angle vs nondimensional pitch rate factor

of air to travel from the leading edge to the trailing edge of the airfoil and is therefore, a measure of the time it takes for stall to fully develop. Hence, the term $\dot{\alpha}(c/V)$ is the $\Delta\alpha$ that can occur before stall effects become significant. The pitch rate has more effect on lift stall than on the moment stall which casues high control loads. Furthermore, the beneficial effects of $\dot{\alpha}$ on retarding the stall are reduced at higher Mach numbers, as illustrated in Fig 3.38, where the stall delay function $\gamma = \Delta\dot{\alpha}_{stall}/\Delta\sqrt{c\dot{\alpha}/2V}$ is a function of

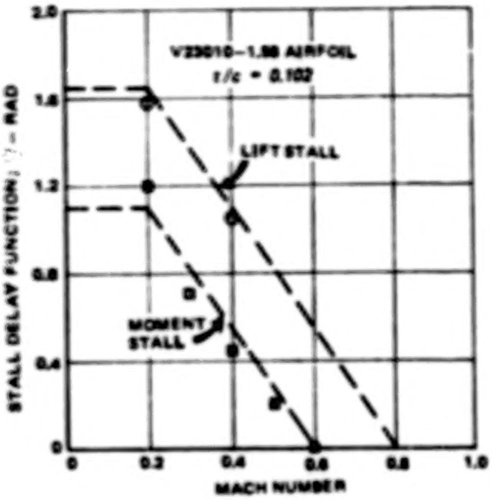

Figure 3.38 Effect of compressibility on stall delay function

Mach number. The parameter γ is simply the slope of the graph presented in Fig 3.37 which is applied to two-dimensional static airfoil data in order to incorporate oscillating airfoil effects in existing rotor analyses, as described in Ref 22.

The other factor identified as having a significant effect on rotor stall is spanwise flow. The radial component of freestream velocity has usually been ignored in the past. However, the total velocity at each blade element is actually larger than the normal component, and it places the blades at an equivalent yaw angle. There are two basic effects of yawed or radial flow. First, the increase in actual velocity augments the section drag as explained in Ch III, Vol I. The second effect is to make the section-lift coefficients, $c_{\ell_{max}}$, referenced to inplane velocities normal to the blade span, appear higher than their actual three-dimensional values.

The effects of dynamic stall and yawed flow on thrust and power required predictions–discussed in detail in Ref 22–are illustrated in Fig 3.39[23]. The baseline theory, using static airfoil data, shows much higher thrust and power required penalties due to stall than indicated by the test data. Incorporating dynamic stall and yawed flow corrections in the analysis significantly improved the high thrust-level correlation. However, theoretical and experimental gaps still remain; for instance, an understanding of the effect of spanwise flow on the hysteresis loop of the unsteady airfoil data.

Improvements in the prediction of torsional load growth in stall have also been obtained. Fig 3.40 shows the correlation of the U.S. Government Program (C-81) with

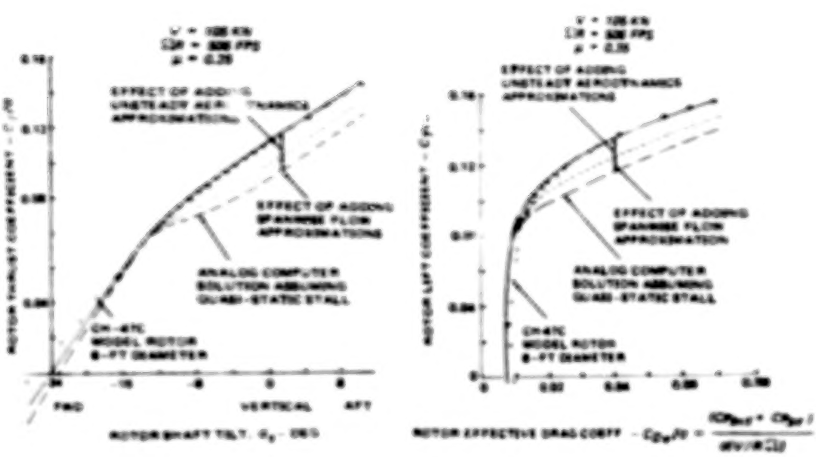

Figure 3.39 Predictions and tests of rotor thrust and lift coefficients

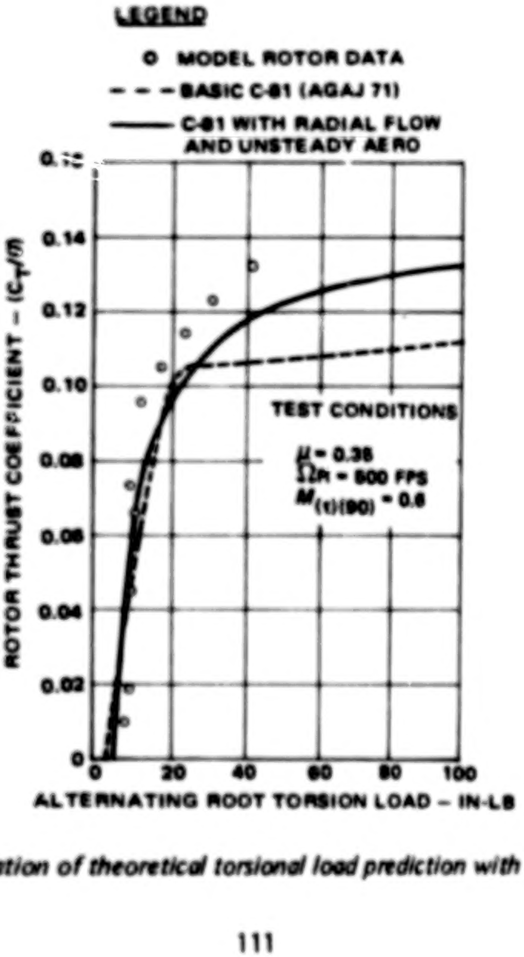

Figure 3.40 Correlation of theoretical torsional load prediction with model rotor data

flight-test data is presented in Figs 3.41 and 3.42. Additional discussions of these analytical techniques can be found in Refs 19, 20, and 21.

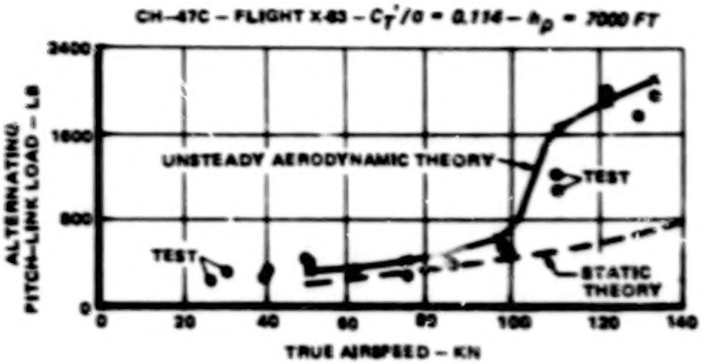

Figure 3.41 Comparison of test and computed pitch-link loads for an airspeed sweep

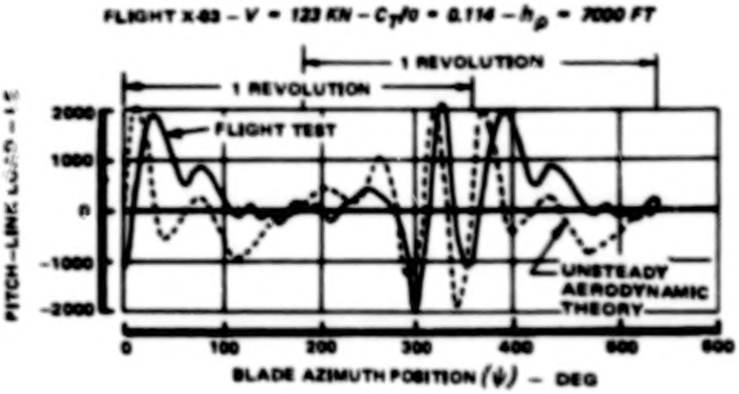

Figure 3.42 Pitch-link load waveform correlation using unsteady aerodynamic theory

6.2 Level-Flight Airspeed/Altitude Structural Flight Envelope

The structural envelopes of helicopters are generally presented as a function of density altitude as shown for the hypothetical helicopter in Fig 3.43. This envelope is based on the wind-tunnel model endurance limit boundaries given in Fig 3.33. The data is given with and without a 10-percent thrust margin to account for turbulence effects. It can be seen that the airspeed envelopes decrease rapidly with altitude due to the increase in rotor $\bar{c}_\ell$ for a given gross weight. Maximum continuous and intermediate power speed capability points at 15,000-lb gross weight are indicated for SL/STD and 4000 ft, 95°F ambient conditions. The aircraft does not have sufficient power in level flight to exceed the structural envelope at these conditions. This relationship between power

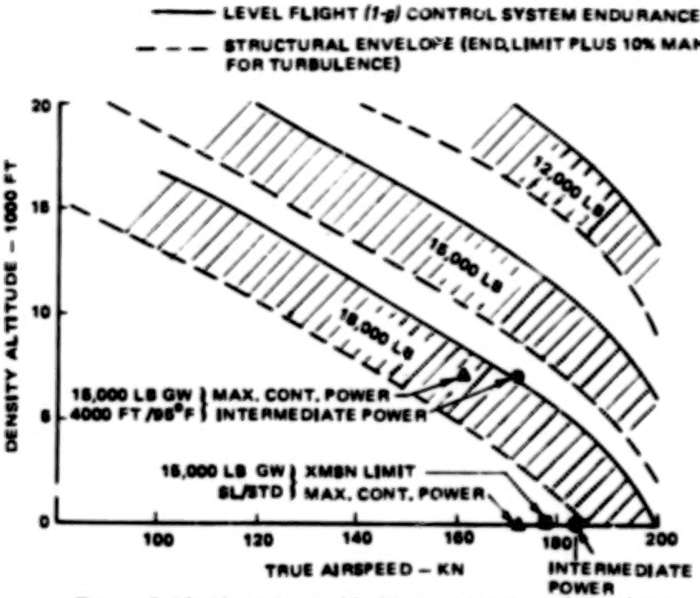

Figure 3.43 Hypothetical helicopter structural envelope

limits and structural limits is a desirable design feature as it reduces the risk of inadvertently operating beyond the structural envelope in level flight.

At high altitudes, the aircraft has sufficient continuous power to exceed the structural airspeed limits as shown in Fig 3.44 for standard day conditions and *W = 15,000 lb*. It is apparent that the structural airspeed decreases more rapidly with altitude than the corresponding power limit envelope.

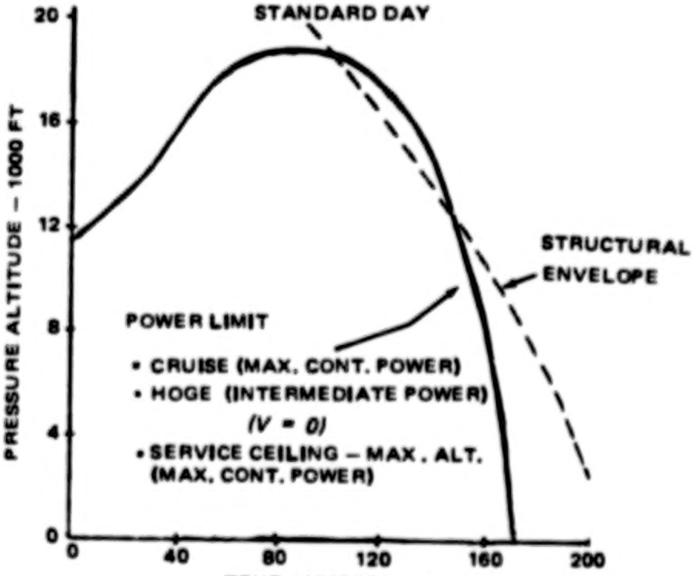

Figure 3.44 Flight envelope at 15,000-lb gross weight

6.3 Maneuver Capability

The current generation of military helicopters is designed to meet specific maneuver requirements such as contour flying where the aircraft operating close to the ground (50–100 ft altitude) must follow the contour of the terrain. In the past, much less emphasis was placed on maneuver capability. Consequently, rotors were sized for hover and cruise efficiency.

A maneuver is defined as *accelerated flight when acceleration* $a = (n - 1)32.2$, where n is the thrust-to-weight ratio (T/W) expressing the load factor, and 32.2 *ft/sec*^{2} is the acceleration of gravity. If the acceleration occurs normal to the freestream velocity, then the flight path will be curved, resulting in a pull-up or banked-turn type of maneuver. The acceleration in this case is centripetal, and is equal to V^2/R where R is the radius of the turn, or pull-up.

The hypothetical helicopter banked-turn maneuver capability at 15,000-lb gross weight and 4000 ft, 95°F is illustrated in Fig 3.45. It is assumed that structural loads during maneuvers cannot exceed the endurance limit (Fig 3.33). However, most of the currently designed helicopters have sufficiently severe maneuver requirements that the life of the components must be defined on the basis of a given percentage of time for operation beyond the endurance limit. The hypothetical helicopter has a 1.35-g rotor limit capability at 150 kn. However, the engine rating does not provide sufficient power to maintain the required thrust during maneuvers. Consequently, the extra energy must be provided by one of the following means:

(1) descent (potential energy)
(2) decreased rotor speed (rotational kinetic energy)
(3) deceleration (translational kinetic energy).

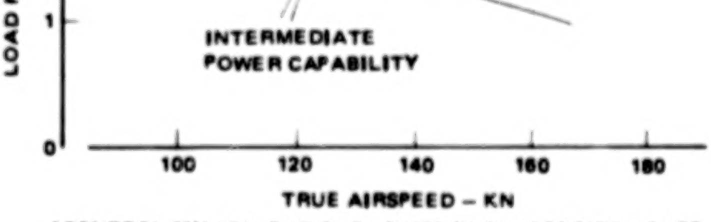

Figure 3.45 Maneuver capability

During contour-flying operations conducted at low altitudes, obviously neither descent nor rotor speed decay are acceptable. Consequently, deceleration must be used in maneuvering beyond the power limits. This will require reducing the forward speed by using cyclic control to tilt the tip-path plane aft. The deficiency in power available (ΔRHP) is compensated by a reduction in airspeed from the initial speed (V_i) to the final speed (V_f) as shown in Eq (3.26).

$$\Delta RHP = (1/1100)(W/g)(V_f^2 - V_i^2)\Delta t \tag{3.26}$$

where

Δt = time increment of the maneuver; s

V = velocity; fps.

Utilizing this type of analysis, time histories of aircraft deceleration, rotor decay, altitude, etc., can be developed. A detailed discussion of the energy tradeoffs during maneuvers is presented in Ref 24.

The rotor limits presented in Fig 3.45 is based on the maneuver C_T/σ boundaries given in Fig 3.33. The difference in level flight and banked-turn maneuver rotor limits is due to pitch rate alleviation (*PRA*) effects. As stated in Ref 25, positive helicopter pitch rates developed during symmetrical pull-ups or banked turns result in a favorable gyroscopic moment acting on the rotor system. This moment affects the blade flapping motion in such a way as to unload the retreating blade and delay the onset of stall. The blade flapping equations can be solved with and without PRA to obtain the corresponding incremental decrease in retreating blade tip angle-of-attack $\Delta\alpha_{(t)270}$.

$$\Delta\alpha_{(t)270} = \frac{-16q_r R}{\gamma(V_t - V)} \tag{3.27}$$

where

γ = blade Lock number $(\rho c_{\ell_\alpha} R^4)/I_b$

q_r = pitch rate (body axes reference system); rad/s

V_t = tip speed fps.

In this equation, the aircraft pitch rate during a banked turn (q_{r_b}) or cyclic pull-up (q_{r_p}) can be approximated by the following expressions[6,26]:

$$q_{r_b} = (32.2/V)[n - (1/n)] \tag{3.28}$$

$$q_{r_p} = (32.2/V)(n - 1) \tag{3.29}$$

where

n = load factor (g's)

V = airspeed; fps

Eqs (3.27)–(3.29) indicate that the stall benefits resulting from pitch rate decrease with increasing forward speed. In addition, the pitch rate and $\Delta\alpha_{(t)270}$ developed for a given load factor are larger for a banked turn than for cyclic pull-up. For example, the pitch rate generated during a 2g banked turn is 1.5 times the corresponding pull-up pitch rate.

The $\Delta\alpha_{(t)270}$ due to pitch rate effects must be combined with trim analysis $\alpha_{(t)270}$ predictions to obtain the incremental load factor increase (Δn) due to PRA, assuming that stall will occur at a given $\alpha_{(t)270}$ value during the maneuver. The graphical procedure for obtaining Δn is shown in Fig 3.46.

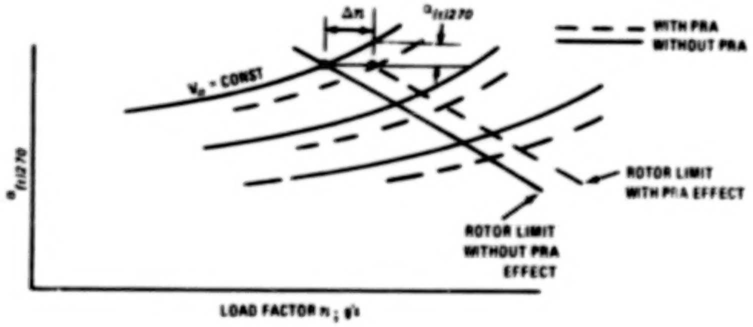

Figure 3.46 Determination of pitch rate alleviation (PRA) effects from trim analysis

The basic gyroscopic moment effects can also be included in the trim program flapping equations in order to account for power required as well as stall limit variations due to pitch rate effects.

7. CALCULATION OF FORWARD–FLIGHT PERFORMANCE CAPABILITY

The methodology for computing forward-flight performance capability as described in this section, applies to the following items:

(1) mission performance analysis
(2) payload/range
(3) payload/endurance
(4) ferry range
(5) speed capability
(6) climb capability
(7) service ceiling
(8) autorotation capability.

7.1 Mission Performance

Mission performance calculations involve computing the payload (cargo, passengers, equipment, etc.) that can be carried during a given mission. The payload (PL) is obtained by subtracting the weight of fuel (W_F) required, plus the weight empty (W_E), and fixed useful load (FUL) determined by the weight of crew plus trapped oil and fuel, from the takeoff gross weight ($TOGW$):

$$PL = TOGW - (W_E + FUL + W_F). \tag{3.30}$$

The maximum practical TOGW should be used to determine the maximum payload capability of an aircraft. The criteria used to determine this weight is a function of the type of takeoff site assumed for the mission. For example, if the takeoff area is surrounded by trees, a vertical climb capability is required; however, if the area is an open space, then the takeoff can be conducted from an IGE wheel height with a gradual transition to forward flight. Operating from helipads located on tops of buildings, oil rig platforms, forest clearings, or other confined areas may require alternate takeoff criteria. For most military missions, TOGW is based either on hover OGE capability at intermediate power, or a specified vertical rate-of-climb level at either intermediate or 95 percent of that power rating. These criteria provide a sufficient performance margin for defining a realistic takeoff weight.

The weight of fuel in Eq (3.30) depends on the type of mission being evaluated. Using the range mission as an example, the various segments of the profile shown in Fig 3.47 are as follows:

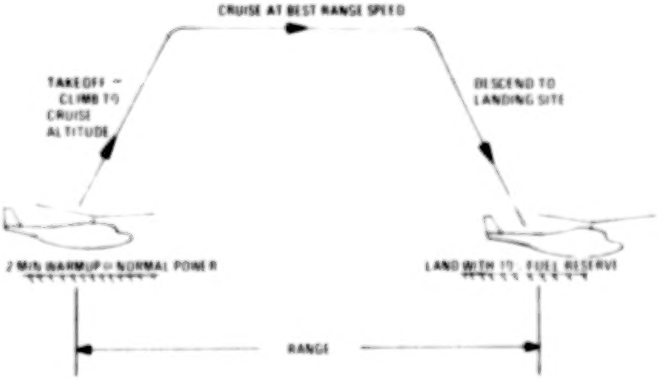
CRUISE AT BEST RANGE SPEED
TAKEOFF — CLIMB TO CRUISE ALTITUDE
DESCEND TO LANDING SITE
2 MIN WARMUP @ NORMAL POWER
LAND WITH 10% FUEL RESERVE
RANGE

Figure 3.47 Mission profile

(1) *Warmup* — Includes fuel consumed to start and check out the aircraft. A fuel allowance of two to five minutes at maximum continuous power is typical.

(2) *Takeoff* — The fuel required for takeoff and transition to forward flight is generally small enough to be neglected when calculating missions where the cargo or payload is carried internally. During missions where the cargo is carried externally, the hover fuel required for the hookup of the load can be significant.

(3) *Climb to Cruise Altitude* — For comparative performance calculations and for missions flown 1000–2000 ft above the takeoff site, climb fuel and distance are usually neglected. Cruise at higher altitudes will require consideration of the climb effect on fuel.

(4) *Cruise at Constant Altitude* — The cruise portion of the mission is generally conducted at airspeeds which provide the maximum range for a given quantity of fuel,

unless the aircraft is limited by power available or structural considerations. This speed is referred to as the *best range speed.*

(5) *Descent to Landing Site* – Because of the lower power settings in descent, the fuel used during this stage of the mission is considered negligible. In addition, no allowance is taken for distance traveled in descent, unless the cruise altitude is significant.

(6) *Landing with Fuel Reserve* – For internal cargo missions where no hover time is required for detaching loads prior to landing, the fuel required to land is negligible. However, it is assumed that the aircraft lands with a specific quantity of fuel reserve, which is typically 10 percent of the initial fuel quantity, or an allowance of sufficient fuel to either cruise at best range speed, or loiter at minimum power speed, for 20 to 30 minutes. The loiter time reserve is generally used for short missions where a 10-percent reserve would be insufficient.

The objective of the range mission is to maximize the distance traveled one way per given quantity of fuel. These missions are generally computed at constant altitude and optimum airspeed conditions; however, aircraft altitude as well as speed can be optimized to further increase the distance traveled. The altitude and airspeed optimization is usually reserved for *ferry-range missions,* discussed later in this section.

Maximum endurance represents another basic mission aimed at maximizing endurance or time on station rather than distance. This mission is typical of search and surveillance operations and is flown at minimum-power speeds (70 to 90 kn), where fuel consumption per unit of time is lowest.

There are many other derivatives of the range and endurance missions such as *radius missions* (cruise out, land, and unload part or all of the payload, and return), *antisubmarine (ASW), mine countermeasures (MCM),* and *vertical replenishments.* However, the basic calculation methods are essentially the same as the range and endurance procedures which are applied to each segment of the mission, while careful account of the fuel is maintained. For missions with more than one cruise segment, some iteration on the distribution of fuel may be required.

In this section, only the typical features of range (constant altitude), endurance, and ferry-range mission performance prediction techniques are presented, using the hypothetical helicopter to illustrate the methods. For a more detailed analysis, the reader is referred to a design handbook[26].

7.2 Payload/Range Capability

Weight empty (W_E) and fixed useful load (FUL) are functions of basic aircraft configurations and number of crew. For the hypothetical helicopter,

$$W_E = 9450\ lb$$

$$FUL = 430\ lb \text{ (2 crew @ 200 lb ea + 30 lb of trapped oil and fuel).}$$

Assuming 4000 ft/95°F ambient conditions, $TOGW_{max} = 16{,}000\ lb$, based on hover OGE capability at intermediate power (Fig 2.25). Substituting these values into Eq (3.30) gives

$$PL = 6120 - W_F.$$

The payload, therefore, decreases as the fuel weight increases until the internal fuel capacity is reached. Further increases in fuel capacity require the addition of auxiliary tanks, which increases the W_E as discussed in the Ferry Range section (6.4).

The tradeoff of payload for fuel and its subsequent influence on the payload-range relationship can be determined by first computing the *specific range* (n.mi/lb of fuel). The specific range is simply the cruise speed V in kn divided by the average fuel consumption $\dot{W}_F$ in units of lb/hr. Then, the incremental range (dR) becomes

$$dR = (V/\dot{W}_F)dW \tag{3.31}$$

where

V = airspeed (kn)

dW = incremental change in weight due to fuel burnoff (lb).

The *total range* in n.mi for a given quantity of cruise fuel (lb) is obtained from Eq (3.31) as

$$R = \int_{W_2}^{W_1} (V/\dot{W}_F)dW \tag{3.32}$$

where

W_1 = initial gross weight

W_2 = W_1 − *fuel burnoff.*

The integral in Eq (3.32) is normally evaluated by graphical methods. The range is equal to the area under a plot of specific range (SR) vs gross weight between the initial W_1 and the final W_2 gross weight after fuel burnoff (Fig 3.48). If the specific range data is reasonably linear between W_1 and W_2, this area can be computed by using the average SR. The $SR = f(W)$ plots are developed from the power required and the engine fuel flow

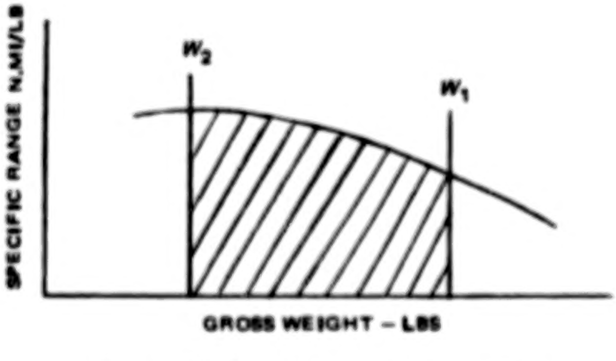

Figure 3.48 Specific range vs gross weight

characteristics at the desired cruise ambient conditions and cruise speeds. Range missions are usually computed at the speed for maximum range. The procedure for computing the best range speed and associated specific range is illustrated in Fig 3.49 (reproduced from Ref 26), and outlined below.

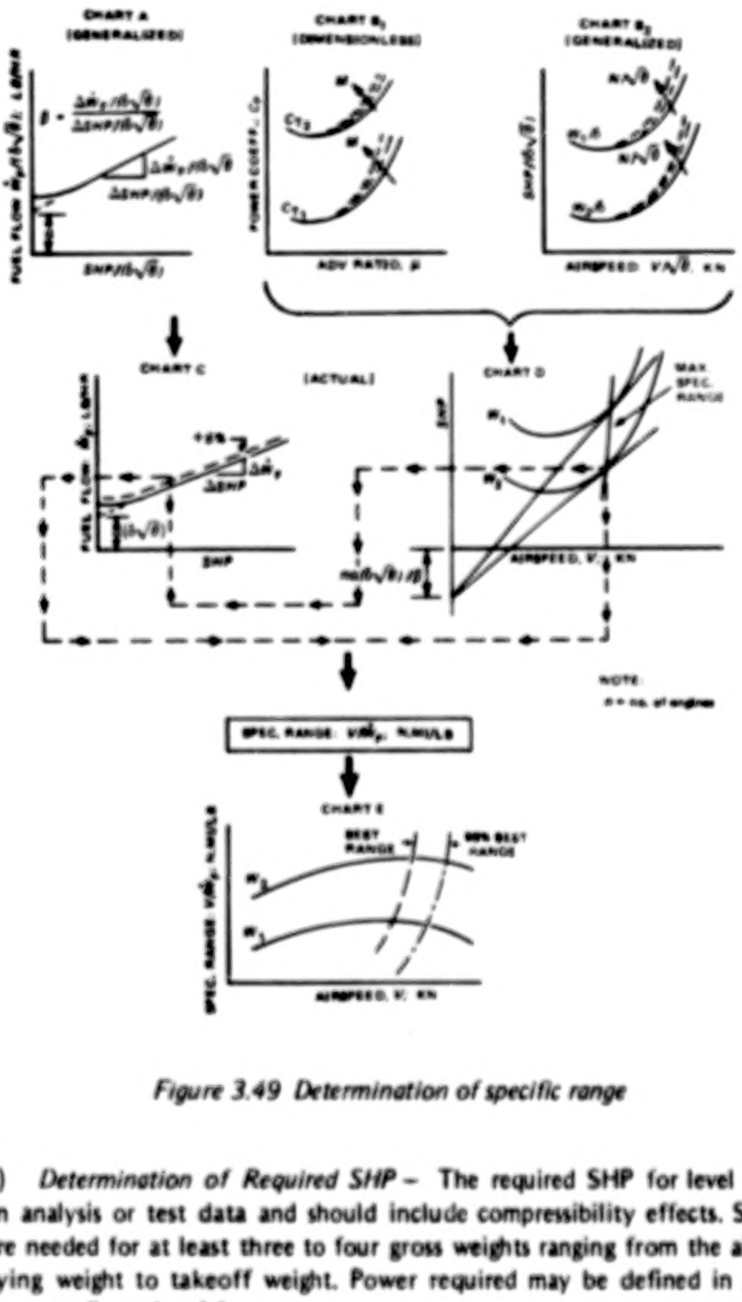
CHART A
(GENERALIZED)
FUEL FLOW $\dot{w}_F/(\delta_2\sqrt{\theta_2})$, LB/HR
$\beta = \frac{\Delta \dot{w}_F/(\delta_2\sqrt{\theta_2})}{\Delta SHP/(\delta_2\sqrt{\theta_2})}$
$\Delta \dot{w}_F/(\delta_2\sqrt{\theta})$
$\Delta SHP/(\delta_2\sqrt{\theta})$
$SHP/(\delta_2\sqrt{\theta_2})$
CHART B_1
(DIMENSIONLESS)
POWER COEFF., C_P
C_{T_2}
C_{T_1}
ADV RATIO, μ
CHART B_2
(GENERALIZED)
$SHP/(\delta_2\sqrt{\theta_2})$
$N/\sqrt{\theta}$
W_2/δ
W_1/δ
AIRSPEED, $V/\sqrt{\theta}$, KN
CHART C
(ACTUAL)
FUEL FLOW, $\dot{w}_F$, LB/HR
+5%
$\Delta \dot{w}_F$
ΔSHP
$(\delta_2\sqrt{\theta})$
SHP
CHART D
SHP
W_1
W_2
MAX.
SPEC.
RANGE
AIRSPEED, V_t, KN
$n\alpha(\delta_2\sqrt{\theta})/\beta$
NOTE:
n = no. of engines
SPEC. RANGE: $V/\dot{w}_F$, N.MI/LB
CHART E
SPEC. RANGE $V/\dot{w}_F$, N.MI/LB
BEST RANGE
99% BEST RANGE
W_2
W_1
AIRSPEED, V, KN

Figure 3.49 Determination of specific range

(1) *Determination of Required SHP* – The required SHP for level flight can be based on analysis or test data and should include compressibility effects. Speed-power polars are needed for at least three to four gross weights ranging from the aircraft minimum flying weight to takeoff weight. Power required may be defined in generalized, referred, or nondimensional form.

(2) *Calculation of Fuel Flow vs Airspeed* – For two-engine aircraft, the SHP required is assumed to be equally divided between the engines. The total fuel flow is calculated using the engine manufacturers' fuel flow vs power relationships at the correct ambient conditions which are usually accounted for by generalized fuel flow ($W_F/\delta\sqrt{\theta}$) and SHP ($SHP/\delta\sqrt{\theta}$) data (Ch I, Sect 3). For many applications, the engine manufacturers' fuel flow is increased 5 percent to account for differences between production engines, variations due to different pilot operating techniques, and engine performance degradation in service. The 5-percent fuel flow adjustment may also be employed when power required estimates are based entirely on theory.

(3) *Computation of* $SR = f(V)$ – The specific range, $SR = V/W_F$ (n.mi/lb), is computed for each weight and plotted as a function of airspeed. The resulting curves reach a maximum, or best range value, at one airspeed. However, the mission cruise speed is generally defined as that corresponding to $0.99(SR)_{max}$. Since the specific range curve is relatively flat near the best range speed, the one-percent loss in range will result in a six or seven-percent increase in cruise speed and a corresponding reduction in mission time. For this reason, almost all best range performance is actually defined at the 99-percent best range conditions.

(4) *Check of Power Available and Structural Airspeed Limits* – The maximum continuous power, transmission, stall, and structural envelope limitations can be indicated on the $SR = f(V)$ graph to determine whether the best range speeds are within the aircraft flying envelope. Many times, an aircraft can fly at best range speeds at low gross weights, but at high weights, is limited to lower speeds.

(5) *Determination of the Final Specific Range vs Gross Weight* – This is done by cross-plotting the specific range data as a function of gross weight.

Step-by-step calculations of specific range for the hypothetical helicopter at 15,000 lb gross weight and 4000 ft/95°F cruise condition is shown in Table III-4. The graphs presented in Figs 3.50 and 3.51 were developed by repeating this procedure for three other weights.

① AIRSPEED V; kn	80	100	120	140	160	170
② SHP_{req} (Fig 3.24)	920	940	1060	1316	1820	2280
③ SHP per engine = ②/2	460	470	530	657	910	1140
④ $SHP/\delta\sqrt{\theta}$ = ③ $/\delta\sqrt{\theta}$*	516	526	594	738	1020	1279
⑤ $\dot{W}_F/\delta\sqrt{\theta}$; lb/hr (Fig 1.7)	381	382	408	456	560	668
⑥ $\dot{W}_F$ per engine = ⑤ × $\delta\sqrt{\theta}$; lb/hr	341	341	365	407	500	596
⑦ $\dot{W}_F$ (2 engines + 5% sfc increase) ⑥ × 2.1; lb/hr	714	715	766	854	1049	1252
⑧ Specific Range SR = ①/⑦; n.mi/lb	0.112	0.140	0.158	0.164	0.152	0.136
NOTE: * $\delta\sqrt{\theta}$ = 0.8932						

TABLE III-4 CALCULATIONS OF SPECIFIC RANGE AT 15,000 LB; 4000 FT/95°F

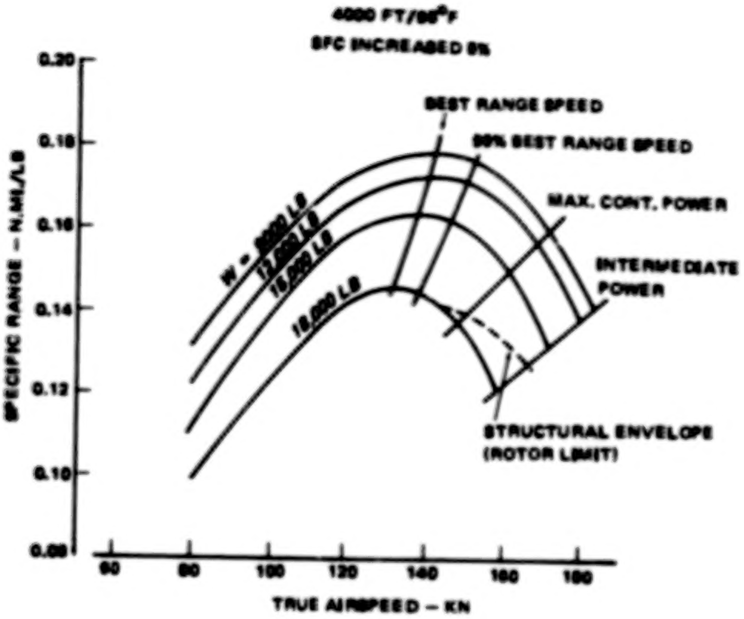

Figure 3.50 Specific range

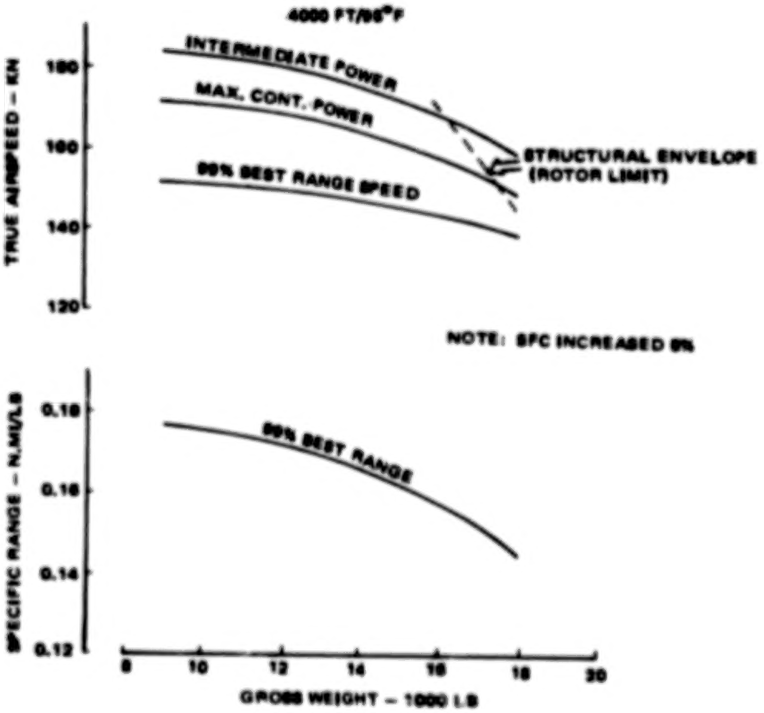

Figure 3.51 Cruise performance

The airspeed for 99-percent best range speed is approximately 7 percent higher than the 100-percent best range values, and is considerably below normal power and structural envelope limits.

Utilizing the specific range curve in Fig 3.51, the mission fuel in Eq (3.30) can be converted to range; leading to a plot of payload vs range (Fig 3.52). Here, the maximum payload at zero range is approximately 6100 lb, and decreases as the fuel required increases with range until the permanent tank fuel capacity is reached. Then, the TOGW must be reduced, or auxiliary tanks must be added to increase the range. The payload and range capability can be determined from this plot for any combination of gross weight and fuel quantity up to the maximum takeoff weight and internal fuel capacity.

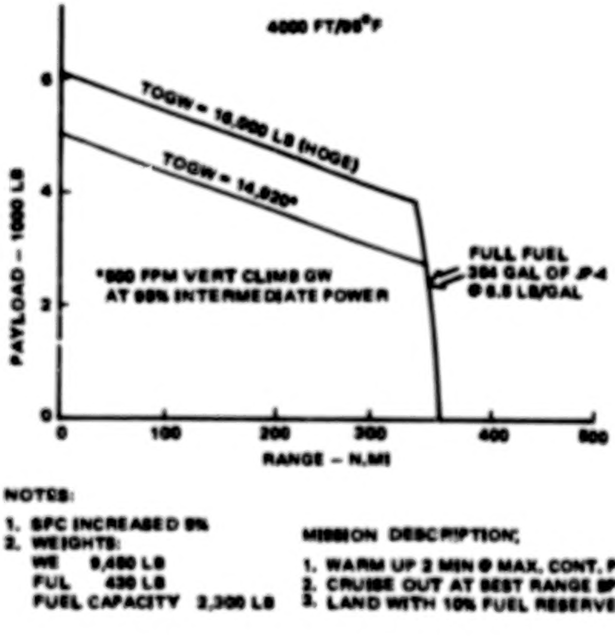

NOTES:

1. SFC INCREASED 5%
2. WEIGHTS:
   WE 9,450 LB
   FUL 430 LB
   FUEL CAPACITY 2,300 LB

MISSION DESCRIPTION:

1. WARM UP 2 MIN @ MAX. CONT. POWER
2. CRUISE OUT AT BEST RANGE SPEED
3. LAND WITH 10% FUEL RESERVE

Figure 3.52 Hypothetical helicopter payload/range capability

A line representing a 500-fpm vertical rate of climb takeoff criteria at 95-percent intermediate power corresponds to *TOGW ≈ 15,000 lb*. This takeoff performance was used to determine the hypothetical helicopter design gross weight since it is representative of current U.S. Army takeoff criteria.

The payload/range curve is determined by first computing the zero and full-fuel points at the maximum takeoff gross weight of 16,000 lb, and connecting the points with a straight line. Intermediate points should be computed using an iterative technique, since neither the payload nor the range is fixed for these calculations. These points, however, do not deviate sufficiently from a straight-line interpolation to justify the additional calculations. The last step is to compute two additional points along the full-fuel line; one intermediate and another, at the zero payload point.

The calculation of payload and range for these points requires a step-by-step accounting system to keep track of the gross weight and fuel weight throughout the mission. Generally, a detailed tabulation sheet similar to the one shown in Table III-5 is used. The sample calculations shown on this sheet use the specific range data presented in Fig 3.51 for the mission described in Fig 3.52.

PROCEDURE	ZERO RANGE	FULL FUEL CONSIDERATIONS		
	PL_{max} $(TOGW_{max})$	PL_{max} $(TOGW_{max})$	ZERO PL	$PL = 0.5PL_{max}$
PAYLOAD CALCULATIONS; lb				
1 Weight Empty	9,450	9,450	9,450	9,450
2 Fixed Useful Load	430	430	430	430
3 Total Fuel[1] = *13*	40	2,300	2,300	2,300
4 PAYLOAD = 5 − (1 + 2 + 3)	6,080	3,820	0	1,910
5 Takeoff Gross Weight	16,000	16,000	12,180	14,090
6 Warmup, 2 min @ max cont[2]	36	36	36	36
7 Gross Weight = *5 − 6*	15,964	15,964	12,144	14,054
8 1/2 Cruise Fuel = *16/2*	0	1,017	1,017	1,017
9 Avg Gross Wt = *7 − 8*	15,964	14,947	11,127	13,037
10 Remaining Cruise Fuel = *16/2*	0	1,017	1,017	1,017
11 Landing Weight = *9 − 10*	15,964	13,930	10,110	12,020
12 *WE + FUL = 11 − (4 + 15)*	9,880	9,880	9,880	9,880
FUEL ANALYSIS; lb				
13 Total Fuel	40	2,300	2,300	2,300
14 Warmup Fuel	36	36	36	36
15 Reserve Fuel = 0.1 x *13*	4	230	230	230
16 Cruise Fuel = *13 − (14 + 15)*	0	2,034	2,034	2,034
RANGE CALCULATION:				
17 *SR* @ Avg *W* (Fig 3.50) (n.mi/lb)	–	0.1627	0.1736	0.1690
18 RANGE = 17 x 16 (n.mi)	0	331	353	344

NOTES: 1. *Specific Fuel Consumption increased 5 percent*

2. *Mission Description:*

   a. Warmup: 2 min @ maximum continuous power

   c. Land with 10 percent fuel reserve

[1] *Full Fuel Weight = 354 gal x 6.5 lb/gal = 2300 lb*

[2] *Warmup fuel calculation at 400 ft/95°F:* $\dot{W}_f$ = *1070 lb/hr (2 engines @ max cont Power)*
Fuel for 2 min = 36 lb

TABLE III-5 PAYLOAD–RANGE CALCULATIONS @ 4000 FT/95°F

The trend of the specific range data with weight is assumed to be sufficiently linear to utilize the mission mid-point weight and associated specific range to compute the total range capability – an exception to this approach would be when constraints such as rotor stall reduces specific range at high gross weights early in the mission; in which case, a segmented mission analysis should be used. The calculations continue until the landing weight is obtained. The fuel reserve and payload is then subtracted from the landing weight as shown in Step 12 of Table III-5. This weight should be equal to $W_E + FUL$.

7.3 Payload/Endurance Capability

Endurance missions require maximum time on station for the purpose of surveillance, loiter, search and destroy, etc. The payload for these missions usually consists of electrical equipment or external armament (torpedoes, missiles, etc.).

Maximum endurance is obtained at the minimum engine fuel flow ($\dot{W}_{F_{min}}$). By calculating $dSHP/dV = 0$ and solving for V, it can be shown that minimum fuel flow vs SHP curve is linear in the range of SHP considered. In most cases, the engine fuel flow is essentially linear over the small range of power required defining the speed power polar "bucket." The exact expression for maximum endurance (t_{max}) is

$$t_{max} = \int_{W_2}^{W_1} (1/\dot{W}_{F_{min}})dW \tag{3.33}$$

where

W_1 = initial gross weight

$W_2 = W_1$ – *fuel burnoff.*

This integral can be evaluated graphically, since the endurance is equal to the area under the plot of $1/\dot{W}_F$ vs gross weight between W_1 and W_2 (Fig 3.53). If $[1/\dot{W}_F = f(W)]$ is linear between W_1 and W_2, then the endurance is computed bydividing the available loiter fuel by the fuel flow at the average mission weight. Otherwise, the area must be divided into small segments and the Δt of each segment added to get the total endurance.

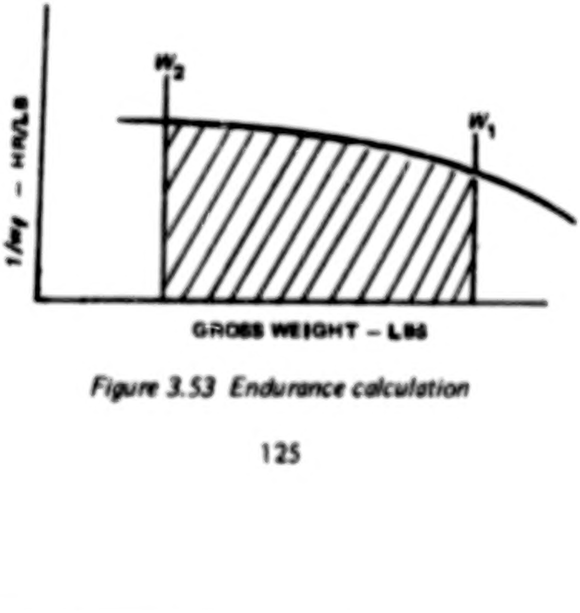

Figure 3.53 Endurance calculation

The procedure for calculating maximum endurance fuel flow is illustrated in Fig 3.54 and outlined below.

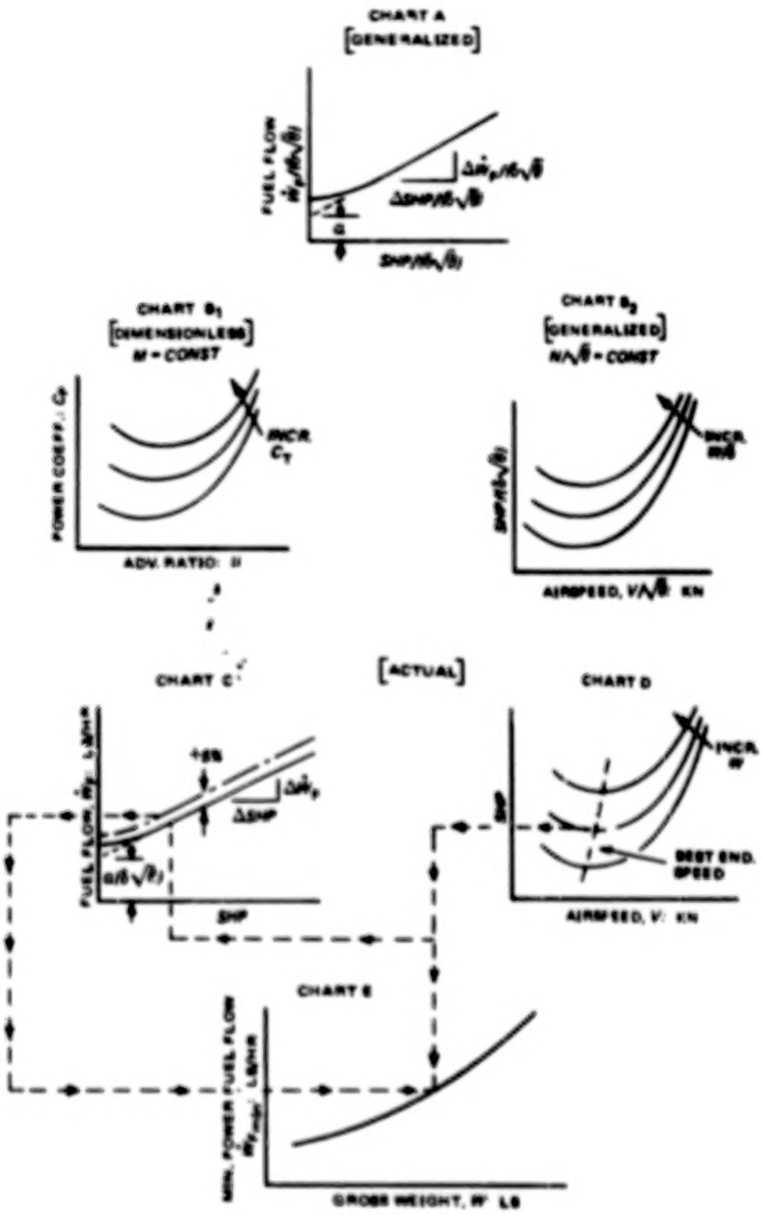
CHART A
[GENERALIZED]
FUEL FLOW $\dot{w}_f/(\delta_0\sqrt{\theta})$
$\Delta\dot{w}_f/\delta_0\sqrt{\theta}$
$\Delta SHP/\delta_0\sqrt{\theta}$
a
$SHP/(\delta_0\sqrt{\theta})$
CHART B₁
[DIMENSIONLESS]
M = CONST
POWER COEFF.: C_P
INCR. C_T
ADV. RATIO: μ
CHART B₂
[GENERALIZED]
$N/\sqrt{\theta}$ = CONST
$SHP/(\delta_0\sqrt{\theta})$
INCR. W/δ
AIRSPEED, $V/\sqrt{\theta}$: KN
CHART C
[ACTUAL]
CHART D
FUEL FLOW, $\dot{w}_f$: LB/HR
+5%
$\Delta\dot{w}_f$
ΔSHP
$a(\delta\sqrt{\theta})$
SHP
SHP
INCR. W
BEST END. SPEED
AIRSPEED, V: KN
CHART E
MIN. POWER FUEL FLOW $\dot{w}_{f_{min}}$: LB/HR
GROSS WEIGHT, W: LB

Figure 3.54 Determination of maximum endurance fuel flow

(1) *Determine Power Required* – As noted above, the maximum endurance fuel flow is computed at minimum power required, based on test or theoretical predictions. It is often convenient to plot the power required for weights from W_E to the maximum *TOGW*, in terms of SHP_{min} vs W for calculation purposes.

(2) *Calculate Fuel Flow* – For two-engine aircraft, each engine is assumed to provide 50 percent of the power required. Therefore, the fuel flow can be calculated using the engine manufacturer's fuel flow versus power relationships at $SHP/2$ and operational ambient conditions. These latter variations are usually accounted for by using generalized fuel flow presented in terms of $\dot{W}_F/\delta\sqrt{\theta}$ and $SHP/\delta\sqrt{\theta}$. For performance calculations, the fuel flow specified by engine manufacturers is usually increased by 5 percent.

Maximum endurance fuel flow for the hypothetical helicopter is shown in Fig 3.55. The data is calculated for a 4000 ft/95°F condition and includes a 5-percent SFC increase. A total of 6 points were used to define this line, with gross weights ranging from 9000 to 18,000 lb. Detailed calculations for a gross weight of 15,000 lb are presented below.

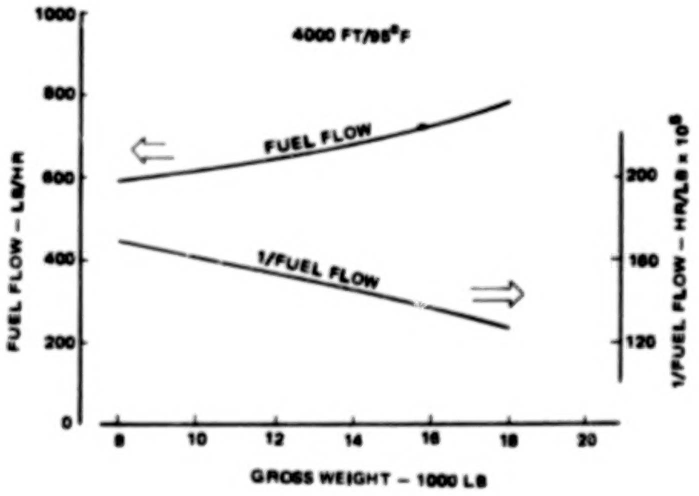

Figure 3.55 Maximum endurance fuel flow

1. Determine the atmospheric constants σ_p and $\delta\sqrt{\theta}$ at 4000 ft/95°F:

$$\sigma_p = 0.8076;$$

$$\delta\sqrt{\theta} = 0.8932.$$

2. Read power required at 15,000 lb from Fig 3.24 at 95°F.

3. Calculate $SHP/\delta\sqrt{\theta}$ per engine:

$$SHP/\delta\sqrt{\theta} = 909/(2 \times 0.893) = 509\,hp.$$

4. Determine the $\dot{W}_F/\delta\sqrt{\theta}$ per engine from Fig 1.7:

$$\dot{W}_F/\delta\sqrt{\theta} = 379\ lb/hr.$$

5. Calculate total fuel flow:

$$\dot{W}_F = (\dot{W}_F/\delta\sqrt{\theta}) \times 2.1 \times \delta\sqrt{\theta};\ \text{where } 2.1 = 2\ engines \times 1.05\ SFC\ increase;$$

$$\dot{W}_F = 711\ lb/hr.$$

The reciprocal of the fuel flow ($1/\dot{W}_F$) for the hypothetical hleicopter is also plotted in Fig 3.55 as a function of gross weight. The $1/\dot{W}_F$ curve is almost linear. Therefore, endurance capability can be computed in one step by dividing the mission fuel by the average fuel flow as described below.

The payload/endurance capability of the hypothetical helicopter is shown in Fig 3.56.

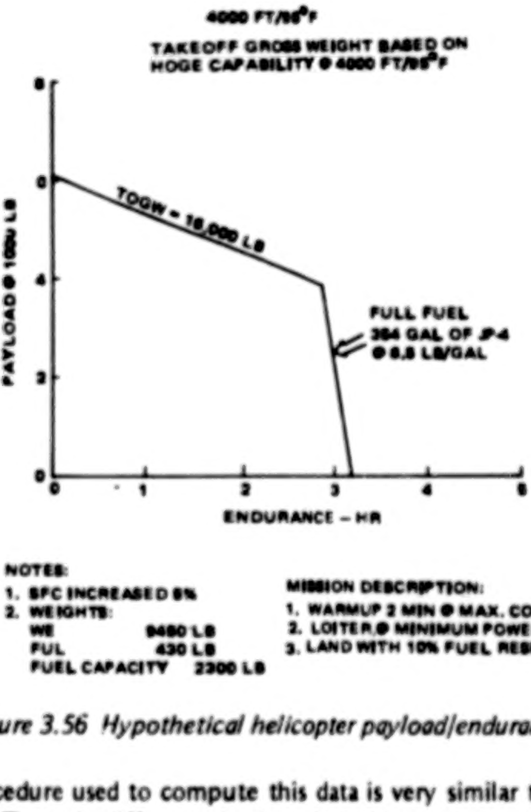

NOTES:
1. SFC INCREASED 5%
2. WEIGHTS:

WE	9480 LB
FUL	430 LB
FUEL CAPACITY	2300 LB

MISSION DESCRIPTION:
1. WARMUP 2 MIN @ MAX. CONT. POWER
2. LOITER @ MINIMUM POWER SPEED
3. LAND WITH 10% FUEL RESERVE

Figure 3.56 Hypothetical helicopter payload/endurance capability

The procedure used to compute this data is very similar to the calculations shown in Table III-5. The only difference in the calculation procedure occurs in steps *17* and *18*, as shown in Table III-6.

PROCEDURE	ZERO RANGE	FULL FUEL CALCULATIONS		
	PL_{max} $(TOGW_{max})$	PL_{max} $(TOGW_{max})$	ZERO *PL*	$PL = 0.5\,PL_{max}$
17 Fuel Flow @ Avg *W* (Fig 3.55); lb/hr	–	705	635	668
18 Endurance = *16/17* hr	0	2.89	3.20	3.05

TABLE III-6 PAYLOAD–ENDURANCE CALCULATIONS

7.4 Ferry-Range Capability

Ferry-range capability is the maximum range achievable with zero payload on either internal fuel capacity or with the addition of auxiliary tanks. The delivery of new or refurbished aircraft over extended distances is an example of ferry-range operation. Since there is no payload or cargo, the cabin area can be filled with auxiliary fuel tanks, or external tanks can be added to further increase range capability. These tanks increase the empty weight from 0.3 lb/gal to 1 lb/gal of auxiliary fuel, depending on the type of tank used. Also the drag of external tanks must be accounted for in establishing new power required vs flying-speed relationships. In ferry flights, the aircraft is usually flown in such a way that as the fuel burns off, the cruise altitude is varied in order to retain the maximum mi/lb values.

To secure additional range for a twin-engine aircraft, it may become necessary to shut down one engine in flight, thus forcing the remaining engine to operate at higher power settings with correspondingly lower sfc values. However, this would be done only under emergency conditions where the fuel supply has become critical.

An example of ferry-range performance capability for the hypothetical helicopter is presented as a function of takeoff weight in Fig 3.57. Here, range performance with integral fuel tanks as well as with the addition of internally mounted auxiliary tanks is shown for standard day conditions. The only limitation to the aircraft ferry-range performance is the criteria for establishing the takeoff gross weight. This is determined by the mode of taking off: hover OGE, IGE, or running takeoff (often performed for this type of mission). However, maximum gross weight restrictions must be observed; for example, the hypothetical helicopter at SL/STD has a W_{max} lower than that corresponding to hover OGE, IGE, or running takeoff criteria. The ferry-range capability at maximum weight is 1160 n.mi. Additional calculations at intermediate weights similar to those described below are required to establish the complete ferry-range capability.

(1) *Determination of Optimum Altitude, Speed, and Weight Schedule* – The procedure for optimizing specific range consists of computing (for selected altitudes and gross weights) specific range values corresponding to the best-range-speed of flight and plotting them in the manner shown in Fig 3.58. Although the information presented in this figure is for the hypothetical helicopter, the indicated trends are typical for current helicopter designs. It can be seen that the specific range is significantly better at higher altitudes; due primarily to an increase in turboshaft engine efficiency plus a

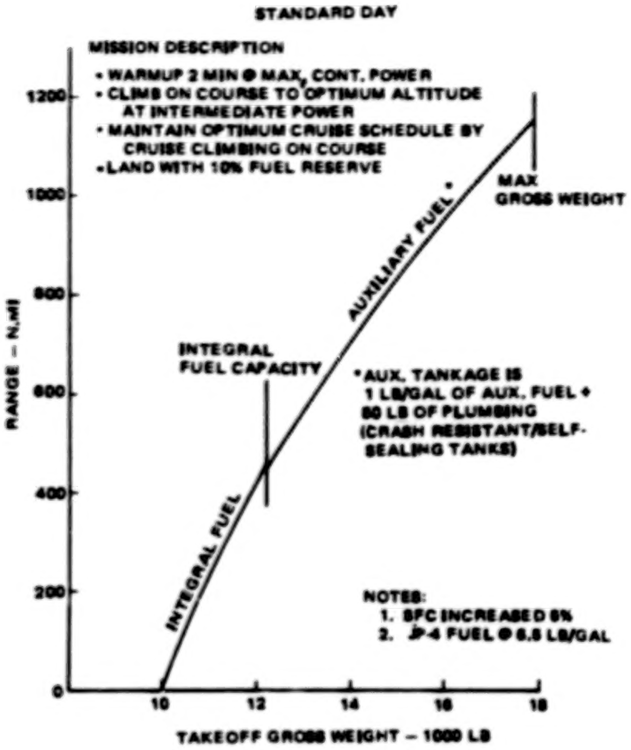

Figure 3.57 Ferry-range capability

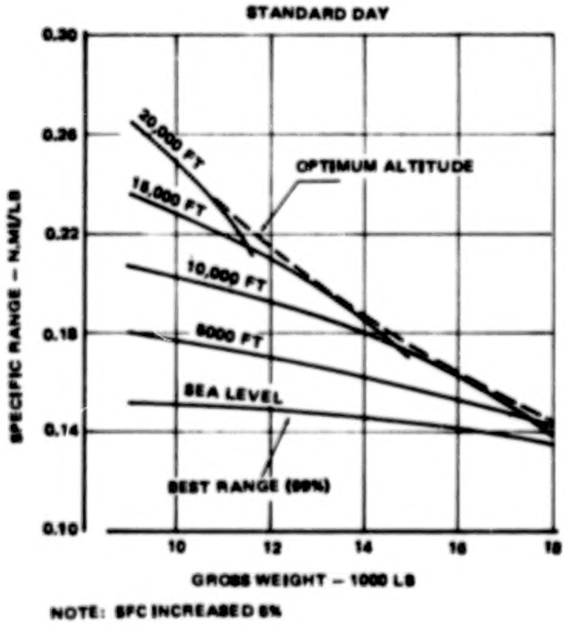

Figure 3.58 Optimum specific range for ferry-range mission

small reduction in power required at low-to-intermediate gross weights. However, at high weights and elevated altitudes, the power required increases rapidly due to stall and compressibility effects, resulting in a large decrease in specific range. The optimum specific range values occur alongaan envelope tangent to the various constant altitude lines. By plotting the altiutde and airspeed associated with each of the tangent points as a function of gross weight, the optimum cruise-climb schedule is established, as exemplified for the hypothetical helicopter in Fig 3.59. This figure shows that in order to obtain maximum range, the aircraft must increase its cruise altitude(up to 20,000 ft) by 175 ft for every 100 lb of fuel burnoff. The cruise airspeed required is approximately 130 kn.

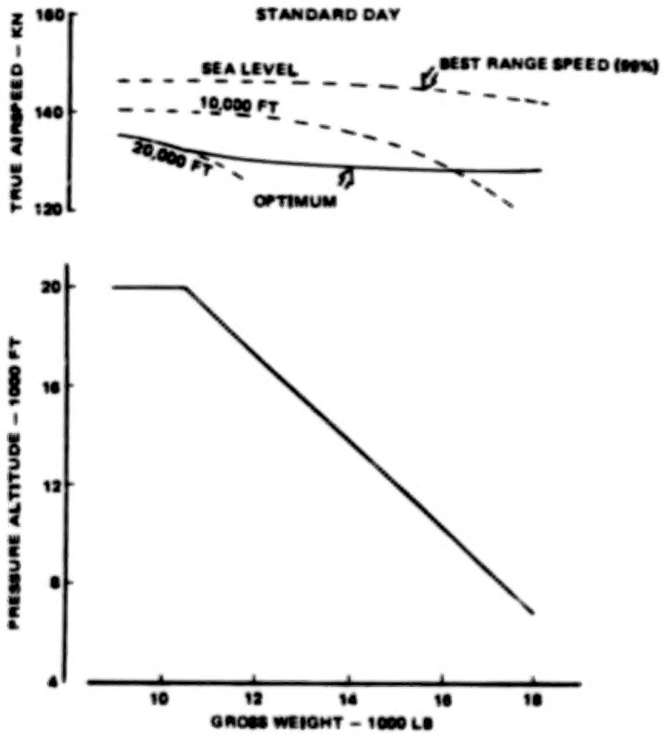

Figure 3.59 Optimum airspeed and altitude for ferry-range mission

(2) *Estimate Initial Climb Fuel and Distance Flown* – Fuel allotments are usually required for climb to the optimum altitude at the beginning of the mission. For example, the hypothetical helicopter operating at a takeoff weight of 18,000 lb must climb to 7000 ft to reach the optimum altitude. At lower takeoff weights, the aircraft must climb to even higher altitudes. To compute the initial climb fuel and distance, it is necessary to know the aircraft rate of climb as a function of both altitude and weight. This performance is usually calculated at either maximum continuous or intermediate power and airspeeds corresponding to minimum power required where the aircraft rate of climb is maximum. This would minimize the time and fuel spent while operating at nonoptimum cruise conditions. The climb fuel and distance calculations are as follows:

$$dt = dh/V_c \tag{3.34}$$

and the initial time to climb (t_{c_i}) from altitude h_1 to h_2

$$t_{c_i} = \int_{h_2}^{h_1} dh/V_c \approx \sum_{1}^{n} \left(\overline{1/V_c}\right)_k \Delta h_k \tag{3.35}$$

where

$$\Delta h_k \equiv h_{k+1} - h_k. \tag{3.36}$$

Fuel to climb is

$$W_{F_{c_i}} \approx \sum_{1}^{n} \bar{\dot{W}}_{F_k} \Delta t_k \tag{3.37}$$

where

$$\Delta t_k = \Delta h_k / V_{c_k}.$$

Ground distance (ℓ) flown during initial climb can be approximated as follows:

$$\ell_{c_i} \approx \sum_{1}^{n} \bar{V}_k \Delta t_k; \tag{3.38}$$

where $\bar{V}_k$ is the average speed of flight corresponding to segment k.

An example of climb fuel and distance calculations are given in Table III-7. Data is shown for an intermediate power climb conducted at minimum-power speed (85 kn) from SL to 7000 ft for a gross weight of 18,000 lb. The calculations are divided into two 3500-ft steps. The total climb fuel required is 66 lb and the distance traveled is approximately 4 n.mi. These values will be used in the sample problem ferry-range calculations.

(3) *Climb Fuel Burned During Cruise* – The optimum specific range data presented in Fig 3.58 is based on level-flight power required and fuel consumption, but does not include the additional fuel needed to climb while cruising. As shown in Table III-8, this climb fuel (38 lb) is sufficiently small that it can be computed using the mission mid-point weight (average weight) and the associated specific range ($\overline{SR}$), while the average rate of climb in cruise is obtained from the altitude gained and flight time. The average increase in power required to achieve this rate of climb (ΔSHP) is computed using the potential energy method. The incremental fuel flow needed to climb during cruise $(\Delta \dot{W}_F)_{cr}$ can then be calculated by multiplying the ΔSHP times the average slope of the engine fuel flow vs SHP curve (β):

ALTITUDE – FT	0	3500	7000
FUEL FLOW:			
$\delta\sqrt{\theta}$	1.0	0.875	0.76
SHP_{av} (INSTALLED)	2900*	2900*	2680
$SHP/2(\delta\sqrt{\theta})$	1450	1657	1763
$\dot{W}_F/2(\delta\sqrt{\theta})$: *Generalized Fuel Flow per Fig 1.7;* LB/HR	741	831	880
TOTAL $\dot{W}_F = (\dot{W}_F/2\delta\sqrt{\theta}) \times 2.1 \times \delta\sqrt{\theta}$; LB/HR	1556	1527	1404
TRUE AIRSPEED; KN	85	85	85
RATE OF CLIMB:			
SHP_{req} (Fig 3.28)	1090	1120	1200
$\Delta SHP = SHP_{av} - SHP_{req}$	1810	1780	1480
$V_c = (\Delta SHP \times 33{,}000 \times 0.85)/W$; FPM	2820	2770	2300

AVERAGE ALTITUDE	1750	5250
AVERAGE FUEL FLOW; LB/HR	1542	1466
AVERAGE RATE OF CLIMB; FPM	2795	2535
AVERAGE TRUE AIRSPEED; KN	85	85
Δ ALTITUDE; FT	3500	3500
Δ FUEL; LB	32.2	33.7
Δ TIME; MIN	1.25	1.38
Δ DISTANCE; N.MI	1.77	1.96

SUMMATION	
Σ FUEL; LB	66
Σ TIME; MIN	2.6
Σ DISTANCE; N.MI	3.7

CONDITIONS:
18,000 LB GROSS WEIGHT
INTERMEDIATE POWER/MIN POWER SPEED
STANDARD DAY
SFC INCREASED 5 PERCENT

* TRANSMISSION LIMITED

TABLE III-7 TIME, FUEL, AND DISTANCE TO CLIMB CALCULATIONS (SL TO 7000 FT)

WEIGHTS (LB)	
① *Weight Empty*	9,480
② *Aux. Tank Wgt (1 lb/gal + 50 lb)*	820
③ *(2) Crew @ 200 lb ea + Trapped Liquids*	430
④ *Fuel (Total)*	7,300
⑤ *TOGW*	18,000
⑥ *2-min Warmup @ Max Cont Power*	47
⑦ *W = ⑤ – ⑥*	17,953
⑧ *Climb to Opt. Alt. (7000 ft – See Fig 3.51)*	66
⑨ *W = ⑦ – ⑧*	17,887
⑩ *1/2 of Cruise Fuel = ㉖ /2*	3,228
⑪ *Average Mission Wgt ⑨ – ⑩*	14,658
⑫ *1/2 of Cruise Fuel = ㉖ /2*	3,229
⑬ *Landing Weight = ⑪ – ⑫*	11,430
⑭ *10% Fuel Reserve*	730
⑮ *W = ⑬ – ⑭*	10,700
⑯ *WE + FUL = ① + ② + ③*	10,700

FUEL ANALYSIS (LB)	
⑰ *Total Fuel + Aux. Tank Wgt = ⑤ – [① + ③]*	8,120
⑱ *Integral Fuel*	2,300
⑲ *Aux Fuel + Aux Tank Wgt = ⑰ – ⑱*	5,820
⑳ *Aux. Fuel**	5,000
㉑ *Total Fuel*	7,300
㉒ *Warmup 2 min @ Max Cont Power = ⑥*	47
㉓ *Initial Climb Fuel = ⑧*	66
㉔ *Reserve (10% of ㉑)*	730
㉕ *= ㉒ + ㉓ + ㉔*	843
㉖ *Total Cruise Climb Fuel = ㉑ – ㉕*	6457

**Assuming a Fuel Weight of 6.5 lb/gal and aux. tank wgt = 1 lb/gal + 50 lb, then ⑳ + (⑳ /6.5) x 1.0 + 50 = 5820; therefore, ⑳ = 5000 lb.*

CLIMB FUEL (CRUISE)	
Ⓐ *Total Cruise Climb Fuel (lb)*	6,457
Ⓑ *Δ Altitude per Fig 3.59 (ft)*	11,000
Ⓒ *Avg Altitude (ft)*	12,500
Ⓓ *Avg Gross Wgt (lb) = ⑪*	14,658
Ⓔ *Avg S.R. per Fig 3.58 (N.MI)*	0.179
Ⓕ *Avg Cruise Speed per Fig 3.59 (kn)*	129
Ⓖ *Distance = Ⓐ x Ⓔ (N.MI)*	1,157
Ⓗ *Time = Ⓖ / Ⓕ (hr)*	8.97
Ⓘ V_c *= Ⓑ /(Ⓗ x 60) (fpm)*	20.4
Ⓙ *ΔSHP = (Ⓓ x Ⓘ)/(33,000 x 0.85)*	10.7
Ⓚ $\dot{W}_F$ *= Ⓕ / Ⓔ (lb/hr)*	721
Ⓛ $\delta\sqrt{\theta}$ *@ Avg Altitude Ⓒ*	0.893
Ⓜ $\dot{W}_F/\delta\sqrt{\theta}$ *x 2.1*	579
Ⓝ $SHP/\delta\sqrt{\theta}$ *(Fig 1.8)*	1,080
Ⓞ β *= Slope of* $\dot{W}_F$ *curve at Ⓝ* $\beta = (\delta\dot{W}_F/\delta\sqrt{\theta})/(\delta\, SHP/\delta\sqrt{\theta})$	0.4
Ⓟ $\Delta\dot{W}_F$ *= Ⓞ x Ⓙ (lb/hr)*	4.3
Ⓠ *Fuel = Ⓟ x Ⓗ (lb)*	38
Ⓡ *Total Cruise Fuel less Climb Fuel = Ⓐ – Ⓠ (lb)*	6,419

RANGE CALCULATIONS

W_1 LB	W_2 LB	ΔW LB	AVG W; LB	AVG SR Fig 3.60	RANGE N.MI.
17887	15887	2000	16887	0.155	310
15887	13887	2000	14887	0.176	352
13887	11468	2419	12678	0.204	494

INITIAL CLIMB DIST	4 N.MI.
TOTAL RANGE	1160 N.MI.

NOTES: 1. STD DAY CONDITIONS
2. SFC INCREASED 5%

TABLE III-8 DETAILED FERRY RANGE CALCULATIONS

$$(\Delta \dot{W}_F)_{cr} = \beta \Delta SHP. \tag{3.39}$$

Finally, the climb fuel in cruise is computed by multiplying $(\Delta \dot{W}_F)_{cr}$ by the cruise time (t_{cr}), where $t_{cr} \approx (W_F \times \overline{SR})/\overline{V}$, and $\overline{V}$ is the average cruise speed. This fuel increment is then set aside and is not used for distance calculations.

(4) *Detailed Ferry-Range Calculations* – An example of step-by-step calculations for the following ferry-range mission is presented in Table III-8.

1. Warm up for 2 minutes.
2. Climb to optimum altitude at intermediate engine power with the speed of flight corresponding to minimum power required.
3. Maintain optimum altitude schedule by continuously climbing when in cruise.
4. Land with 10 percent fuel reserve.

Calculations are presented for standard day conditions and *TOGW = 18,000 lb.* Auxiliary fuel is added, assuming an auxiliary tankage weight empty of 1 lb/gal (typical of self-sealing, crash-resistant internal tanks) plus 50 lb for plumbing (pumps, lines, etc.).

The tabulations shown in Table III-8 are divided into; a weight and fuel analysis, cruise climb fuel analysis, and range calculations. Subtracting the relatively small 38 lb of cruise climb fuel from the total cruise fuel gives an equivalent level flight quantity of 6,419 lb. This weight is then combined with the level flight specific range data to compute range by integrating the area under the optimum specific range curve between the initial gross weight of 17,887 lb , and the final weight of 11,468 lb after burnoff. The total amount of fuel is so large that it appears advisable to divide the integrated area into two 2000- and one 2419-lb segments, and summing the range increments. The final step in the calculations is to add the ~4 n.mi. initial climb distance from Table III-7 to the cruise distance of 1156 n.mi. for the rotal ferry range of 1160 n.mi.

7.5 Speed Capability

The level flight speed capability of helicopters is determined by matching the power available with the power required while observing transmission and rotor-stall limits. Maximum continuous power available is used to compute maximum normal speeds while intermediate, or 30-min power ratings are used to define dash speed capability. An example of maximum normal speed for the hypothetical helicopter at 4000 ft/95°F and SL/STD ambient conditions as a function of gross weight is shown in Fig 3.60. It should be noted that the aircraft is primarily limited by the maximum continuous power at both ambient conditions.

7.6 Forward-Flight Climb Capability

Forward-flight climb performance is determined from the potential energy relationship discussed in Ch III, Sect 4:

$$V_c = \Delta SHP 33{,}000 k_{p_c}/W \tag{3.40}$$

where

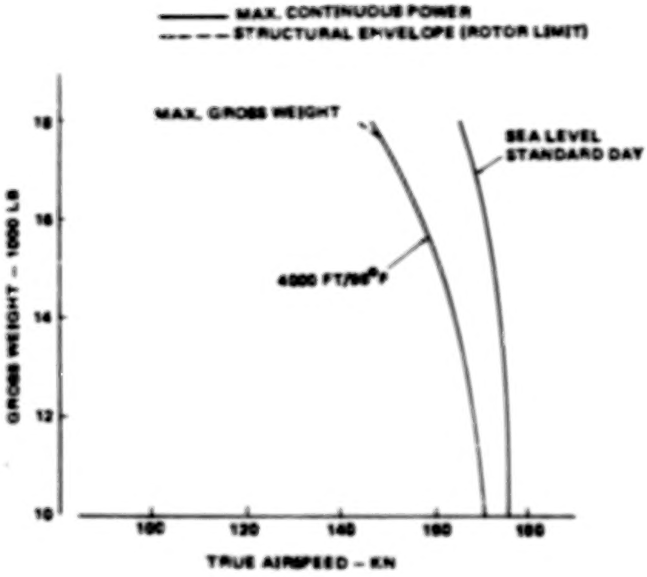

Figure 3.60 Speed capability

V_c = rate of climb; fpm

$\Delta SHP = SHP_{av} - SHP_{req}$

k_{p_c} = climb efficiency factor.

The highest $\Delta\ SHP$ values occur at speeds of 70 to 90 kn. Consequently, most climb performance is calculated in this speed range. Maximum continuous power is used for dual engine normal operation, and intermediate power for emergency one-engine-inoperative (*OEI*) conditions. Examples of both dual and single-engine climb performance capabilities of the hypothetical helicopter are presented in Fig 3.61. Using $k_{p_c} = 0.85$ and the minimum power required given in Fig 3.28, the rate of climb was computed as a function of gross weight at SL/STD and 4000 ft/95°F. In the latter case, the aircraft has a 1100-fpm dual-engine max. cont. power climb capability at a weight of 18,000 lb. Detailed sample calculations for this point are presented below.

1. Determine density ratio at 4000 ft/95°F (see Ch 1, Sect 4):

$$\sigma_p = 0.8076.$$

2. Calculate referred weight:

$$W/\sigma_p = 22{,}288\ lb.$$

3. Using the data in Fig 3.28, determine referred rotor horsepower required:

$$(RHP/\sigma_p)_{req} = 1360\ hp.$$

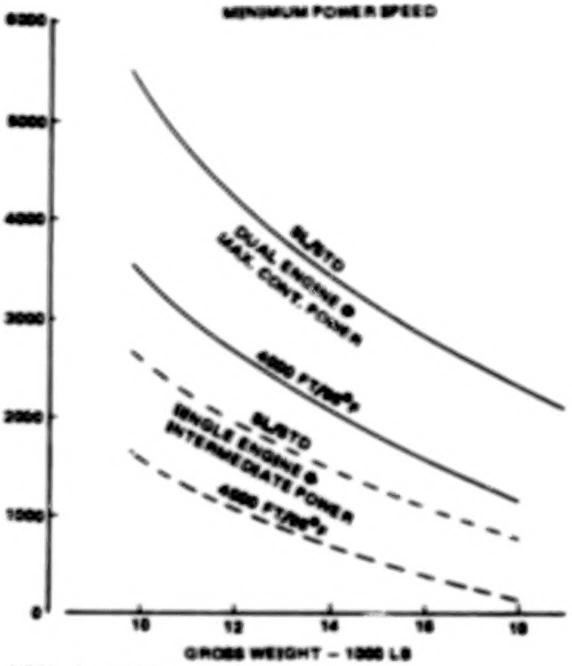

NOTE: $\delta_{p_c} = 0.85$

Figure 3.61 Forward flight climb capability

4. Calculate SHP_{req}:

$$SHP_{req} = [(RHP/\sigma_p) \times (\sigma_p/0.98)] + 30 = 1150\,hp.$$

5. From Fig 1.5, determine uninstalled shaft horsepower and then compute installed shaft horsepower available:

$$SHP_{av} = 0.99 SHP_{uninst}.$$

6. Compute excess shaft horsepower:

$$\Delta SHP = SHP_{av} - SHP_{req} = 705\,hp.$$

7. Finally, using Eq (3.40),

$$V_c = 1100\,fpm.$$

7.7 Service Ceiling

Service ceiling (h_{serv}) is the altitude at which the maximum rate of climb is reduced to 100 fpm. Standard day $h_{serv} = f(W)$ of the hypothetical helicopter is shown in Fig 3.62. This figure shows that at $W = 15{,}000\,lb$, $h_{serv} = 19{,}200\,ft$ when both engines are at maximum continuous power, and drops to $h_{serv} = 13{,}700\,ft$ with one engine operating at intermediate power.

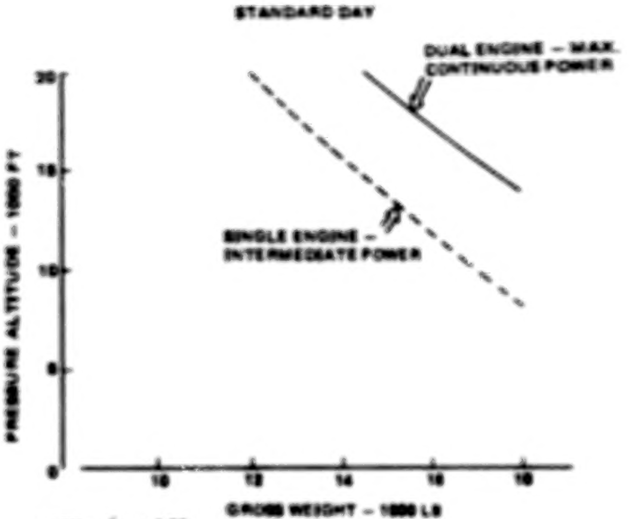

Figure 3.62 Service ceiling vs gross weight

The procedure for calculating service ceiling performance consists of computing the incremental power required to climb at 100 fpm, using Eq (3.23) and adding this increment to the level flight minimum power required plot shown in Fig 3.[illegible]. The power available is then compared with power required for various altitudes to obtain the service ceiling gross weight capability at each altitude. In actual operation, altitude restrictions other than power limitations (e.g., structural limits, excessive vibration, and flying qualities) may define the service ceiling. Determination of gross weight vs pressure altitude corresponding to the single-engine service ceiling is shown in Table III-9.

PRESSURE ALTITUDE: FT	0	5,000	10,000	15,000	20,000
TEMPERATURE; °F	59.0	41.2	23.3	5.5	−12.3
σ_p	1.0	0.862	0.738	0.629	0.533
SHP_{av} (FIG 1.7)	1684	1406	1238	1072	924
RHP_{av} $0.98(SHP_{av} - 30)$	1621	1349	1181	1021	876
RHP/σ_p	1621	1565	1601	1623	1644
W/σ_p; LB (FIG 3.28)	22,820	22,800	22,880	22,700	22,600
W; LB	22,820	19,720	16,890	14,280	12,020

NOTE: STANDARD DAY CONDITIONS
MINIMUM POWER SPEED
ONE-PERCENT ENGINE INSTALLATION LOSSES

TABLE III-9 SINGLE–ENGINE SERVICE CEILING CAPABILITY

7.8 Autorotation

Steady-state autorotational rates of descent (V_d) in forward flight (engines inoperative) are computed using Eq (3.39), where $\Delta SHP = SHP_{req}$:

$$V_d = (SHP \times 33{,}000 \times k_{p_d})/W; \text{ in fpm.} \tag{3.41}$$

Typically, $k_{p_d} \approx 1.0$ in autorotation, as discussed in Sect 5.2 of this chapter.

An example of autorotational rates of descent at $W = 15{,}000\ lb$ and SL/STD conditions is shown in Fig 3.63. Here, V_d is plotted as a function of airspeed, and it can be noted that the $V_d = f(V)$ curve has the shape of a speed power polar with the minimum $V_d = 2000\ fpm$ occurring at minimum-power speed.

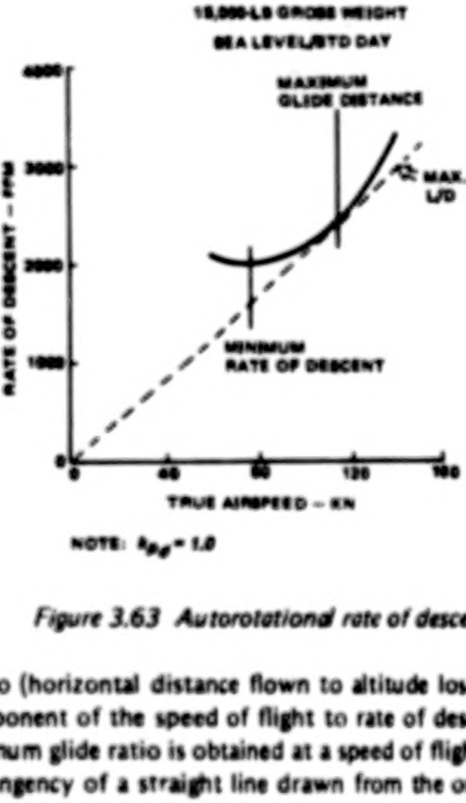

NOTE: $k_{p_d} = 1.0$

Figure 3.63 Autorotational rate of descent

The glide ratio (horizontal distance flown to altitude lost) is equal to the ratio of the horizontal component of the speed of flight to rate of descent (Fig 3.63). It can be seen that the maximum glide ratio is obtained at a speed of flight representing an abscissa of the point of a tangency of a straight line drawn from the origin of coordinates to the $V_d = f(V)$ curve. For the hypothetical helicopter, the optimum glide speed is 113 kn, or 37 kn above the speed for minimum rate of descent.

The airspeed for maximum glide distance is also the speed for maximum total aircraft L/D_e, where lift is equal to gross weight and equivalent drag, $D_e = 550SHP_{req}/V$. This is shown by solving Eq (3.41) for SHP_{req} and substituting it into the drag expression. The resulting equation is

$$L/D_e \approx (V/V_d)k_{p_d}$$

where V and V_g are of the same units. It can be seen that L/D_e is proportional to the aircraft glide slope; therefore maximum L/D_e occurs at the speed for maximum glide distance.

References for Ch III

1. Hoerner, S.F. *Fluid Dynamic Drag.* Published by the author, 1965 edition.

2 Gabriel, E. *Drag Estimation V/STOL Aircraft.* Boeing Vertol Report D8-2194-1, September 1968.

3. Keys, C. and Wiesner, R. *Guidelines for Reducing Helicopter Parasite Drag.* Included in AHS Report of AHS Ad Hoc Committee on Rotorcraft Drag. 31st Annual Forum, Washington, D.C. May 1975.

4. Julian, D. *HLH Hub Drag Review.* Boeing HLH Report D301-10100-3, April 1972.

5. Delany, N.K. and Sorensen, N.E. *Low-Speed Drag of Cylinders of Various Shapes.* NACA TN 3038, November 1953.

6. Perkins, C.D. and Hage, R.E. *Airplane Performance Stability and Control.* Published by John Wiley & Sons, Inc., New York. Ninth Printing, May 1963.

7. Biggers, J.L., McCloud, J.L., and Patterakis, P. *Wind-Tunnel Tests of Two Full-Scale Helicopter Fuselages.* NASA TND-1548, October 1962.

8. McDonnell Douglas Corporation. *USAF Stability and Control DATCOM.* AF33/616/-6460. Principal Investigator, D.E. Ellison, October 1960.

9. Prouty, R. *Tip Relief for Drag Divergence.* Journal of the Americal Helicopter Society, Vol. 16, No. 4.

10. LeNard, J.M. and Boehler, G.D. *Inclusion of Tip Relief in the Prediction of Compressibility Effects on Helicopter Rotor Performance.* USAAMRDL Tech. Report 73-71, December 1973.

11. LeNard, J.M. *A Theoretical Analysis of the Tip Relief Effect on Helicopter Rotor Performance.* USAAMRDL TR 72-7, August 1972.

12. Davis, S. Jon and Wisniewski, J.S. *User's Manual for HESCOMP, the Helicopter Sizing and Performance Computer Program.* Boeing Vertol Report D210-10699-1 (Contract NAS2-6107), NASA CR-152018, Ames Research Center, Moffett Field, Ca., Sept. 1973.

13. McCormick, B.W., Jr. *Aerodynamics of V/STOL Flight.* Academic Press, 1967.

14. Washizu, Kyuichiro, et al. *Experiments of a Model Helicopter Rotor Operating in the Vortex Ring State.* Journal of Aircraft, Vol 3, No 3, May-June 1966.

15. Dadone, Leo V. and Fukushima, T. *A Review of Design Objectives for Advanced Helicopter Rotor Airfoils.* Presented at the American Helicopter Symposium on Helicopter Aerodynamic Efficiency, Hartford, Conn., March 1975.

16. Benson, R.G., et al. *Influence of Airfoils on Stall Flutter Boundaries of Articulated Helicopter Rotors.* Presented at the 28th Annual National Forum of the American Helicopter Society (Preprint No 621), May 1972.

17. Hoffstedt, D.J., et.al. *Flight Test of Advanced Geometry Boron Blades.* USAAMRDL TR72-65, D210-10486-1, Eustis Directorate, February 1973.

18. Tanner, W.H. *Charts for Estimating Rotary-Wing Performance in Hover and at High Forward Speeds.* NASA CR-114, November 1964.

19. Ormiston, R. A. *Comparison of Several Methods of Predicting Loads on a Hypothetical Helicopter Rotor.* Journal of the American Helicopter Society, Vol 19, No 4, October 1974.

20. Gabel. R. *Current Loads Technology for Helicopter Rotors.* AGARD Conference Proceedings 122, August 1973.

21. Terzanin, F.J., Jr. *Prediction of Control Loads due to Blade Stall.* Journal of the American Helicopter Society, Vol 17, No 2, April 1972.

22. Gormont, R.E. *A Mathematical Model of Unsteady Aerodynamics and Radial Flow for Application to Helicopter Rotors.* USAAMRDL, TR72-67, D210-10492-1, Eustis Directorate, May 1973.

23. Harris, F.D., Tarzanin, F.J., and Fisher, R.K., Jr. *Rotor High-Speed Performance, Theory vs Test.* Journal of the American Helicopter Society, Vol 15, No 3, July 1970.

24. Wells, C.D. and Wood, T.L. *Maneuverability – Theory and Application.* AHS Preprint No 640, May 1972.

25. Brown, E.L. and Schmidt, P.S. *The Effect of Helicopter Pitching Velocity on Lift Capability.* Journal of the American Helicopter Society, Vol 8, No 4, October 1963.

26 Department of the Army. *Engineering Design Handbook – Helicopter, Part One, Preliminary Design.* AMCP 706-201, U.S. Army Material Command, August 1974.

Performance

27. Wiesner, Wayne and Kohler, Gary. *Tail-Rotor Design Guide.* USAAMRDL TR-73-99 D210-10687-1, Eustis Directorate, January 1974.

CHAPTER IV

WINGED HELICOPTER PERFORMANCE

A question that both designers and operators often ask themselves is whether any benefits could be derived from adding a lifting wing to a conventional helicopter. To place this problem in a proper perspective, a complete performance envelope is presented in this chapter wherein a fixed wing was added to the hypothetical helicopter described in the preceding chapters; however, the design gross weight remains the same as for the original configuration.

Principle notation for Chapter IV

AR	wing aspect ratio	
b	wing span	ft
C_D	wing, or body drag coefficient	
C_f	skin friction drag coefficient	
$C_L = L_w/\frac{1}{2}\rho V^2 S_w$	wing lift coefficient	
$C_T' = L_R/\pi R^2 \rho V_t^2$	rotor lift coefficient	
c	wing chord	ft
c_d	section drag coefficient	
c_ℓ	section lift coefficient	
$c_{\ell\alpha}$	slope of the lift curve	deg^{-1} or rad^{-1}
D	wing, or body drag	lb
d	rotor diameter	ft
f_e	equivalent flat-plate area	ft^2
g	acceleration of gravity	32.2fps^2
h	height, or altitude	ft
IGE	in-ground-effect	
i	angle-of-incidence	deg or rad
k_f	fillet factor	
k_g	ground-effect factor	
k_k	discrete roughness coefficient	
k_ℓ	longitudinal location factor	
k_p	climb efficiency factor	
k_{pd}	descent correlation factor	
k_t	wetted area factor	
$k_{3\text{-}D}$	three-dimensional drag correction factor	
k_v	vertical load factor	
$k_{v\ell}$	vertical location factor	
k_{wf}	wing fuselage interference drag factor	
L	lift	lb
M	moment	ft.lb
OGE	out-of-ground effect	
q	freestream dynamic pressure	psf
R	rotor radius	ft

Performance

R_e	Reynolds number	
S	wing area	ft^2
T	rotor thrust	lb
$TOGW$	takeoff gross weight	lb
V	velocity of aircraft translation	fps or kn
W	weight	lb
w	width	ft
X	propulsive force (+ forward)	lb
α	angle-of-attack	deg or rad
β	rotor downwash angle	deg or rad
Δ	increment	
δ_F	flap deflection	deg
ζ	distance from rotor disc perimeter	ft
κ	induced drag factor	
ρ	air density	slugs/cu.ft
σ	rotor solidity	

Subscripts

c	climb
e	equivalent, or exposed
F	flap
f	fuselage
i	induced
id	ideal
P	planform
R	rotor
r	root
t	tip
t	total
t	horizontal tail
tpp	tip-path-plane
w	wing
we	wetted

Superscript

$\bullet$	derivative with respect to time

1. INTRODUCTORY REMARKS

There are no winged production helicopters at this time except, perhaps, the Mil-6 in the USSR. So-called "wings" on operational aircraft as the CH-46 Sea Knight and AH-1J Cobra are actually stubs used as support structures for stores or as fuel tanks, and contribute very little to lift in forward flight. Development and testing of experimental machines (e.g., the Sikorsky Black Hawk Model S67 and the Boeing Vertol Model 347) should provide an insight into actual and potential gains, as well as problems associated with the addition of lifting wings for pure helicopters.

A wing was added to the Model 347 (Fig 4.1) primarily as a means of improving maneuver capability; however, the overall performance was adversely affected, and efforts were directed toward minimization of the performance penalties, thus reducing the "price" paid for having a much more maneuverable configuration. Although the Model 347 is a tandem, the vast technical documentation – wind tunnel data and flight test results – acquired during the development of this aircraft is of universal value, and is quoted throughout this presentation.

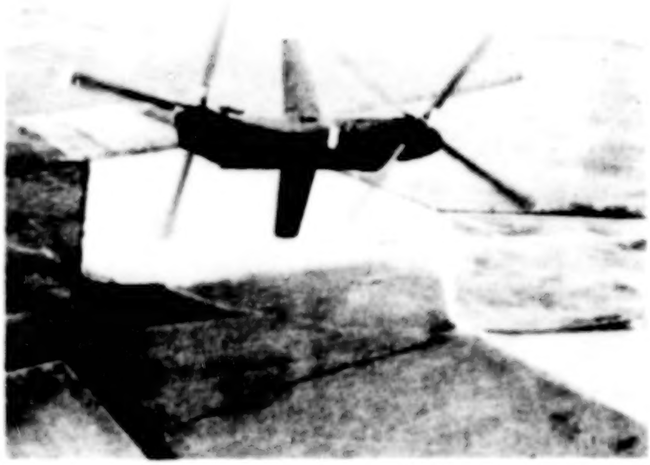

Figure 4.1 Model 347 winged helicopter in flight

Techniques for estimating wing effects on hover and forward flight are given in this chapter; including sample calculations for a 101-ft^2 wing added to the hypothetical helicopter evaluated in Chs II and III. A brief discussion of sizing a wing to meet a given maneuver requirements and methods of optimizing the level flight rotor unloading are provided, and a direct comparison of both wing-off and winf-on performance is obtained with primary emphasis on estimating the incremental wing effects on performance.

It will be shown later in this chapter that the wing installation would increase the weight empty and, unless tilted, would result in increased download in hover as well as in vertical and near-vertical climb. In high-speed regimes of flight (forward flight, climb and V_{max} capability), benefits of installing a wing would accrue only when the rotor operates on the edge of stall inception, where unloading of the rotor would result in a reduction of power required. It should be recognized that performance improvements can be obtained by combining wing unloading with the provision of auxilliary propulsion and slowing down the main rotor. However, these approaches are outside the scope of this text; consequently, in this chapter, efforts will be restricted to the so-called classic winged helicopters.

2 DESCRIPTION OF THE WINGED HELICOPTER

The geometry and primary physical characteristics of the hypothetical winged helicopter are illusrtrated in Fig 4.2. It is assumed that the design gross and maximum weights of the winged configuration are identical to that of the pure helicopter (see Ch I). However, the weight empty is increased by 350 lb, which includes the weight of the wing (3.5 lb/ft^2 of wing planform area)[1] and the required fuselage structural modifications.

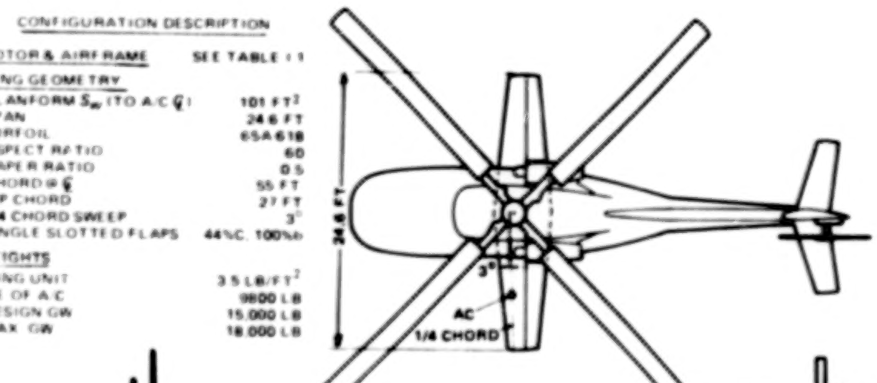

CONFIGURATION DESCRIPTION	
ROTOR & AIRFRAME	SEE TABLE I 1
WING GEOMETRY	
PLANFORM S_w (TO A/C ℄)	101 FT^2
SPAN	24.6 FT
AIRFOIL	65A618
ASPECT RATIO	6.0
TAPER RATIO	0.5
CHORD @ ℄	5.5 FT
TIP CHORD	2.7 FT
1/4 CHORD SWEEP	3°
SINGLE SLOTTED FLAPS	44%C, 100%b
WEIGHTS	
WING UNIT	3.5 LB/FT^2
WE OF A/C	9800 LB
DESIGN GW	15,000 LB
MAX GW	18,000 LB

Figure 4.2 Hypothetical winged helicopter

A brief outline of the details involved in defining the hypothetical wing geometry is presented below.

2.1 Planform Area/Flap Geometry

The wing planform area, including the projected area in the fuselage cutout region is $S = 101$ ft^2. The wing was sized to provide 2-g, or a 60° banked turn maneuver capability at airspeeds from 100 to 170 kn at 4000 ft/95°F (Fig 4.3). Due to rotor stall limits, the pure helicopter has a less than 2-g capability over the entire speed range, and this deficiency increases with increasing airspeed. Installation of the 101 ft^2 wing meets the 2-g criteria at low speeds and exceeds the requirement at 160 to 180 kn.

To satisfy the 2-g requirement without producing excessive download in hover, full-span, 44-percent chord, single-slotted flaps deflected 30° are used as illustrated at the bottom of Fig 4.3. Without wings, the wing area needed to satisfy maneuver requirements at 125 to 130 kn would amount to 162 ft^2 versus 101 ft^2 with flaps. This reduction in area decreases the hover download by 2.6 percent of the gross weight for a wing having an aspect ratio of 6 (Fig 4.4).

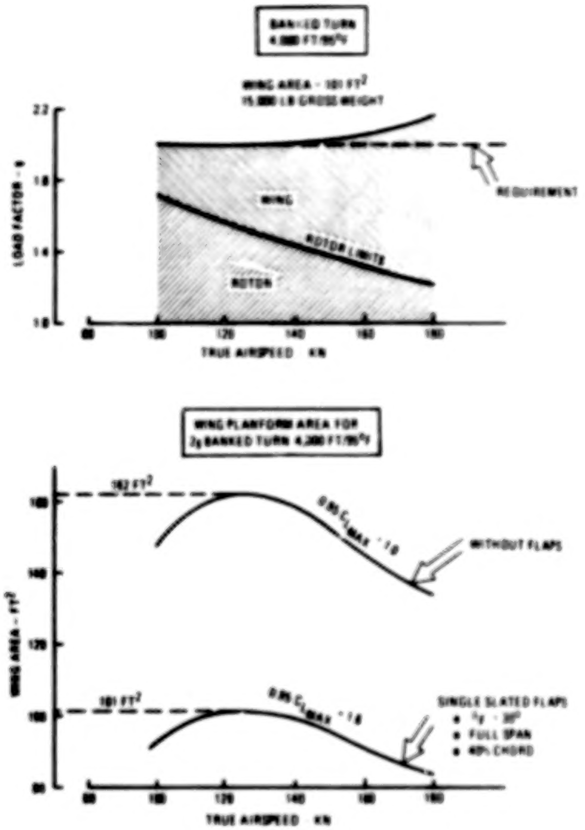

Figure 4.3 Winged helicopter maneuver capability

It can be seen from Fig 4.4 that the flaps, when deflected 80°, provide an additional 0.7 percent reduction in hover download. Other, more complicated, methods of download alleviation are also shown, including a schematic of umbrella installations (later illustrated in Fig 4.11), and wing rotation. However, in order to illustrate the potential magnitude of wing download, flap deflection is assumed as the sole method of reducing this effect.

The flap geometry and aerodynamic characteristics used for the hypothetical helicopter aircraft are based on theoretical and wind-tunnel studies which indicate that flap effectiveness for single-slotted configurations tends to decrease at deflection angles above 30° and for flap chords exceeding 40 to 50 percent of the wing chord. Because of the availability of wind-tunnel data, a 44-percent flap was selected for the hypothetical helicopter. The $C_{L_{max}}$ values used in Fig 4.3 are based on wind-tunnel model test results adjusted for Reynolds number and fuselage cutout effects as shown in Fig 4.5. The Reynolds number correction is based on two-dimensional data[2,3]; and the cutout correction is based on the empirical span calculation described later in this chapter.

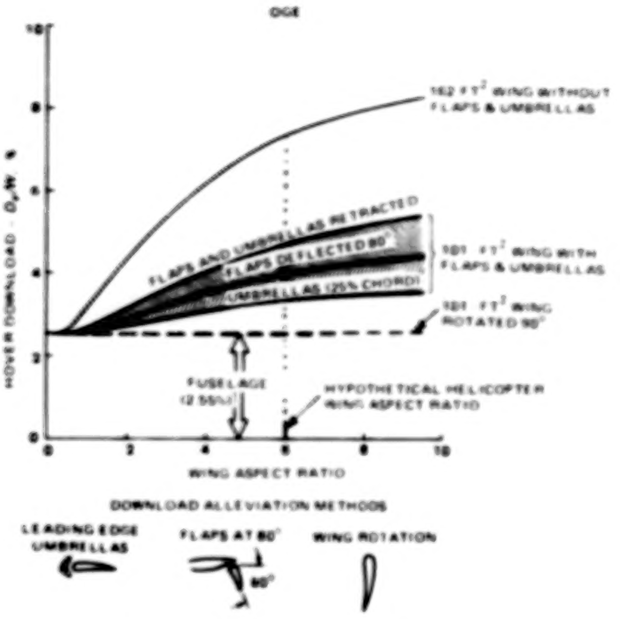

Figure 4.4 Effect of wing geometry on hover download

The design $C_{L_{max}}$ is 95 percent of the true $C_{L_{max}}$ to allow a margin for gusts and to prevent stall buffeting during maneuvers. The flaps can be deflected upwards to decrease wing lift during autorotation, where high wing angles-of-attack ($\alpha \approx 20°$) can compromise autorotation performance and cause roll control problems. Also, flap deflection shifts the wing zero-lift angle-of-attack which, during maneuvers, reduces the fuselage pitch-up attitude to achieve a given wing lift. This provides increased pilot visibility and reduces aircraft deceleration as described later in this chapter.

The method of controlling flap deflections as a function of flight conditions was demonstrated on the Model 347 (Fig 4.6). Vertical acceleration measurements were used to automatically control the flap position to maximize the vehicle g capability. Collective pitch setting was used to position the flaps for autorotational descent. Automatic control of wing incidence and differential flap amgles were employed for download alleviation and roll control. However, as previously stated, wing control of the hypothetical helicopter is limited to flap deflection at a fixed incidence angle.

2.2 Wing Aspect Ratio

An aspect ratio of 6 was selected for the hypothetical helicopter as a reasonable compromise with respect to hover download induced drag and structural weight. For example, increasing the aspect ratio to 9 would extend the wing further into the higher velocity rotor downwash region and increase the hover download as shown in Fig 4.4. Lowering the aspect ratio below 6 is undesirable because of increased wing induced drag.

Since the hypothetical wing is designed for maximum lift, the question of the effect of aspect ratio on $C_{L_{max}}$ must be answered. Theoretical and test analyses have shown that there is no noticeable variation of $C_{L_{max}}$ with aspect ratio.[4]

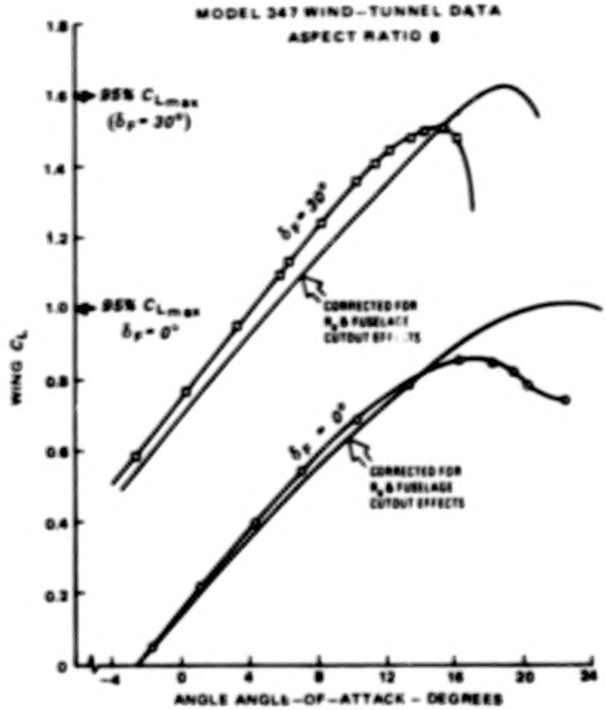

Figure 4.5 Determination of wing $C_{L_{max}}$ from the 1/11-scale Model 347 wind-tunnel data

2.3 Taper Ratio

The taper ratio $c_t/c_r = 0.5$ is based on a root chord (c_r) determined by projecting the wing leading and trailing edges to the fuselage centerline. Wing taper provides considerably more actual wing thickness at the root where bending moments are maximum. $c_t/c_r = 0.5$ also provides a small download benefit by positioning most of the planform inboard. In addition, theoretical induced power calculations[2] indicate that $c_t/c_r = 0.5$ results in the closest approximation to an elliptical lift distribution, required for minimization of induced drag. However, this benefit of taper is relatively small compared to the effect of wing cutout on induced drag as discussed later in this chapter.

In terms of $C_{L_{max}}$, a large taper (low c_t/c_r values) is undesirable because it increases the outboard c_ℓ values at a given total wing C_L, resulting in a small decrease in wing $C_{L_{max}}$[4]. The $c_t/c_r = 0.5$ value therefore, is a compromise between $C_{L_{max}}$ effects, induced drag, and structural requirements.

2.4 1/4–Chord Sweep

The hypothetical wing sweep angle was kept to a minimum (3°) in order to maximize the wing lift capability during maneuvers. Sweep induces spanwise flow which

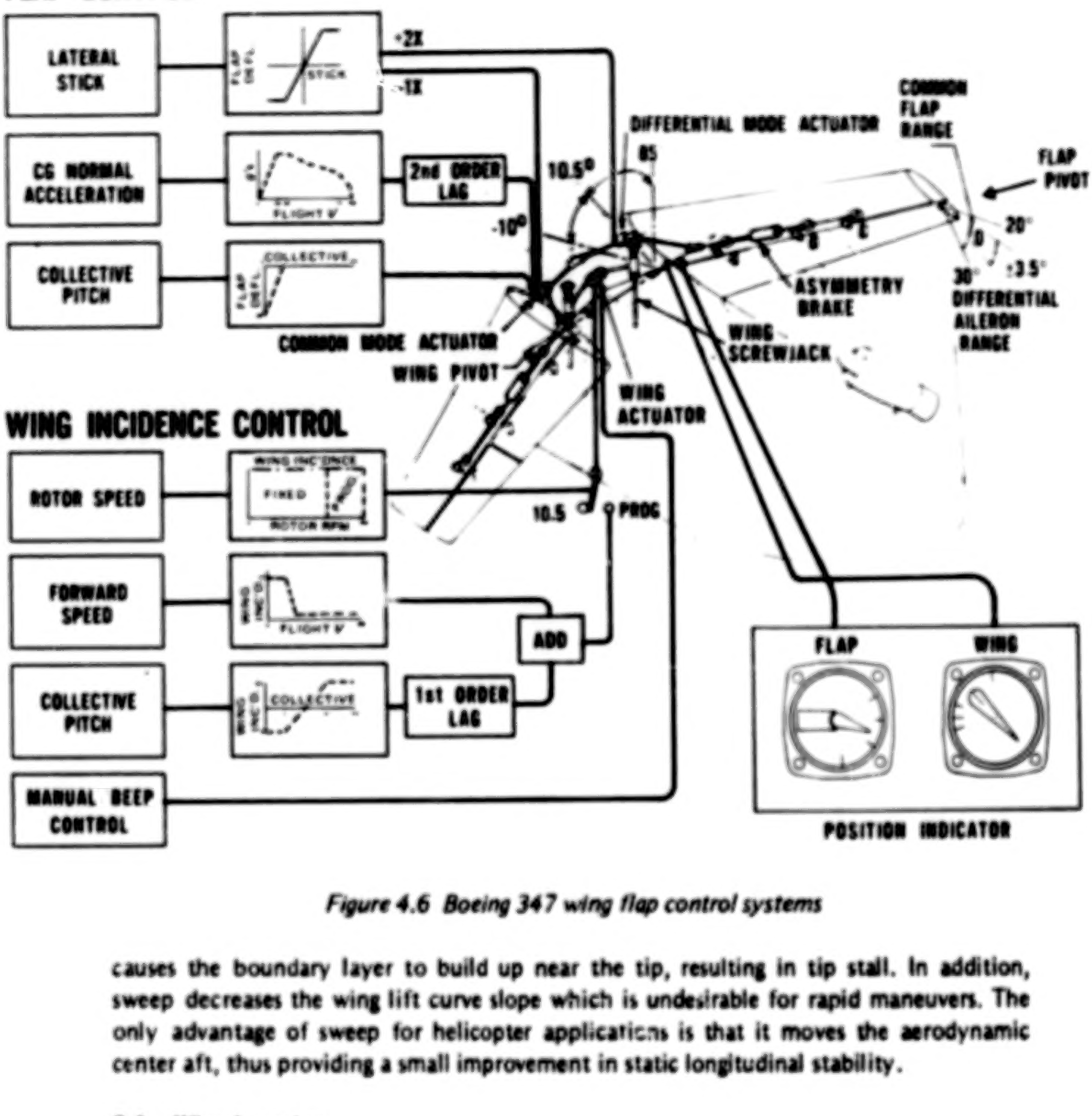

Figure 4.6 Boeing 347 wing flap control systems

causes the boundary layer to build up near the tip, resulting in tip stall. In addition, sweep decreases the wing lift curve slope which is undesirable for rapid maneuvers. The only advantage of sweep for helicopter applications is that it moves the aerodynamic center aft, thus providing a small improvement in static longitudinal stability.

2.5 Wing Location

The wing is positioned on top of the fuselage as shown in Fig 4.2. This is done in order to provide easy access to the cabin and to prevent the wing carry-through-structure and controls from reducing the cabin space. In addition, the high-wing arrangement provides a small reduction in hover download and a small improvement in airframe angle-of-attack stability. However, in this location, the wing is in close proximity to the engine inlet and flow disturbances due to the wing could cause engine performance problems.

In the considered case, the aerodynamic center of the wing is positioned directly beneath the rotor hub. However, if the longitudinal stability of the wing-off configuration is marginal, then the wing aerodynamic center should be located further aft. This is particularly true for autorotation flight conditions where nose-up pitching must be avoided.

2.6 Airfoil Section

The airfoil for the wing of the hypothetical helicopter is the 65A-618 section, where *A* indicates that the trailing edge cusp, present in the 65_3 618, was removed to simplify the manufacture of the wing[2]. (Fig 4.7). The aerodynamic characteristics leading to the selection of this airfoil are listed below:

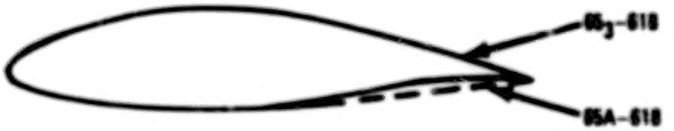

Figure 4.7 65A-618 airfoil section

(1) Low profile drag at trim c_l, ($c_d = 0.007$ at $c_l = 0.4$)
(2) High $c_{l_{max}}$, ($c_{l_{max}} = 1.5$)
(3) Gentle trailing edge stall characteristics
(4) High lift-curve slope ($c_{l_\alpha} = 0.114$ *per deg*)
(5) Sufficient maximum thickness (18 percent) and favorable chordwise thickness distribution for structural efficiency and low weight.

Low drag is desirable for maximum cruise performance, while the high $c_{l_{max}}$, gentle stall characteristics and high lift curve slope are required for good maneuver performance. The two-dimensional characteristics of this airfoil are defined for a Reynolds number of 4.7×10^6, corresponding to a 150-kn, 4000 ft/95°F condition.

3. HOVER AND VERTICAL CLIMB PERFORMANCE

The primary effect of a wing on hover OGE, IGE, and vertical climb performance is an increase in download. The methods used to estimate these effects are identical to the procedures outlined in Ch II. Sample calculations are provided below to illustrate the application of these techniques to the winged aircraft.

3.1 Wing Download OGE

The wing download increment OGE is computed by combining test-measured downwash velocity profiles (Fig 2.19) with the estimated wing drag coefficients shown in Eqs (2.7) to (2.11). In these equations, the radial stations are measured along the wing span rather than along the fuselage centerline. Detailed sample calculations for the hypothetical helicopter are presented in Table IV-1. As noted, with flaps deflected 80° down, the total download amounts to 3.97 percent of gross weight, or 1.42 percent more than for the baseline aircraft without wings. At 4000 ft/95°F, this penalty is equivalent to a 227-lb reduction in hover OGE gross-weight capability.

STEP	①	②	③	④	⑤	⑥	⑦	⑧	⑨
ITEM	C (FT)	C/R (%)	x_{n+1}	x_n	ΔA_v	C_{D_v}	w (FT)	C_{D_v} [illegible]	$\Delta D_v/T$ (%)
CALCULATION PROCEDURE		① /.25	SEE FIG 2.19		③-④	SEE FIG 4.8	SECTION WIDTH	⑤ × ⑦ [illegible]	2(⑥ × ⑧)
1 WING TIP	12.5	50	203	134	69	1.00	2.78	[illegible]	1.30
2 WING ROOT	20.6	82.4	205	203	2	0.7	3.75	[illegible]	.03
3 FUSELAGE CENTERLINE	25.0	100	-	205	-	-	-	-	-
								WING D_v/T	1.33
								FUSELAGE D_v/T	2.49*
								TOTAL D_v/T	3.82
								TOTAL D_v/W	3.97

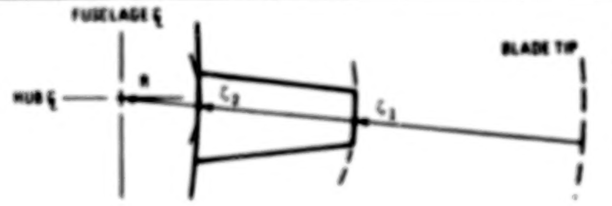

*TABLE II-1

TABLE IV-1 HOVER OGE DOWNLOAD CALCULATION (δ_F = 80°)

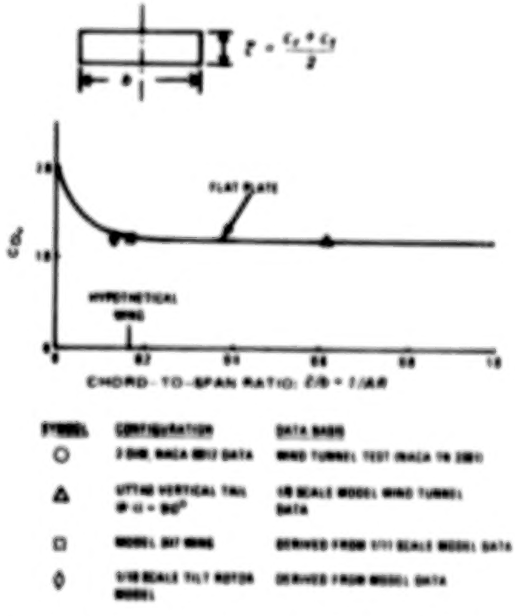

Figure 4.8 Effect of wing aspect ratio on C_{D_v}

The wing vertical drag coefficient used in these calculations depends on the type of alleviation devices employed. In the simplest case of a plain wing, the C_{D_v} is close to the drag of a flat plate normal to the freestream velocity, as shown in Fig 4.8. The drag coefficient of wings with an aspect ratio of $AR \leq 6$ is $C_{D_v} = 1.2$. At $AR > 6$, the drag coefficient increases rapidly, becoming *2.0* in the two-dimensional case.

The effect of download alleviation methods on the wing vertical drag coefficient is shown in Fig 4.9. Drag coefficients for flaps deflected 80°, leading edge umbrellas and wing rotation presented in this figure are based on wind-tunnel tests of the 1/11-scale Model 347 and tilt-rotor 1/10-scale models. As noted, the 80° flap deflection reduced the drag coefficient from 1.2 to approximately 1.0. Flap deflections between 70° and 80° represent the minimum download settings, as illustrated by the tilt-rotor test results[1] shown in Fig 4.10. Flap deflections of this magnitude also reduce the projected wing area. For example, deflecting the 44-percent chord flaps 80° reduces the planform area by approximately 30 percent.

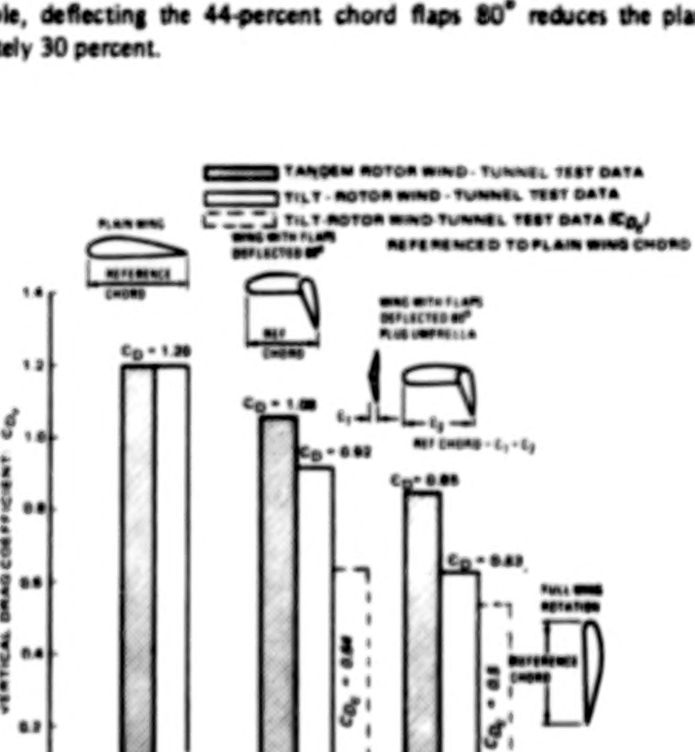

Figure 4.9 Effect of download alleviation methods on C_{D_v}

As indicated in Fig 4.4, the combined effect of flap deflection on C_{D_v} and planform area is to decrease the hypothetical helicopter wing download penalty by 40 to 50 percent. In Table IV-1, C_{D_v} was used to compute the download of the hypothetical wing. In the cutout region, $C_D = 0.7$ was assumed, which is the average of the wing $C_D = 1.06$ and the fuselage $C_D = 0.4$.

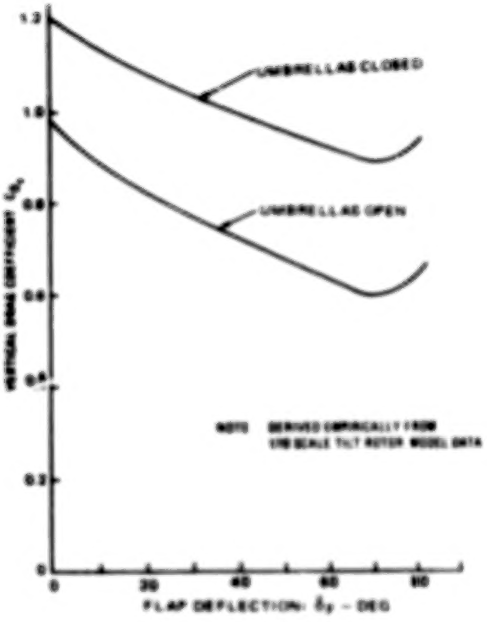

Figure 4.10 Effect of flap deflections on C_{D_V}

By combining the 80° flap deflection with leading-edge umbrellas, the wing drag coefficient can be further reduced. As shown in Fig 4.9, C_{D_V} as low as 0.63 has been measured for this configuration. The improvement in flow conditions below the wing due to the umbrella and flaps is evident in the flow visualization photographs in Fig 4.11. Umbrella installations, when open, typically reduce the exposed wing chord by 15 to 20 percent. The net effect of the combined umbrella and flap deflection is to reduce the wing download penalty by approximately 70 percent, as noted in Fig 4.4.

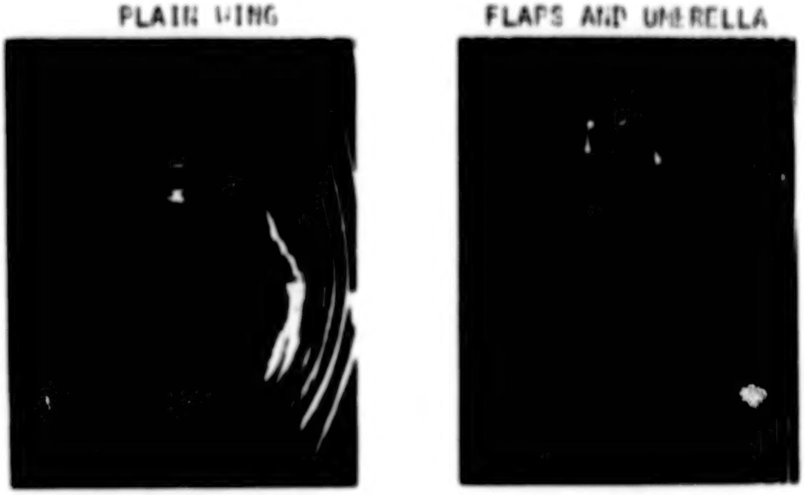

Figure 4.11 Two dimensional smoke studies of a wing

The other download alleviation method (Fig 4.9) is to rotate the wing a full 90°. The C_{D_v} for this wing geometry is $C_{D_v} = 0.01$. This technique essentially reduces the wing download to zero (Fig 4.4).

3.2 Wing Download IGE

Due to the increase in local pressure on the lower surface of the wing, the incremental hover download decreases considerably as the aircraft descends from OGE to IGE conditions. Test data for a winged helicopter is not available to define this reduction; however tilt-rotor studies indicate that the fuselage download reductions shown in Fig 2.24 will give a conservative estimate of wing download in ground effect. It can also be seen from this figure that the ratio of IGE to OGE download (k_g) varies with the height of the fuselage or wing above the ground. For example, at a wheel height of 5 ft, the hypothetical wing download correction factor (k_{g_w}) is 0.25 and the corresponding fuselage factor $k_{g_f} = 0.09$. The total download factor for the combined fuselage plus wing configuration (k_{g_t}) is

$$k_{g_t} = (\bar{D}_{v_f} + \bar{D}_{v_w})_{IGE} / (\bar{D}_{v_f} + \bar{D}_{v_w})_{OGE} \tag{4.1}$$

where

$\bar{D}_{v_f}$ = relative fuselage vertical drag $\equiv D_{v_f}/W$
$\bar{D}_{v_w}$ = relative wing vertical drag $\equiv D_{v_w}/W$
W = gross weight.

Substituting the OGE download values for the hypothetical aircraft shown in Table IV-1, and the IGE factors described above into Eq (4.1),

$$k_{g_t} = \frac{(0.09 \times 0.0255) + (0.25 \times 0.0142)}{0.0397} = 0.1472.$$

As described in Ch II, IGE performance is computed by correcting the OGE gross weight calculations by the factor W_{IGE}/W_{OGE} determined by rearranging Eq (2.14). The other variables in this equation are k_g, $(D_v/W)_{OGE}$, and thrust ratio T_{IGE}/T_{OGE}, where the thrust ratio is 1.14, as shown in Fig 2.22. Substituting the winged helicopter parameters k_{g_t} and D_v/W in Eq (2.14):

$$\frac{W_{IGE}}{W_{OGE}} = 1.14 \; \frac{1 + 0.0397}{1 + (0.1472 \times 0.0397)} = 1.178.$$

The winged helicopter gross weight ratio, therefore, is 0.8 percent higher than the baseline wingless design ($W_{IGE}/W_{OGE} = 1.17$).

3.3 Hover Ceiling

The OGE and IGE hover ceiling performance at 95°F, with and without the 101-ft^2 wing installed, is shown in Fig 4.12. These results were obtained using the download corrections defined above and the rotor performance computed in Ch II. The winged

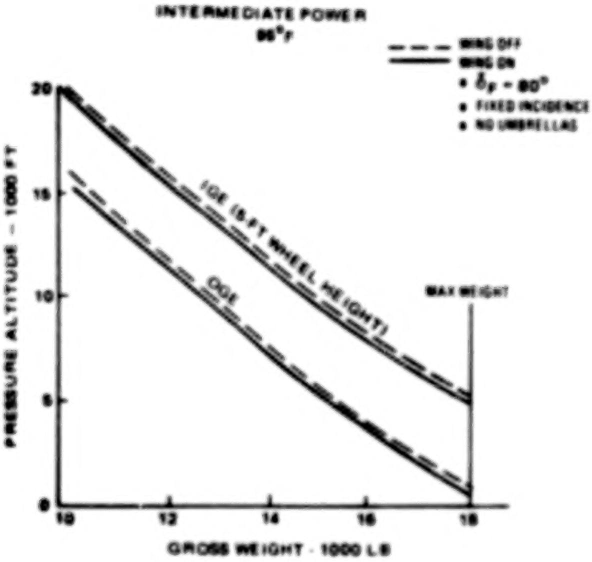

Figure 4.12 Hover ceiling IGE and OGE

configuration includes flaps deflected 80°. It can be seen that the wing causes either a 500-ft loss of altitude or a 200-lb reduction in hover gross weight when hovering OGE. For hover IGE, the losses are 250 ft, or 100 lb.

3.4 Vertical Climb Performance

In vertical climb, the primary effect of installing a wing is to increase the download resulting from the downwash velocity component. At small rates of climb ($V_c < 1000$ *fpm)*, the hypothetical winged helicopter will have a 1.42 percent less gross weight capability than shown in Fig 2.26. At 4000 ft/95°F, this is equivalent to a 150-fpm reduction in vertical climb performance.

For a more accurate assessment of wing download effects at higher rates of climb ($V_c > 1000$ *fpm*), the incremental wing download must be added to the fuselage download calculations shown in Table II-4 to determine new factors, k_1, k_2 and k_3. The revised factors are then substituted into Eq (2.27) to compute the climb gross weight, as illustrated in Table II-3.

4. FORWARD FLIGHT PERFORMANCE

A detailed discussion of winged helicopter level flight power required is presented in this section along with an analysis of the wing's effect on climb and descent performance, as well as maneuver capability. Much of the data is based on Vertol winged helicopter wind-tunnel and flight-test programs, and test results summarized by Lynn[6].

4.1 Effect of Wings on Parasite Drag/Power

A summary drag breakdown for the hypothetical wing configuration is presented in Fig 4.13. Wing drag, consisting of wing profile drag, induced drag and rotor/wing interference effects, is shown in this figure as a function of airspeed and wing C_L for a 15,000-lb gross weight aircraft at 4000 ft/95°F. The largest component is the rotor-on-wing interference drag which at $C_L = 0.4$, accounts for over 50 percent of the wing drag at 150 kn. At lower speeds, the interference drag represents an even larger percentage of the total wing drag. As noted in the lower half of this figure, the interference drag at 150 kn does not vary significantly for C_L values above 0.6, while the wing induced drag increases proportionally to ${C_L}^2$. An evaluation of each of these drag components is presented on the following pages.

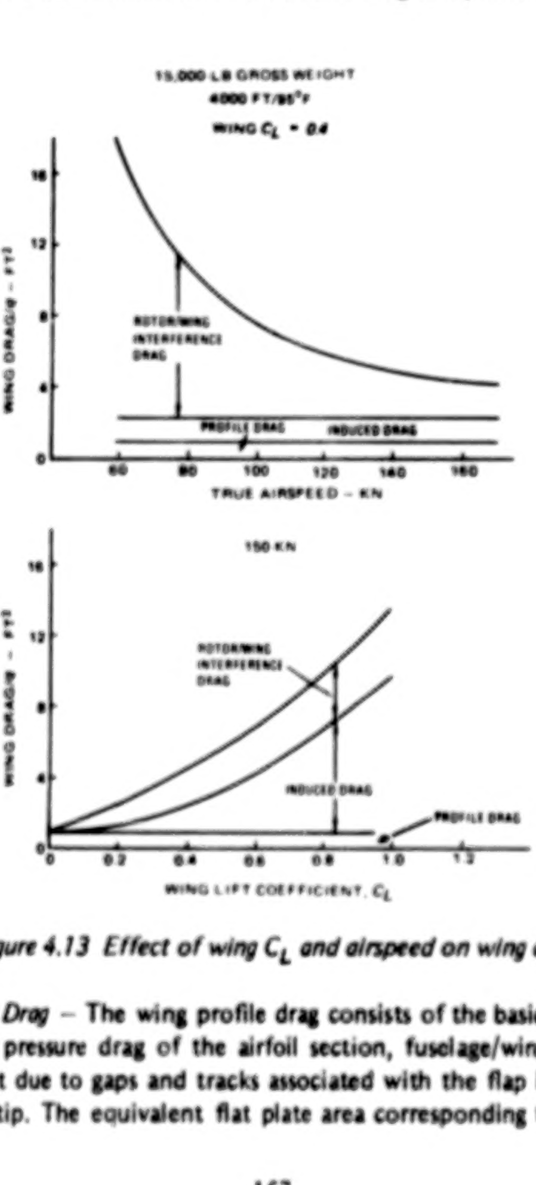

Figure 4.13 Effect of wing C_L and airspeed on wing drag

Wing Profile Drag – The wing profile drag consists of the basic skin friction of the exposed area and pressure drag of the airfoil section, fuselage/wing interference drag, the drag increment due to gaps and tracks associated with the flap installation, and the drag of the wing tip. The equivalent flat plate area corresponding to wing profile drag

(f_{e_w}) can be computed as follows:

$$f_{e_w} = C_f S_{w_e}(1 + k_{3\text{-}D} + k_k) + \Delta f_{e_t} + \Delta f_{e_i} + \Delta f_{e_F} \tag{4.2}$$

where

C_f = skin friction drag coefficient of a flat plate
S_{w_e} = wing exposed wetted area
$k_{3\text{-}D}$ = factor accounting for 3-D effects
k_k = discrete roughness correction
Δf_{e_t} = tip drag
Δf_{e_i} = wing/fuselage interference drag
Δf_{e_F} = drag due to flap tracks and gaps.

The parameter C_f in Eq (4.2) is the turbulent flat plate friction drag defined previously in Fig 3.2 as a function of Reynolds number and surface roughness. It is assumed that turbulent conditions exist over the entire wing on all airfoils including the so-called laminar flow airfoils such as the 65-series employed on the hypothetical helicopter. This is due to the fact that the manufacturing roughness is usually so high that laminar flow cannot be maintained over any significant area. This often results in higher drag values than were measured during two-dimensional wind-tunnel testing on idealized models, which are generally sufficiently smooth to permit the development of some degree of laminar flow near the leading edge. This difference is illustrated by a comparison of the predictions of Eq (4.2) with the two-dimensional tests[2] presented in Table IV-2. This data is determined at $c_\ell = 0$; therefore, the cambered airfoils (65_3–618) airfoil at cruise c_ℓ will show even larger discrepancies between tests of smooth models and predictions, since the minimum c_d for these airfoils occurs at the design c_ℓ and not at $c_\ell = 0$. For example, the 65_3–618 airfoil c_d decreases from 0.0075 at $c_\ell = 0$ to 0.007 at the design c_ℓ which, for this airfoil, is $c_\ell = 0.6$.

AIRFOIL	PREDICTED c_d	EXPERIMENTAL c_d (REF 2)	$R_e \times 10^6$
65_3–618	0.009	0.0075	4.7
0012	0.00816	0.0059	6
23012	0.00816	0.0072	6

TABLE IV-2 COMPARISON OF PREDICTED AND MEASURED SECTION DRAG COEFFICIENTS AT $c_\ell = 0$

t/c; %	k_t
12	2.042
18	2.077
24	2.12

TABLE IV-3 WETTED AREA FACTOR

The exposed wetted area, S_{w_e}, is equal to $S_{p_e} \times k_t$ where S_{p_e} is the exposed planform area outboard of the fuselage cutout (61 ft^2) and k_t is the planform area factor (wing airfoil perimeter divided by the chord). The factor k_t for various airfoil t/c values is given in Table IV-3.

The total hypothetical wing profile drag coefficient (C_{D_0}) based on the wing planform area extending to the fuselage centerline ($S = 101\ ft^2$) is $C_{D_0} = 0.0095$. This value will be used in all subsequent power required sample calculations.

The $k_{3\text{-}D}$ term in Eq (4.2) accounts for the three-dimensional effect of airflow supervelocity on skin friction and pressure drag. As shown in Fig 4.14 (based on empirical data[7,8]), the skin friction drag and pressure drag increase with increasing airfoil thickness-to-chord ratio (t/c). For the 65-series or other laminar flow airfoils where the maximum thickness is located further aft than in conventional ones, there is less skin friction drag, due to lower average supervelocity; however, moving the maximum thickness aft increases the pressure drag. For airfoils with $t/c < 27$ percent, the $k_{3\text{-}D}$ factor decreases as the maximum thickness location moves aft. However, for $t/c > 27$ percent, the $k_{3\text{-}D}$ factor increases. For the hypothetical wing design with $t/c = 18$ percent, and maximum t/c occurring at approximately 40 percent, $k_{3\text{-}D} = 0.37$.

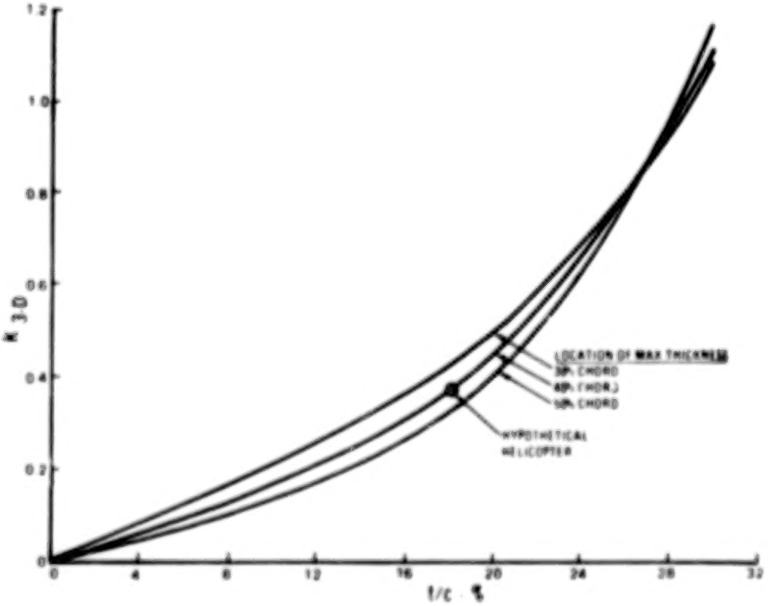

Figure 4.14 Three-dimensional effects for wing and tail surfaces

The terms k_k and Δf_{e_t} in Eq (4.2) are the roughness correction and wing-tip drag. The three-dimensional flow past the tip has a lower average supervelocity than that of the two-dimensional conditions found inboard; therefore, if rounded tips are employed to prevent local separation, the Δf_{e_t} term will be zero or negative[7]. The roughness correction for a wing with flush rivets over the first one-third and mushroom rivets over the aft two-thirds, is 7 percent ($k_k = 0.07$). Using round-head rivets over the entire chord increases this correction to 9 percent. The 7-percent value is assumed for the hypothetical helicopter.

The next term in Eq (4.2), Δf_{e_i}, is the drag due to wing/fuselage interference effects. This drag component comes from the superposition of supervelocities at the wind-body intersection, resulting in increased pressure drag due to a more adverse trailing edge pressure gradient. The interference drag is a function of the airfoil thickness ratio, wing vertical and longitudinal location, location of airfoil maximum thickness, and fillet size and shape. An empirical expression for the interference drag is as follows[7,8]:

$$\Delta f_{e_i} = 1.5(t/c)_{wf}^3 (c_{wf})^2 k_f k_{v\ell} k_L \tag{4.3}$$

where

$(t/c)_{wf}$ = wing thickness/chord ratio at the fuselage
c_{wf} = wing chord measured at the fuselage; ft
k_f = fillet factor
$k_{v\ell}$ = vertical location factor, and
k_ℓ = longitudinal location factor.

Eq (4.3) was developed for conventional airfoils; however, Ref 7 indicates that it is valid for laminar flow profiles if optimum size fillets are employed. The optimum fillet extends beyond the trailing edge of the wing, and has a radius-to-chord ratio of approximately 8 percent. It provides an approximate reduction in interference drag of 35 percent ($k_f = 0.65$). The hypothetical helicopter is assumed to have the required fillet radius on the lower surface; however, the upper surface intersects the nacelles and the resulting discontinuity reduces the fillet effectiveness; therefore, $k_f = 1.0$ is used.

The longitudinal location factor in Eq (4.3) is $k_\ell = 1.0$ for wings located approximately at the midpoint (longitudinally) of the fuselage[7]. The vertical location factor varies from $k_{v\ell} = 1.0$ for the mid-wing configuration to $k_{v\ell} = 2.0$ for high or low wing locations.

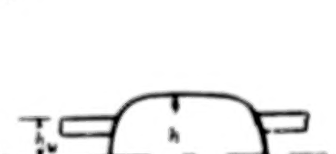

For High or Low Wing, $|h_w/(h/2)| = 1.0$:

$k_{v\ell} = 2.0$

For Mid-Fuselage Location, $h_w/(h/2) = 0$:

$k_{v\ell} = 1.0$

Figure 4.15 Vertical location factors

The interference drag is higher for high- or low-wing installations due to the thicker boundary layer at the acute wing-body intersection. For designs such as the hypothetical helicopter with $|h_w/(h/2)| = 0.7$, the factor $k_{vL} = 1.4$. Substituting the hypothetical helicopter location factors in Eq (4.3), and noting thar $t/c = 0.18$ and $c_{wf} = 4.58$ ft; $\Delta f_{e_I} = 0.257$ ft^2.

The last term, Δf_{e_F}, in Eq (4.2) is the drag due to exposed flap tracks (or actuators) and gaps remaining after the flaps are retracted. Ref 7 indicates that the gaps due to full-span flaps increase the basic wing drag by approximately 3 percent, while drag contributions of the flap track and exposed actuator vary, depending on their individual locations. The hypothetical wing design is assumed to be relatively clean with a combined gap and track drag equal to 5 percent of the basic wing drag.

The total hypothetical wing profile drag can be calculated using the variables derived above and assuming that $C_f = 0.00357$ and the exposed wetted area $S_{w_e} = 127$ ft^2. This C_f value corresponds to $R_e = 4.7 \times 10^6$ (150 kn, 4000 ft/95°F); assuming a surface roughness of $k = 1.2 \times 10^{-3}$ inches (Fig 3.2). Substituting these values in Eq (4.2) gives

$$f_{e_w} = [0.00357 \times 127(1 + 0.37 + 0.07) + 0.257]1.05 = 0.955 \text{ ft}^2 .$$

Wing Induced Drag – The wing induced drag coefficient (based on S) as defined from the lifting-line theory[2] is

$$C_{D_i} = C_L{}^2/AR_e\kappa \qquad (4.4)$$

where

AR_e = effective wing aspect ratio

κ = induced drag factor

C_L = wing lift coefficient.

Standard fixed-wing reference texts often refer to κ as the Oswald efficiency factor. It accounts for the increase in induced drag due to deviations of the wing spanwise distribution from the optimum elliptical shape, and is a function of wing taper and aspect ratio[2]. If the wing is twisted, additional factors must be applied.

The effective aspect ratio AR_e in Eq (4.4) is the geometric aspect ratio ($AR = b^2/S$) corrected for fuselage cutout effects, where b is the total span (wing-tip to wing-tip). The effective aspect ratio is lower than the geometric aspect ratio but, because of wing-lift carry-over effects, is higher than that obtained by using the portion of the wing span outboard of the fuselage cutout. Pressure measurements in this region have shown that the lift extends onto the fuselage – resulting in an effective semispan ($b_e/2$) as shown in Fig 4.16. By defining a wing-fuselage induced drag factor, $\kappa_{wf} = (b_e/b)^2$,

$$AR_e = \kappa_{wf} AR. \qquad (4.5)$$

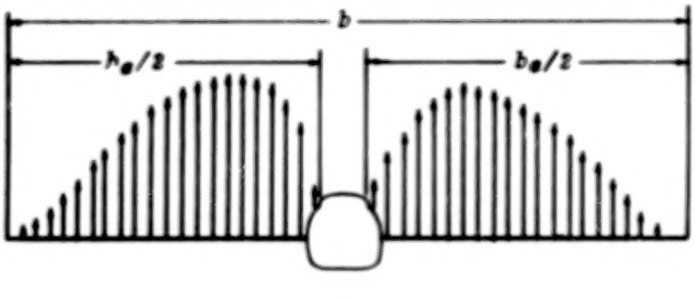

Figure 4.16 Wing-lift carryover

The factor κ_{wf} is determined empirically from wind-tunnel measurements by plotting the incremental wing test results in terms of C_D versus C_L^2, as shown in Fig 4.17.

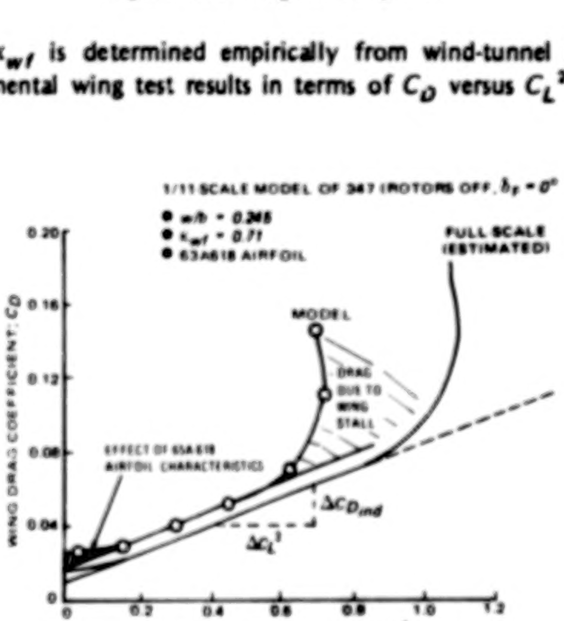

Figure 4.17 Determination of fuselage/wing interference factor κ_{wf}

The nonlinear region at low-lift coefficient values evident in this figure is due to the increase in profile drag with decreasing c_ℓ; characteristic of the 65A-618 airfoil (design $c_\ell = 0.6$). The nonlinear region at high C_L^2 values is due to wing stall. The full-scale wing will have a larger linear C_L^2 region due to the effect of Reynolds number on $C_{L_{max}}$ and the profile drag will be lower. Using the slope of the linear portion of this curve $(\Delta C_D/\Delta C_L^2)$ and κ (Ref 2), Eq (4.4), when rearranged, becomes

$$\kappa_{wf} = (\Delta C_L^2/\Delta C_D)(1/\pi AR\kappa).$$

Values of κ_{wf} for other wing/fuselage configurations are presented in Fig 4.18 as a function of the fuselage width-to-wing span ratio w/b. As shown, κ_{wf} decreases with increasing amounts of wing cutout, and is independent of flap angle setting and aspect ratio. The factor κ, used to establish κ_{wf}, is also shown as a function of AR and taper ratio c_t/c_r. As κ increases, AR decreases and is maximum at $c_t/c_r \approx 0.5$, indicating that lower AR wings with $c_t/c_r \approx 0.5$ have lift distributions close to being elliptical in shape. For the hypothetical wing, $w/b = 0.325$, $\kappa_{wf} = 0.62$, and $\kappa = 0.996$. The effective aspect ratio of this configuration is $AR_e = 3.72$, or almost 40 percent less than the geometric value.

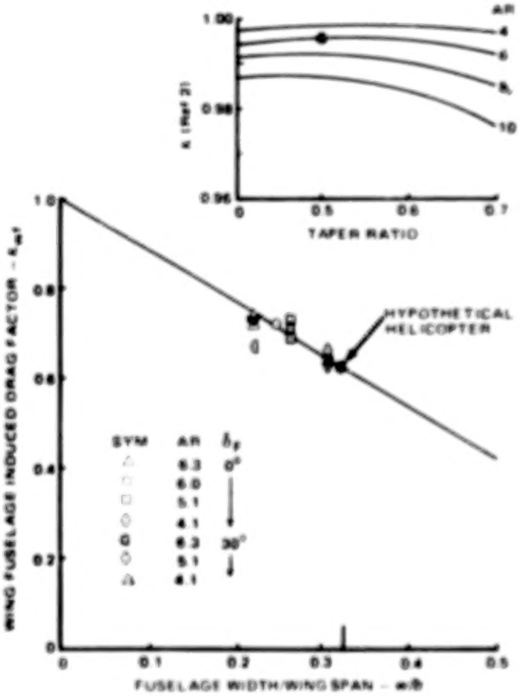

Figure 4.18 Effect of fuselage width on κ_{wf}

Rotor/Wing Interference Drag – Rotor/wing interference drag ($D_{i_{rw}}$) occurs because the wing is located in the downwash of the rotor. As shown in Fig 4.19, the rotor downwash tilts the wing lift vector aft relative to the aircraft forward speed (remote velocity), thus creating a rotor induced wing-drag component $D_{i_{rw}} = L_w \sin\beta$; with β denoting the downwash angle $\beta = \tan^{-1}(v/V_o)$, where v is the rotor downwash at the wing, and V_o is the velocity of the freestream. Using basic momentum theory relationships and assuming fully developed downwash velocities at the wing $[v = (2v_{id})]$, the following relationship for $D_{i_{rw}}$ can be derived:

$$D_{i_{rw}} = L_R L_w / 2\pi R^2 q \qquad (4.6)$$

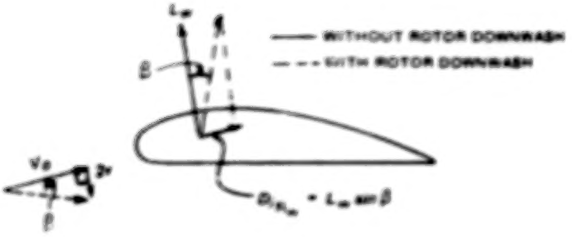

Figure 4.19 Effect of rotor downwash on wing aerodynamic forces

where

L_R = rotor lift
L_w = wing lift
q = freestream dynamic pressure, $\frac{1}{2} V_o^2 \rho$.

Therefore, the interference drag decreases rapidly with speed, and increases with aircraft weight.

Although theory predicts rotor downwash amounting to the average induced velocity ($v = v_{id}$) for wing locations close to the rotor disc center (see Vol I, Fig 3.20), the validity of Eq (4.6), based on the $v = 2v_{id}$ assumption, has been confirmed by flight test measurements of local downwash angles obtained on the CH-46 tandem-wing experimental helicopter. In addition, these measurements showed that the rotor downwash on the right wing was higher than on the left, with the fully-developed value at cruise airspeeds being $v = 2v_{id}$. The hypothetical wing is located closer to the rotor than the CH-46 installation; therefore, the assumption of fully-developed flow is conservative. Eq (4.6) can also be developed from the biplane theory[9,10].

Effect of Wing on Fuselage Attitude – The main rotor tip-path plane for the winged aircraft must be tilted further forward than for the pure helicopter trim condition. This is needed to (1) provide the additional propulsive force required to overcome the wing drag, and (2) to compensate for the reduced rotor thrust resulting from the rotor unloading. This is the reason why auxiliary propulsion is required to achieve very high speeds.

The tip-path plane angle required for the hypothetical aircraft with and without the wing installed is shown in the upper half of Fig 4.20. Calculations based on the simplified equation $a_{TPP} = tan^{-1}[(D_f + D_w)/W]$ and on the trim analysis computer program indicate that at $W = 15{,}000\ lb$, wing $C_L = 0.4$, and a cruise speed of $V = 150\ kn$ at $4000\ ft/95°F$ ambient condition, the tip-path plane must be tilted forward about 2° further than for the wing-off case.

In order to achieve trim about the pitch axis ($\Sigma M = 0$), the fuselage attitude must also become more negative in order to alleviate the incremental nose-down moment created by tilting the tip-path plane relative to the plane normal to the shaft. This change in attitude results in an increased drag and download. The change in fuselage angle-of-attack per degree of tip-path plane tilt depends primarily on the size and incidence of the

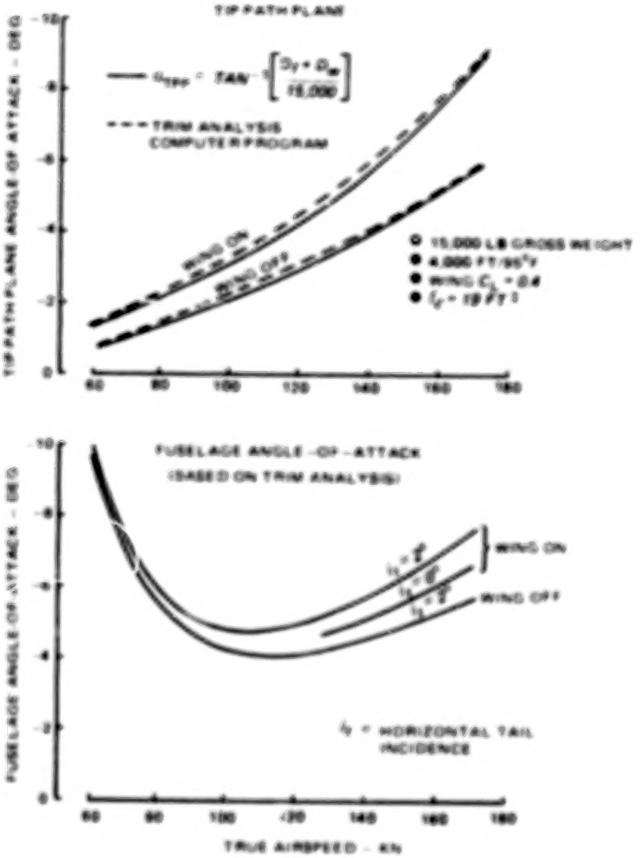

Figure 4.20 Effect of wing on rotor and fuselage angle-of-attack

horizontal tail, the effective hinge offset of the rotor, and c.g. location. Because of the horizontal tail moment contribution, the fuselage angle-of-attack adjustment will be less than the change in tip-path angle as shown at the bottom of Fig 4.20. For the hypothetical helicopter with fixed horizontal tail incidence ($i_t = 2°$), a tip path plane angle inclination change of −2° varies the fuselage cruise angle-of-attack by −1.3°. The resulting increase in fuselage drag and download (Fig 3.10) causes a 2 percent rise in cruise power required at 4000 ft/95°F. Two methods of alleviating this penalty are (1) increase the built-in forward inclination of the main rotor shaft to reduce the fuselage nose-down cruise attitude, and (2) reduce the horizontal tail incidence as noted in Fig 4.20, provided the associated tip-path inclination does not lead to an unacceptable excess of structural loads (i.e., shaft or blade flap-bending loads) or excessive longitudinal control travel. Experimental data illustrating the effect of horizontal tail incidence on the fuselage angle-of-attack of a winged helicopter can be found in Ref 11.

4.2 Effect of Wing Unloading on Induced and Profile Power of the Rotor

Unloading the main rotor may, in principle, decrease its induced and profile power. However, in cruise, the induced power represents a relatively small percentage of the total power required, while the profile power is relatively insensitive to thrust changes unless the rotor is operating at high thrust and forward speeds where stall and compressibility effects become significant. Furthermore, it should be remembered that the rotor diameter is almost always at least twice as large as the wing span. Thus, even neglecting the rotor-wing interaction, the transference of the lift from the rotor to the wing is synonymous with shifting the load from a lift generator having a more favorable (lower) span loading to that of a higher one. Consequently, the combined induced drag of the unloaded rotor and the unloading wing becomes higher than for the rotor alone

The hypothetical helicopter basic wing-off shaft horsepower required developed in Ch III (Fig 3.24) is presented in Fig 3.21 as a function of main rotor lift (thrust component normal to the freestream velocity) for the 4000 ft/95° condition. Here, it is shown that unloading the rotor by 20 percent at 150 kn and 15 000-lb gross weight would reduce the power required by 10 percent if there were no additional power penalties because of the wing. This reduction assumes no change in parasite power.

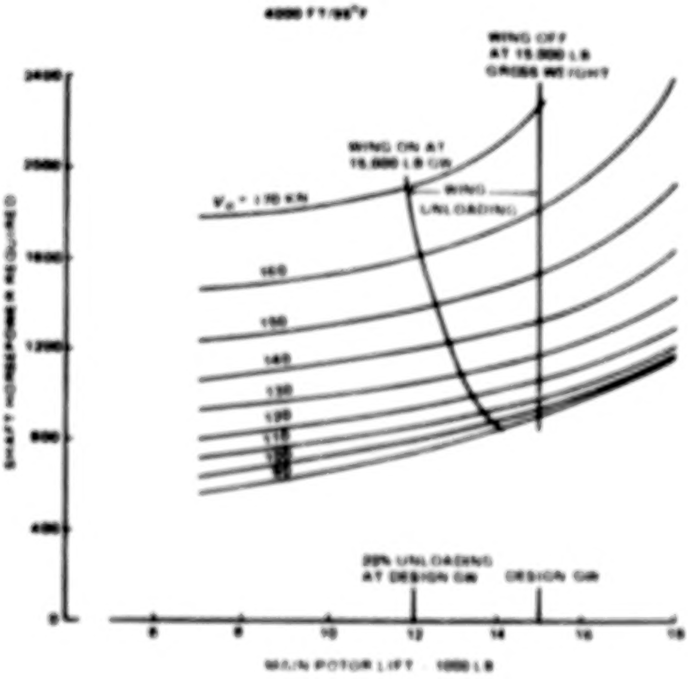

Figure 4.21 Effect of reducing main rotor lift (unloading) on power required

Wind-tunnel testing conducted by Vertol as well as NASA and Bell model tests[8] indicate that the full induced and profile rotor-power required benefits of rotor unloading described above were obtained with no significant unfavorable wing interference effects on the rotor; however these benefits must be combined with wing drag calculations to determine the optimum unloading for minimum total power required as outlined below.

4.3 Determination of Optimum Cruise Unloading

In the considered case, the wing was sized to meet maneuver requirements. Consequently, to minimize level flight performance penalties, the cruise rotor unloading, wing C_L, and incidence angle must be selected in such a way as to make the total power required as low as possible or, in other words, to maximize the total aircraft W/D_e where $D_e = SHP \times 550/V_e$. For example, to make the power required of the winged configuration equal to, or lower than, that of the wingless aircraft, the unloading must be selected in such a way that gains in rotor profile plus induced power must exceed or be equal to the increase in parasite power due to the wing.

EFFECT OF WING LIFT ON TOTAL AIRCRAFT L/D_e

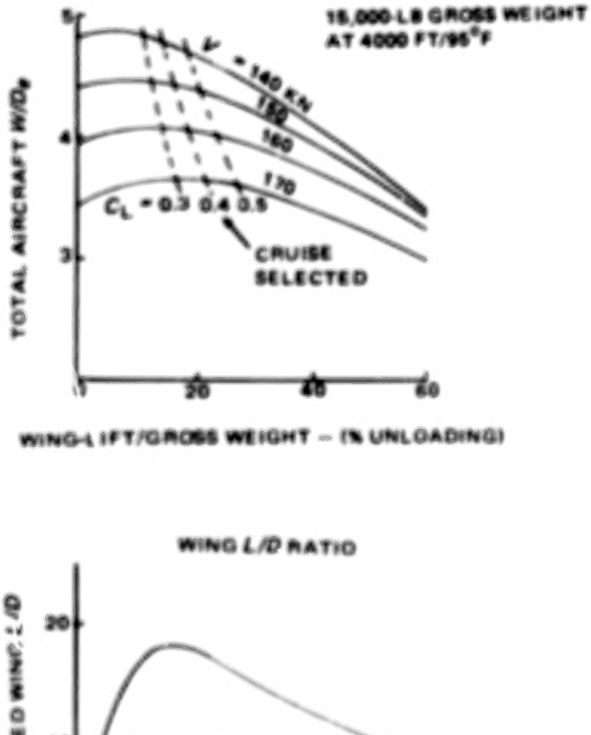

WING L/D RATIO

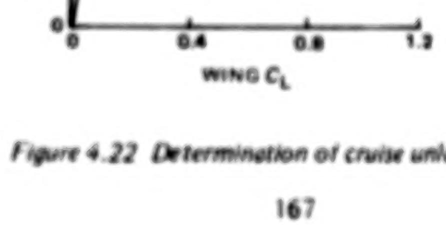

Figure 4.22 Determination of cruise unloading (C_L)

The calculation procedure used to determine wing C_L for the hypothetical helicopter cruising at 4000 ft/95°F, and a gross weight of 15,000 lb is shown in Fig 4.22. In the upper portion of this figure, total aircraft $L/D_e \approx W/D_e$ is presented as a function of wing unloading for cruise speeds of 140 to 170 kn. Isolated wing L/D is presented as a function of wing C_L in the lower half of this figure. The maximum total aircraft W/D_e occurs at an unloading of 10 percent for cruise speeds of 140 to 150 kn and increases to 15 percent at 170 kn. This optimum unloading corresponds to $C_L = 0.3$; however, since the W/D_e curves are relatively flat in this region, a slightly higher C_L of 0.4 was selected in order to reduce the wing download at forward c.g. positions and low airspeeds where the wing α becomes negative. The isolated wing L/D at $C_L = 0.4$ is within 2 percent of the maximum value.

The optimum wing unloading can also be readily determined using rotor maps[12]. Rotor maps are charts of isolated rotor lift versus propulsive force defined for constant power required levels, as illustrated for 170 kn in Fig 4.23 for the hypothetical helicopter. This data, presented in nondimensional form, is based on the Vertol isolated rotor vortex theory computer program (Ch III). The optimum unloading is obtained in one step by simply placing the unloaded rotor thrust versus wing plus fuselage drag trim line on the rotor map and noting where the minimum power required occurs. Rotor maps are particularly useful in cases where the rotor configuration is optimized in conjunction with the wing unloading to achieve improved total aircraft cruise W/D_e. In this case, the geometry of the unloaded rotor can be selected to operate at nondimensional lift levels $(L/qd^2\sigma)$ corresponding to maximum rotor L/D_e[13]. The hypothetical helicopter maximum rotor L/D_e is also noted in Fig 4.23.

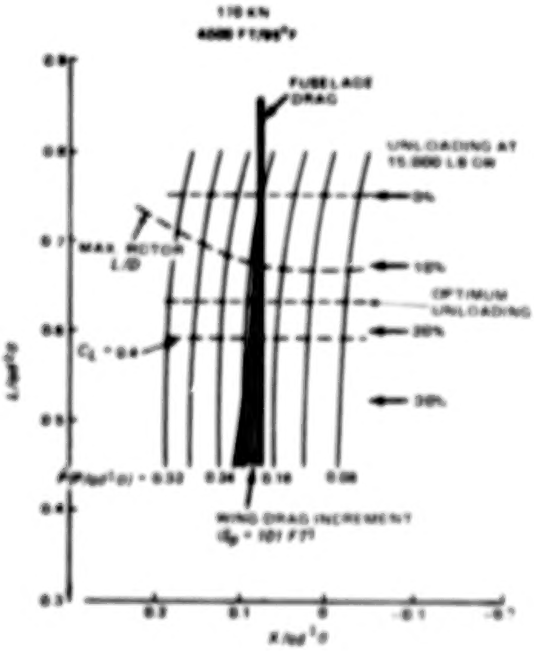

Figure 4.23 Rotor map method of optimizing winged aircraft cruise performance

The total aircraft $W/D_e = f(V)$ relationship associated with operating the wing at $C_L = 0.4$ is shown in Fig 4.24. In spite of the unloading optimization, the W/D_e of the winged helicopter is 2 percent lower than that of the wingless configuration at best range speed. However, at speeds above 160 kn, unloading by the wing provides an improvement due to stall alleviation.

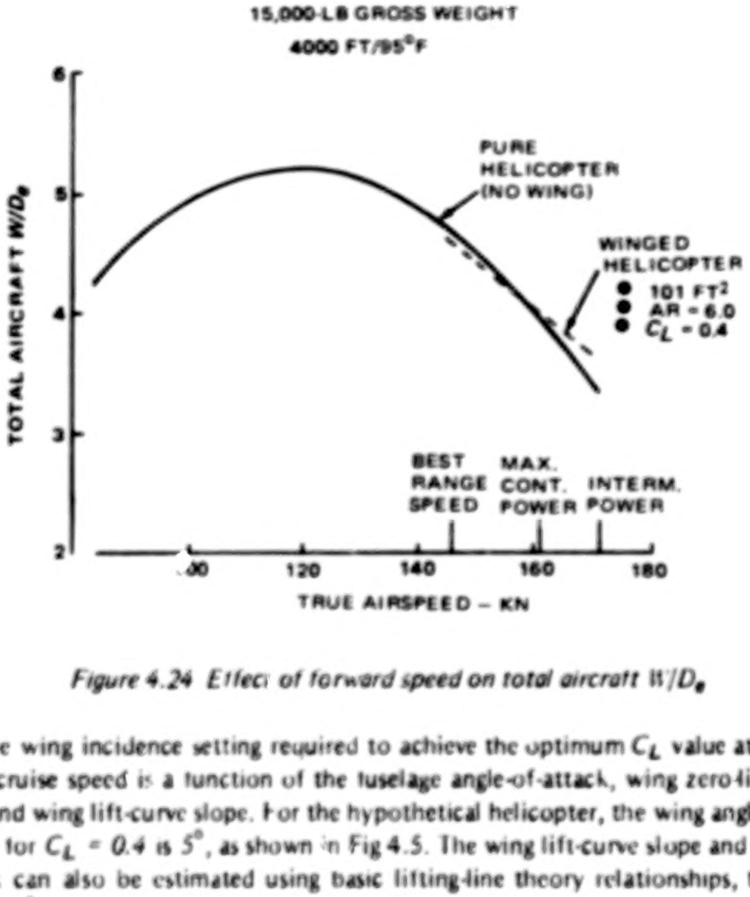

Figure 4.24 Effect of forward speed on total aircraft W/D_e

The wing incidence setting required to achieve the optimum C_L value at the design mission cruise speed is a function of the fuselage angle-of-attack, wing zero-lift angle-of-attack, and wing lift-curve slope. For the hypothetical helicopter, the wing angle-of-attack required for $C_L = 0.4$ is 5°, as shown in Fig 4.5. The wing lift-curve slope and zero angle-of-attack can also be estimated using basic lifting-line theory relationships, two-dimensional data[2], and the effective aspect ratio described previously. Assuming the fuselage cruise angle-of-attack is -5°, the hypothetical wing incidence setting required to achieve $C_L = 0.4^\circ$ is $i_w = 10^\circ$.

The above discussion of wing angle-of-attack refers to the average angle of the right and left-wing panels. However, during the CH-46 tandem-wing program, angle-of-attack measurements showed as much as 4° lateral asymmetry in the downwash field at cruise airspeeds. The right-wing panel (counterclockwise forward rotor rotation) consistently showed lower angles-of-attack and higher downwash angles. Vertol nonuniform downwash analyses and USSR theoretical considerations[13] confirm the existence of a lateral downwash asymmetry. Differential incidence can be used to correct for this effect and prevent asymmetric stall from causing unfavorable roll control problems.

Sample calculations for the hypothetical helicopter illustrating the effect of the wing on level flight power required and mission performance capability are described in this section.

Total Power Required – The hypothetical single-rotor helicopter level flight power required with and without the wing installed, is presented in Fig 4.25 for 4000 ft/95°F conditions. At low gross weights, the wing increases the power required, while at high gross weights, the power required decreases, due to alleviation of stall and compressibility effects. It should be noted that at $W = 18{,}000\ lb$, the power reducing effect of the wing extends to the minimum power speed.

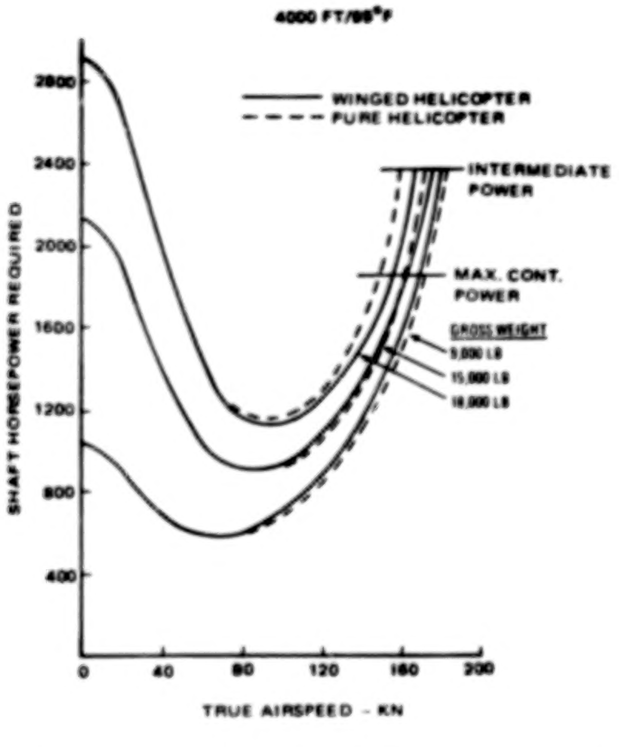

Figure 4.25 Level flight power required at 4000 ft/95°F

The wing-off data shown in this figure was derived in Ch III, and the wing effects were calculated as described above, with the following simplifying assumptions:

(1) Wing $C_L = 0.4$ at all airspeeds
(2) Wing does not affect α_f
(3) Wing profile drag coefficient $C_{D_o} = 0.009$
(4) Rotor downwash is fully developed at the wing location.

These assumptions permit one to calculate power requried for the hypothetical winged helicopter by adjusting the baseline aircraft power required as shown for $W =$

15,000 lb in Table IV-3. The parasite power correction defined in Ch III, Sect 3.3, was applied to all wing calculations.

Payload–Range Capability – The effect of the wing on payload range capability for 4000 ft/95°F conditions is shown in Fig 4.26. The winged helicopter payload capability at zero range is 550 lb lower than that of the baseline aircraft because of (1) reduction of hover OGE gross weight by 200 lb through wing downloading, and (2) a 350-lb increase in weight empty. In terms of range, the wing reduces the full fuel range performance by 10 n.mi, due to increased cruise power required at best range speed as shown in Fig 4.27. The best range speed for a 15,000-lb gross weight aircraft, with and without the wing, is 145 kn.

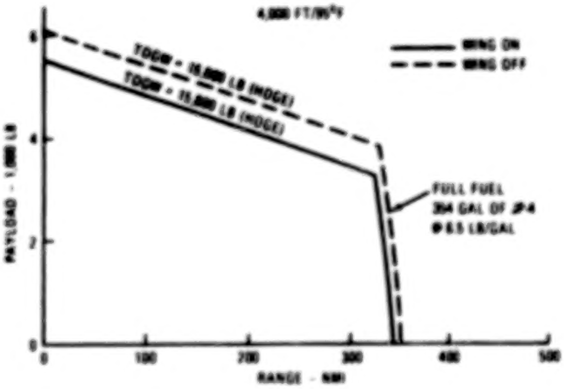

NOTES:

1) SFC INCREASED 5%

2) WEIGHTS (LB):

	WING OFF	WING ON
WEIGHT EMPTY	9,450	9,800
FIXED USEFUL LOAD	430	430
FUEL CAPACITY	2,300	2,300

MISSION DESCRIPTION

1) WARM UP 2 MIN @ MAX. CONT. POWER
2) CRUISE OUT AT BEST RANGE SPEED
3) LAND WITH 10% FUEL RESERVE

Figure 4.26 Winged helicopter payload–range capability

Speed Capability – The wing has no effect on the hypothetical helicopter maximum continuous power speed capability at 15,000-lb gross weight; however, at heavier weights, its presence is beneficial due to the alleviation of stall and compressibility (Fig 4.27). It can be seen that the hypothetical winged helicopter does not have sufficient power to exceed the structural envelope in level flight if operated within the maximum weight and intermediate power limits. The increase in the level flight (1-g) structural envelope, as defined by the hypothetical rotor control system endurance limit, is presented in Fig 4.28 as a function of density altitude. Additional details concerning the stall boundary can be found in Ch III.

15,000-LB GROSS WEIGHT
4000 FT/95°F

①	②	③	④	⑤	⑥	⑦	⑧	⑨	⑩	⑪	⑫	⑬	⑭	⑮	⑯	⑰	⑱
60	9.86	995.9	0.4	0.01375	0.009	0.02275	2.298	398.3	14602	15.23	17.53	0.145	1.0	31.9	−42	1040	1030
80	17.52	1769.5	↓	↓	↓	↓	↓	707.4	14293	8.39	10.69	0.193	0.990	46.4	−50	915	911
100	28.24	2852	↓	↓	↓	↓	↓	1141	13859	5.06	7.35	0.241	0.945	67.4	−56	930	940
120	39.43	3982	↓	↓	↓	↓	↓	1593	13407	3.50	5.80	0.290	0.890	94.7	−65	1060	1090
140	53.67	5421	↓	↓	↓	↓	↓	2168	12832	2.46	4.76	0.338	0.825	132.5	−90	1320	1363
160	70.09	7079	↓	↓	↓	↓	↓	2832	12168	1.79	4.09	0.386	0.735	191.7	−195	1610	1607
170	79.13	7992	↓	↓	↓	↓	↓	3197	11803	1.53	3.83	0.410	0.685	203.8	−370	2260	2094

NOMENCLATURE:

1. SPEED OF FLIGHT, V: KN
2. DYNAMIC PRESSURE, q: PSF
3. $q \times S_w$: ② × 101
4. WING LIFT COEFFICIENT: C_L
5. WING INDUCED DRAG COEFFICIENT: $C_{D_i} = C_L^2/\pi A K_{iw}$*
6. WING PROFILE DRAG COEFFICIENT: C_{D_0}
7. WING DRAG COEFFICIENT: C_D = ⑤ + ⑥
8. WING EQUIVALENT DRAG: D_w/q = ⑦ × 101
9. WING LIFT: L_w = 0.4 × ③
10. ROTOR LIFT, T_r: LB
11. Δf_e OF WING DUE TO ROTOR: D_{iw_r} = ⑨ × ⑩ $/2q^2\pi R^2$
12. TOTAL f_e OF WING + ROTOR: D/q = ⑧ + ⑪
13. $\mu \equiv V/V_t$
14. PROPULSIVE EFFICIENCY: η_p
15. WING SHP = ⑫ × ② × 1.65 × ① /(550 × 0.88)
16. ΔSHP_r DUE TO UNLOADING: (FIG 4.21)
17. SHP, WING−OFF: (FIG 3.24)
18. SHP, WING−ON: ⑰ + ⑯ + ⑮

NOTE: * $\pi A K_{iw} = 11.64$

FIGURE IV-3 WINGED HELICOPTER FORWARD FLIGHT POWER REQUIRED CALCULATIONS

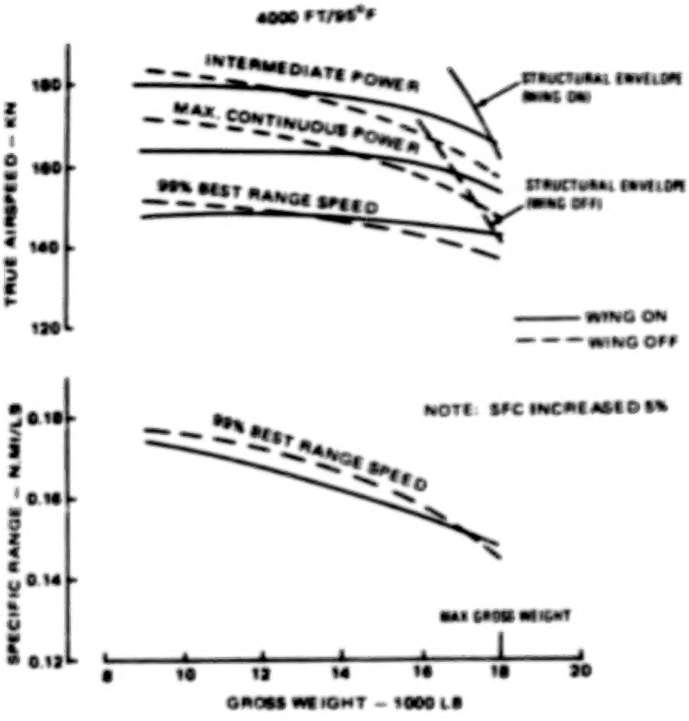

Figure 4.27 Comparison of wing-on and wing-off airspeed and specific range vs gross weight

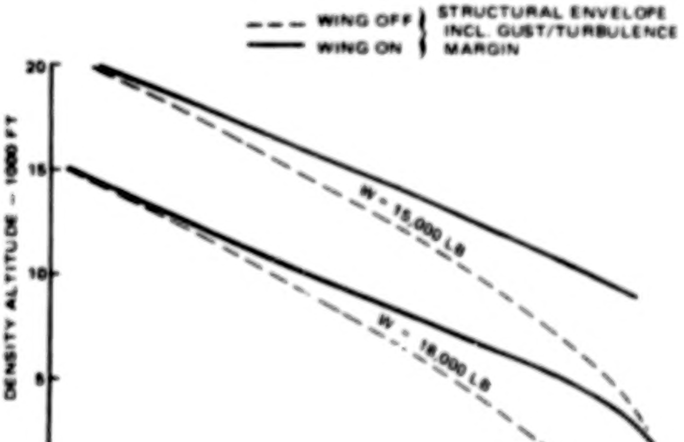

Figure 4.28 Winged helicopter structural envelope

4.5 Climb and Autorotation

The effect of the climb and descent velocity component on wing angle-of-attack and C_L at minimum power speed is shown in Fig 4.29. It can be seen that for rates of climb $V_c > 1000$ *fpm*, the wing with fixed incidence and 0° flap angle produces a download. In descent, the wing angle-of-attack increases and at autorotational rates of descent, the wing angle-of-attack approaches 20° which is well into stall.

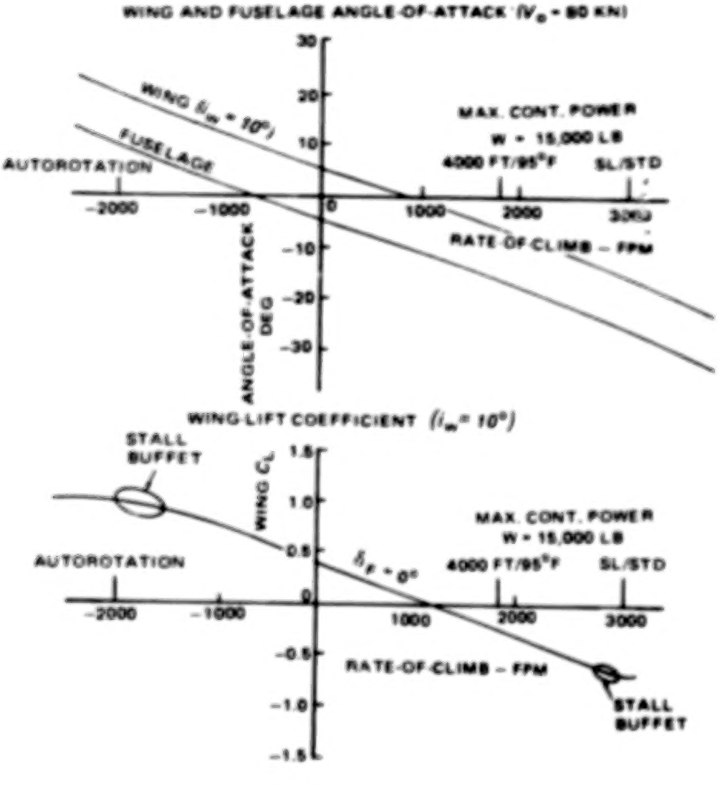

Figure 4.29 Wing C_L and α in climb and descent

These high C_L values and the resulting rotor unloading can cause excessive rotor speed decay during entry into autorotation. Also, control power (moments) is reduced; caused by the reduction in rotor thrust. To alleviate these effects, and the wing download in climb, a variable incidence wing can be used, with the angle-of-attack determined as a function of collective setting and airspeed; however, this design is complex and increases weight empty. Other solutions to the problem are to use flaps or spoilers to control the wing lift. A detailed parametric study is required to optimize the wing-rotor control system.

To illustrate the basic techniques and considerations involved in computing the effect on wings on climb and autorotation performance, sample calculations for the hypothetical helicopter are presented below.

Climb Performance – The effect of installing the wing on dual-engine climb capability at 4000 ft/95°F is shown in Fig 4.30 for the following configurations:

(1) Fixed incidence, flap setting $\delta_F = 0°$
(2) Fixed incidence, variable δ_F $(C_L = 0)$
(3) Variable incidence $(C_L = 0.4)$.

This climb performance was derived by using the simplified climb prediction method described in Ch III (assuming $k_p = 0.85$).

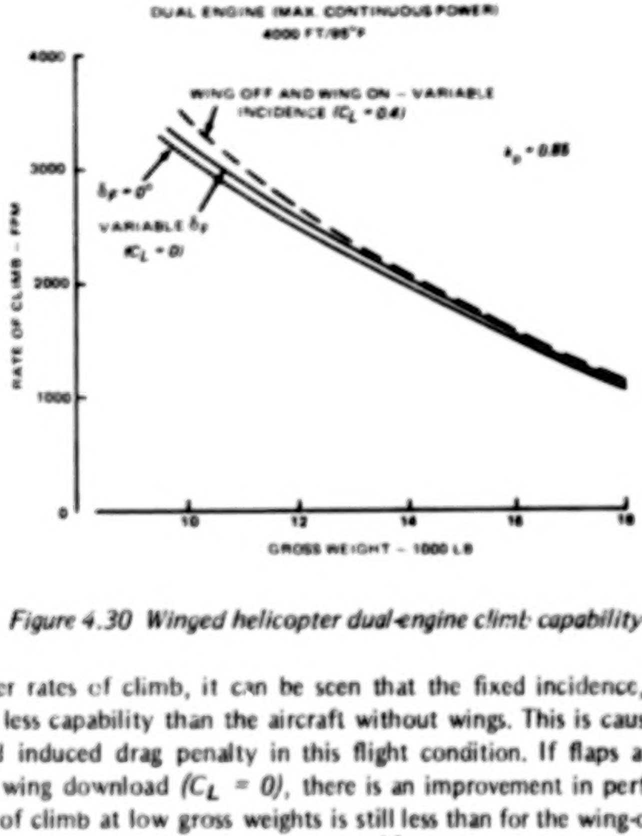

Figure 4.30 Winged helicopter dual-engine climb capability

At higher rates of climb, it can be seen that the fixed incidence, $\delta_F = 0°$, configuration has less capability than the aircraft without wings. This is caused by the wing download and induced drag penalty in this flight condition. If flaps are deflected to eliminate the wing download $(C_L = 0)$, there is an improvement in performance; however, the rate of climb at low gross weights is still less than for the wing-off case because of the incremental wing and flap drag at $C_L = 0$[14]. To eliminate the flap drag, the wing design must be modified to include variable incidence. As noted in Fig 4.30, the variable incidence configuration $(C_L = 0.4)$ has approximately the same climb performance as the aircraft without wings.

The flap angle required to obtain $C_L = 0$ (fixed incidence configuration) is shown in Fig 4.31. It is apparent from this figure that the effectiveness of single-slotted flaps begins to deteriorate at $\delta_F = 30°$, resulting in a maximum practical setting of 45°. At 3000 fpm, the hypothetical helicopter requires $\delta_F = 45°$ to obtain $C_L = 0$. Since wing incidence is fixed, it is not possible to obtain the optimum level flight $C_L = 0.4$ at these rates of climb solely by the use of flaps.

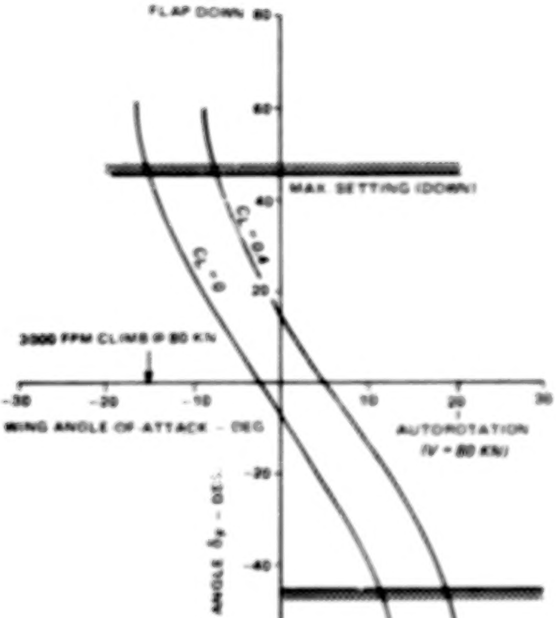

Figure 4.31 Flap settings required to obtain $C_L = 0$ and 0.4

The effect of wings on single-engine service ceiling capability is shown in Fig 4.32. Here, it is assumed that $\delta_F = 0°$ and $C_L = 0.4$ since, at a 100 fpm rate of climb, the wing angle-of-attack does not significantly vary from that in level flight. By unloading the rotor at high altitudes and high rotor lift coefficients, the wings improve the aircraft ceiling capability through reduced power increments associated with blade stall.

Autorotation — As noted in Fig 4.29, steady-state autorotation results in high wing C_L values. This causes two basic problems.: (1) rotor speed decay during entry, and (2) reduced roll control power due to diminished thrust from unloading of the rotor. In addition, roll disturbances can occur as a result of asymmetric wing stall, thus increasing the roll control problem. As described in Ref 6, the second problem is somewhat alleviated with hingeless rotors since this configuration produces greater control moments at low thrust levels. Articulated rotors with small hinge offsets require more rotor thrust for equivalent roll and pitch control.

Rotor speed decay initially occurs upon autorotation entry, and it will continue unless there is a sufficiently low collective setting available to achieve steady-state autorotation within such various aerodynamic and structural limits as rotor stall, longitudinal cyclic limits, blade flapping, and fuselage attitude restrictions. In addition, if the minimum collective setting is too low, it can cause rotor over-speed at high gross weights.

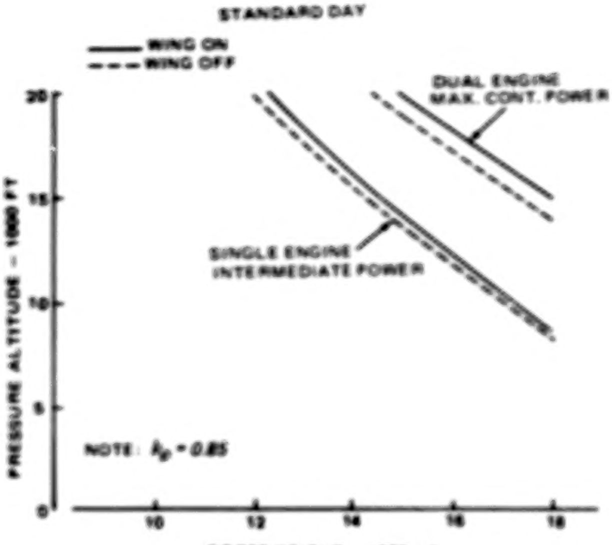

Figure 4.32 Winged helicopter service ceiling

Configuration variables such as adjustable horizontal tail incidence, coupled with wing control devices must be used to achieve autorotation within the various constraints over the full range of operating conditions.

To prevent the difficulties described above, the wing lift must be reduced during autorotation. The complexity of the wing control system or the amount of special devices (spoilers, flaps, incidence controls, etc.) required to reduce the wing lift depends on the wing size and amount of unloading. Ref 6 indicates that small wings with $(L_w/W)_{max} < 0.3$ may be permanently installed. For the hypothetical helicopter at 15,000 lb gross weight and 4000 ft/95°F, $L_w/W = 0.42$ at 150 kn; assuming $C_{L_{max}} = 1.0$ (Fig 4.5). Therefore, because of the size of the wing, special control devices would be necessary.

Flaps were selected as a *special device* to reduce wing lift to illustrate winged helicopter autorotation calculation techniques. As shown in Fig 4.31, the minimum wing C_L that can be obtained for the hypothetical helicopter within the effective range of the flaps ($\delta_F = \pm 45°$) is $C_L \approx 0.4$. The flap schedule and profile drag increment[14] required to keep $C_L = 0.4$ is presented in Fig 4.33 as a function of airspeed. Autorotation capability is computed by taking the wing-on level flight power required (Fig 4.25), and adding the parasite power associated with the flap deflection needed to achieve $C_L = 0.4$. Then the rate of descent is calculated, using the potential energy method described in Ch III, where $k_{pd} = 1.0$.

The resulting performance for 4000 ft/95°F and design gross weight is shown in Fig 4.34. For the wing at a fixed incidence, it can be seen that the flap deflection necessary to maintain $C_L = 0.4$ increases the hypothetical helicopter minimum rate of descent from 2000 fpm to 2300 fpm. This penalty becomes higher with flight velocity, primarily because flap drag also increases with speed. The effect of employing variable incidence rather than flaps to maintain $C_L = 0.4$ is also presented in Fig 3.34. As shown, the variable incidence approach eliminates the flap penalty and reflects only the difference in wing-on and wing-off level flight power required.

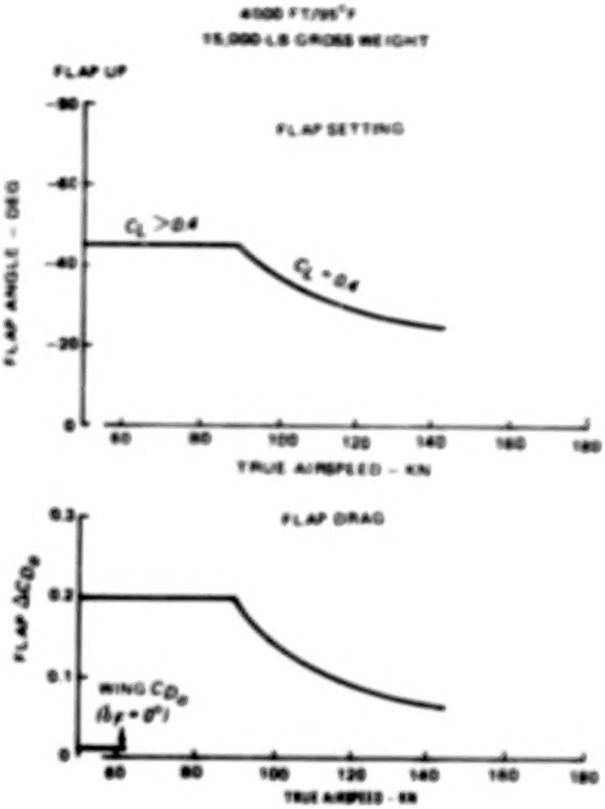

Figure 4.33 Flap angle and flap drag in autorotation ($C_L = 0.4$)

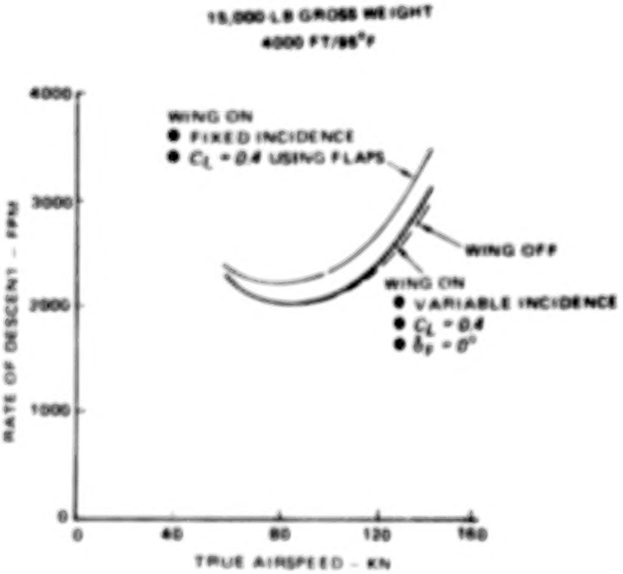

Figure 4.34 Winged helicopt :r autorotational rate of descent

4.6 Maneuver Capability

A summary of the winged helicopter maneuver capability at 15,000 lb gross weight and 4000 ft/95°F is presented in Fig 4.35 where load factor, deceleration and fuselage attitude required are shown as functions of airspeed for a banked turn. A wing flap setting of $\delta_F = 30°$ is assumed in these calculations, and $0.95\,C_{L_{max}} = 1.6$ (Fig 4.5). This wing-lift coefficient is used to provide a margin for gusts and to reduce wing buffeting during the maneuver. The wing angle-of-attack at $C_L = 1.6$ is $\alpha_w = 17.4°$. To achieve this, the fuselage angle-of-attack (α_f) must increase by approximately 12.5° from the level flight $\alpha_f = -5°$; assuming a nominal wing incidence angle of 10°. The rotor tip-path plane angle-of-attack (α_{tpp}) must also increase in order to initiate the maneuver and obtain a balance of longitudinal rotor, fuselage, and horizontal tail moments during the maneuver. To accomplish this, the hypothetical helicopter will require approximately 1° of α_{tpp} change per 0.6° of α_f, as discussed previously in Sect 4.1. The rotor thrust vector is now tilted aft and, when combined with the wing and fuselage drag, results in deceleration ($-\dot{V}$). The deceleration can be expressed in g's as

$$\dot{V} = -(D_w + D_f - X)/W$$

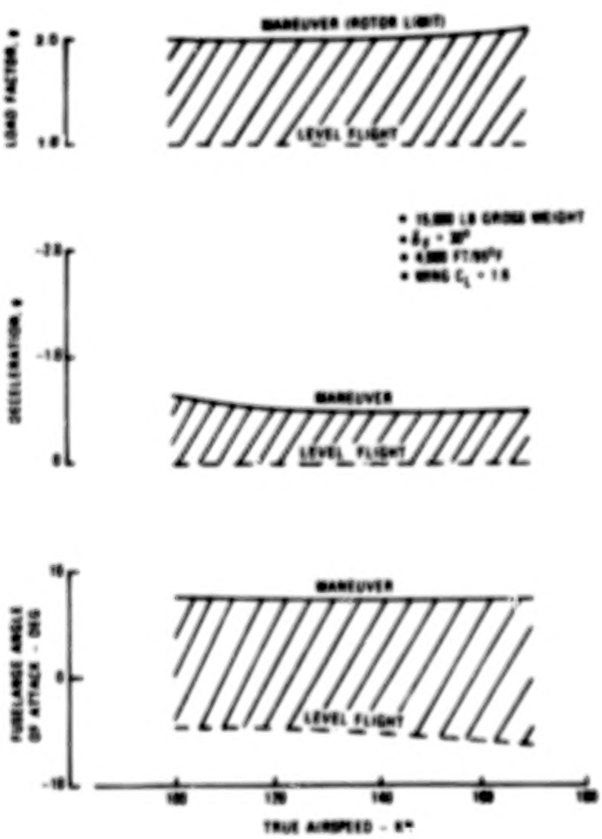

Figure 4.35 Winged helicopter maneuver capability

where

D_w = wing drag; lb
D_f = fuselage drag; lb
X = rotor propulsive force (defined negative if directed aft); lb

As indicated in Fig 4.35, the hypothetical winged aircraft has a $\dot{V} = 0.5g$ deceleration at 150 kn which is equivalent to an airspeed loss of 10 kn per second during the maneuver. No power limits are shown in this figure because the rotor is operating at an equivalent descent angle-of-attack. That is, the rotor propulsive force is sufficiently negative to reduce the power required below the power available. The power margin ($\Delta SHP = SHP_{av} - SHP_{req}$) could have been used to decrease the propulsive force $X = \Delta D_e/\eta_p$ where $\Delta D_e = 550(\Delta SHP)/1.689(V_o)$ and η_p is the propulsive efficiency (the reader is referred to Ch III, Section 3.3). However, this would require changing the horizontal tail incidence during the maneuver in order to keep $\Sigma M = 0$. Deceleration defined by power limits can also be determined using the rotor map method described previously in this chapter (Fig 4.23). This method is also useful in identifying control limits as defined by flying quality or stress considerations.

Decreasing X-force reduces the retreating blade angle-of-attack as well as power required. Therefore, operating at reduced or negative propulsive forces allows the rotor to achieve higher lift levels before stall inception occurs. The stall flutter parameter method or the inplane torque technique (described in Ch III, Sect 6.1) can be used to estimate the propulsive force effects on rotor limits. Model rotor data illustrating the influence of $X = \bar{X}/qd^2\sigma$ on stall flutter type boundaries is presented in Fig 4.36. Additional experimental results can be found in Ref 15. This data indicates that the variation in stall boundaries with $\bar{X}$ is relatively small for μ values up to 0.3. For this reason, the 1-g ($\bar{X} \approx 0.1$) boundary defined in Ch III was used for the maneuver calculations presented above; however, the level flight limits were adjusted for banked turn pitch rate alleviation effects.

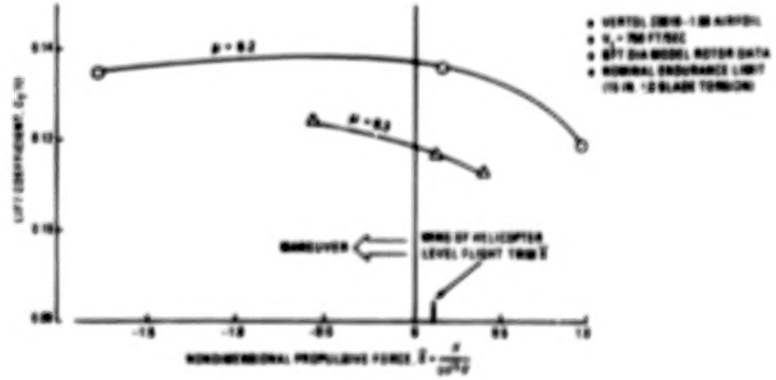

Figure 4.36 Effect of propulsive force on stall boundaries

References for Ch IV

1. Davis, S. Jon and Wisniewski, J. *User's Manual for HESCOMP, the Helicopter Sizing and Performance Computer Program.* Boeing Vertol Report D210-10699-1 (Contract NAS2-6107), NASA CR-152018, Ames Research Center, Moffett Field, Ca. Sept. 1973.

2. Abbott, I.H. and Doenhoff, A.E. *Theory of Wing Sections.* Dover Publications, Inc., 1959 Edition.

3. Loftin, L.K. and Poteat, M.I. *Aerodynamic Characteristics of Several NACA Airfoil Sections at Seven Reynolds Numbers from 0.7×10^6 to 9.0×10^6.* NACA RM No. L8B02, 1948

4. McCormick, B.W., Jr. *Aerodynamics of V/STOL Flight.* Academic Press, 1967.

5. Fry, B. *Design Studies and Model Tests of the Stowed Tilt-Rotor Concept, Vol. III, Appendices.* AFFDL-TR-71-62, July 1971.

6. Lynn, R.R. *Wing-Rotor Interactions.* Journal of Aircraft, Vol. 3, No. 4, July-August, 1966.

7. Gabriel, E. *Drag Estimation V/STOL Aircraft.* Boeing Vertol Rpt. D8-2194-1, Sept. 1968.

8. Hoerner, S.F. *Fluid Dynamic Drag.* Published by the Author, 1965 Edition.

9. von Mises, Richard. *Theory of Flight.* Dover Publications, Inc., 1959.

10. Durand, W.F. *Aerodynamic Theory,* Vol II. Durand Reprinting Committee, 1943.

11. Dumond, R.C. and Simon, D.R. *Flight Investigation of Design Features of the S-67 Winged Helicopter.* Journal of the American Helicopter Society, Vol. 18, No. 3, July 1973.

12. Kisielowski, E., et.al. *Generalized Rotor Performance.* USAAVLABS TR-66-83, R-390, 1966.

13. Baskin, V.E., et.al. *Theory of the Lifting Airscrew.* Translated from Russian to English by W. Z. Stepniewski. NASA TT F-823, February 1976.

14. Royal Aeronautical Society. *Data Sheets. Vol. 4*, RAeS, London, England.

15. Landgrebe, A.J. and Ballinger, E.C. *A Systematic Study of Helicopter Rotor Stall Using Model Rotors.* Preprint No. 804, 30th Annual National Forum of the American Helicopter Society, May, 1974.

TABLE OF CONTENTS

Preface . . . iii 1/A8

CHAPTER I **Introductory Considerations** . . . 1 1/A10

1. Description of the Hypothetical Helicopter Configuration . . . 2 1/A11
1.1 Weights . . . 3 1/A12
1.2 Main Rotor and Tail Rotor Geometry . . . 4 1/A13
1.3 Transmission Limits . . . 7 1/B2
1.4 Airframe Configuration . . . 8 1/B3

2. Performance Summary . . . 8 1/B3

3. Engine Performance . . . 9 1/B4
3.1 General Characteristics of Shaft Turbines . . . 9 1/B4
3.2 Power Ratings & Effects of Ambient Conditions on Engine Characteristics . . . 10 1/B5
3.3 Powerplant for Hypothetical Helicopter . . . 11 1/B6
3.4 Engine Power Constraints . . . 13 1/B8
3.5 Engine Installation Losses . . . 14 1/B9

4. Standard Day Atmosphere . . . 15 1/B10

References for Chapter I . . . 19 1/B14

CHAPTER II **Single-Rotor Helicopter & Vertical-Climb Performance** . . . 20 1/C1

1. Hover Out-of-Ground-Effect Performance . . . 22 1/C3
1.1 General Procedure . . . 22 1/C3
1.2 Power vs Thrust Calculations . . . 23 1/C4
1.3 Example of the Main Rotor Power Required . . . 27 1/C8
1.4 Tail-Rotor Power Required . . . 34 1/D1
1.5 Fuselage Download . . . 37 1/D4
1.6 Transmission and Accessory Losses . . . 43 1/D10

2. Hover In-Ground-Effect (IGE) Performance . . . 44 1/D11
2.1 Rotor Thrust Variation, IGE . . . 44 1/D11
2.2 IGE Download . . . 44 1/D11

3. Hover Ceiling OGE and IGE . . . 46 1/D13

4. Vertical-Climb Capability . . . 48 1/E1
4.1 Detailed Analysis . . . 48 1/E1
4.2 Simplified Vertical Climb Predictions . . . 54 1/E8

References for Chapter II . . . 56 1/E10

CHAPTER III **Forward-Flight Performance** 57 1/E11

1. Introductory Remarks 59 1/E13

2. Drag Estimates 60 1/E14

2.1 Drag of Streamlined Components 61 1/F1
2.2 Drag of Nonstreamlined Components 65 1/F5
2.3 Trim Drag 69 1/F9
2.4 Miscellaneous Items 72 1/F12
2.5 Net Engine Thrust 73 1/F13
2.6 Detailed Sample Drag Calculations for the Hypothetical Helicopter 74 1/F14

3. Methodology for Determining Level-Flight Power Required 78 1/G4

3.1 Trim Analysis Computer Program 79 1/G5
3.2 Nonuniform Downwash (NUD) Correction 82 1/G8
3.3 Parasite Power Correction 87 1/G13
3.4 Determination of Low-Speed Power Required 88 1/G14

4. Examples of Level-Flight Power Required Predictions for the Hypothetical Single-Rotor Aircraft 90 2/A6

4.1 Power Required Based on the Trim Analysis 90 2/A6
4.2 Simplified SHP_{req} Estimates vs Trim Analysis Program 94 2/A10

5. Power Required in Climb and Descent 98 2/A14

5.1 Climb Power Required 99 2/B1
5.2 Descent Power Required 100 2/B2

6. Level Flight and Maneuver Airspeed Envelope 101 2/B3

6.1 Rotor Stall Limits Methodology 103 2/B5
6.2 Level-Flight Airspeed/Altitude Structural Envelope 112 2/B14
6.3 Maneuver Capability 114 2/C2

7. Calculation of Forward-Flight Performance Capability 116 2/C4

7.1 Mission Performance 116 2/C4
7.2 Payload/Range Capability 118 2/C6
7.3 Payload/Endurance Capability 125 2/C13
7.4 Ferry-Range Capability: 129 2/D3
7.5 Speed Capability 135 2/D9
7.6 Forward-Flight Climb Capability 135 2/D9
7.7 Service Ceiling 137 2/D11

References for Chapter III 140 2/D14

CHAPTER IV **Winged Helicopter Performance** 143 2/E3

1. Introductory Remarks 144 2/E4

2. Description of the Winged Helicopter 146 2/E6

2.1 Planform Area/Flap Geometry 146 2/E6
2.2 Wing Aspect Ratio 148 2/E8
2.3 Taper Ratio 149 2/E9
2.4 1/4-Chord Sweep 149 2/E9
2.5 Wing Location 150 2/E10
2.6 Airfoil Section 151 2/E11

3. Hover and Vertical-Climb Performance 151 2/E11
3.1 Wing Download OGE 151 2/E11
3.2 Wing Download IGE 155 2/F1
3.3 Hover Ceiling 155 2/F1
3.4 Vertical Climb Performance 156 2/F2

4. Forward-Flight Performance 156 2/F2
4.1 Effect of Wings on Parasite Drag/Power 157 2/F3
4.2 Effect of Wing Unloading on Induced and Profile Power of the Rotor 165 2/F11
4.3 Determination of Optimum Cruise Unloading 167 2/F13
4.4 Level Flight Performance 169 2/G1
4.5 Climb and Autorotation 174 2/G7
4.6 Maneuver Capability 179 2/G12

References for Chapter IV 181 2/G14

CHAPTER V **Tandem-Rotor Helicopter Performance** 182 3/A5

1. Introductory Remarks 183 3/A6

2. Description of the Tandem-Rotor Helicopter 184 3/A7
2.1 Overlap 184 3/A7
2.2 Gap/Stagger 185 3/A8
2.3 Weights 186 3/A9
2.4 Fuselage Configuration 186 3/A9
2.5 Rotor Hub 186 3/A9
2.6 Engines/Transmissions 187 3/A10

3. Hover Performance 187 3/A10
3.1 Isolated Rotor Power Required 187 3/A10
3.2 Induced Power Overlap Correction 187 3/A10
3.3 Fuselage Download, OGE 188 3/A11
3.4 Ground-Effect Correction 192 3/B3
3.5 Total Hover Power Required Sample Calculations 193 3/B4
3.6 Hover Ceiling Capability 185 3/A8

4. Forward-Flight Performance 195 3/B6
4.1 Level Flight Power Required 195 3/B6
4.2 Power Required in Climb and Descent 206 3/C5
4.3 Structural Envelope 207 3/C6
4.4 Performance Capability 210 3/C9

References for Chapter V 213 3/C12

Appendix A *Performance Guarantees* 214 3/C13
Appendix B *Aircraft Growth* 223 3/D9

CHAPTER V

TANDEM–ROTOR HELICOPTER PERFORMANCE

In order to provide an additional comparison of the single-rotor hypothetical helicopter with other conventional helicopter configurations, a complete performance envelope for a tandem is provided in this chapter. As in the case of the winged version, design gross weight and power installed is assumed to be the same as for the hypothetical machine discussed in Chapters I–III.

Principal Notation for Ch V

C_D	body drag coefficient	
C_{D_e}	body drag coefficient based on maximum sectional area	
$C_P = 550\,HP/\pi R^2 \rho V_t^3$	power coefficient	
$C_T = T/2\pi R^2 \rho V_t^2$	helicopter thrust coefficient	
$C_T' = T/\pi R^2 \rho V_t^2$	rear rotor thrust coefficient	
D	drag	lb
d	rotor diameter	ft
d_s	stagger (distance between rotor axes)	ft
f_e	equivalent flat-plate area	ft^2
g	rotor gap (elevation of one rotor over another)	ft
g	acceleration of gravity	32.2 fps^2
H	height	ft
h	altitude	ft
IGE	in-ground effect	
k_d	download correction factor	
k_g	download factor IGE	
k_{ind}	induced power correction factor	
k_{ov}	induced power correction factor due to overlap	
k_p	climb efficiency factor	
k_{pd}	descent calculation factor	
k_v	download factor	
M	Mach number	
M	moment	ft-lb
N	rotational speed	rpm
OGE	out-of-ground effect	
$ov = 1 - d_s/d$	overlap	
p	atmospheric pressure	lb/ft^2, or inches of Hg
R	rotor radius	ft
r	radial distance from rotor axis	ft
T	total rotor thrust	lb
T	absolute temperature	K
T'	rear rotor thrust	lb

V	aircraft velocity	fps, or kn
v	induced velocity	fps
W	weight (gross weight in particular)	lb
w	width	ft
X	propulsive force (negative aft)	lb
y	lateral distance	ft
γ_o	aft rotor elevation angle	deg, or rad
Δ	increment	
$\delta = p/p_o$	ambient pressure ratio	
ϵ	downwash angle	deg, or rad
$\theta = T/T_o$	ambient absolute temperature ratio	
θ_f	fuselage pitch attitude	deg, or rad
$\mu \approx V/V_t$	rotor advance ratio	
ρ	air density	slugs/ft^3
$\sigma = bcR/\pi R^2$	rotor solidity	
σ_p	air density ratio	
ψ	blade azimuth angle	deg, or rad
ψ	yaw angle	deg

Subscripts

c	climb
d	descent
f	fuselage
fr	front rotor
h	hover
id	ideal
iso	isolated
l	local
n	sequence indicator
o	sea level
ov	overlap
rr	rear rotor
sr	single rotor
t	tip
v	vertical

Superscript

—	nondimensional

1. INTRODUCTORY REMARKS

Techniques for predicting tandem-rotor helicopter performance are presented in this chapter. These techniques are based on methodology developed and refined during the CH-46, CH-47, Model 347, and HLH programs. The basic prediction method consists of an isolated rotor analysis as described in Chs II and III, combined with empirical interference corrections resulting from the mutual aerodynamic effects of the two rotors. This correction was obtained from tandem-rotor, wind-tunnel testing of the UHM (Universal Helicopter Model) shown in Fig 2.20. To illustrate the methodology, sample performance calculations for a hypothetical tandem-rotor aircraft are presented and the results compared with those of the single-rotor aircraft discussed in Chs I, II, and III.

2 DESCRIPTION OF THE TANDEM–ROTOR HELICOPTER

A three-view drawing of the hypothetical helicopter is presented in Fig 5.1, and a detailed configuration definition is given in Table V-1. In this table, the tandem-rotor aircraft is assumed to have the same design gross weight, disc loading, solidity, number of blades per rotor, tip speed, airfoil section, and twist as the single-rotor helicopter. Therefore, the nondimensional isolated main rotor performance (C_P, C_T, μ and M_t) developed for the single-rotor aircraft can be applied to the tandem-rotor helicopter. A brief discussion of the tandem-rotor helicopter configuration is presented below.

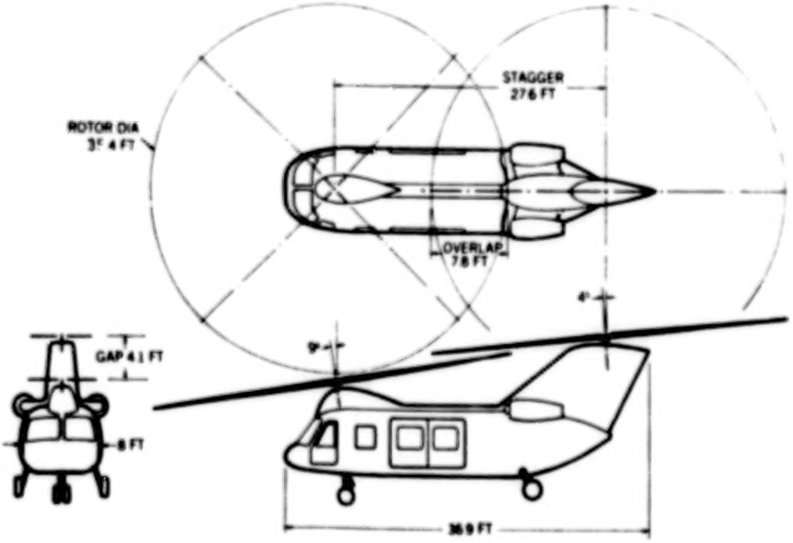

Figure 5.1 Three-View drawing of the hypothetical tandem-rotor helicopter

2.1 Overlap

The definition of overlap is $ov = 1 - d_s/d$, where d_s is the distance between rotors (stagger), and d is the rotor diameter. As noted in Table V-1, the hypothetical helicopter ov is 22 percent. This is about the maximum permissible value for a high solidity, four-bladed rotor because of intermeshing blade clearance limits; however, it can be increased to 34 percent by reducing the number of blades to three per rotor, as in the case of the CH-46 and CH-47 aircraft.

WEIGHTS*	
MAXIMUM GROSS WEIGHT	18,000 LB
DESIGN GROSS WEIGHT	15,000 LB
DISC LOADING	7.64 LB/FT^2
WEIGHT EMPTY	9,450 LB
FIXED USEFUL LOAD	430 LB
FUEL CAPACITY	2,300 LB
ROTOR GEOMETRY	
DIAMETER	35.4 FT
CHORD	17.0 IN
SOLIDITY*	0.102
TIP SPEED*	700 FPS
NUMBER OF BLADES/ROTOR*	4
AIRFOIL*	V23010–1.58
TWIST*	-10°
CUTOUT(r/R)*	20%
RPM	378.1
OVERLAP/DIAMETER	22%
GAP/STAGGER	0.15
TYPE	ARTICULATED
CYCLIC SCHEDULE	CH–46C
AIRFRAME	
PARASITE DRAG	24.7 FT^2
LANDING GEAR*	FIXED
ENGINES (HYPOTHETICAL)*	
RATING SL/STD (INTERMEDIATE/MAX.CONT)	1600/1300
LAPSE RATE	6.0 HP/°F
INSTALLATION LOSSES	1%
TRANSMISSION RATINGS*	
DUAL ENGINE	2900 SHP
SINGLE ENGINE	1600 SHP

*IDENTICAL TO SINGLE–ROTOR CONFIGURATION (TABLE I–1)

TABLE V-1 CONFIGURATION DESCRIPTION OF THE TANDEM–ROTOR HELICOPTER

2.2 Gap/Stagger

The vertical location of the aft rotor relative to the forward rotor is defined as the gap (g), and the relative horizontal position is defined as stagger (d_s) (Fig 5.1). This terminology was derived from biplane theory, since the rotor-rotor interference effects in forward flight are similar to the mutual interference between biplane wings. In addition to the rotor-rotor interference including blade loads and performance, the fuselage clearance, and the effect on weight empty were also taken into consideration when choosing the gap-stagger ratio. The Model 347 gap stagger ratio of $g/d_s = 0.15$ was selected for the hypothetical helicopter. Wind-tunnel testing has shown that increasing this ratio reduces the aft rotor loads and power required; however, it would require an extension of the aft shaft and pylon which would increase the weight empty.

2.3 Weights

The weight empty shown in Table V-1 is assumed to be equal to that of the hypothetical single-rotor configuration. UTTAS preliminary design studies[1] indicate that because of the cutouts in the structure required for side access, the airframe of the tandem is heavier than the corresponding single-rotor fuselage; however, the rotor system weight is lower because of the smaller rotor diameter required to achieve the same disc loading. The net result is that there is no significant difference in total weight empty between single and tandem-rotor aircraft having design weights on the order of 15,000 to 18,000 lb. For the purpose of comparison, the hypothetical tandem-rotor aircraft design gross weight, maximum gross weight, and fuel capacity are also assumed to be equal to those of the single-rotor configuration.

2.4 Fuselage Configuration

The tandem-rotor aircraft fuselage (Fig 5.1) is assumed to have the same nose and forward cabin geometry as the single-rotor helicopter (Fig 1.1), but the aft section of the cabin was lengthened to achieve adequate clearance between the rotors. In addition, the engines were moved aft to drive the combining transmission located in the aft pylon. The afterbody contraction was slightly modified to reduce the size of the fairing between the nacelle and the fuselage resulting from the aft movement of the engines.

The geometry of the forward and aft pylons were determined by directional stability considerations. Unlike single-rotor aircraft which use the tail rotor to augment directional stability, the tandem must rely on the aft pylon geometry. The thickness of the aft pylon is approximately 25 percent of the chord in order to enclose the aft shaft and transmissions. For airfoils of this thickness, truncating of the trailing edge is often employed to improve pylon effectiveness by reducing the degree of trailing edge separation[2,8]. The CH-47C, for example, has a truncated aft pylon trailing edge.

The forward pylon produces a directionally unstable yawing moment about the aircraft c.g. The CH-46 and CH-47 have openings near the pylon leading edge (bleed slots) to achieve improved directional stability. The hypothetical helicopter forward pylon has a low profile shape to minimize the destabilizing side force, while also reducing the drag of the upper controls and forward transmission.

2.5 Rotor Hub

The hub of the tandem-rotor aircraft is assumed to be articulated, with a small hinge offset of 2 percent of the radius. This type of rotor rather than hinglesss was selected because directional control is achieved by differential sideward tilting of the thrust vectors (lateral cyclic pitch). Therefore, the hub moments created by a hingeless rotor would not provide any significant control moments, but would contribute to an increase of the shaft bending loads. This is particularly true for directional control where the differential lateral hub moment would "twist" the fuselage without directly contributing to yaw control.

2.6 Engines/Transmissions

The engine performance and transmission limits described in Ch I for the single-rotor aircraft are also assumed for the tandem. Consequently, comparisons of tandem and single-rotor aircraft performance will reflect differences only in power required. It should be noted that for the tandem, each rotor drive system must be designed to accept more than 50 percent–usually up to 60 percent–of the total rated power since the load-sharing between the rotors varies with flight condition and c.g. position.

3. HOVER PERFORMANCE

The procedure for computing tandem-rotor helicopter hover performance consists of determining the isolated forward and aft rotor power required (see Ch II) and then applying an empirical overlap correction to the induced power component. In addition, the effect of increased induced velocity in the overlap region on fuselage download must be taken into account. Details of this calculation procedure are discussed below.

3.1 Isolated Rotor Power Required

Isolated forward and aft rotor power required is determined by using the vortex theory computer analysis or the "shortcut" techniques described in Ch II. Since the rotors of the hypothetical tandem helicopter have the same twist, solidity, airfoil section, and number of blades as the main rotor of the single-rotor configuration, the nondimensional C_P, C_T and M_t data shown in Fig 2.6 is applicable to each of the tandem rotors. Furthermore, since the tandem also has the same disc loading and tip speed as the single-rotor aircraft, it can be seen that the isolated main rotor referred power required shown in Fig 2.7 is also directly applicable when predicting the combined forward and aft rotor performance. The only differences in total shaft horsepower required between the hypothetical single-rotor and tandem helicopters can be attributed to the overlap correction, elimination of the tail rotor, and somewhat different download levels.

3.2 Induced Power Overlap Correction

Overlapping rotors in hover, as well as tandem configurations in forward flight, have an induced power higher than that of the two isolated rotors combined. By defining k_{ov} as the ratio of the total induced power required in hover by both overlapping rotors to the sum of induced power needed (under the same conditions) by the two isolated ones, the total induced power required (P_{ind}) can be expressed as

$$P_{ind} = k_{ov} k_{ind_h} (T/550)\sqrt{T/4\rho\pi R^2} \qquad (5.1)$$

where

T = total thrust (forward plus aft rotors)

k_{ind_h} = isolated rotor induced power correction factor in hover (Figs 2.9 and 2.10).

The above-defined factor k_{ov} is a function of the amount of rotor overlap as shown by the model test data in Fig 5.2. The data exhibits considerable scatter which may be partially explained by the variations in gap or vertical location of the rotors among the various models tested. This results in varying degrees of rotor wake development, or contraction, as the downwash approaches the adjoining rotor, thus leading to a different level of aerodynamic interaction for the same amount of overlap. More testing is required to fully explore and separate the individual effects of gap and overlap.

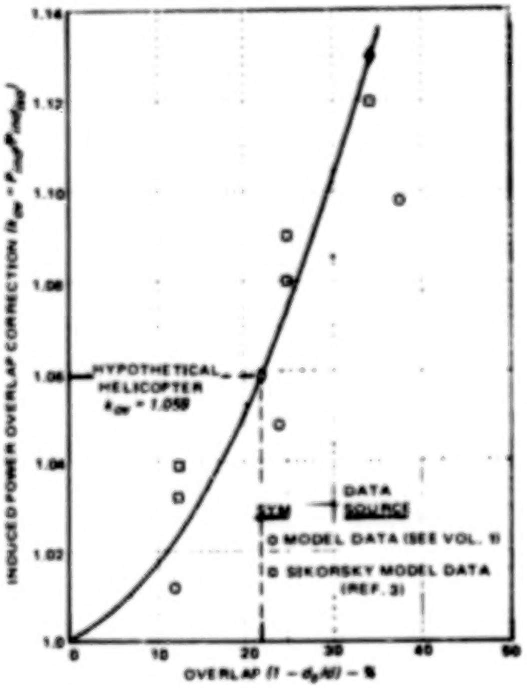

Figure 5.2 Induced power correction for rotor overlap

The curve faired through the UHM data in Fig 5.2 has been used successfully to predict CH-47, CH-46, and Model 347 hover power required when combined with isolated rotor power predictions determined by the vortex theory computer program described in Ch II. Using this line as a reference for the hypothetical helicopter, $k_{ov} = 1.059$. At the design thrust level, a 5.9 percent increase in induced power corresponds to an approximate 5 percent rise in total power required.

3.3 Fuselage Download, OGE

Hover download is computed by integrating the local downwash velocity distributions along the fuselage centerline as described in Ch II. The fuselage is divided into segments as shown in Fig 5.3, and the vertical drag of each segment ΔD_{v_n} is computed as follows:

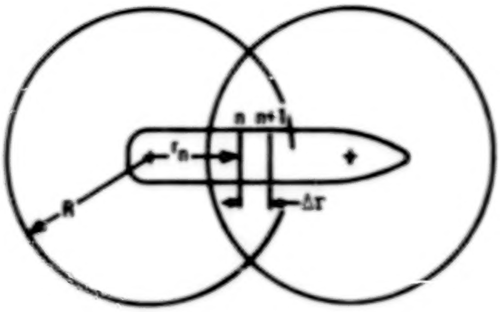

Figure 5.3 Incremental fuselage area for download calculation

$$D_{v_n}/T = C_{D_{v_n}} w_n / 8\pi R^2 \left(k_{v_{n+1}} - k_{v_n}\right) \qquad (5.2)$$

where

T = total thrust of both rotors,

and $$k_{v_n} = \int_0^{(r/R)_n} (v/v_{id})^2 \, d(r/R)$$

where

r/R = relative distance along fuselage from forward rotor centerline
w_n = fuselage width at station n
$v_{id} = \sqrt{T/4\rho\pi R^2}$ = ideal induced velocity.

Eq (5.2) is similar to Eq (2.11); however, the constant in the denominator is increased from 4 to 8 to reflect the difference in the number of rotors.

The integrated downwwsh velocity factor k_v is shown in Fig 5.4 for tandem-rotor configurations of 0, 22, and 34 percent overlap. These factors were derived from the wind-tunnel measurements presented in Fig 5.5. Pressure tapes located at various stations on the fuselage were employed to record the local downwash velocity in the overlap region.. As shown in this figure, the downwash velocity in the overlap area increases as the overlap increases. For example, for 22 percent overlap, the maximum velocity ratio (occurring midway between the rotors), is $v/v_{id} = 2.8$, while for isolated rotors, this ratio amounts to *2.1*. A tandem-rotor helicopter, therefore, will have a higher download than a single-rotor aircraft having the same basic fuselage shape.

Sample download calculations are presented in Table V-2. Here, the 22-percent overlap integrated downwash velocity distribution is applied to the hypothetical helicopter. The fuselage is divided into four segments, with the vertical drag coefficient (C_{D_v}) of each segment equal to the values defined in Ch II. As noted, the total download-to-gross-weight ratio is $D_v/W = 6.34$ *percent*. This value is 2.5 times higher than the single-rotor download of 2.55 percent. A comparison of the tandem and single-rotor

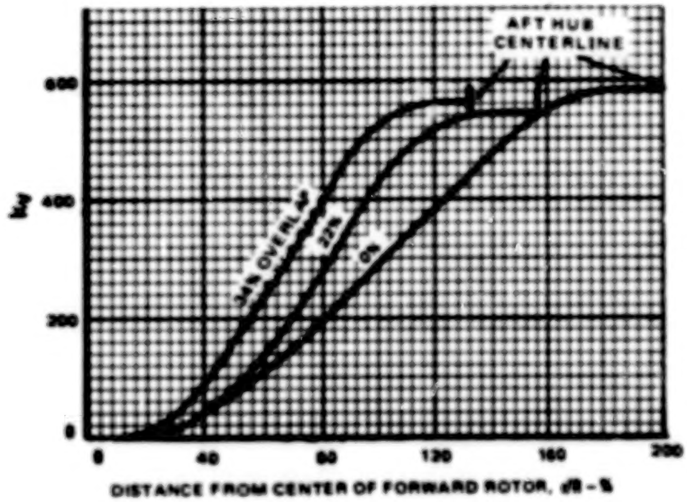

Figure 5.4 Tandem rotor integrated nondimensional downwash velocity (k_v)

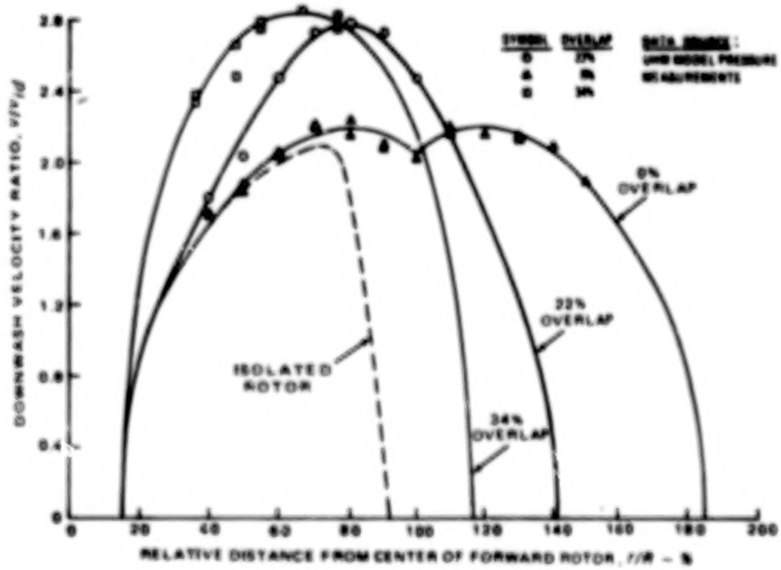

Figure 5.5 Tandem-rotor hover downwash velocity distribution at the fuselage

breakdowns (Tables V-2 and II-1) show that the primary differences occur in the cabin and engine nacelle contributions due to the increase in downwash velocity acting on the cabin, and movement of the nacelles out of the blade cutout region.

STEP	①		②		③	④	⑤	⑥	⑦	⑧	⑨
ITEM	r_n	r_{n+1}	$(r/R)_n$	$(r/R)_{n+1}$	$k_{v_{n+1}}$	k_{v_n}	Δk_v	C_{D_v}	w; FT	$C_{D_v} w/8\pi R$	$\Delta D_v/T$; %
PROCEDURE	DISTANCE FROM FWD ROTOR C_L (FT)		①/17.7 (%)		SEE FIGS 5.3 & 2.19		③ – ④	SEE FIG 2.17	SECTION WIDTH	⑥$_v$ × ⑦ /8π × 17.7	⑧ × ⑤
SECTION											
1. COCKPIT*	3.6	4.8	20.7	27.6	214	207	7	0.5	5.9	0.00663	0.046
2. CABIN											
	3.5	5.4	20.0	31.1	17	0	17	0.4	3.8	0.00344	0.058
	3.5	17.3	20.0	98.0	420	0	420	0.4	8.0	0.00719	3.020
3. NACELLE	17.3	23.5	98.0	135.0	541	420	121	1.2	8.6	0.02320	2.807
4. AFTERBODY	23.5	24.2	135.0	139.0	545	541	4	0.5	5.5	0.00618	0.025

$\Sigma D_v/T = 5.96\%$

$\Sigma D_v/W = 6.34\%$

* NOTE: USE ISOLATED ROTOR DOWNWASH (FIG 2.19)

TABLE V-2 DETAIL SAMPLE CALCULATION OF THE TANDEM–ROTOR HELICOPTER HOVER DOWNLOAD

3.4 Ground Effect Corrections

The effect of operating IGE is to provide thrust augmentation at a fixed power setting and a reduction in fuselage download. A semi-empirical method of correcting the OGE gross weight is employed to account for these effects, as described in detail in Ch II. The specific empirical corrections applicable to tandem-rotor helicopters and sample calculations for the hypothetical helicopter are presented below.

Thrust Variations, IGE – As shown in Fig 5.6, the ratio of rotor thrust IGE to thrust OGE for the tandems-when presented as a function of rotor height to diameter ratio (*H*/*d*)–agrees well with the single-rotor faired data in Ch II. It can be seen that the thrust ratio for the hypothetical tandem-rotor aircraft operating at a 5-ft wheel height is 1.047 (*H*/*d* = *0.54*). This thrust ratio is lower than for the single-rotor configuration because the tandem requires greater fuselage-to-rotor clearance than the hingeless single-rotor helicopter, and has a smaller rotor diameter for the same disc loading. In Fig 5.7, the hub centerlines are assumed to be at an equal distance from the ground in order to simplify the calculations. The actual trim attitude depends primarily on shaft incidence and longitudinal cyclic input which, for tandems, generally varies automatically as a function of airspeed. Actual hovering attitude can be determined from a trim analysis; however, for most calculations, the simplifying assumption of equal hub heights is acceptable.

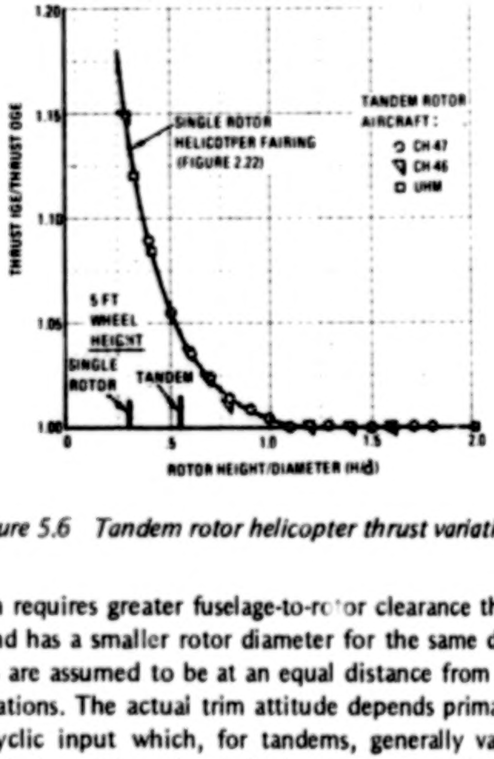

Figure 5.6 Tandem rotor helicopter thrust variation IGE

Download Variation, IGE – The variation of tandem and single-rotor aircraft download occurring in ground effect is presented in Fig 5.8 as a function of the fuselage height above the ground (H_f). The download factor k_g is defined as the ratio of download IGE to download OGE, and is based on model testing. Due to increased downwash velocity over the center of the fuselage, the tandem-rotor helicopter benefits more from ground effect at a given H_f/d than the single-rotor aircraft. However, the tandem-rotor

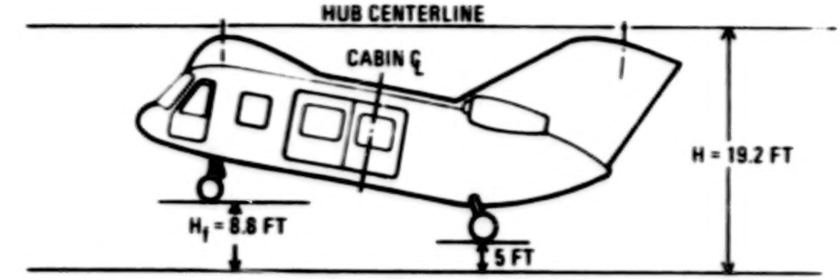

Figure 5.7 Hypothetical helicopter rotor/fuselage

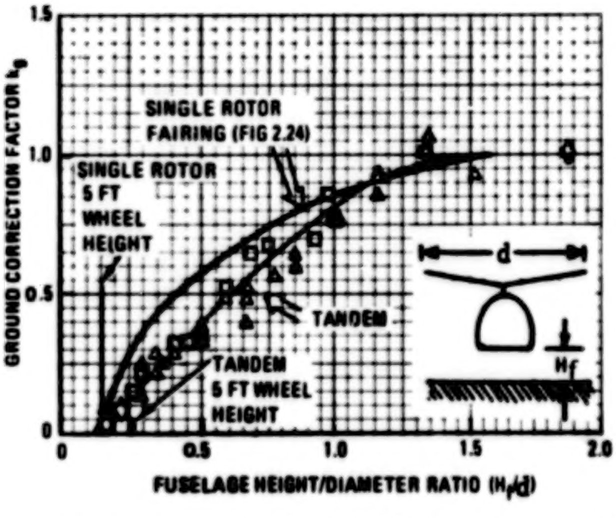

Figure 5.8 Tandem-rotor helicopter IGE download correction

diameter is smaller than that of the corresponding single-rotor aircraft for the same design disc loading, which tends to reduce the IGE benefits. At a wheel height of 5 ft, the hypothetical tandem-rotor download factor $k_g = 0.14$ at $H_f/d = 0.25$, while the hypothetical single-rotor value is $k_g = 0.09$ at $H_f/d = 0.16$.

Gross-Weight Correction, IGE – Substitution of the hypothetical helicopter thrust ratio, k_g, and *OGE* download in Eq (2.14) gives the tandem-rotor, gross-weight ratio as $W_{IGE}/W_{OGE} = 1.10$. The corresponding single-rotor weight ratio is 1.17 (Ch II). Therefore, the tandem derives less benefit from ground effect than the single-rotor aircraft.

3.5 Total Hover Power Required Sample Calculations

Sample calculations of power required in hover for the hypothetical helicopter at 4000 ft/95°F ambient conditions are presented in tabular form in Table V-3. The

①	TOTAL T/σ_p – LB $(T/\sigma_p)_{fr} + (T/\sigma_p)_{rr}$	25080	22800	20520	18240	15960
②	TOTAL ISOLATED ROTOR RHP/σ_p $(RHP/\sigma_p)_{fr} + (RHP/\sigma_p)_{rr}$ PER FIG 2.7	3460	2952	2474	2033	1676
③	$(RHP/\sigma_p)_{ind}$ $(RHP/\sigma_p)_{ind_{fr}} + (RHP/\sigma_p)_{ind_{rr}}$ PER FIG 2.7	3100	2612	2163	1747	1380
④	$(\Delta\, RHP/\sigma_p)_{ind_{ov}}$ (OVERLAP CORRECTION) ③ $\times$ 0.059	183	154	128	103	81
⑤	TOTAL RHP/σ_p ② $\times$ ④	3643	3106	2602	2133	1767
⑥	SHP (⑤ $\times\ \sigma_p)/0.98 + 30$	3032	2589	2174	1788	1478
⑦	W_{OGE} – LBS ① $\times\ \sigma_p \times 0.9404$	19050	17316	15594	13853	12121
⑧	W_{IGE} – LBS ⑦ $\times$ 1.10	20955	19048	17142	15238	13333

NOTE: 4000 FT/95°F

TABLE V-3 HOVER POWER REQUIRED SAMPLE CALCULATIONS

isolated rotor performance, rotor overlap corrections, download adjustments, and IGE corrections described above are used in these calculations – assuming that each rotor carries exactly half of the total thrust. The total isolated power required and induced power are obtained from Fig 2.7, and the transmission and accessory losses are assumed to be equal to the single-rotor aircraft values derived in Ch II, Sect 2.5.

A comparison of the total hover shaft horsepower required determined in Table V-3 with the corresponding single-rotor values developed in Ch II, is presented in Fig 5.9. At 4000 ft/95°F and 15,000 lb gross weight, the tandem-rotor helicopter requires 60 hp, or 3 percent less hover OGE power than the single-rotor aircraft. This power

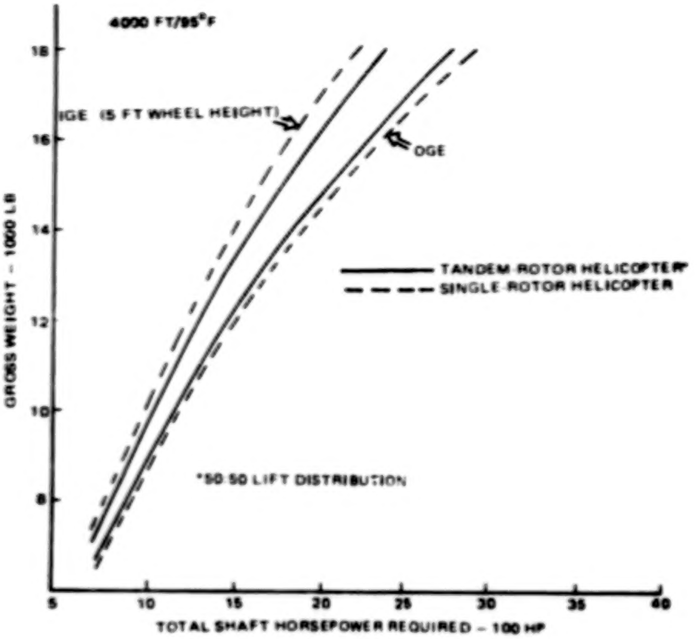

Figure 5.9 Hover power required

decrement reflects the difference between the gain in performance capability due to the absence of the tail-rotor power (13 percent of the total single-rotor SHP required) versus losses resulting from overlap (6 percent of the total SHP), and increased download (equivalent to 4 percent SHP increase) However, for IGE conditions, the single-rotor aircraft requires less power than the tandem for a wheel height of 5 ft (Fig 5.9). This is due to the lower relative rotor and fuselage heights (H_r/d and H_f/d) of the single-rotor configuration. At 15,000 lb gross weight, the resulting net increase in power required for the tandem amounts to 105 hp, or 6 percent.

3.6 Hover Ceiling Capability

A comparison of the tandem and single-rotor helicopter hover ceiling capability for 95°F ambient conditions and intermediate power is presented in Fig 5.10. Here, the tandem hover OGE gross weight at 4000 ft/95°F is 16,400 lb versus 16,000 lb for the single-rotor configuration. However, in ground effect, the tandem has approximately 800 lb less gross-weight capability.

4. FORWARD–FLIGHT PERFORMANCE

4.1 Level Flight Power Required

Tandem-rotor helicopter level flight performance calculations consist of determining the aircraft drag, isolated forward and aft rotor power required (Ch III), and then applying an induced power correction to the aft rotor performance to account for aerodynamic interference effects. Rotor stall boundaries are also affected by the interference effects.

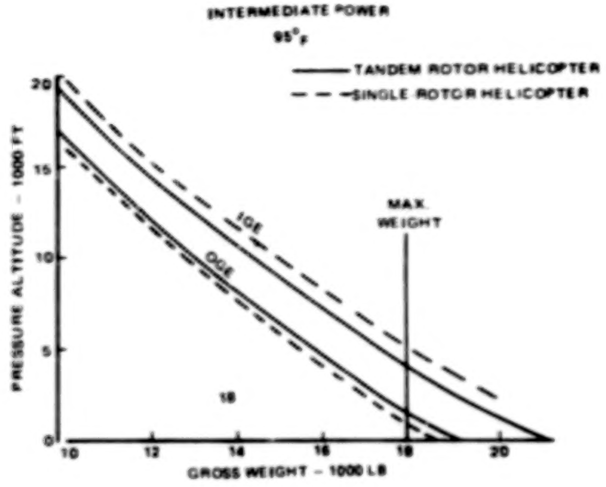

Figure 5.10 Hover ceiling

Parasite Drag – The parasite drag of the hypothetical tandem is $f_e = 25\ ft^2$ versus $f_e = 19.1$ for the single rotor. A comparison of the data presented in Table V-4 with the single-rotor parasite drag breakdown given in Table III-1 shows that 70 percent of this drag variation, or 4.1 ft^2, can be attributed to the higher drag of articulated rotors when compared to hingeless rotors (see Fig 3.9). In addition, the fuselage afterbody contraction ratio of the tandem is lower than that of the single-rotor design, resulting in increased pressure drag. The drag of the forward and aft pylon of the tandem is approximately equal to that of the single-rotor helicopter tail rotor hub plus vertical and horizontal tail.

The width and height of the tandem-rotor helicopter cabin was assumed to be equal to that of the single-rotor design. However, it is stretched lengthwise to provide a 22 percent overlap in the distance between the rotors. Therefore, the cabin width could be reduced by approximately 20 percent and still provide the same internal volume for payload. This procedure would reduce f_e by approximately 0.6 ft^2 from the value shown in Table V-4.

The trim drag of 1 ft^2 shown in this table corresponds to $\alpha_f = -6°$ rather than $\alpha_f = -5°$ used for the single-rotor configuration. The tandem α_f is based on a trim analysis similar to the single-rotor program described in Ch III. The fuselage characteristics input for the single and tandem-rotor aircraft are shown in Table 3.14. The single-rotor helicopter fuselage trim angle-of-attack shown in Fig 5.11 is much more sensitive to c.g. position than the tandem because it must change attitude as the c.g. is varied in order to achieve a moment balance. In contrast, the lift of the tandem helicopter is simply redistributed between the rotors, utilizing differential collective pitch control to trim the aircraft at various c.g. positions with little attitude variations. This also provides the

ITEM	WETTED AREA (FT^2)	FRONTAL AREA (FT^2)	$C_{D_e}; C_f$	INTERF. FACTOR I	Δf_e (FT^2)	f_e (FT^2)	COMMENTS
BASIC FUSELAGE							
SKIN FRICTION DRAG	617		0.00255		1.84	2.94	PRESSURE DRAG DUE TO REDUCED
PRESSURE DRAG		46	0.024		1.10		AFTERBODY CONTRACTION
AFT PYLON							
SKIN FRICTION AND PRESSURE DRAG	184		0.003	1.2	1.44	1.44	SEE CH III
FORWARD PYLON							
PYLON		5.8	0.10		0.58	0.82	C_{D_e} BASED ON CH–46 TESTING
EXPOSED SHAFT		0.17	1.2	1.2	0.24		
ROTOR HUBS						8.41	BASED ON TANDEM ARTICULATED ROTOR HUB DRAG TRENDS (FIG 3.9)
LANDING GEAR						4.90	SAME AS SRH (SEE CH III)
TRIM DRAG (Δf_e for $\Delta \alpha_f = -6°$)						1.0	
ENGINE NACELLES						1.7	SAME AS SRH (SEE CH III)
ROUGHNESS & LEAKAGE						1.3	6% } SEE CH III
PROTUBERANCES						2.1	10% }
COOLING LOSSES						0.3	
					TOTAL	25.0	

TABLE V-4 TANDEM–ROTOR HELICOPTER DRAG ESTIMATION

tandem with a larger c.g. range; however, because of nonoptimum load sharing between the rotors, some penalty in rotor power and stall speed may be encountered.

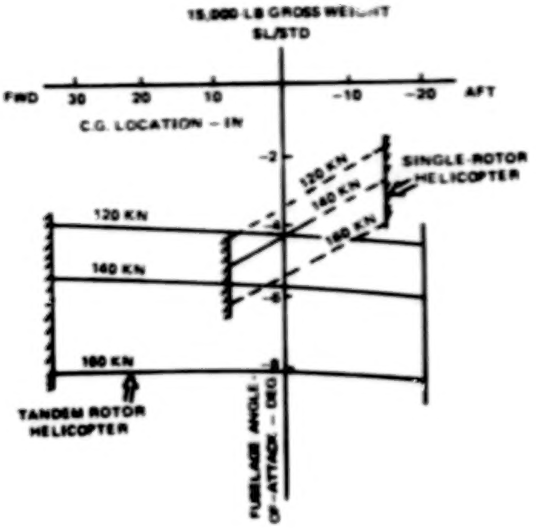

Figure 5.11 Effect of c.g. on fuselage angle-of-attack

The effect of airspeed on fuselage angle-of-attack is also evident in Fig 5.11. At speeds above 140 kn, the tandem has a considerably larger nose-down angle-of-attack than the single-rotor helicopter. This is due to the increased drag of the tandem and differences in longitudinal cyclic pitch angles. The hypothetical tandem cyclic angles are assumed to be input automatically as a function of forward speed, or dynamic pressure, according to a cyclic trim schedule similar to the CH-47 aircraft (Fig 5.12). Unlike single-rotor aircraft, the pilot of the tandem generally does not control the longitudinal cyclic input. The large nose-down pitch attitudes of the tandem at high speeds can be reduced by increasing the automatic cyclic trim inputs, provided it does not cause unacceptable increases in noise, vibration, and stress levels. An alternate method would be to increase the built-in forward inclination of the shaft.

Rotor-Rotor Interference Effects – In forward flight, the aft rotor operates in the wake of the forward rotor. The total axial velocity component of flow through the rear rotor is larger than for the isolated one. Consequently, its induced power is also higher. As described in Vol I, Ch II.6, this interference effect can be expressed in terms of the factor k_{ind}, which is defined as $P_{ind}/2P_{id}$, where P_{ind} is the total forward and aft rotor induced power, including rotor-rotor interference effects, as well as tip losses and blade root cutout effects. The term P_{id} is the ideal induced power of one rotor. As shown by the wind-tunnel data in Fig 5.13, the induced power k_{ind} is a function of the elevation of the rear rotor above the centerline of the forward rotor streamtube, h_{rr} (see Vol I, Fig 2.21). A summary of this data was used in the theoretical correlation presented in Vol I, and includes a 10-percent correction for tip losses and blade root cutout effects. Fig 5.13 shows that the factor k_{ind} is maximum ($k_{ind} = 2.11$) at $h_{rr}/R \approx 0$, where the forward rotor wake passes directly through the aft rotor. The magnitude of k_{ind} decreases when the forward rotor streamtube moves above the rotor, as encountered in autorotation or below the rotor, as found in level flight and climb.

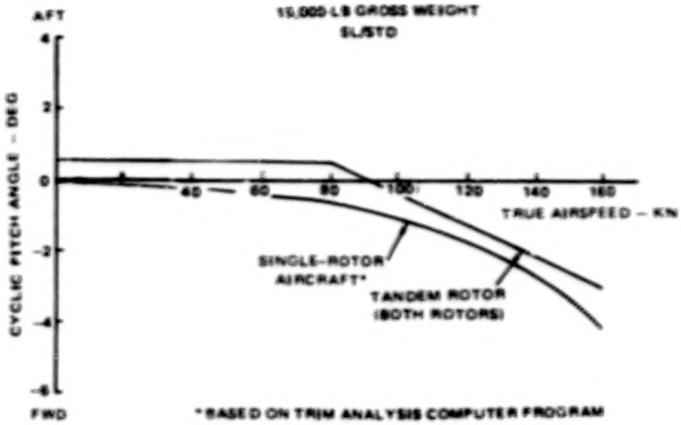

Figure 5.12 Hypothetical tandem-rotor helicopter cyclic trim schedule

The empirical results shown in Fig 5.13 agree with predictions based on the momentum theory considerations described in Vol I. In addition, biplane theory[4] has been used successfully to predict rotor-rotor interference effects by assuming an effective wing span-to-diameter ratio of 0.85 in level flight, and 1.0 in autorotation. The theoretical aspects of rotor-rotor interference effects are also discussed in Ref 5.

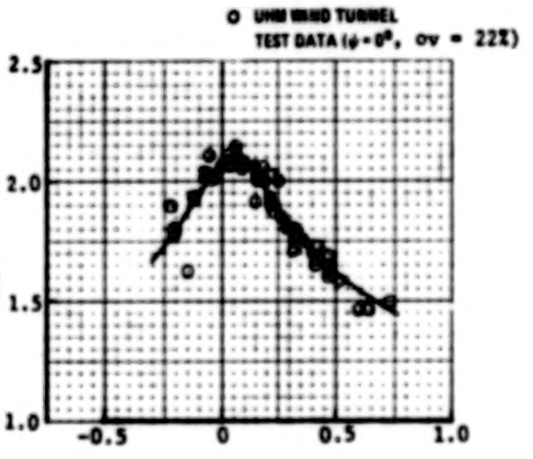

Figure 5.13 Interference effect of the forward rotor on the rear rotor induced power

The test data in Fig 5.13 was obtained for a 22-percent overlap model configuration where rotor wake separation distance h_{rr} was varied by changing the forward rotor thrust, shaft angle, anf forward speed. However, the trends agreed reasonably well with the 0 and 34-percent overlap test data using the h_{rr}/R technique. Correlation of the various overlap configurations might be further improved if the longitudinal as well as the vertical location of the aft rotor hub relative to the forward rotor streamtube is taken into account. Additional study of this effect is required.

In order to use Fig 5.13 for the hypothetical tandem, the value of parameter h_{rr}/R as a function of the rotor overlap (*ov*) and the forward wake separation angle γ

shown in Fig 5.14 should be determined. The angle γ is a function of aircraft pitch attitude (θ_f), forward rotor downwash angle (ϵ), and aft rotor hub elevation angle (γ_o). The specific relationships are:

$$h_{rr}/R = -2(d_s/d)\tan\gamma \qquad (5.3)$$

and

$$\gamma = \theta_f - \epsilon - \gamma_o \qquad (5.4)$$

where

$\epsilon = \tan^{-1}(k_d v/V)$; deg

$\gamma_o = \tan^{-1}(g/d_s)$; deg

v = forward rotor induced velocity based on momentum theory

$v = v_o\sqrt{-\tfrac{1}{2}(V/v_o)^2 + \sqrt{\tfrac{1}{4}(V/v_o)^4 + 1}}$

$v_o = \sqrt{T/4\rho\pi R^2}$.

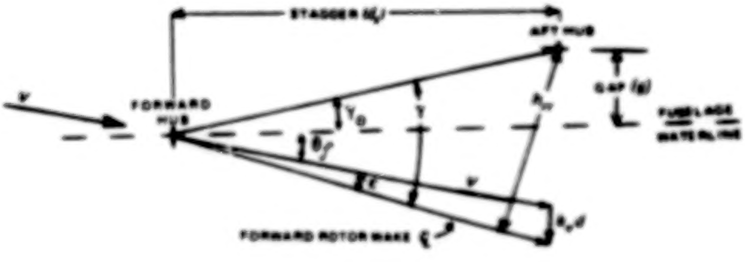

Figure 5.14 Definition of wake separation distance; h_{rr}

The factor k_d accounts for the variation in local downwash velocity v from the ideal value v where $v = k_d v$. The k_d value was determined empirically[4] from test data as follows:

$$k_d = 0.043/(\mu + 0.043). \qquad (5.5)$$

It should be noted that test data for 0, 22, and 34 percent overlap configurations have shown no significant interference effects of the aft rotor on the forward one. Theoretical predictions[5] have generally confirmed these results.

Level Flight Power Required Calculations – A comparison of power required at 4000 ft/95°F for the hypothetical tandem and single-rotor helicopters is shown in Fig 5.15. The tandem has higher power required at all airspeeds above 20 kn, and the largest percentage increase in the minimum power range. Since both aircraft have the same solidity disc loading, tip speed, airfoil section, etc., at a given gross weight, the combined induced and profile powers of the two isolated rotors of the tandem are identical to those of the main rotor of the single-rotor configuration. Therefore, the differences

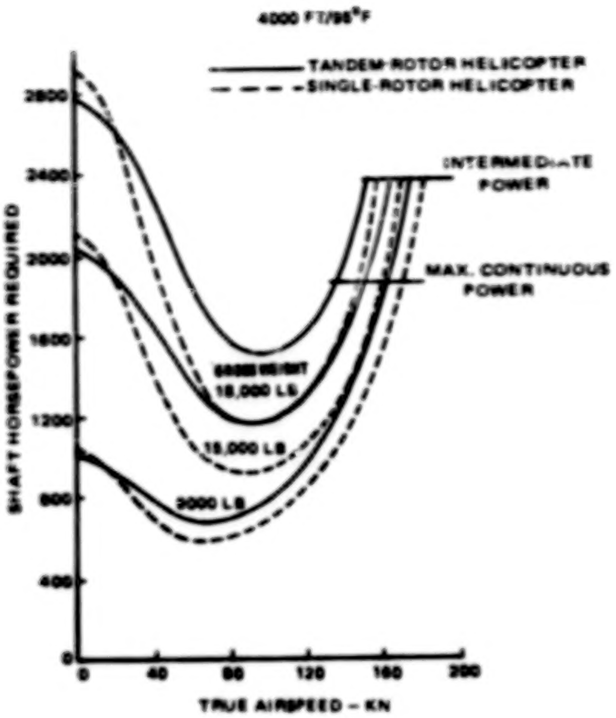

Figure 5.15 Level flight power required

in power required are primarily due to rotor-rotor interference effects and the difference in the parasite drag. These power differences are clearly visible in Fig 5.16, where a comparison is made for the design gross weight. The interference effect decreases, while the parasite power increment increases with *V*. The incremental tail rotor power required for the single-rotor configuration is not shown in this figure, since it represents less than 5 percent of the cruise power required.

The high minimum power required characteristic of tandems results in reduced one-engine-inoperative capability. To improve operational constraints imposed by this condition, various techniques such as reducting the main rotor tip speed and flying with a nose-right yaw angle are used. Decreasing the tip speed reduces the profile power, while employing right yaw tends to reduce the rotor-rotor interference effects by moving the aft rotor out of the wake of the forward rotor in order to decrease the induced power. The performance benefits of yaw angle have been verified by H-21, CH-46, and CH-47 flight-test measurements as well as model tests conducted by both Vertol in the USA and Azuma in Japan[7].

An example of the effect of yaw angle on the CH-47C power required is presented in Figs 5.17 and 5.18. Data is shown for nose-right attitudes only, since less benefit was observed in left yaw. The differences in performance between left and right yaw are attributed to the lateral downwash asymmetry of the forward rotor wake. For aircraft with the forward rotor turning counterclockwise, it was shown—both theoretically (see Vol I, Fig 4.28) and experimentally (flight tests and wind-tunnel model tests)—that

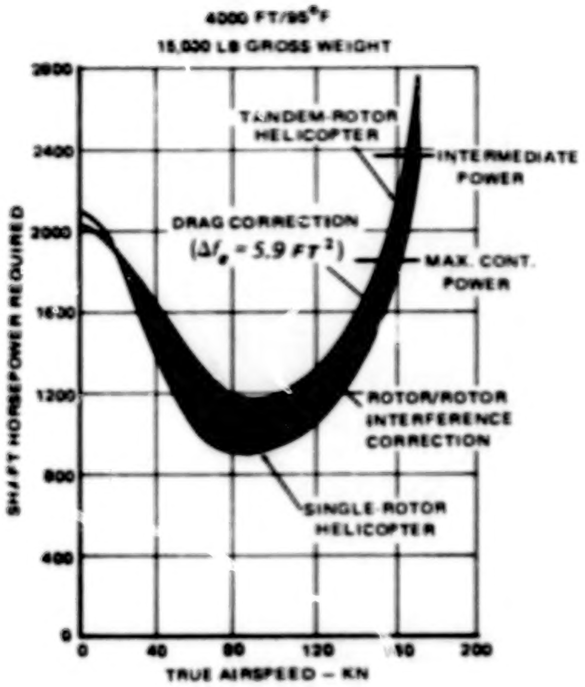

Figure 5.16 Comparison of tandem and single-rotor helicopter power required

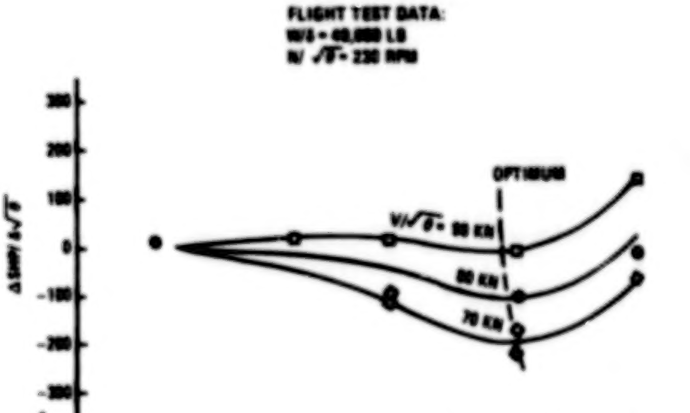

Figure 5.17 Effect of yaw angle on CH-47B power required

on the advancing side of the rotor, higher downwash velocities are generated than on the retreating side. Therefore, right yaw moves the rear rotor away from the high downwash region of the forward rotor wake, while left yaw produces the opposite effect.

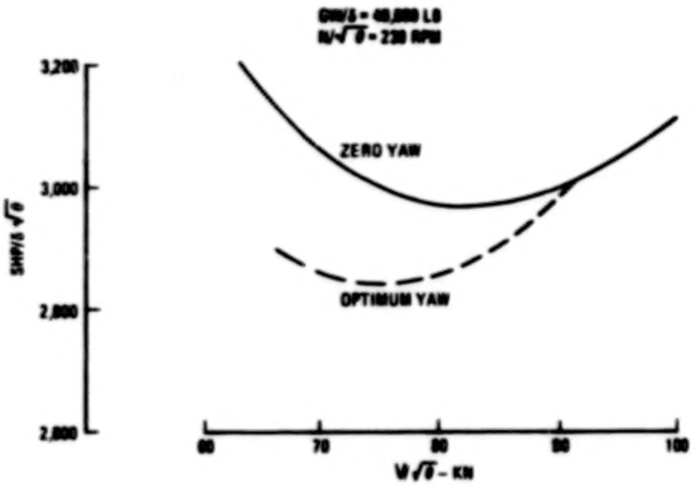

Figure 5.18 Effect of airspeed on yawed performance for the CH-47B

It can be seen from Fig 5.17 that the power required decreases as yaw angle increases until an optimum angle is obtained, and then begins to increase as the fuselage parasite drag effects begin to offset the reduction in induced power. The drag penalty of yaw also causes the benefits of yaw angle to diminish with increasing airspeed as shown in Fig 5.18.

The effect of yaw angle on induced power is illustrated by the UHM model data in Fig 5.19. Here, the induced power factor k_{ind} is shown as a function of the lateral location of the aft rotor relative to the centerline of the forward streamtube (y_{rr}/R). The equivalent yaw angle for a 22-percent overlap configuration is also indicated. This data

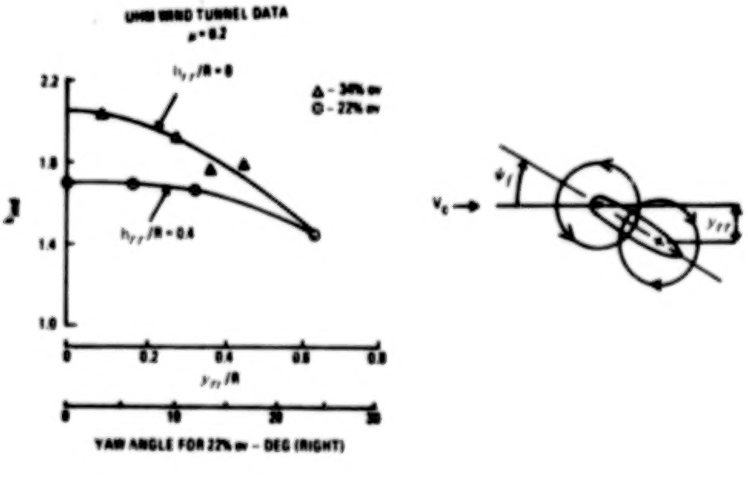

Figure 5.19 Effect of yaw angle induced power

is determined for the direction of rotation noted in the figure, and includes the effect of varying the vertical location of the aft rotor relative to the forward rotor (h_{rr}/R). It can be seen that the benefits of yaw decrease as h_{rr}/R increases. Additional data and theoretical analyses of the effect of yaw angle on the induced power of tandems can be found in Refs 5 and 7.

Detailed sample calculations of the hypothetical tandem-rotor helicopter power required are given in Table V-5. The initial steps (① to ③) consist of determining rotor power required for the isolated forward and aft rotors $(RHP_{fr} + RHP_{rr})_{iso}$ utilizing the single-rotor power required (SHP_{sr}) presented in Ch III, less 4 percent for the tail rotor, 2 percent for transmission losses, and 30 hp for accessories:

$$(RHP_{fr} + RHP_{rr})_{iso} = 0.94\, SHP_{sr} - 30.$$

In steps ④ to ⑪ , the increase in rear-rotor induced power due to rotor-rotor interference is computed, using the curve given in Fig 5.13 and the appropriate h_{rr}/R value. A fuselage attitude (angle of fuselage centerline or waterline relative to the remote velocity) of -2° was assumed for all airspeeds. As shown by the trim data in Fig 5.20, -2° represents a mean attitude for airspeeds between 60 and 150 kn. The assumption of a constant attitude causes the power required predictions to be optimistic by approximately 3 percent at 80 kn, and conservative by less than 1 percent at 150 kn. Where additional accuracy in the low-speed range is required, a value of $\theta_f \approx 0^\circ$ should be used. Test pilots, when inquired about desirable aircraft attitude in cruise, indicated that the fuselage angle should not exceed the 4° to 5° nose-down value as shown in Fig 5.20.

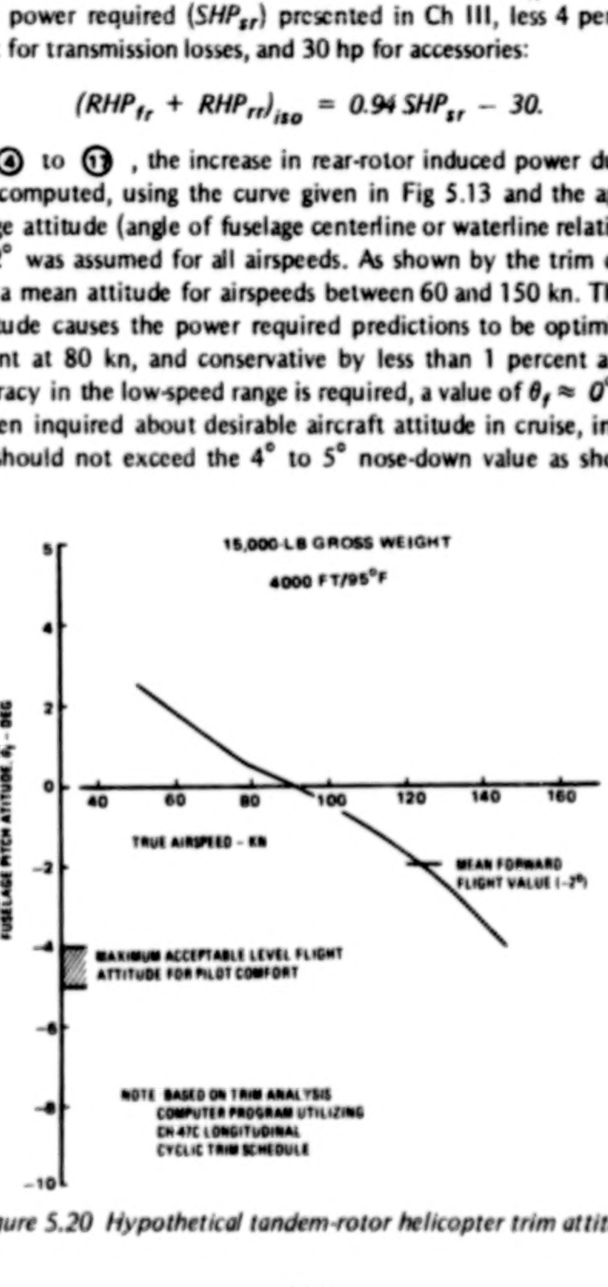

Figure 5.20 Hypothetical tandem-rotor helicopter trim attitude

4,000 FT/95°F
GROSS WEIGHT: W = 15,000 LBS

STEP NO. ①	②	③	④	⑤	⑥	⑦	⑧	⑨	⑩	⑪	⑫	⑬
V (KN)	SHP_{ST} FIG 3.24	$(RHP_{fr} + RHP_{rr})_{iso}$ * [(2)×0.94-30]	P_{id} $\frac{W^2}{2\rho\pi R^2 V 1.69}$	P_{ind} ** ④ × 1.1	v_f (FPS) EQ 5.5	v_{fr}/V $\frac{⑥}{① \times 1.69}$	k_d EQ 5.5	ε (DEG) $\tan^{-1}$ ⑧×⑦	θ_f (DEG)	η_o (DEG) $\tan^{-1}\left[\frac{s}{d_s}\right]$	γ (DEG) ⑩-⑨-⑪	d_s/R (1 − [illegible])×2
60	1040	948	534	587	19.24	0.1899	0.228	2.48	−2	8.53	−13.01	1.56
80	915	830	401	441	14.65	0.1084	0.182	1.13	↓	↓	−11.66	↓
100	930	844	320	352	11.76	0.0696	0.151	0.60			−11.13	
120	1060	966	267	294	9.75	0.0461	0.129	0.36			−10.89	
140	1320	1211	229	252	8.42	0.0356	0.113	0.23			−10.76	
160	1810	1671	200	220	7.35	0.0272	0.100	0.16			−10.69	
170	2260	2094	189	208	6.90	0.0240	0.094	0.13			−10.66	

①	⑭	⑮	⑯	⑰	⑱	⑲	⑳	㉑
V (KN)	h_{rr}/R -⑬ tan ⑫	k_{ind} FIG 5.13	$P_{id} \times k_{ind}$ ⑮×④	ΔP_{ind} ⑯ − ⑤	Δf_e (FT²) 24.7 − 19.1	η_p FIG 3.21	ΔRHP $\frac{⑱\ \frac{1}{2}\rho(V\,1.69)^3}{550\ ⑲}$	SHP $\frac{③ + ⑰ + ⑳}{0.98} + 30$
60	0.36	1.74	929	342	5.6	1.00	10	1357
80	0.322	1.79	718	277	↓	0.99	24	1183
100	0.307	1.81	579	227		0.945	50	1174
120	0.300	1.82	486	192		0.890	92	1306
140	0.297	1.82	417	165		0.825	156	1593
160	0.294	1.82	364	144		0.735	261	2149
170	0.294	1.82	344	136		0.680	337	2649

*ISOLATED FORWARD PLUS AFT ROTOR POWER REQD.

SHP_{ST} = SINGLE ROTOR HELICOPTER POWER REQD.

** P_{ind_i} = P_{id_i} CORRECTED FOR TIP LOSSES AND CUTOUT EFFECTS.

TABLE V CALCULATIONS OF POWER REQUIRED FOR A TANDEM-ROTOR HELICOPTER IN LEVEL FLIGHT

4.2 Power Required in Climb and Descent

A comparison of single and tandem-rotor power required in climb and descent is shown in Fig 5.21. This data refers to a gross weight of 15,000 lb, SL/STD conditions, and a true airspeed of 80 kn, based on a tandem-rotor trim analysis computer program which includes the rotor-rotor interference correction defined in Fig 5.13. As shown in Fig 5.21, the tandem exhibits a more gradual rise in power required with rate of climb than the single-rotor aircraft. At climb rates between 0 and 1000 fpm, the difference in slope ($\Delta SHP/\Delta V_c$) reflects an increase in the climb efficiency factor (k_p) from 0.85 for the single-rotor helicopter (Ch III) to 0.95 for the tandem. The increased efficiency of the tandem in climb is attributed to (1) the elimination of tail rotor power requirements, which are sizeable at the higher main rotor power and torque levels associated with climb, and (2) a decrease in rotor-rotor interference effects with increasing rates of climb. The climb velocity component increases the nose-down fuselage angle-of-attack which, according to Eqs (5.3) and (5.4), increases the distance between the forward rotor wake and the aft centerline (h_{rr}/R) and thus, reduces the induced power factor k_{ind}.

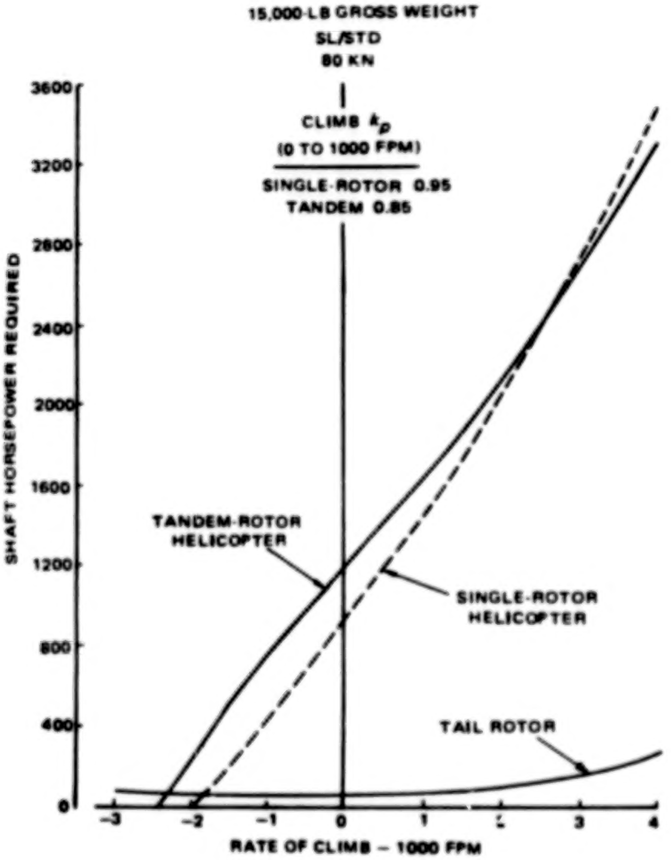

Figure 5.21 Power required in climb and descent

As noted in Ch III, k_p varies with weight and airspeed; however, flight test measurements and theoretical trim analyses for various tandem-rotor aircraft indicate that tandems have average climb k_p values on the order of 0.85 to 0.95 at minimum power speed, while corresponding single-rotor k_p values vary from 0.8 to 0.9. For the hypothetical tandem-rotor aircraft, a k_p of 0.95 is assumed.

As indicated in Fig 5.21, the average slopes of the rate of descent vs SHP curves for the two aircraft are almost identical. This implies that the descent correction factor $k_{pd} = 1.0$ developed in Ch III (Fig 3.29) for the single-rotor aircraft is also applicable to the hypothetical tandem-rotor helicopter. Test measurements on tandem and single-rotor aircraft show that the use of $k_{pd} = 1.0$ will usually give a conservative estimate of autorotation rate-of-descent.

A closer look at Fig 5.21 reveals that the slope of the SHP vs $-V_c$ curve for the tandem varies in a way which implies that during low-rate partial-power descent, the k_{pd} of the tandem is slightly higher than for the single-rotor configuration; after which both k_{pd}'s become approximately equal and finally, as the state of full autorotation is approached ($SHP \to 0$), the tandem k_{pd} becomes lower than for the single-rotor machine.

The results noted above reflect the variation of k_{ind} with descent rate. As the descent rate increases, h_{rr}/R decreases until it eventually becomes negative as the forward rotor wake moves above the aft rotor. The factor k_{ind} increases as h_{rr}/R decreases until $h_{rr}/R = 0$ is reached; then as the absolute value of h_{rr}/R begins to grow again, k_{ind_t} starts to decrease (Fig 5.13) until at autorotational descent rates, it is approximately equal to the level flight value. In the single-rotor configuration, the SHP vs $-V_c$ curve retains a practically constant slope; thus indicating an almost constant k_{pd} value. This is due to the fact that because of the unloading effects of the cambered vertical tail in forward flight (Fig 5.21), the tail rotor power is so low that its possible variation from level powered flight to autorotation has little effect on the rate of descent.

The power required for a 100-fpm climb and minimum power speed is shown in Fig 5.22 as a function of gross weight and Mach number—assuming that $k_p = 0.95$. Level-flight power-required is also given. This data in used in subsequent service ceiling and climb capability calculations.

4.3 Structural Envelope

The structural envelope of tandems is typically limited by rotor loads due to stall or the effect of stall on aircraft flying qualities. As described in Ch III, Sect 6.1, the control loads rise abruptly as the rotor begins to stall until they reach the endurance limit of the control system. In addition, stall inception is accompanied by a reduction in the amount of thrust produced per degree of control input. Since the tandem depends on differential collective pitch rather than cyclic for longitudinal control, this can lead to control deterioration, thus creating a restriction to speed based on flying qualities. However, only speed limits resulting from rotor loads due to stall will be considered in this section.

The primary difference between single and tandem rotor stall boundaries results from the effect of operating the aft rotor in the wake of the forward rotor. Isolated rotor and tandem aft-rotor lift coefficient boundaries (C'_T/σ) based on model data are presented in Fig 5.23 as a function of nondimensional propulsive force ($\bar{X}$) for $\mu = 0.3$.

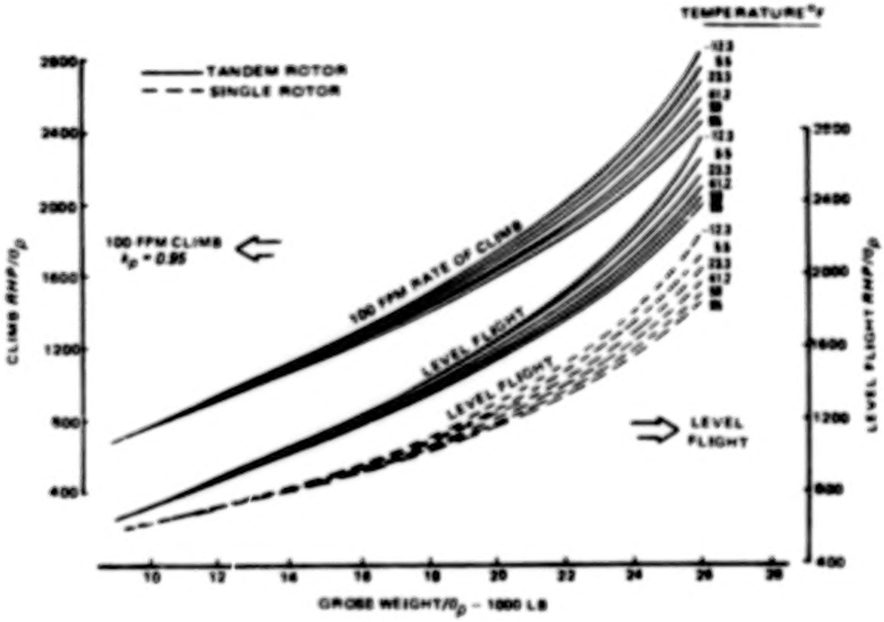

Figure 5.22 Tandem-rotor helicopter minimum power required

With the forward rotor operating at $C'_T/\sigma = 0.08$, rotor-rotor interference effects reduce the rear rotor moment stall inception boundary by $\Delta C'_T/\sigma = 0.01$. This increment is essentially constant at all positive $\bar{X}$ values and decreases slightly at highly negative $\bar{X}$ conditions.

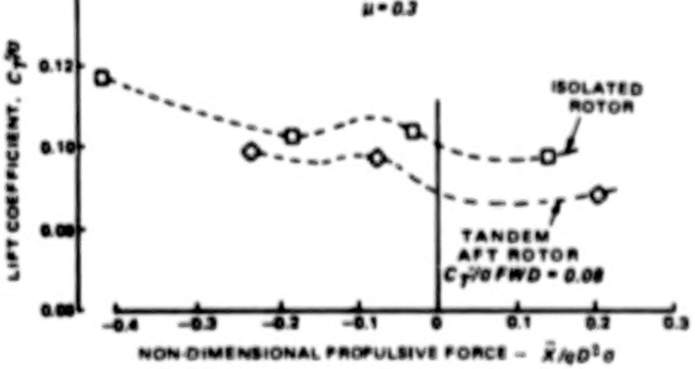

Figure 5.23 A comparison of moment stall inception boundaries (isolated and tandem aft rotors)

The rear rotor stall boundary for the hypothetical helicopter (Fig 5.24) is obtained by applying the $0.01\Delta C'_T/\sigma$ reduction to the isolated rotor endurance limits shown in Fig 3.33. The distribution of thrust between the rotors will determine whether the forward or aft rotor is critical. For example, thrust distribution for the hypothetical tandem as defined by the trim analysis program for a neutral c.g. (c.g. located midway between the rotors on a line normal to the line connecting the rotor hubs) is shown in Fig 5.24. In this case, due to a higher thrust level, the forward rotor stalls before the aft one. This thrust distribution is dictated by the negative fuselage pitching moment generated at the nose-down attitude required at high speeds which must be counteracted by increased forward rotor thrust to achieve pitching moment balance ($\Sigma M = 0$). To identify the most critical c.g. locations, an analysis of the thrust distribution must be obtained for maximum forward and aft c.g. positions. However, in order to simplify the hypothetical sample calculations, the forward and aft rotor thrust is assumed to be equal. In addition, the stall boundary is decreased by 10 percent to provide a margin for turbulence (see Ch III).

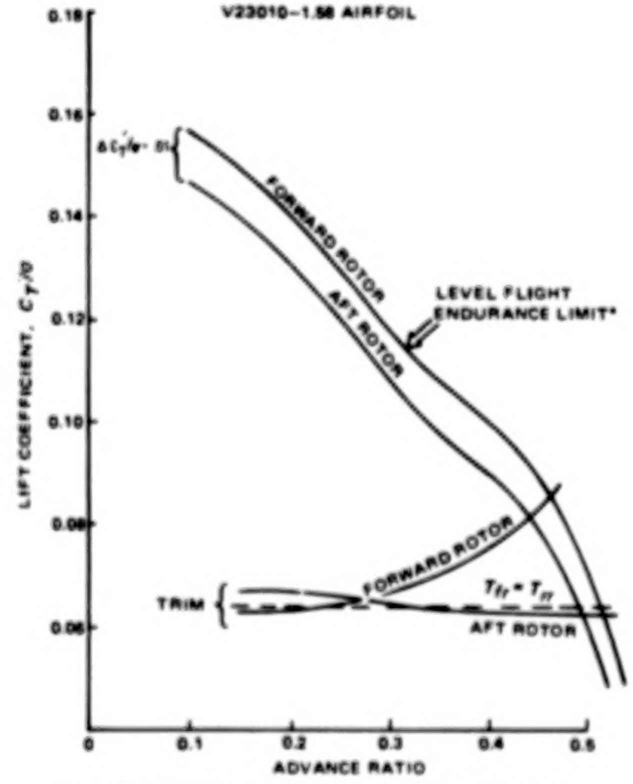

*HYPOTHETICAL ENDURANCE LIMIT = 3X UNSTALLED ALTERNATING TORSIONAL LOAD

Figure 5.24 Hypothetical tandem-rotor helicopter stall limit boundaries

4.4 Performance Capability

Payload-Range Relationship A comparison of the payload-range performance of the single and tamdem-rotor hypothetical helicopters at 4000 ft/95°F is shown in Fig 5.25. As noted, the takeoff gross weight is defined by hover OGE criteria. Because of its superior OGE hover capability, the tandem has a payload advantage at the low to intermediate range values. However, its full-fuel range capacity is lower because of higher parasite drag and rotor interference effects.

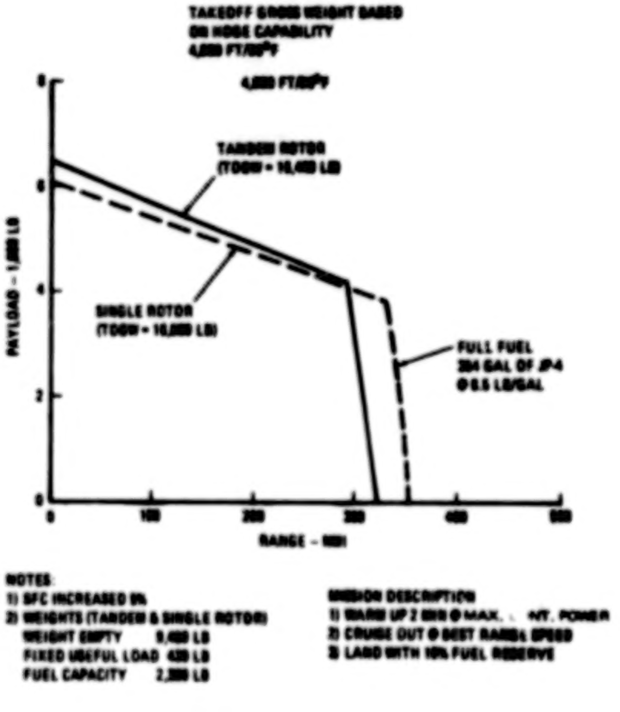

Figure 5.25 Payload-range capability

Cruise performance inputs used in the range calculations are presented in Fig 5.26. Specific range data for tandem and single-rotor aircraft is shown in the lower half of this figure and a speed capability comparison is given in the upper half. The tandem and single-rotor best range speed is approximately the same; however, the tandem specific range is 10 percent lower than the single-rotor values. At weights above 16,000 lb, the airspeed of the tandem is limited by its structural envelope where, due to rotor-rotor interference effects, it becomes 20 kn lower than the single-rotor boundary.

Speed Capability – The speed of the tandem and single-rotor helicopters at maximum continuous and intermediate power is also indicated in Fig 5.26. At a gross weight of 15,000 lb, the tandem speed capability is 151 kn for maximum continuous power, and 162 kn for intermediate power (structural envelope limit) versus 161 and 171 kn, respectively, for the single-rotor aircraft.

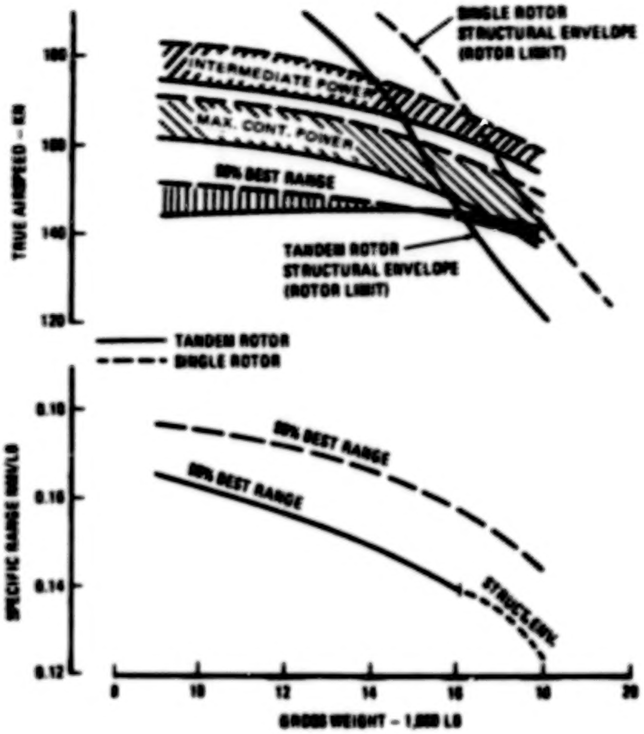

NOTE: SFC INCREASED 5%

Figure 5.26 Cruise performance at 4000 ft/95°F

Service Ceiling – A comparison of tandem and single-rotor helicopter service ceiling capability for standard day conditions is presented in Fig 5.27. Because of the higher minimum power required of the tandem, its OEI (one engine inoperative) service ceiling is 9000 ft at 15,000 lb gross weight, while the corresponding ceiling for the single-rotor aircraft amounts to 13,700 ft. Also, the dual-engine ceiling of the tandem is 1500 ft less than that of the single-rotor configuration.

Climb Capability – The tandem and single-rotor helicopter climb capability at 4000 ft/95°F is shown in Fig 5.28. It can be seen that the tandem has less dual and single-engine capability at all gross weights. However, at lower weights and higher rates of climb, this deficiency decreases as the induced power becomes lower and thus, the effects of rotor interference diminishes.

Autorotation Capability – The hypothetical tandem-rotor helicopter autorotation rate of descent at 4000 ft/95°F and 15,000 lb gross weight is presented in Fig 5.29 for a descent calculation factor of $k_{pd} = 1.0$. The autorotational rate of descent for the tandem-rotor helicopter is 500 to 600 fpm higher than for the single-rotor aircraft at both minimum descent airspeed and speed for maximum glide distance. This is due primarily to the increased rear rotor induced power caused by rotor-rotor interference.

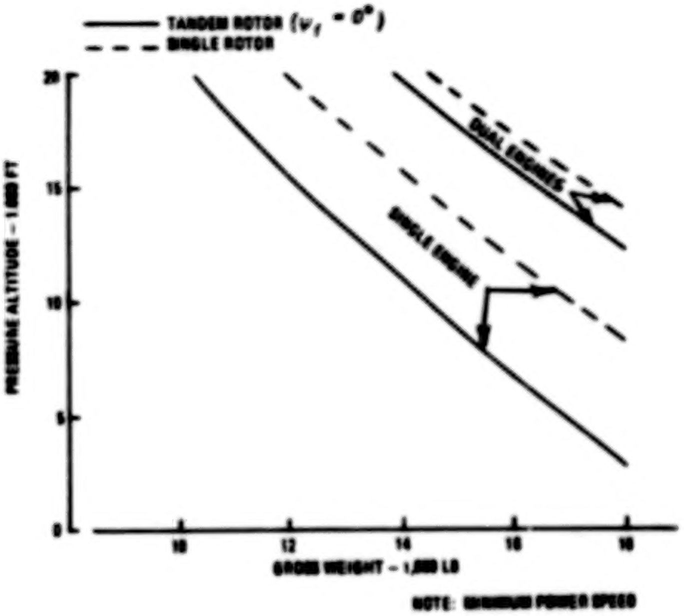

Figure 5.27 Standard day service ceiling capability

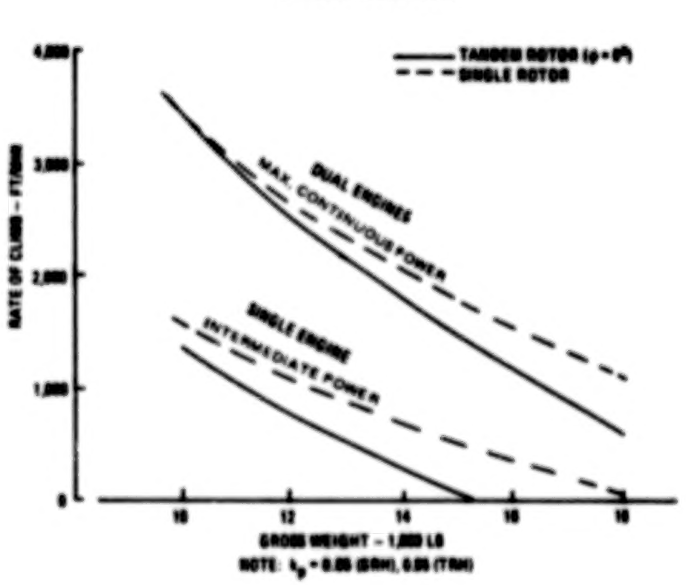

Figure 5.28 Climb Capability at 4000 ft/95° F

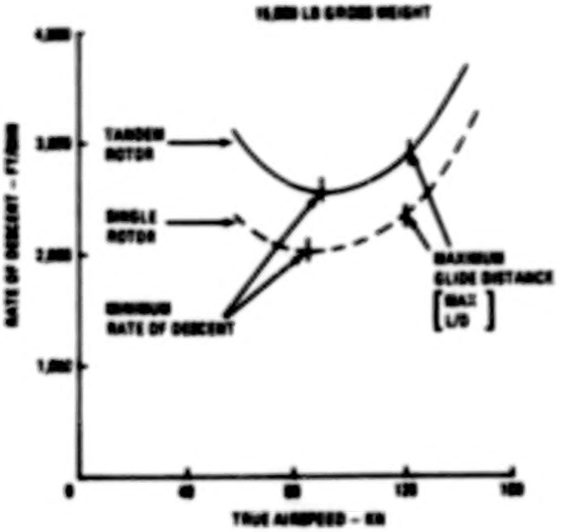

Figure 5.29 Autorotational rate of descent at 4000 ft/95° F

References for Ch V

1. Boeing Vertol Company. *UTTAS Concept Formulation Study.* Contract DAAJ02-69-C-0011, 1968.

2. Hoerner, S.F. *Fluid Dynamic Drag.* Published by the author, 1965 Edition.

3. Dutton, W.J. *Parametric Analysis and Preliminary Design of a Shaft-Driven Rotor System for a Heavy-Lift Helicopter.* USAAVLABS Technical Report 66-56, Sikorsky Aircraft Div. of United Aircraft Corp., February 1967.

4. Durand, W.F. *Aerodynamic Theory.* Vol. II, Durand Reprinting Committee, 1943.

5. Baskin, V.E., et al. *Theory of the Lifting Airscrew.* Translated from Russian to English by W. Z. Stepniewski, NASA TT F–823, February 1976.

6. Davis, S. Jon and Wisniewski, J.S. *User's Manual for HESCOMP, the Helicopter Sizing and Performance Computer Program.* Boeing Vertol Report D210-10699-1 (Contract NAS2-6107), NASA CR-152018, Ames Research Center, Moffett Field, Ca. Sept. 1973.

7. Azuma, A., et al. *Effect of Yaw on Tandem-Rotor Helicopter, Part III.* Institute of Space and Aeronautical Science, University of Tokyo, Japan, February 1969.

8. Hoerner, S.F. *Base Drag and Thick Trailing Edges.* Journal of Aeronautical Sciences. October 1950.

PERFORMANCE GUARANTEES

Before initiating performance calculations, the accuracy of the intended theoretical methodology must be established. The level of accuracy required for preliminary design or trade studies is usually lower than that required for final proposals to the government or private customers. An evaluation of the reliability of prediction techniques is especially important prior to presenting guaranteed performance figures, since noncompliance may result in cost penalties or possible cancellation of the program.

The accuracy of performance methodology is best verified by comparing predictions with flight test data. Examples of such comparisons are presented in Fig A.1 for a single-rotor (BO–105), and in Fig A.2 for a tandem-rotor (Model 347) configuration. It can be seen from these figures that the test data agrees reasonably well with the predictions based on the methods described previously, as well as with the material contained in Ref 1 from which the figures were taken. While these comparisons represent a satisfactory substantiation of performance evaluation for preliminary design studies, a more detailed quantitative assessment is required in order to determine specific guaranteed values. With respect to this subject, a statistical approach can be helpful in selecting performance guarantees. The basic method of analysis consists of examining the accuracy of the theoretical predictions and evaluating the tolerances associated with the acquisition of flight test data, since final guarantee compliance will ultimately be determined in this manner. Numerical examples for the hypothetical helicopter are included to illustrate the calculation procedure. It should be noted that the theoretical performance

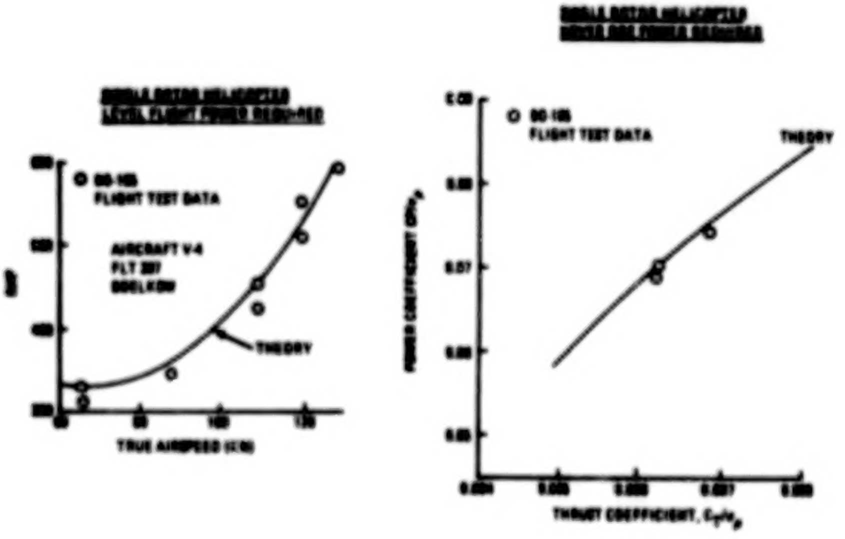

(a) (b)

Figure A.1 Comparisons of predicted and flight-test measured performance for a single-rotor helicopter

tolerances assigned to the sample problems are also hypothetical, and are intended for demonstration purposes only.

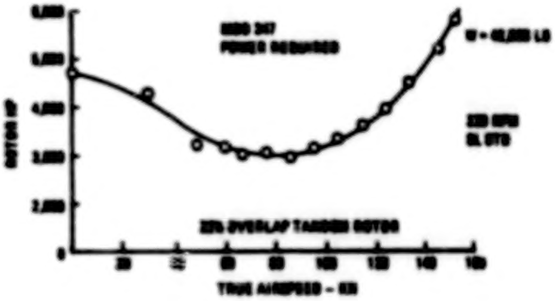

Figure A.2 Comparison of predicted and flight-test measured power required for a tandem

1. Guarantee Items

The performance items to be guaranteed for a new design or for growth versions of existing aircraft are usually specified by the customer and negotiated with the manufacturer. The performance guarantees selected are normally associated with a specific design mission and typically include the following: (a) hover capability, (b) payload, (c) radius, (d) endurance, (e) cruise speed, and (f) one-engine-inoperative service ceiling and speed capability.

When the guarantees are negotiated, the ground rules for determining compliance should be well defined. For instance, the engine performance used to compute the guarantees, the aircraft external configuration (drag), and details of flight testing should be agreed upon and specified in the contract.

2. Method of Analysis

The procedure for establishing performance guarantees consists of determining—as objectively as possible—the probability that a given performance level can be achieved, and then selecting a specific value, depending on the risks and competitive pressures involved. The probability values assigned to a given performance level are determined by evaluating both the accuracy of theoretical predictions and the tolerances associated with flight-test measurements. The most optimistic as well as the most pessimistic incremental values are then assigned to each element or step in the analytical predictions and flight-test reduction system. In this way, for each performance item (say, horizontal speed of flight at given ambient conditions and prescribed power setting) two levels (x'_1 and x'_2) can be established: one – the lowest x'_1, where probability of at least meeting the performance level in the accepted flight measurements will be very high (99.8%); and another – x'_2, where the probability of achieving that level will be very low (0.13%). In other words, it may be stated that the probability (P) of the actual measured value (x), being lower than x'_1, will be $P(x < x'_1) = 0.13\%$ and conversely,

$P(x \leqslant x_2) = 99.87\%$. Between these two extremes lie intermediate values of that performance item, thus representing various levels of the probability of achieving them.

For those who are not familiar with engineering statistics and thus may not grasp the significance of the above-mentioned 0.13 and 99.87 percentages, some basic techniques of dealing with probabilities are briefly outlined (Ref 2, Ch 7).

Normal Distribution – The so-called normal (Gaussian) distribution represents the most widely used method of determining the probability of a deviation of the random variable (x) from its mean value μ. One states that x has the normal distribution $N(\mu,\sigma^2)$ if its *probability density function (pdf)* is

$$f(x) = \frac{1}{\sigma\sqrt{2\pi}} \exp\left[-\frac{1}{2\sigma^2}\left(x - \mu\right)^2\right], \qquad -\infty < x < \infty, \tag{A1}$$

where the symbol σ is the *standard deviation* of x from its *mean value* (μ). σ is determined from the so-called variance (σ^2) which, for continuous functions, is defined as

$$\sigma^2 = \int_{-\infty}^{\infty} (x - \mu)^2 f(x)dx \tag{A2}$$

or for a finite number (n) of known differences between μ and x, σ^2 can be found from the following equation:

$$(n - 1)\sigma^2 = \sum_{j=1}^{n} (x_j - \mu)^2 . \tag{A3}$$

Remembering that the arithmetic mean (μ) is $\mu = (1/n) \sum_{j=1}^{n} x_j$,

Eq (A3) can be rewritten in a form more suitable for practical application:

$$(n - 1)\sigma^2 = \sum_{j=1}^{n} x_j^2 - (1/n)\left(\sum_{j=1}^{n} x_j\right)^2 \tag{A3a}$$

The shape of the normal *pdf* curve corresponding to $f(x)$ given by Eq (A1) is shown in Fig A.3.

It can be seen that the normal *pdf* curve is symmetrical about the mean value μ, and points of inflection are located at $\pm\sigma$ from the μ value line.

The probability that some value x will be smaller or equal to a given value x', $P(x \leqslant x')$ can now be expressed from Eq (A1) as follows:

$$P(x \leqslant x') = \int_{-\infty}^{x'} \frac{1}{\sigma\sqrt{2\pi}} \exp\left[-\tfrac{1}{2}\left(\frac{x - \mu}{\sigma}\right)^2\right]dx. \tag{A4}$$

It should be noted that $(x - \mu)/\sigma$ represents the ratio of the difference between x and its mean value (μ) to the standard deviation (σ). This ratio can be treated as a new variable; $z \equiv (x - \mu)/\sigma$, and Eq (A4) can be rewritten as follows:

$$P(x \leq x') = \int_{-\infty}^{(x' - \mu)/\sigma} \frac{1}{\sqrt{2\pi}} e^{-z^2/2}\, dz = \Phi\left(\frac{x' - \mu}{\sigma}\right) \tag{A4a}$$

It is interesting to note that for $x = \mu$, $z = 0$; and for $x = \mu \pm 3\sigma$, $z = \pm 3$. This relationship between the z and x scales can also be seen in Fig A.3. Furthermore it can be shown that Eq (A4a) expresses the statement of probability that $x \leq x'$ is the same as the probability that $z \leq (x' - \mu)/\sigma \equiv z'$ (shaded area in Fig A.3).

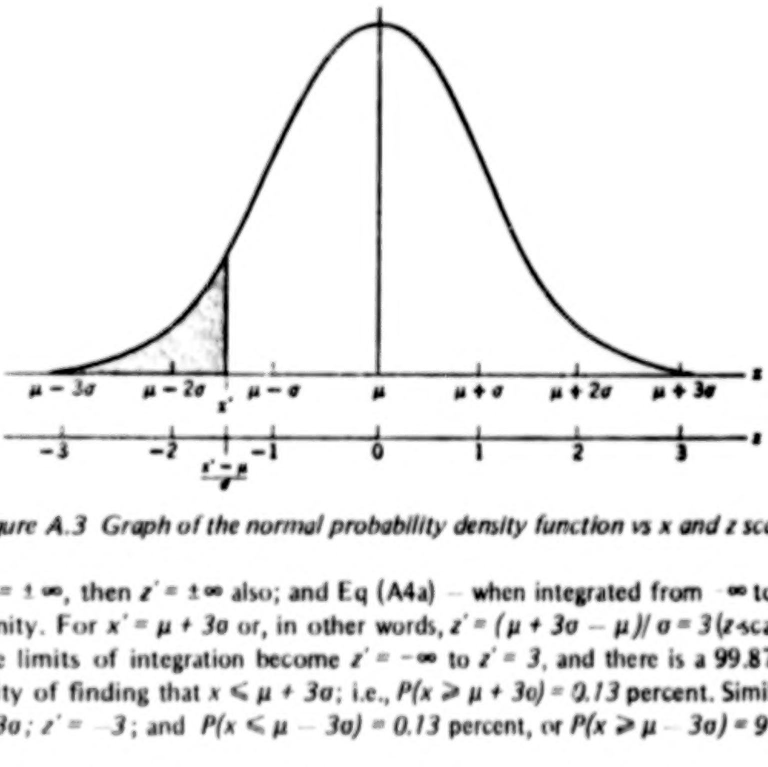

Figure A.3 Graph of the normal probability density function vs x and z scales

When $x' = \pm\infty$, then $z' = \pm\infty$ also; and Eq (A4a) – when integrated from $-\infty$ to ∞ – becomes unity. For $x' = \mu + 3\sigma$ or, in other words, $z' = (\mu + 3\sigma - \mu)/\sigma = 3$ (z-scale in Fig A.3); the limits of integration become $z' = -\infty$ to $z' = 3$, and there is a 99.87 percent probability of finding that $x \leq \mu + 3\sigma$; i.e., $P(x \geq \mu + 3\sigma) = 0.13$ percent. Similarly, for $x' = \mu - 3\sigma$; $z' = -3$; and $P(x \leq \mu - 3\sigma) = 0.13$ percent, or $P(x \geq \mu - 3\sigma) = 97.87$ percent.

The character of the complete variation of probabilities within the $x = \mu \pm 3\sigma$ or $z \pm 3$ limits is shown in Fig A.4. However, instead of taking readings from a chart such as this, the so-called probability paper (Fig A.5) is often used for determining probabilities, or checking the distribution of sampling. By plotting the probability expressed by Eq (A4) on logarithmic paper, a straight-line is obtained. Such graphs are used in determining the probability levels when establishing guarantees for various performance items. The procedure described below is an example of guaranteed values for high-speed level-flight velocity.

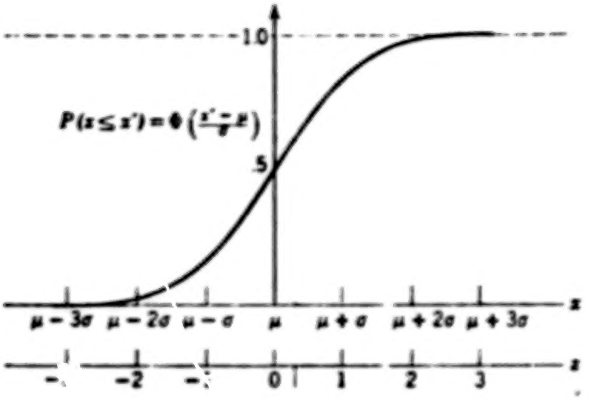

Figure A.4 Character of variation of probabilities corresponding to the normal pdf

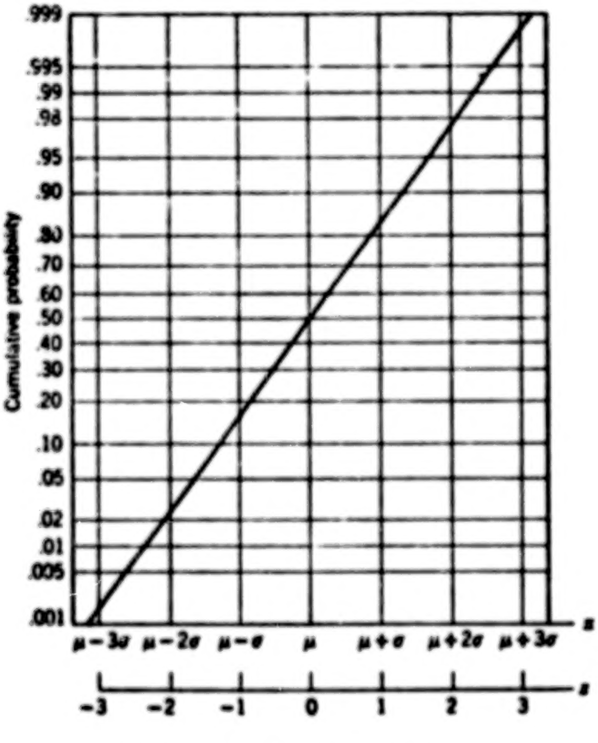

Figure A.5 Probability paper

Example of Performance Guarantee Determination – The procedure of establishing the most pessimistic (V_{pes}) and most optimistic (V_{opt}) value, the true airspeeds achievable under given ambient conditions and power settings are shown in Table A-1.

ITEMS	SENSITIVITY (K)	EXPECTED DEVIATION $(\Delta$ *VALUE*$)$		VARIANCE $\sigma_n^2 = [K(\Delta \text{ VALUE})/3]^2$			
		MOST PESSIMISTIC	MOST OPTIMISTIC	MOST PESSIMISTIC		MOST OPTIMISTIC	
				$-3\sigma_n$	σ_n^2	$3\sigma_n$	σ_n^2
		PREDICTION TOLERANCES					
ROTOR HP REQUIRED	−0.467 KN/% HP	6% HP	−3% HP	−2.8 KN	0.872	1.4 KN	0.218
ENGINE INSTALLATION LOSSES & RAM RECOVERY	−0.467 KN/%	1%	−1%/HP	−0.467	0.02423	0.467	0.02423
TRANSMISSION & ACCESSORY LOSSES	−0.0182 KN/HP	16 HP	−16 HP	−0.291	0.0094	0.291	0.0094
		FLIGHT TEST TOLERANCES					
POWER REQUIRED	−0.467 KN/% HP	2% HP	−2% HP	−0.934	0.0969	0.934	0.0969
WEIGHT	−0.0015 KN/LB	150 LB	−150 LB	−0.225	0.005625	0.225	0.005625
AIRSPEED	1 KN/KN	2 KN	−2 KN	−2 KN	0.444	2 KN	0.444
			$\sigma^2 = \Sigma\sigma_n^2$	1.452		0.7982	
			3σ, KN	−3.62		2.68	
			$V_{pes} = 173 - 3.61 \approx 169.4$ KN			$V_{opt} = 173 + 2.67 \approx 175.7$ KN	

TABLE A-1 DETERMINATION OF EXTREME V_{max} VALUES

It is assumed that each of the considered items represents the 3σ-type deviation from the calculated value of $V = 173\ kn$. The total variance (σ^2) is the sum of particular variances $(\sigma_n{}^2)$ and it is again assumed that the most pessimistic value will be given by $173 - 3\sigma\ (V_{pes} = 169.4\ kn)$, and the most optimistic by $173 + 3\sigma\ (V_{opt} = 175.7\ kn)$.

If V_{opt} represents the $\mu + 3\sigma$ situation, then the probability of reaching or exceeding that value is only 0.13 percent. By contrast, the probability that measured flight velocity values will be equal or better than the most pessimistic $(173 - 3\sigma)$ figure will amount to 97.87 percent. Points (0.13%, 175.7 kn) and (99.87%, 169.4 kn) are marked on the probability paper (Fig A.6). It should be noted that in this figure, the coordinate axes are reversed in comparison with Fig A.5.

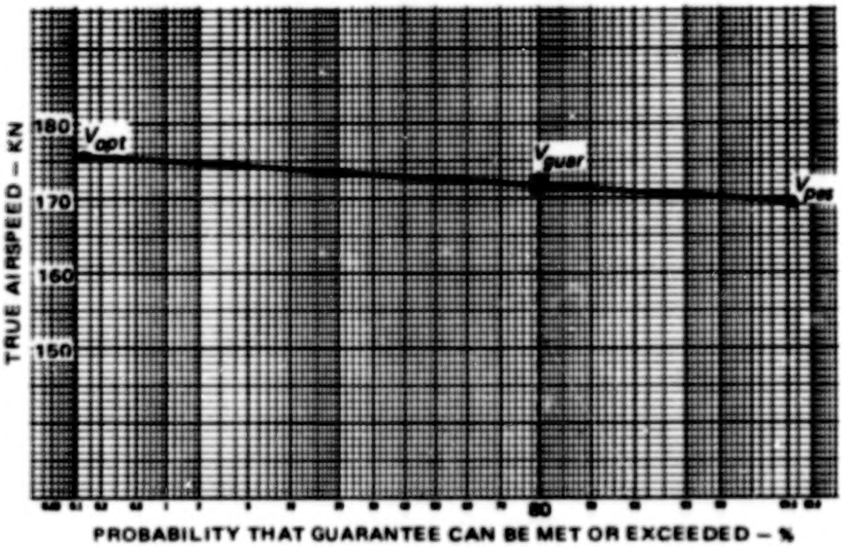

Figure A.6 Determination of probability

The normal probability distribution for the interim velocity values $(169.4 < V < 175.7)$ is obtained by joining the two points in Fig A.6 by a straight line. It can now be seen that should one desire an 80 percent probability that actual flight-test values will be either better than, or at least equal to, the guaranteed velocity (V_{guar}), then $V_{guar} = 171.5\ kn$ should be quoted.

Prediction Variables – The accuracy of performance predictions depends on both the number and values of the considered variables. For example, if nondimensional data obtained from flight tests of a similar aircraft or prototype is used as the basis for predictions, both the number and tolerance limits of the variables will be low. Conversely, if unsubstantiated theory is used to estimate the performance of advanced aircraft, the number of variables influencing the answer and the magnitude of the tolerance limits will be high. For this reason, it is essential that performance guarantees are based on the best validated performance methodology available.

The major factors affecting the accuracy of hover and forward-flight performance predictions are listed in Table A-II where it is assumed that there is no available prototype test data, and the estimates are based exclusively on the analytical computations presented in Chs II and III.

FLIGHT REGIME	ITEM	PREDICTION VARIABLE
HOVERING	1	MAIN & TAIL ROTOR POWER REQUIRED
	2	DOWNLOAD
	3	ENGINE INSTALLATION LOSSES
	4	TRANSMISSION & ACCESSORY LOSSES
	5	GROUND EFFECT
VERTICAL CLIMB	1–4	SEE HOVER
	5	CLIMB EFFICIENCY FACTOR
HORIZONTAL FLIGHT	1–4	SEE HOVER. IN ITEM 1, ATTENTION SHOULD BE GIVEN TO THE PARASITE DRAG ESTIMATE OF THE AIRFRAME & BLADE PROFILE DRAG CONTRIBUTION

TABLE A-II PREDICTION VARIABLES

Test Tolerances – The tolerances on test data are primarily a function of the type and accuracy of the instrumentation, and the specific prototype or production aircraft selected for the compliance evaluation. A list of the parameters generally recorded during a performance evaluation program and the accuracy of typical instrumentation employed for guarantee compliance testing is presented in Table A-III.

ITEM	MEASUREMENT	TOLERANCE
1	POWER (FROM FUEL FLOW OR ROTOR TORQUE)	±2%
2	TRUE AIRSPEED	±2 KN
3	GROSS WEIGHT	±150 LB*
4	ROTOR RPM	UP TO ±1/4 RPM
5	ALTITUDE	DEPENDS ON ALTIMETER POSITION ERROR & READING ERROR
6	OUTSIDE TEMPERATURE	±1°C
7	WHEEL-HEIGHT, IGE	DEPENDS ON ARRANGEMENT
NOTE: ITEMS 4, 5, AND 6 INFLUENCE TOLERANCES OF POWER MEASUREMENTS		

*For aircraft of the 15,000-lb gross weight class

TABLE A-III FLIGHT–TEST PERFORMANCE MEASUREMENTS AND THEIR TOLERANCES

References for Appendix A

1. Davis, S. Jon and Wisniewski, J.S. *User's Manual for HESCOMP, the Helicopter Sizing and Performance Computer Program.* Boeing Vertol Report D210-10699-1 (Contract NAS2-6107), NASA CR-152018, Ames Research Center, Moffett Field, Ca. Sept. 1973.

2. Guttman, Irwin; and Wilks, S.S. *Introductory Engineering Statistics.* John Wiley & Sons, N.Y. 1965.

APPENDIX B

AIRCRAFT GROWTH

The weight empty of the completed prototype aircraft is often higher than originally predicted. This is due to changes in equipment weight, configuration modifications and the accuracy of statistical weight prediction trends employed during early design phases when detailed component drawings were not available. During the service life of an aircraft, its weight empty increases even further with time, as illustrated in Fig B.1 for typical tandem and single-rotor helicopters. It can be se seen from this figure that even at the first flight of these aircraft, the weight empty was as much as 5 percent higher than the initial predictions. This trend of weight empty increases with time and continues, after the first flight, at a rate of between 0.5 and 1.5 percent per year; due mainly to product improvement programs. For example, four years after the start of production qualification testing, the CH-47 empty weight was approximately 15 percent over the original predicted value.

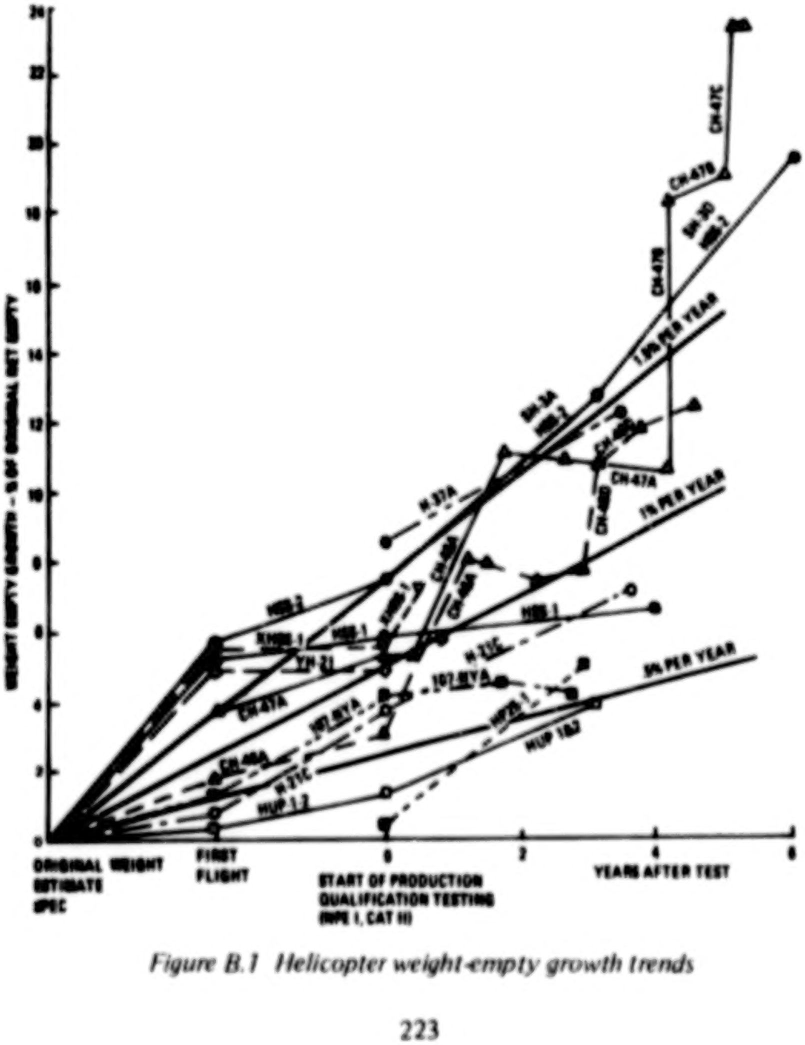

Figure B.1 Helicopter weight-empty growth trends

As a result of this trend, the payload-range capability will decrease, unless the increase in weight empty is counterbalanced by a suitable aircraft growth consisting of various design modifications leading to improvements in performance capability. The effect of increasing the weight empty on the payload/range relationship, assuming no aircraft growth – constant takeoff power available and power required – for the hypothetical single-rotor aircraft is shown in Fig B.2.

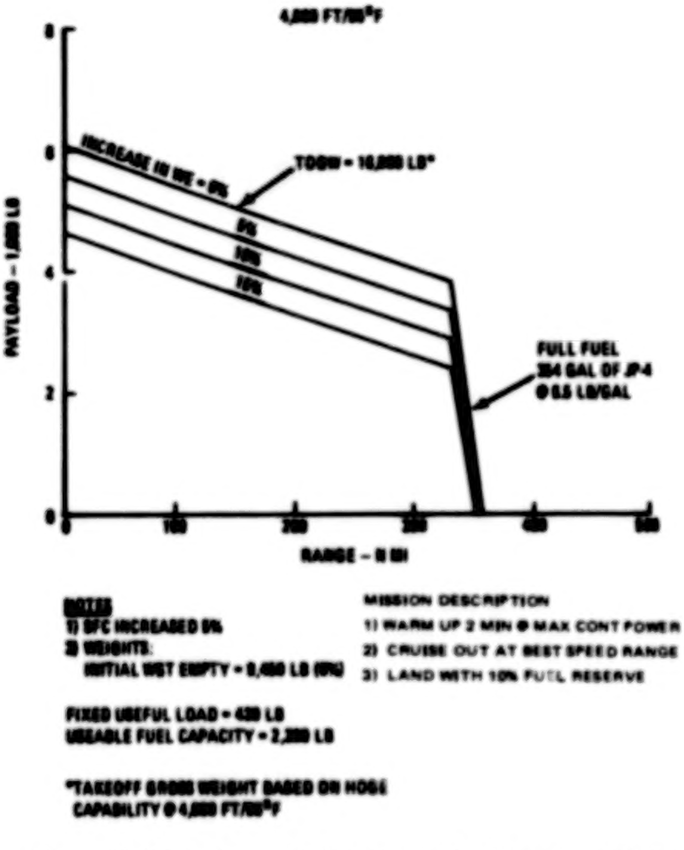

NOTES
1) SFC INCREASED 5%
2) WEIGHTS:
INITIAL WET EMPTY = [illegible] LB (0%)

FIXED USEFUL LOAD = 420 LB
USEABLE FUEL CAPACITY = 2,300 LB

***TAKEOFF GROSS WEIGHT BASED ON HOGE CAPABILITY @ 4,000 FT/95°F**

MISSION DESCRIPTION
1) WARM UP 2 MIN @ MAX CONT POWER
2) CRUISE OUT AT BEST SPEED RANGE
3) LAND WITH 10% FUEL RESERVE

Figure B.2 Hypothetical helicopter payload/range capability

The takeoff gross weight of 16,000 lb noted in this figure is based on a hover OGE takeoff criteria at 4000 ft/95°F and 100 percent intermediate power. Weight empty increases of 5, 10, and 15 percent are indicated. The incremental increase in weight empty results in an identical reduction in payload capability for a fixed takeoff weight (*TOGW*), as defined in the following equation:

$$TOGW = W_E + PL + W_F + FUL$$

where

W_E = weight empty

PL = payload

W_F = weight of fuel

FUL = fixed useful load.

At the full-fuel point, the 5-percent increase in weight-empty causes a 12-percent reduction in maximum payload capability. The variation in range capability at constant payload is relatively small (2 n.mi., or 0.6 percent). This is due to the increase in average mission gross weight associated with increased weight empty.

The payload/range capability can be maintained in spite of increases in weight empty by increasing the takeoff gross weight, or growing the aircraft. This increase in operational gross weight can be achieved by either modification of operational techniques, or changes in design. The latter approach is usually associated with the concept of aircraft growth, as it consists of (1) increasing the power available, (2) modifying the rotor system to decrease the power required, (3) a combination of these items, and (4) selection of alternate takeoff criteria.

The design changes required to achieve higher operational gross weight result in secondary increases in weight empty (ΔW_{E_2}) and mission fuel (ΔW_F) associated with the higher weight. The secondary increases in weight empty are due to the following required design changes:

(1) Fuel tanks must be enlarged to accommodate the additional mission fuel required.

(2) Landing gear must be strengthened to maintain the design touchdown rate of descent at the higher weight.

(3) Rotor control system must be strengthened.

(4) Body structure must be strengthened to maintain the design load factor.

(5) Drive system must be strengthened because of increased power required.

(6) Hub and blades must be modified because of higher loads.

(7) Horizontal tail size must be increased to maintain acceptable stability level.

(8) Weight of engines if uprated.

(9) Tail boom weight increases if the main rotor radius is increased.

The secondary changes in weight empty (ΔW_{E_2}) due to these items can be estimated from trend curves presented as a function of gross weight. Therefore, the total change in gross weight (ΔGW) required to maintain constant payload-radius capability is as follows:

$$\Delta GW = \Delta W_{E_1} + \Delta W_{E_2} + \Delta W_F.$$

Dividing this expression by the initial increase in weight empty (ΔW_{E_1}) gives the growth factor (GF):

$$GF = \Delta GW/\Delta W_{E_1} = 1 + (\Delta W_{E_2}/\Delta W_{E_1}) + (\Delta W_F/\Delta W_{E_1}).$$

Typically, growth factors vary from 1.5 to 2.0. Assuming that $\Delta W_F/\Delta W_{E_1} \approx 0.1$ and $GF = 1.5$, then

$$\Delta W_{E_2}/\Delta W_{E_1} \approx 1{:}2.5.$$

Therefore, a 2.5-lb initial increase in weight empty results in a total weight empty rise of 3.5 lb ($\Delta W_{E_1} + \Delta W_{E_2}$), and the takeoff gross weight (*TOGW*) required to achieve constant performance is as follows:

$$TOGW = W_{E_0} + FUL + 1.5\Delta W_{E_1} + W_{F_0} + \Delta W_F + PL \qquad \text{(B 1)}$$

where

W_{E_0} = original weight empty
W_{F_0} = initial fuel
ΔW_F = increase in mission fuel.

The effect of using Eq (B1) to predict the TOGW for 5, 10, and 15 percent increases in initial weight empty is shown in Fig B.3. A fixed mission requirement of 331 n.mi. range and a payload of 3820 lb was assumed for these calculations.

INITIAL INCREASE IN WE – %	TOTAL WEIGHT EMPTY – LB	FIXED USEFUL LOAD – LB	TOGW – LB	PAYLOAD – LB	FUEL* – LB
0	9,480	420	16,000	3,820	2,280
5	10,180	420	16,767	3,820	2,347
10	10,878	420	17,522	3,820	2,404
15	11,577	420	18,297	3,820	2,480

*FUEL FOR FIXED RANGE OF 331 N. MI

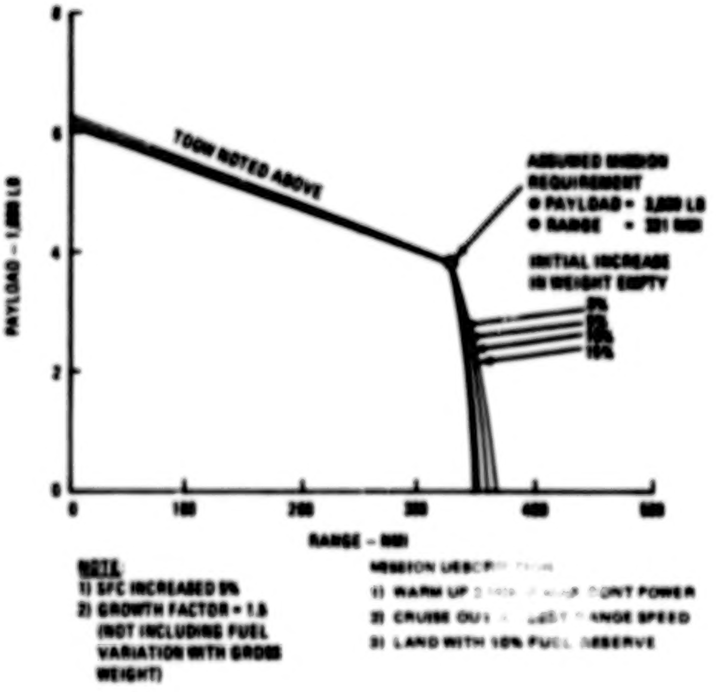

Figure B.3 Gross weight growth required to maintain a fixed payload range capability

Here, an increase of the initial weight empty by 5 percent requires a corresponding 5 percent increase in gross weight. The small variations in payload at zero range and the variation in range approaching zero payload (full-fuel) are due to the nonlinear effect of gross weight on mission fuel. The variation of mission fuel with weight used for sizing the fuel tanks is shown in Fig B.4.

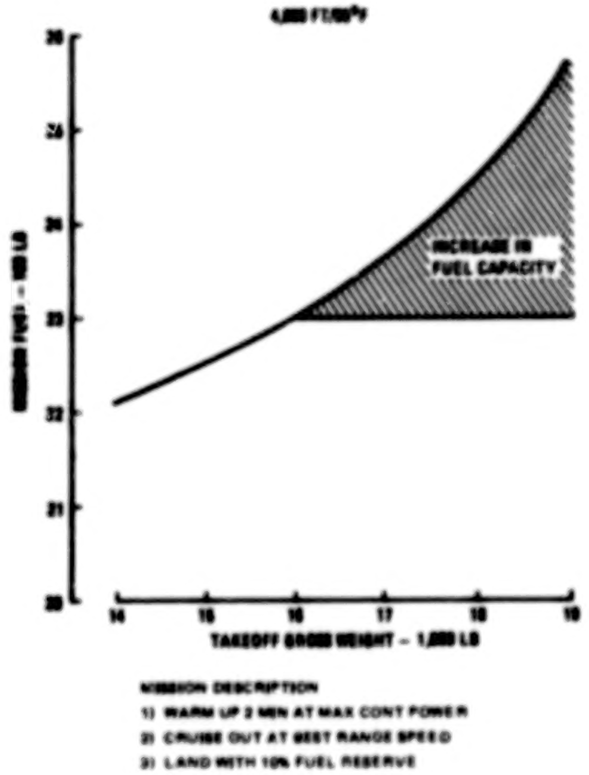

Figure B.4 Fuel required for 331 n.mi. range

In order to take off at the gross weights given in Fig B.3, an increase in engine power is necessary (Fig B.5). It is assumed that the takeoff weight is defined by hover OGE capability at 4000 ft/95°F and 100 percent intermediate power. Power levels required for constant payload as well as constant payload/range are indicated in this figure. It is noted that the percentage increase in power required is almost twice as large as the percentage rise in initial weight empty.

With respect to the powerplant, the question arises whether the required power ratings shown in Fig B.5 can be obtained through growth of the original engine and, if so, what would be the time and cost required to develop these ratings.

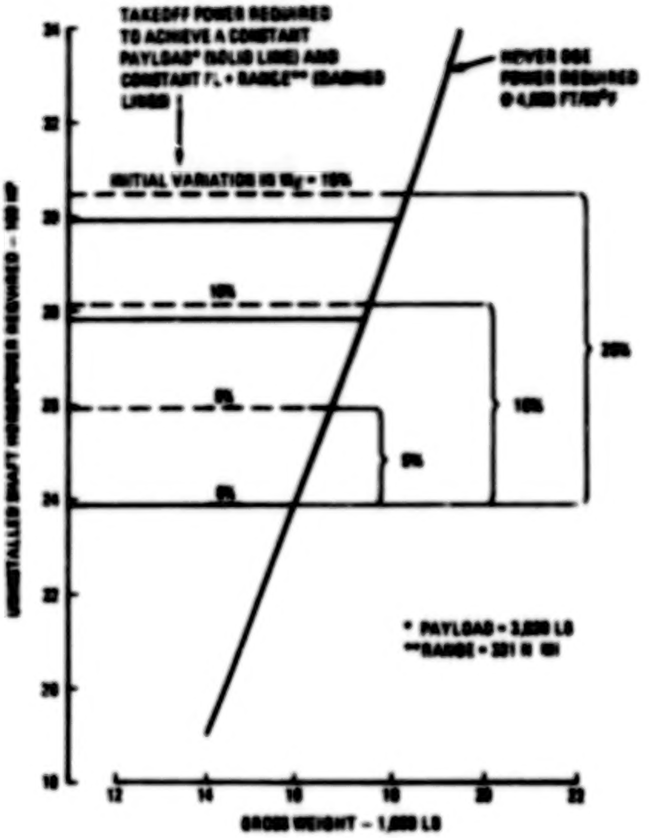

Figure B.5 Takeoff power required to achieve constant payload/range

Some typical production engine growth trends versus years after completion of the initial production testing (MQT) are presented in Fig **B.6**. Statistics indicate that the first 10 to 15 percent increase in engine power occurs 2 to 3 years after the initial MQT. This growth is generally achieved by simply increasing the turbine inlet temperature (TIT) with no significant engine modification. Extensive modification and redesign of the basic engine is usually required to achieve upratings beyond 10 to 15 percent. For example, to obtain engine growth beyond 10 to 15 percent but less than 50 percent, turbine blade cooling is normally needed as well as the addition of another compressor stage. The addition of another turbine may be necessary to increase the power available beyond 50 percent.

It is apparent from Figs **B.5** and **B.6** that the engine modifications required to compensate for initial discrepancies in weight empty of less than 5 percent can be achieved with minimum engine redesign and within approximately 2 to 3 years of the initial MQT. The increase in engine performance required for larger weight-empty variations would call for major engine redesign. Because of the cost and time needed to develop these ratings, the following options are available: (1) redesign the rotor system to decrease

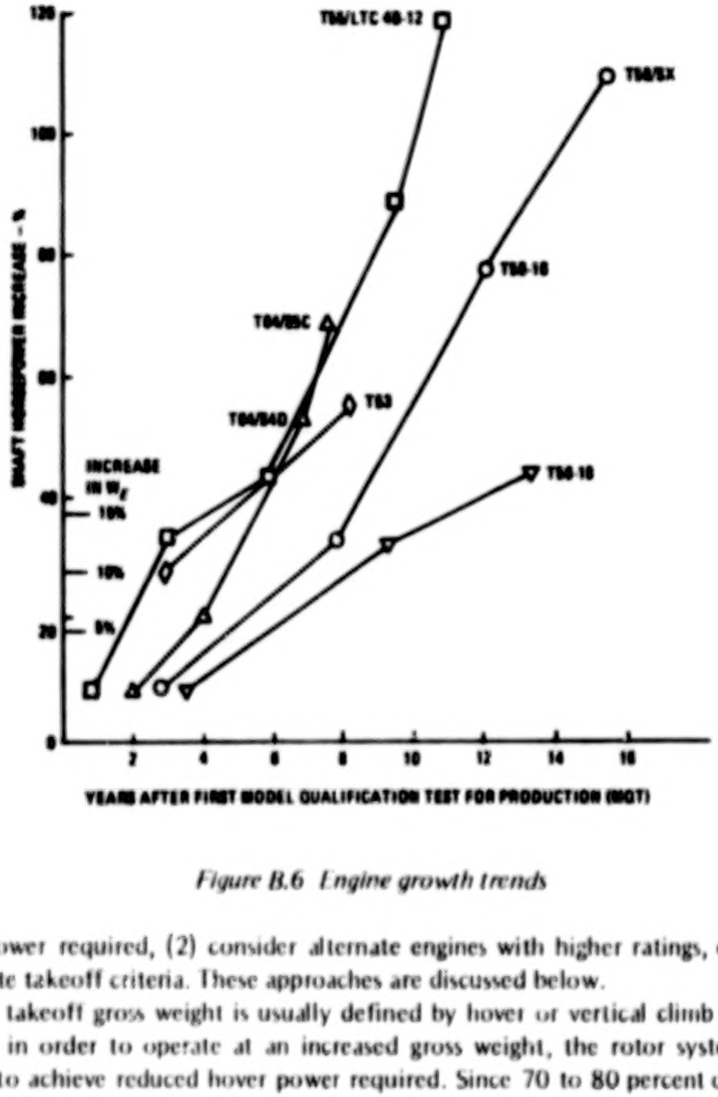

Figure B.6 Engine growth trends

takeoff power required, (2) consider alternate engines with higher ratings, or (3) select an alternate takeoff criteria. These approaches are discussed below.

The takeoff gross weight is usually defined by hover or vertical climb capabilities; therefore, in order to operate at an increased gross weight, the rotor system must be modified to achieve reduced hover power required. Since 70 to 80 percent of the single-rotor aircraft hover power required may be attributed to the main rotor induced power, the largest payoff in takeoff performance can be obtained by reducing this component. As noted in Ch II, the induced power is primarily a function of disc loading and twist. In principle, some gains can be achieved through improved design of the blade tips; but usually the improvements are too small to serve alone as a basis for rotorcraft growth. It should also be noted that the degree of twist is generally limited by forward-flight load considerations. Consequently, rotor radius remains as the most practical design variable.

Dimensionally moderate, but significant performance-wise increases in the main rotor radius can be obtained by adding a section to the tip or by installing a shank extension at the blade root. The tip extension is more desirable from a performance viewpoint since it avoids the small penalty associated with increased blade root cutout[1]. If the chord remains constant, the solidity decreases with increasing radius. The actual blade area, however, increases with radius, resulting in reduced rotor $\bar{c}_\ell$ at a given gross weight. In addition, the rotor rpm must be reduced if the original tip speed and tip Mach number are to be maintained, as assumed in subsequent sample calculations.

When contemplating an extension of the main rotor radius, the side-effects should be considered; for instance, the necessity for, and extent of, fuselage and rotor mast modifications to preserve the necessary clearances and, if the fuselage were extended, what influence would it have on aircraft balance, etc.

The effect of increasing the main rotor radius of the hypothetical single-rotor helicopter on hover OGE gross-weight capability at 4000 ft/95°F is shown in Fig B.7. Takeoff power levels of 100 and 110 percent (uprated engine) are indicated in this figure, while the tip speed and blade chord are assumed constant. The gross-weight capability appears to increase linearly with rotor radius at the rate of 500 lb/ft; however, extrapolation of this data to larger radii shows that thrust (T) developed at a constant power varies as follows: $T \sim R^{2/3}$.

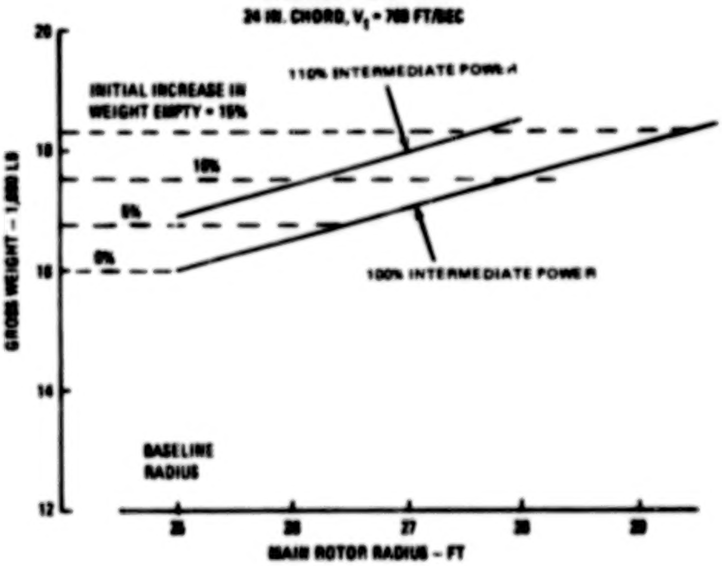

Figure B.7 Effect of radius on HOGE gross weight

The takeoff gross weights required to maintain constant payload and range capability are noted in Fig B.7 for initial empty weight variations of 5, 10, and 15 percent. A growth factor of 1.5 was assumed to account for the effect of radius change on weight empty. The gross weight values also reflect the influence of increasing radius on cruise fuel requirements. The takeoff weight associated with the 5-percent increase in weight empty can be achieved without increasing the radius, if the engines are uprated to 110 percent of initial rating. The larger deviations in empty weight of 10 and 15 percent require the 10 percent power uprating plus radius increases of 1.2 and 2.7 ft, respectively. An additional 2 ft of radius would be required if the engines were not uprated.

The rotor $\bar{c}_\ell$ or C_T/σ values associated with the gross weight variations in Fig B.7 are presented in Fig B.8. This figure shows that the rotor C_T/σ decreases slightly as the radius increases. This occurs because the blade area increases more rapidly than the hover gross weight. Therefore, increasing the radius will not reduce the aircraft airspeed envelope if it is defined by rotor stall considerations.

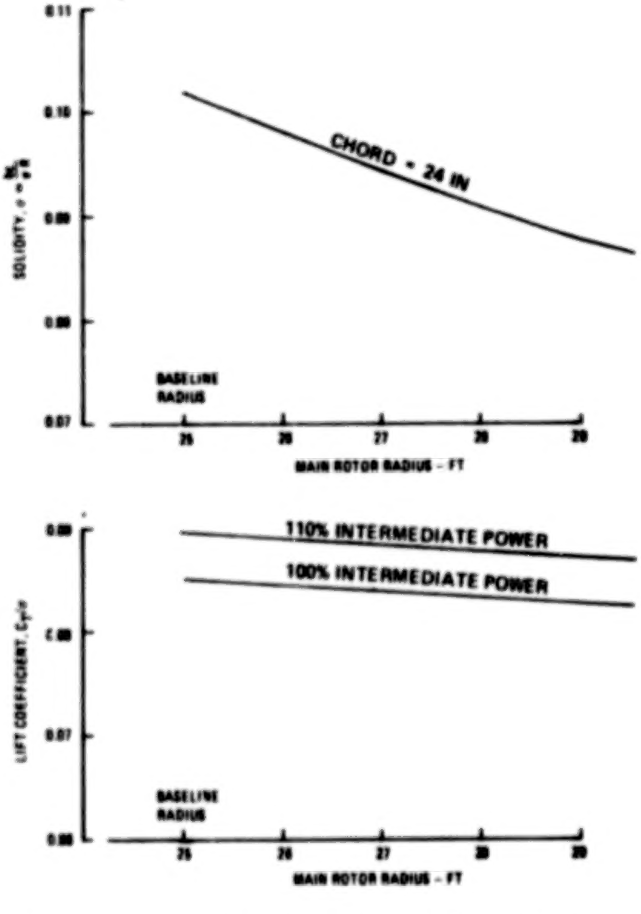

Figure B.8 Effect of rotor radius on solidity and C_T/σ

The effect of varying the main rotor radius on hover performance is computed utilizing the nondimensional power required in Fig 2.6. The main rotor profile and induced power components are nondimensionalized separately because the solidity varies with radius (constant chord). The induced power is nondimensionalized in terms of C_P and C_T as it is primarily a function of the disc area, while the profile power must be defined in terms of C_T/σ and C_P/σ as it is a function of blade area. If the solidity rather than the chord is held constant, then the C_P/C_T data can be applied directly to obtain power required. The blade tip Mach number and tip speed are assumed constant in order to avoid the variation of compressibility power increments with radius. In order to simplify the calculations, tail rotor power, transmission and accessory losses, and engine installation losses are assumed to be a fixed percentage of the total SHP available.

Increasing the main rotor radius will require extending the tail boom to maintain clearance between the main and tail rotors. Redesign of the tail rotor may also be needed, due to increased power available and reduced main rotor rotational speed (rpm). The effect of these design changes on weight empty are included in the growth factor as described previously in this appendix. The growth factor of 1.5 however, does not include the variation in the fuel required with that of the rotor radius.

The effect of gross weight on mission fuel required for the 331 n.mi. mission radius is illustrated in Fig B.9. Here, it is noted that a 3-ft increase in the radius resulted in an 83-lb rise in cruise fuel for a 16,000-lb takeoff weight. This penalty is primarily due to the increase in profile power associated with the enlarged blade area. At constant chord and tip speed, the profile power is proportional to the radius, assuming that the average rotor $\bar{c}_d$ remains the same as before.

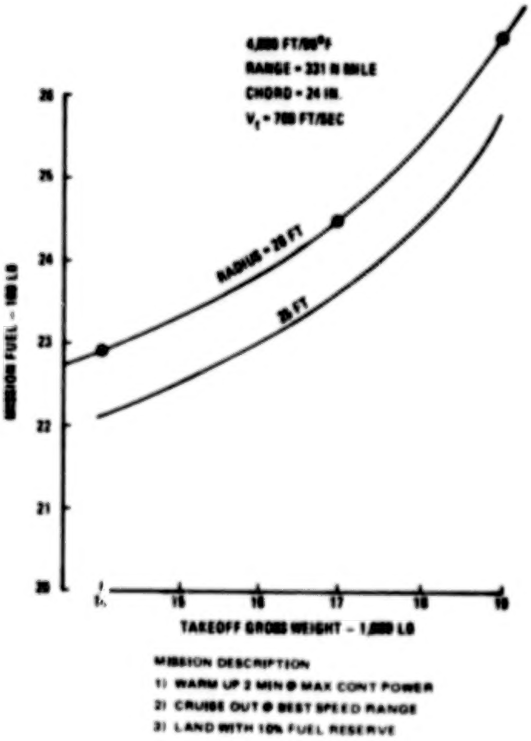

Figure B.9 Effect of rotor radius on mission fuel

Another means of increasing the takeoff gross weight without uprating the engines or modifying the rotor system design is to select an alternate takeoff criteria. For example, if IGE rather than OGE capability were used for the hypothetical helicopter mission, the increase in takeoff weight previously indicated in Fig B.3 could have been met. As noted in this figure, the maximum weight required is 18,307, while the takeoff gross weight capability at 4000 ft/95°F, 100 percent intermediate power IGE (5-ft wheel height) is 18,730 lb. However, the maximum weight limit of 18,000 lb would have to be increased.

The problem with using IGE criteia is that it may not provide a sufficient power margin for climb from a confined area such as a small clearing surrounded by tall trees. The takeoff distance required to clear a given object increases substantially if initiated at full takeoff power from an IGE wheel height because the benefits of ground disappear rapidly during transition. At speeds above 50 kn, there is no significant reduction in power required when operating in ground effect[2]. In fact, more performance capability than provided by hover OGE criteria is often specified to provide a sufficient operational margin. For instance, the current takeoff criteria for Army missions such as the UTTAS mission specify a 500-fpm vertical climb capability at 95 percent of the intermediate power.

References for Appendix B

1. Fradenburgh, E.A. *Aerodynamic Factors Influencing Overall Hover Performance*. Paper No. 7, AGARD CPP-111, September 1972.

2. Cheeseman, I, and J.J.A. Bennett. *The Effect of the Ground on a Helicopter Rotor in Forward Flight*. Published in British Aerospace and Armament Experimental Establishment Report No. AAEE/2/88, July 1955.

1. Report No. NASA CR-3083	2. Government Accession No.	3. Recipient's Catalog No.

4. Title and Subtitle Rotary-Wing Aerodynamics Volume II - Performance Prediction of Helicopters	5. Report Date January 1979
	6. Performing Organization Code
7. Author(s) C. N. Keys Revised and Edited by W. Z. Stepniewski	8. Performing Organization Report No.
	10. Work Unit No.
9. Performing Organization Name and Address Boeing Vertol Company Philadelphia, Pa.	11. Contract or Grant No. NAS2-7007
	13. Type of Report and Period Covered Contractor Report
12. Sponsoring Agency Name and Address National Aeronautics and Space Administration Washington, D. C. 20546	14. Sponsoring Agency Code

15. Supplementary Notes

16. Abstract

Application of theories presented in Volume I, as well as special methods of procedures applicable to performance prediction is illustrated first, on an example of the conventional helicopter described in Chapter I, and then winged and tandem configurations. Chapter II deals with performance prediction of conventional helicopters in hover and vertical ascent. In Chapter III, various approaches to performance prediction in forward translation are presented. Chapter IV deals with performance problems previously discussed in Chapters II and III; only this time, a wing is added to the baseline configuration, and both aircraft are compared with respect to their performance. In Chapter V, this comparison is extended to a tandem. Appendices on methods for estimating performance guarantees and growth of aircraft concludes this volume.

17. Key Words (Suggested by Author(s)) Performance Prediction, Classic Helicopter, Winged Helicopter, and Tandem Helicopter	18. Distribution Statement Unclassified Star Category - 02

19. Security Classif. (of this report) Unclassified	20. Security Classif. (of this page) Unclassified	21. No. of Pages 233	22. Price* $9.50

*For sale by the National Technical Information Service, Springfield, Virginia 22161

NASA-Langley, 1979

END

APR. 30, 1979